



저작자표시-비영리-변경금지 2.0 대한민국

이용자는 아래의 조건을 따르는 경우에 한하여 자유롭게

- 이 저작물을 복제, 배포, 전송, 전시, 공연 및 방송할 수 있습니다.

다음과 같은 조건을 따라야 합니다:



저작자표시. 귀하는 원저작자를 표시하여야 합니다.



비영리. 귀하는 이 저작물을 영리 목적으로 이용할 수 없습니다.



변경금지. 귀하는 이 저작물을 개작, 변형 또는 가공할 수 없습니다.

- 귀하는, 이 저작물의 재이용이나 배포의 경우, 이 저작물에 적용된 이용허락조건을 명확하게 나타내어야 합니다.
- 저작권자로부터 별도의 허가를 받으면 이러한 조건들은 적용되지 않습니다.

저작권법에 따른 이용자의 권리는 위의 내용에 의하여 영향을 받지 않습니다.

이것은 [이용허락규약\(Legal Code\)](#)을 이해하기 쉽게 요약한 것입니다.

[Disclaimer](#)

이학박사 학위논문

Study of Energetic Astronomical Phenomena  
with Time-series Observation:

Active Galactic Nucleus  
and Gravitational Wave Source

고에너지 천문학적 현상에 대한 시계열 관측 연구:  
활동성은하핵과 중력파 천체

2021년 8월

서울대학교 대학원  
물리·천문학부 천문학전공  
김 준 호



Study of Energetic Astronomical Phenomena  
with Time-series Observation:

Active Galactic Nucleus and Gravitational Wave Source

고에너지 천문학적 현상에 대한 시계열 관측 연구:

활동성은하핵과 중력파 천체

지도교수 임 명 신

이 논문을 이학박사 학위논문으로 제출함

2021년 8월

서울대학교 대학원  
물리천문학부 천문학전공

김 준 호

김준호의 이학박사 학위논문을 인준함

2021년 8월

위원장 이 형 목

부위원장 임 명 신

위 원 우 중 학

위 원 김 상 철

위 원 김 민 진



**Study of Energetic Astronomical Phenomena  
with Time-series Observation:  
Active Galactic Nucleus  
and Gravitational Wave Source**

by

Joonho Kim  
(joonho@astro.snu.ac.kr)

A dissertation submitted in partial fulfillment of the requirements for  
the degree of

**Doctor of Philosophy**

in

Astronomy

in

Astronomy Program

Department of Physics and Astronomy

Seoul National University

Committee:

Professor Hyung Mok Lee

Professor Myungshin Im

Professor Jong-Hak Woo

Doctor Sang Chul KIM

Professor Minjin Kim



# ABSTRACT

In this thesis, the energetic astronomical phenomena, active galactic nucleus (AGN) and gravitational wave (GW) source, were studied with time-series observation. They emit large amounts of energy and play an important role in the history of the Universe.

Variability is one of the typical characteristics of AGN. In Particular, short-term variability is used to constrain the structure of the accretion disk around the super massive black hole (SMBH). For this study, time-series observation data with the Korea Microlensing Telescope Network (KMTNet) are obtained on three separate nights for 2.5 - 5 hours with 20 - 30 minute cadence which targets the COSMOS field. In the field, 394 AGNs are selected by four selection methods that are X-ray, mid-infrared, radio selection and SDSS quasars. Variable AGNs are classified in  $\chi^2$ -test at a photometric accuracy of  $\sim 0.02$  mag for the sources with  $\sim 18$  mag in R band. However, the variable AGN fraction shows 0 - 8 % which is a statistically null result. Only eight AGNs (2 %) are variable with a variability amplitude of  $\sim 0.1$  mag in two filters or two nights.

Reverberation mapping (RM) is a method to measure the size of broad line region (BLR) and the SMBH mass of AGN using the variability and the line width of the broad emission line (BEL). In general, it needs spectroscopic monitoring and it is hard to study large amounts of AGN samples. Another way is to use medium-band photometry which filter width is enough to cover BEL. Five nearby AGNs are observed by a 0.43 m telescope for  $\sim 3$  months with three medium-bands. The result of the time lag estimation between continuum and  $H\alpha$  using JAVELIN software gives 1.5 - 15.9 days and they are consistent with previous studies of spectroscopic RM. When the medium-band photometric RM is used with a wide-field telescope such as KMTNet, tens of thousands AGNs can be studied.

The photometric RM with medium-bands is applied for six Palomar-Green quasars. They are monitored for May. 2018 - Sep. 2020 with three medium-band filters. The time lags of  $H\beta$  and  $H\gamma$  BELs are measured using JAVELIN. The results agree with the correlation between time lag (BLR radius) and the luminosity of the previous studies,

but the intrinsic scatter of 0.37 dex is higher than previous studies of 0.19 dex. The mass of SMBH is calculated using the time lag and the line width and it agrees with the single epoch measurement method.

Three GW events (GW190408, GW190412, and GW190503) detected by the LIGO and Virgo are followed up by optical telescopes. The events are binary black hole (BBH) mergers which are not expected to emit electromagnetic (EM) counterparts in general. Assuming the special environments emitting EM counterparts, high probable regions are observed by Gravitational-wave Electromagnetic Counterpart Korean Observatory (GECKO). The observation started 1.6 - 6.0 hours after the GW alert and 29 - 63 deg<sup>2</sup> are covered with a depth of  $\sim 22.5$  mag in R-band. However, no possible EM counterparts were detected in all events. Using the image depth of the GW190503 event, the magnitude of the EM counterpart of BBH is constrained as  $M_g > -18.0$  AB mag within 1 day from the GW event. If the kilonova with a luminosity distance of  $< 400$  Mpc and a 90% localization area of  $< 50$  deg<sup>2</sup>, GECKO follow-up observation can find the optical counterpart within a few hours after the GW alert in the future.

The results from this thesis show that multiple scientific questions regarding AGNs and GW sources can be answered with time series observations, observational facilities, and unique capabilities such as the round-the-clock observations with a wide-field telescope for intra-day cadence AGN variability, the medium-band RM of AGNs, and GW EM counterpart observation.

**Keywords:** active galactic nuclei; AGN; quasar; supermassive black hole; variability; KMTNet; gravitational wave; optical follow-up

***Student Number:*** 2015-22602

# Contents

<b>Abstract</b>	<b>i</b>
<b>List of Figures</b>	<b>vii</b>
<b>List of Tables</b>	<b>x</b>
<b>1 Introduction</b>	<b>1</b>
1.1 Time-series Astronomy . . . . .	1
1.2 Active Galactic Nucleus . . . . .	2
1.3 Variability of AGN . . . . .	4
1.4 Reverberation Mapping of AGN . . . . .	6
1.5 Gravitational Wave Source . . . . .	8
1.6 Research Purpose and Thesis Outline . . . . .	9
<b>2 Intra-night optical variability of AGN in the COSMOS field with the KMTNet</b>	<b>13</b>
2.1 Introduction . . . . .	13
2.2 Observation . . . . .	16
2.3 Data analysis . . . . .	18
2.4 AGN Samples . . . . .	18
2.4.1 X-ray selected AGNs . . . . .	19
2.4.2 Mid-Infrared selected AGNs . . . . .	20
2.4.3 Radio selected AGNs . . . . .	20

2.4.4	SDSS DR7 quasars catalog . . . . .	23
2.4.5	Short summary on AGNs selected from different methods . . . . .	23
2.5	Variability of AGN . . . . .	27
2.6	Results . . . . .	32
2.7	Discussion and Conclusion . . . . .	37
<b>3</b>	<b>Medium-band Photometry Reverberation Mapping of Nearby Active Galactic Nuclei</b>	<b>57</b>
3.1	Introduction . . . . .	57
3.2	Sample and Observation . . . . .	60
3.3	Medium-band Photometry and Light Curve . . . . .	61
3.4	AGN Variability . . . . .	78
3.5	Result: Medium-band Based Time Lags . . . . .	78
3.6	Discussion: Implications for future medium-band RM study . . . . .	84
3.7	Summary . . . . .	87
<b>4</b>	<b>Reverberation Mapping of Six PG Quasars with Medium-band Photometry</b>	<b>89</b>
4.1	Introduction . . . . .	89
4.2	Data . . . . .	91
4.2.1	Sample selection . . . . .	91
4.2.2	Observation . . . . .	94
4.3	Photometry . . . . .	94
4.4	Variability . . . . .	102
4.5	Time Lag . . . . .	102
4.6	Discussion . . . . .	108
4.6.1	$H\beta$ and $H\gamma$ time lag comparison . . . . .	108
4.6.2	Time lag uncertainty versus observational parameters . . . . .	108
4.6.3	Comparison with the known AGN correlations . . . . .	110
4.7	Summary . . . . .	114

<b>5</b>	<b>GECKO Optical Follow-up Observation of Three Binary Black Hole Merger Events, GW190408_181802, GW190412, and GW190503_185404115</b>	
5.1	Introduction . . . . .	115
5.2	Gravitational Wave Events . . . . .	118
5.2.1	GW190408 . . . . .	119
5.2.2	GW190412 . . . . .	119
5.2.3	GW190503 . . . . .	120
5.3	Observation . . . . .	120
5.3.1	Telescopes . . . . .	120
5.3.2	Basic observation strategy . . . . .	122
5.3.3	Observations . . . . .	123
5.4	Data Analysis and Transient Search . . . . .	137
5.5	Transient Search Result . . . . .	141
5.6	Discussion . . . . .	142
5.6.1	Limits on BBH EM Counterpart Brightness . . . . .	142
5.6.2	Comparison with Kilonova Light-curve Models . . . . .	143
5.6.3	Prospects for Rapid Follow-up Observation . . . . .	145
5.6.4	Need for Deep Reference Images . . . . .	146
5.7	Summary . . . . .	146
<b>6</b>	<b>Conclusion</b>	<b>149</b>
	<b>Bibliography</b>	<b>153</b>
	<b>요약</b>	<b>167</b>



# List of Figures

1.1	Unification model of AGN . . . . .	3
1.2	Correlation between the mass of SMBH and the bulge mass . . . . .	5
1.3	The continuum and $H\beta$ emission line light curves of Mrk 335 . . . . .	7
2.1	Mid infrared color-color diagram of the KMTNet detected sources . . .	21
2.2	The distribution of 1.4GHz radio power and redshift of the KMTNet detected sources . . . . .	22
2.3	Positions of the selected AGNs . . . . .	24
2.4	The apparent magnitude in $R$ band and redshift of selected AGNs . . .	25
2.5	The apparent magnitude and redshift histogram of AGNs . . . . .	26
2.6	The standard deviation of the $R$ band magnitudes versus the mean $R$ band magnitude . . . . .	28
2.7	The standard deviation of the $R$ band magnitudes versus the mean pho- tometric error . . . . .	29
2.8	$\sigma_{LC}$ , $\chi^2$ and 1-p with their apparent magnitude . . . . .	30
2.9	The light-curves of eight variable AGNs . . . . .	36
3.1	SDSS spectrum of Mrk 1310 and transmission curves of the medium- band filters . . . . .	62
3.2	The images of the five AGNs in $m675$ . . . . .	63
3.3	Comparison between the spectra and the medium-band photometry . .	64
3.4	The continuum and the $H\alpha$ emission line light curves . . . . .	66

3.5	Continued of Figure 3.4 . . . . .	67
3.6	Time lag measurement results for the five AGNs . . . . .	80
3.7	Comparison of the time lag results between this study and previous studies	85
3.8	The time lag uncertainty decreases with $S/N \times \text{excess variability} \times t_{\text{lag}}/\Delta t$	86
4.1	The medium-band filter transmission curves on the spectra . . . . .	95
4.2	The first epoch image of the six AGNs . . . . .	96
4.3	The light-curves of the continuum and $H\beta$ of all AGNs. . . . .	98
4.4	Continued of Figure 4.3 . . . . .	99
4.5	The light-curves of the continuum and $H\gamma$ of all AGNs. . . . .	100
4.6	Continued of Figure 4.5 . . . . .	101
4.7	The histogram of the time lags . . . . .	103
4.8	Comparison between the time lags derived from JAVELIN and ICCF . .	107
4.9	Correlation of the time lag uncertainties with $S/N$ , $\sigma_{\text{excess}}$ , $t_{\text{lag}}/\Delta t$ , $t_{\text{lag}}/t_{\text{obs}}$ , and duty dycle. . . . .	109
4.10	BLR radius of $H\beta$ emission line and $5100 \text{ \AA}$ luminosity (R-L) relationship	111
4.11	Comparison between black hole mass measurements . . . . .	112
5.1	The localization and coverage of tiling observation for three GW events	121
5.2	Three transients found in the follow-up observation of GW190412 event	138
5.3	Comparison of different model light curves of kilonova and the KMTNet image depths . . . . .	144

# List of Tables

2.1	KMTNet-CTIO observations on the COSMOS field . . . . .	17
2.2	Classification of X-ray selected AGNs in $R$ band of the 2016 April data	19
2.3	The number of detected and variable AGNs with their fraction in the bracket . . . . .	34
2.4	Information of eight variable AGNs . . . . .	35
2.5	List of observed AGNs . . . . .	41
3.1	List of the monitored AGNs . . . . .	61
3.2	The continuum and the $H\alpha$ emission line light curve of five nearby AGNs	68
3.2	The continuum and the $H\alpha$ emission line light curve of five nearby AGNs	69
3.2	The continuum and the $H\alpha$ emission line light curve of five nearby AGNs	70
3.2	The continuum and the $H\alpha$ emission line light curve of five nearby AGNs	71
3.2	The continuum and the $H\alpha$ emission line light curve of five nearby AGNs	72
3.2	The continuum and the $H\alpha$ emission line light curve of five nearby AGNs	73
3.2	The continuum and the $H\alpha$ emission line light curve of five nearby AGNs	74
3.2	The continuum and the $H\alpha$ emission line light curve of five nearby AGNs	75
3.2	The continuum and the $H\alpha$ emission line light curve of five nearby AGNs	76
3.2	The continuum and the $H\alpha$ emission line light curve of five nearby AGNs	77
3.3	Variability and time lag of monitored AGNs. . . . .	83
4.1	List of the monitored AGNs . . . . .	93
4.2	Variability of targets . . . . .	97
4.3	Time lag and black hole mass of monitored AGNs . . . . .	106

5.1	Target GW events . . . . .	118
5.2	Tiling observation summary of the three GW events . . . . .	126
5.2	Tiling observation summary of the three GW events . . . . .	127
5.2	Tiling observation summary of the three GW events . . . . .	128
5.2	Tiling observation summary of the three GW events . . . . .	129
5.2	Tiling observation summary of the three GW events . . . . .	130
5.3	Galaxy observation of GW190412 . . . . .	131
5.3	Galaxy observation of GW190412 . . . . .	132
5.3	Galaxy observation of GW190412 . . . . .	133
5.3	Galaxy observation of GW190412 . . . . .	134
5.3	Galaxy observation of GW190412 . . . . .	135
5.3	Galaxy observation of GW190412 . . . . .	136
5.3	Galaxy observation of GW190412 . . . . .	137
5.4	Observation summary . . . . .	139
5.5	List of detected transients and transient candidates . . . . .	140
5.6	List of moving objects . . . . .	141

# Chapter 1

## Introduction

### 1.1 Time-series Astronomy

Time-series astronomy begun with the history of astronomy. Ancient people observed the Sun and found the change of its position and sunspot. Also, the Moon showed the change of its position and phase. Their changes over time affect the earth in various ways such as season, weather, and tide. So, they are used to make the calendar and became the standard of the time for humans. In the Middle Ages, observations of the movements of planets over the sky brought us toward heliocentric theory from geocentric theory. Like this, astronomers mainly studied positional changes over time of celestial objects, especially for solar system objects. In modern astronomy, this kind of study is developed to observe stars and have found their proper motion or parallax.

Not only the positional change, time-series observations report brightness changes for various objects. The first one is periodic variability which are mainly stars. Due to the pulsations, stars like Cepheids and RR Lyrae show periodicity. The period shows correlation with the luminosity and has an important role in the cosmic distance ladder of the local Universe. Some binary stars or star - planet binary are observed to have periodicity from their eclipse of each other. Using the light-curves of them, we can estimate their properties like mass and orbital radius.

Second variable sources are transient objects which are suddenly observed in the

sky, such as, novae, kilonovae, supernovae, gamma-ray bursts, and tidal disruption events. The transients are usually the results of the explosion or collision of stars and they emit large amount of energy. These energy emitted to the space have affected the evolution of the Universe in some ways. Also, type Ia supernovae is another member of the distance ladder of the distant Universe as a standard candle. After the operation of gravitational wave detectors, a kilonova was observed as a counterpart of gravitational wave detection. Because the gravitational wave detectors have low positional accuracy, electromagnetic follow-up observations of transients are important.

Another one is stochastic variability. It is found from the accretion systems like active galactic nuclei (AGNs). Its variability has been used to estimate the size and mass of the system. In particular, AGNs emit lots of energy comparable to its host galaxy and they also influence to the history of the Universe.

From recent development of gravitational wave detectors and future time-series observations with large telescopes like Large Synoptic Survey Telescope, faint and distant variable sources become promising targets to study. In the near future, many of such objects will be observed with time-series data. Statistical analysis of them is expected to improve our understanding of the Universe. In this thesis, two energetic astronomical phenomena, AGN and gravitational wave source, are studied with time-series observations.

## **1.2 Active Galactic Nucleus**

AGN is one of the energetic phenomena in the Universe. In the observational perspective, it shows some characteristics, such as bright central region, broad and/or narrow emission lines, multi-wavelength continuum emission from X-ray to radio, relativistic jet, and variability. But, not every AGN shares these properties. Historically, it makes astronomers believe that energetic features of many kinds of AGNs (Seyfert galaxy, quasar, radio galaxy, blazar, and others) come from different origin.

Theoretical predictions tell us that only the inward accretion flow of matter to supermassive black hole (SMBH) accounts for lots of energy from such a compact region.

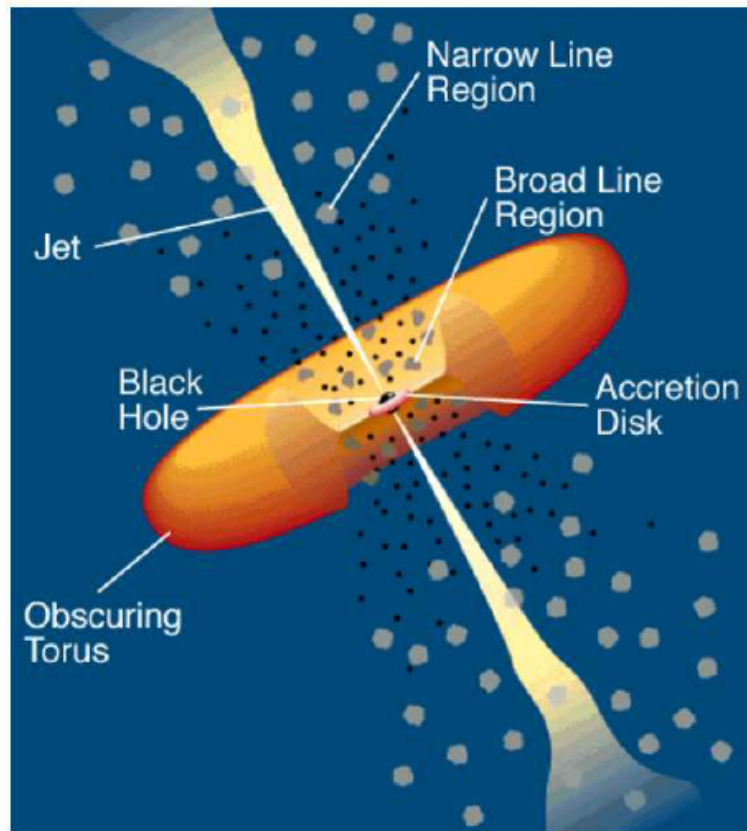


**Figure 1.1.** Schematic diagram for the unification model of AGN from Urry & Padovani (1995).

Antonucci (1993), Urry & Padovani (1995), and Urry (2003) present classical version of unification model of AGN (Figure 1.1). To involve the observational characteristics of AGN, the model consists of central SMBH, accretion disk, broad and narrow line regions, obscuring torus, and jet. Then, the different kinds of AGNs can be explained by the viewing angle from the Earth. Recent studies with earth-sized radio interferometer (Event Horizon Telescope) observed a black hole in the center of a radio galaxy and it confirmed the existence of SMBH of the unification model of AGN (EHT Collaboration et al. 2019).

A radio source, 3C 273 was observed with a redshift of 0.158 in the spectral analysis which was a high redshift at the time (Schmidt 1963). This kind of object is named

as quasar and we realize now that the quasar is a kind of AGNs. Because of the high bolometric luminosity of  $L_{\text{bol}} \sim 10^{42} - 10^{48} \text{ erg s}^{-1}$  (Woo & Urry 2002) which is similar to or brighter than the rest of its host galaxy, AGNs can be found in very high redshift as far as 7.642 (Wang et al. 2021). It means that we can explore from the present Universe to the past Universe until reionization era with AGN.

Another importance of AGN is the effect on their host galaxy. In the SMBH system, the mass is one of the representative parameters and it can be measured using the variability. It is found that the masses of SMBHs have a good correlation with the velocity dispersions of the bulges (Kormendy & Ho 2013) implying the coevolution of SMBHs and its host galaxies (Figure 1.2). Also, due to the enormous energy emissions from AGNs, they affect star formation of the host galaxies by heating the gas. It is expected to solve the overcooling problem in cosmological simulations of  $\lambda$ -CDM models that too many massive galaxies are formed than the number obtained from the observations. In this way, AGNs would have made effect on the Universe as one of the energetic sources. To know the role of AGNs in the history of the Universe, it is worth to study properties and mechanisms of AGN.

### 1.3 Variability of AGN

Variability is one of the important properties of AGNs. First report of optical variability of AGNs (Matthews & Sandage 1963) is found in the same year with the discovery of the first quasar. Sharing the history of quasars, studies on the AGN variability have been made for more than half a century.

So far, multiwavelength variability from X-ray to radio has been reported in various observations. Also, there are many studies that present AGN variability in short-term of days (or hours), to year timescale (Ulrich et al. 1997). The short-term variability from hours to days is an evidence for the subparsec sized compact energy source. However, considering very high luminosity of AGNs, it is hard to be explained by a star or a star cluster and need another efficient mechanism. Therefore, it has been an evidence for a central SMBH with accretion disk as the energy source of AGNs. Meanwhile, the long-

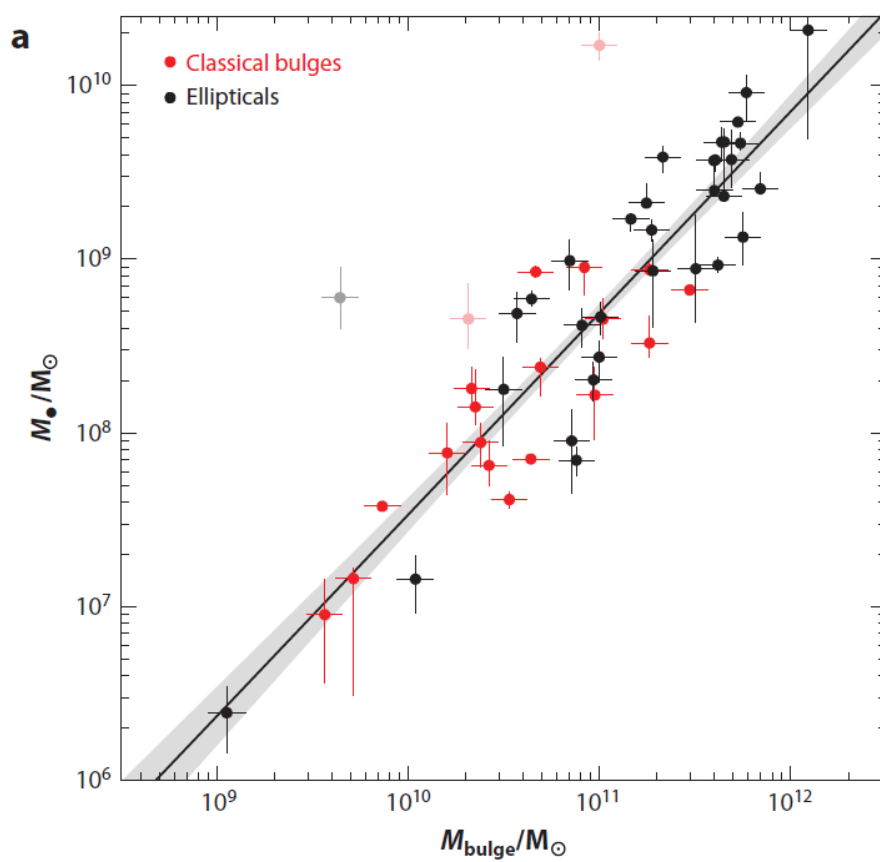


**Figure 1.2.** Correlation between the mass of SMBH and the bulge mass from Kormendy & Ho (2013).

term monitoring campaigns have started before the 21th century for few AGNs. As one of the best examples, NGC 5548 have been observed from 1988 (Peterson et al. 1999). Peterson et al. (1999) found that the AGN variability in NGC 5548 is non-periodic and the variability amplitude is higher in longer timescale than that in shorter timescale.

Some studies are have to establish correlation between the variability and the AGN properties. The anticorrelation between the optical variability and the luminosity is initially reported by Hook et al. (1994) and Giveon et al. (1999). On the other hand, some efforts of finding correlation of variability with black hole mass or eddington ratio show no or weak correlation. Most of the investigations of such correlations are based on the long-term variability of months to years timescale. Therefore, correlation of the AGN properties with the short-term variability is needed to be studied.

## 1.4 Reverberation Mapping of AGN

Using two AGN characteristics, the variability and the broad emission lines (BELs), we can measure the sizes of the broad line regions (BLRs) and the masses of SMBHs. It is one of the direct measurement methods of the SMBH mass, and called reverberation mapping (RM). The technique, RM, is suggested by Blandford & McKee (1982) and later developed by Peterson (1993).

If the continuum flux is variable by the instability of the accretion disk, it is echoed in BLR and photoionized BELs are observed with variability. Because of the distance of BLR from the accretion disk, light curves of the continuum and BEL show the time lag (Figure 1.3). Also, together with the line width of BEL, which is the velocity of BLR, we can estimate the virial mass of SMBH as Equation (1.1),

$$GM_{\text{BH}} = fR_{\text{BLR}}(\Delta V)^2 \quad (1.1)$$

where,  $G$  is the gravitational constant,  $M_{\text{BH}}$  is the mass of SMBH,  $f$  is the scale factor depending on the BLR structure,  $R_{\text{BLR}}$  is the characteristic radius of BLR, and  $\Delta V$  is the width of BEL.

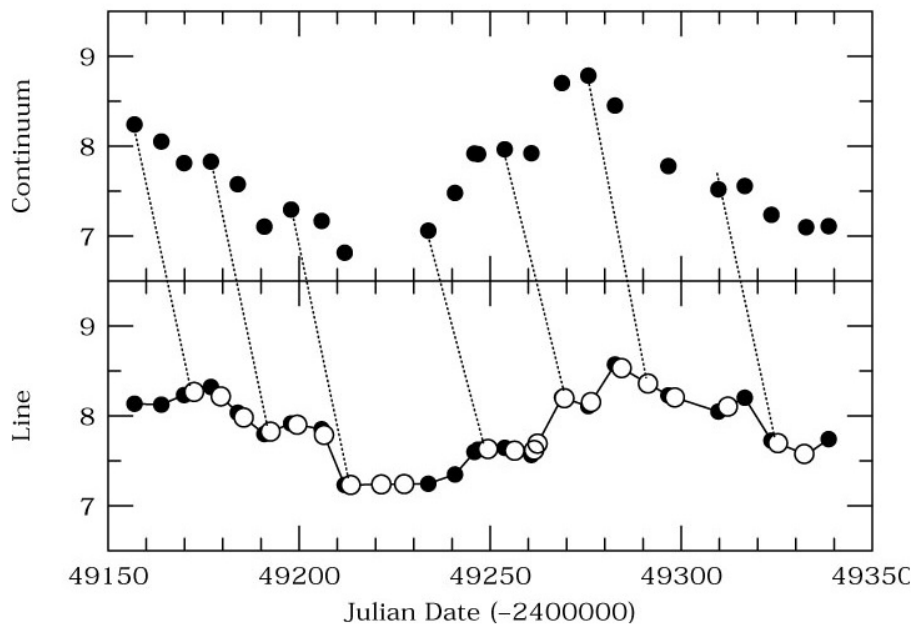


**Figure 1.3.** The continuum and  $H\beta$  emission line light curves of Mrk 335 from Peterson (2001).

The RM results show tight relationship between the BLR radius and the continuum luminosity (Kaspi et al. 2000) which is theoretically expected in the photoionization. Using the relation, we can estimate the mass of SMBH with the luminosity and the line width from single epoch spectroscopy without time-series observations. But the sample for the RM study is an order of hundred that is too small number, and still need monitoring for more AGN samples.

However, there are some difficulties in studying RM. It needs spectroscopic monitoring for months to years and massive amounts of observation time is essential. Especially, high luminosity AGNs are expected to have longer time lag of a few years from the relation between the BLR radius and the luminosity. Moreover, the anticorrelation between the variability and the luminosity makes it hard to study RM for AGNs in the high luminosity end.

## 1.5 Gravitational Wave Source

The merger of compact binary objects, such as neutron stars or black holes, is another energetic astronomical phenomena in the Universe. We can observe the electromagnetic (EM) wave as an afterglow, if both of the merging objects are not the black holes. Also, it radiates the highest amplitude of the gravitational wave (GW) comparing to the weaker GW of the normal rotation phase of the binary system.

GW is one of the anticipations of the general relativity, but direct observation of GW is not made because of the difficulty of making the GW detector sensitive enough. Indirect observation of GW is performed by Taylor & Weisberg (1982, 1989) which found orbital decay of a binary pulsar system and they are awarded the 1993 Nobel Prize in Physics.

Thanks to the developments of engineering, laser interferometers, Laser Interferometer Gravitational-Wave Observatory Collaboration and Virgo Collaboration (LVC), are constructed for the direct observation of GW and finally detected GW from the binary black hole merger in 2015 September 14 (Abbott et al. 2016). Confirming the general relativity again, Rainer Weiss, Kip Thorne and Barry Barish received the 2017

Nobel Prize in Physics.

In 2017 August 17, LVC observed a GW from the binary neutron star merger (Abbott et al. 2017a). The gamma-ray burst is detected two seconds after the GW detection (Abbott et al. 2017c). Also, about 17 hours after the GW detection, optical counterpart is found at NGC 4993 by observations in Chile (Abbott et al. 2017b). It was the first EM counterpart of GW sources and opened the multimessenger astronomy era.

In the GW analysis, the distance and the redshift is measured and it can be used to constrain cosmological constants. To reduce the uncertainty in the redshift, it is needed to observe the EM counterparts and get the redshift with higher accuracy in the spectroscopy. Also, the observation of the EM counterparts can give the clues on the collision mechanism of the compact binary merger and their environment. The origin of heavy elements (heavier than iron) like gold is not clear. From the r-process of energetic phenomena like the neutron star merger, less known part of the heavy elements formation can be studied.

## 1.6 Research Purpose and Thesis Outline

The research purpose of this thesis is to tackle several outstanding questions on energetic astrophysical phenomena such as AGNs and GW sources with time-series observations with various unique observational facilities. In particular, we will try to address the following issues: (i) the fraction of AGN with intra-day variability with KMTNet which can monitor the sky 24 hrs a day; (ii) the development of a new medium-band technique to perform RM study on AGNs; and (iii) to utilize a round-the-clock observational capability of KMTNet to search for EM counterparts of GW sources. Scientific purpose of each topic as well as the thesis outline are given below.

AGN variability in short-term timescale of hours to days tells us the variation in the smallest region of AGN and it is important to measure the size of the accretion disk. However, so far, the short-term variability has been studied for only a small number of AGNs. In Chapter 2, we examine the short-term variability of hundreds of AGNs in

the COSMOS field with a timescale of hours. We utilize AGN samples that are selected in four different ways, and study the fraction of AGNs showing short-term variability. We expect that our result will place a useful limit on the fraction of AGNs showing intra-day variability.

Another issue of AGN variability is the time lag between the continuum and the broad line flux variabilities. Some studies have used photometry data for RM with broad-band, medium-band, narrow-band, or combination of them. Such a method has an advantage over the traditional spectroscopic RM in that the observation of more than one object is possible in a single frame observation, and it demands the observation time much less than spectroscopy. As a new approach, we tried medium-band photometric RM to test the feasibility of the technique. Chapter 3 describes our medium-band RM study on a number of AGNs with short time lags ( $<$  weeks), demonstrating that the medium-band RM is indeed a promising technique. Chapter 4 describes the application of the medium-band RM to an AGN sample with longer time-lags (weeks or longer) and we also estimate the mass of SMBH in these AGNs. The results suggest that a dedicated wide-field telescope employing medium-band filters can be used to perform RM on thousands of AGNs.

As a next topic of the time-domain studies of energetic phenomena, we investigate if there are EM emissions associated with binary black hole mergers by observing GW events. In general, binary black hole mergers are not expected to emit EM waves. If special environments exist around black holes where dense gases (e.g., AGN accretion disk) may interact with the space-time distortion caused by the merger, EM signals may be detected. During the third observation run of the LIGO/Virgo GW detectors that lasted from April, 2019 to March, 2020, we observed a number of GW events with GECKO, our optical telescope network, to study EM counterparts of GW events. Among these followed up by us, we report the results on three GW events that are caused by binary black hole mergers. Search results for the optical counterparts of the GW events and our follow-up observation strategy are remarked in Chapter 5, along with the lessons learned from these observations.

Finally, the thesis is concluded in Chapter 6.



## Chapter 2

# Intra-night optical variability of AGN in the COSMOS field with the KMTNet<sup>†</sup>

### 2.1 Introduction

Flux variability is characteristic for an active galactic nucleus (AGN). Because they are hard to resolve spatially, variability is widely used to study the size, mass, and structure of AGN. Observations have discovered that AGN variability appears not only in various wavelengths, but also shows various timescales from hours to years. The results show an increase in variability amplitude at shorter wavelengths and longer timescales (see references therein). In addition, there is an inverse correlation between long-term variability and luminosity while there is a positive correlation between long-term variability and redshift, as discovered by Uomoto et al. (1976) and Pica & Smith (1983).

Unfortunately, the origin of variability is not completely known. Generally, instability in the accretion disk or radio jet have been suggested as explanations for the AGN variability. For the accretion disk, physical timescales could be correlated with the

---

<sup>†</sup>This chapter is a revised version of the article published in *Journal of the Korean Astronomical Society* in August 2018 (Kim et al. 2018).

variability of AGN. Hour-scale, day-scale, and year-scale variability correspond to light crossing timescale, dynamical timescale, and thermal timescale of the accretion disk, respectively (Frank et al. 2002). Therefore, the intranight optical variability (INOV), which corresponds to the light crossing timescale, can be used to study violent variation at the smallest AGN size and structure. However, hour-scale variability has not been studied as much as longer timescale variability as it needs intensive monitoring with high cadence. It is also hard to detect, because of the minuscule variability from  $\sim 10^{-1} - 10^{-3}$  mag.

Previous results on this subject present mixed results that require careful examination. This is because different types of AGN show different INOV activities and the depths of the data vary between different studies. Several consensuses and controversial issues can be summarized as below.

First, sub-classes of AGN such as radio-loud AGN and blazars are found to have a high probability of exhibiting INOV. The ballpark number is 20-100% for the fraction or the duty cycle of radio-loud quasars and blazars with INOV at the level of a few percent or more (Jang & Miller 1995, 1997; Romero et al. 1999, 2002; Stalin et al. 2005; Goyal et al. 2010, 2013a). On the other hand, radio-quiet AGN show INOV much less frequently, but the results are more controversial than the case for radio-loud AGN. In general, it is accepted that the INOV is found in none or only a few percent of radio-quiet AGN of various kinds when the variability amplitude of a few percent is examined (Romero et al. 1999; Webb & Malkan 2000; Klimek et al. 2004; Bachev et al. 2005; Carini et al. 2007; Kumar et al. 2016), where the variability amplitude is defined as the ratio of the standard deviation of the AGN light curve versus the observational error being  $> 2.576$  or so (99% confidence; Jang & Miller 1997). Webb & Malkan (2000) examined INOV of 20 Seyfert 1 AGN, and found no INOV with the upper limit on the amplitude of the variation of 0.03 mag for time scales of 1 hr or less. However, they found the AGN variation at 25 to 27 hr level for two of their sample. Their photometric error is 0.02 mag. No INOV is found for 18 high luminosity quasars at  $z > 2$  in which the photometric errors are of order of 0.02 to 0.05 mag (Bachev et al. 2005). At a similar

photometric error accuracy, Klimek et al. (2004) found only one occasion of INOV of 0.045 mag change among 33 nights of the data for six Seyfert 1 galaxies, suggesting the duty cycle of 3% at the level of 0.05 mag variability. Using photometric data at an accuracy of 0.02 mag, Carini et al. (2007) find no INOV among 7 quasars (5 radio-quiet and 2 radio-intermediate). Kumar et al. (2016) examined the INOV of 10 weak emission line quasars (WLQ) in the hope of identifying BL Lacs with a peculiar property, but they found no INOV among 18 observing sessions. Their work has photometric error of 0.03 to 0.06 mag, so INOV of 0.1 mag or larger should have been detected.

When smaller amplitudes of INOV are examined, the results are rather mixed. Examining the INOV amplitude down to about 1%, several studies find 10-40% of radio-quiet quasars show INOV with the duty cycle of 10-20% (Jang & Miller 1995, 1997; Romero et al. 1999, 2002; Gopal-Krishna 2000, 2003; Webb & Malkan 2000; Stalin et al. 2004a,b, 2005; Klimek et al. 2004; Bachev et al. 2005; Gupta & Joshi 2005; Carini et al. 2007; Goyal et al. 2010, 2012, 2013a; Joshi et al. 2011; Kumar et al. 2016), while several other studies that examined INOV at a similar level do not find such evidence (Petrucci et al. 1999; Romero et al. 1999). For example, Goyal et al. (2013a) find that about 40% of radio-quiet quasars exhibit INOV, and 20% if limited to the variability amplitude of  $\sim 3\%$ . The duty cycle, on the other hand, is found to be 10% (or 6% at the variability amplitude  $> 3\%$ ) for these objects. However, at a similar photometric accuracy, Romero et al. (1999) examined the INOV of 8 radio loud quasars, radio quiet quasars, and BL Lacs, finding no convincing case for INOV among radio-quiet quasars. At a slightly worse photometric accuracy (0.5%), Petrucci et al. (1999) found no INOV among 22 Seyfert 1 galaxies.

More recently, the high cadence photometry data from the *Kepler* mission (30 min cadence) are being studied to examine the short-term variability of AGN (e.g, Mushotzky et al. 2011, Carini & Ryle 2012, Wehrle et al. 2013, Revalski et al. 2014, Chen & Wang 2015, Edelson et al. 2014, Kasliwal et al. 2015, Shaya et al. 2015, Dobrotka et al. 2017). Aranzana et al. (2018) examined the variability of 252 AGN with  $R < 19$  mag. The power spectral density (PSD) of these objects in this study are

consistent with white noise of a few tenths of a percent error for most objects, although a few objects seem to show  $\sigma > 1\%$  with the PSD following a power-law. However, no statistical inferences have been made about the fraction of AGN for INOV.

Obviously our understanding of the demography of the INOV among AGN can be improved considering the small sample sizes in most of the previous studies. Furthermore, inhomogeneously sampled data, observed at different nights, bands, and telescopes, have made it difficult to compare various results about the variability of AGN. The Korea Microlensing Telescope Network (KMTNet) is a network of three 1.6m telescopes that are designed to study microlensing events without a gap in observing times (Kim et al. 2016a). This facility offers an excellent opportunity to study INOV of a large number AGN of different kinds, and to do so, we are conducting a project named KMTNet Active Galactic Nuclei Variability Survey (KANVAS). In this paper, we present the results from our pilot study of KANVAS. In Section 2.2, we introduce the KMTNet and observations while Section 2.3 presents an analysis of KMTNet data. Section 2.4 describes the AGN selection method, and their characteristics. Sections 2.5 and 2.6 present the variable AGN and their results. Finally, we discuss and conclude this results in Section 2.7.

## 2.2 Observation

The main research program of the KMTNet is to monitor galactic bulge and discover exoplanets. However, in seasons when the galactic bulge cannot be observed, other science programs were allocated observing time. Our study is one of these non-bulge science programs of the KMTNet. The KMTNet is composed of three 1.6m telescopes located in Chile (CTIO), South Africa (SAAO), and Australia (SSO), with a  $4\text{ deg}^2$  field of view and  $0.4''$  pixel size. The 24 hour, wide-field monitoring system allows all-day continuous monitoring of AGN.

In this Chapter, we present observations of the COSMOS field (10:00:28.6 +02:12:21) using the KMTNet. For this pilot study, we use three nights worth of data that were taken at the CTIO station. The first observation was 2015 February 18 where we ob-

Table 2.1. KMTNet-CTIO observations on the COSMOS field

Date yyyy.mm.dd	Band	Duration time	Exposure time per epoch	# Epoch	Seeing	$5\sigma$ Depth [mag] per epoch
2015.02.18	<i>B</i>	$\sim 2.5$ h	360s	5	$1.5 - 2.0''$	22.5 - 22.7
	<i>V</i>	$\sim 2.5$ h	240s	5	$1.5 - 1.8''$	22.2 - 22.4
	<i>R</i>	$\sim 2.5$ h	180s	5	$1.4 - 1.8''$	21.8 - 22.3
	<i>I</i>	$\sim 2.5$ h	180s	5	$1.4 - 1.9''$	21.1 - 21.4
2015.03.21	<i>B</i>	$\sim 5$ h	600s	13	$2.0 - 2.3''$	21.4 - 22.6
	<i>R</i>	$\sim 5$ h	270s	13	$1.5 - 2.1''$	20.4 - 22.1
2016.04.08	<i>B</i>	$\sim 4$ h	600s	11	$1.6 - 2.1''$	22.7 - 23.0
	<i>R</i>	$\sim 4$ h	270s	11	$1.3 - 1.9''$	21.9 - 22.3

tained the COSMOS field data for  $\sim 2.5$  hours of observation using *B*, *V*, *R*, and *I* bands. On 2015 March 21, we observed the COSMOS field again for  $\sim 5$  hours using *B* and *R* bands. Finally, on 2016 April 8, another observation was performed for  $\sim 4$  hours in *B* and *R* bands. Two to five consecutive frames, each with 1.5-2 min exposure time were taken in each band sequentially. The 2-5 frames are combined to produce a deeper single epoch image with a total exposure time of 3-10 min. Approximately, 5-13 sets of these data were taken, to produce 20-30 min cadence data per filter. The seeing conditions, which were measured using SExtractor, were  $\sim 1.6''$  on 2015 February 18,  $\sim 2.0''$  on 2015 March 21, and  $\sim 1.8''$  on 2016 April 8. However, the weather condition was very unstable on 2015 March 21 and we excluded 4 epochs of data. Furthermore, the depth of the March data is shallower than for other dates and the observation log is provided in Table 2.1.

## 2.3 Data analysis

The basic data reduction, such as bias correction and flat-fielding, was done by the KMTNet pipeline at the KMTNet data center. We then performed astrometry, image stacking, and photometry calibration on the reduced data. First, we conducted astrometry following the basic process provided by the KMTNet team – Astrometric Calibration for the KMTNet Data<sup>0</sup>. We used SExtractor (Bertin & Arnouts 1996), SCAMP (Bertin 2006), and SWarp (Bertin et al. 2002) software packages for astrometry and achieved astrometric accuracy of  $\sim 0.2''$ . SWarp is used again for co-addition of 2-5 frames that were taken consecutively at a given epoch. Because seeing condition varied during the night, systematic bias could be introduced when fixed aperture is used for photometry. To make images have similar seeing conditions, we applied Gaussian convolution based on the seeing FWHM of each image (i.e., downgrade the seeing FWHM of all images to the worst seeing image). Then, SExtractor was used again with  $S/N = 5$  limit to produce source catalogs of the convolved images. In the 2015 February observation, there were  $\sim 50,000$ ,  $\sim 65,000$ ,  $\sim 90,000$ , and  $\sim 80,000$  detected sources in  $B$ ,  $V$ ,  $R$ , and  $I$  bands, respectively, with a median photometric uncertainty of  $\sim 0.1$  mag. For the photometry calibration of the detected sources, we used the magnitudes of stellar sources from the photometric catalog of the COSMOS field (Capak et al. 2007). For the 2015 February data, the image depths at  $5\sigma$  detection (point source) are 22.6, 22.3, 22.2, and 21.3 magnitudes in  $B$ ,  $V$ ,  $R$ , and  $I$  bands, respectively. Hereafter, we only use  $8''$  aperture magnitude. This aperture covers  $> 95\%$  of total flux and it corresponds to 3-4 times of the maximum seeing FWHM.

## 2.4 AGN Samples

We selected AGN in X-ray, mid-infrared, radio, and optical bands. The multi-wavelength catalogs and our source catalogs are matched using 1 arcsec radius and the closest source within the radius is selected. Typically, between different catalogs, the coordi-

---

<sup>0</sup><http://kmtnet.kasi.re.kr/kmtnet-eng/astrometric-calibration-for-kmtnet-data>

Table 2.2. Classification of X-ray selected AGNs in  $R$  band of the 2016 April data

Classification	Unobscured	Obscured	no Classification	Total
Broad-line AGN	55	1	0	56
non Broad-line AGN	1	4	0	5
no Classification	3	1	3	7
Total	59	6	3	68

nate differences are at the level of 0.2 to 0.4 arcsec for the matched sources. AGN are excluded from our selection in cases of saturation or column pattern in the KMTNet image, proximity to a bright source, or if any other source is within the aperture size used for photometry. In addition, we only selected AGN where the photometric error is smaller than 0.2 mag in our data. The following subsections describe AGN selection at different wavelengths. Since the number of selected AGN depends on the different depths for each observed night and band, we provide ranges for the number of detected AGN.

#### 2.4.1 X-ray selected AGNs

X-ray selected AGN are taken from Civano et al. (2012), where they classified AGN as broad line AGN (BLAGN) or not (non-BLAGN) if spectra were available, and obscured or unobscured AGN based on fitting their spectral energy distribution. There are 549 AGN identified in the  $0.9 \text{ deg}^2$  field of view covered by the Chandra-COSMOS catalog, but due to the depth of the KMTNet observations, only about 25–90 X-ray AGN are detected in the KMTNet images, depending on the date of the observing run and the filter. Table 2.2 shows an example of the X-ray detected AGN classification for the 2016 April data (also see Table 2.3 for the number of X-ray matched AGN). Roughly  $\sim 80\%$  of them are unobscured broad-line AGN. The X-ray flux range in 0.5–10 keV

is  $2.6 \times 10^{-15} - 1.6 \times 10^{-13} \text{ erg cm}^{-2} \text{ s}^{-1}$  while the X-ray luminosity is  $5.4 \times 10^{41} - 2.0 \times 10^{44} \text{ erg s}^{-1}$ .

### 2.4.2 Mid-Infrared selected AGNs

Lacy et al. (2004) and Stern et al. (2005) suggest mid-infrared (MIR) color-color selection of AGN with Spitzer IRAC photometry. This method can effectively select more obscured AGN, though deeper IRAC data reveal contamination from normal galaxies. Here, we employed the recent selection method defined by Donley et al. (2012) to minimize contamination. From the Spitzer-COSMOS IRAC 4-channel photometry catalog (Sanders et al. 2007) which covers  $2 \text{ deg}^2$  of the COSMOS field, aperture corrected  $1.9''$  photometry is used at the  $5\sigma$  sensitivity limit in all channels. Consequently, 64–174 MIR selected AGN are detected in our data, depending on the date of the observation and the filter (Figure 2.1).

### 2.4.3 Radio selected AGNs

Radio sources in general are either AGN or star-forming galaxies, but bright radio sources are known to be mostly AGN. At the same time, the brightness of radio sources is known to evolve as a function of redshift. To differentiate AGN from star-forming galaxies, Magliocchetti et al. (2014) suggest a selection based on the radio power like

$$\begin{aligned} P_{1.4\text{GHz}} &> 10^{21.7+z} [W/\text{Hz}/\text{sr}] && \text{if } z \leq 1.8 \\ P_{1.4\text{GHz}} &> 10^{23.5} [W/\text{Hz}/\text{sr}] && \text{if } z > 1.8 \end{aligned} \quad (2.1)$$

Here, the radio power at 1.4 GHz,  $P_{1.4\text{GHz}}$ , is calculated as

$$P_{1.4\text{GHz}} = F_{1.4\text{GHz}} D_L^2 \times (1+z)^{\alpha-1}, \quad (2.2)$$

where  $F_{1.4\text{GHz}}$  is the observed flux at 1.4 GHz,  $D_L$  is the luminosity distance, and  $\alpha$  is the power law index of the radio spectrum  $F_\nu \sim \nu^{-\alpha}$ , and a canonical value of  $\alpha = 0.7$  is chosen here (e.g., Smolcic et al. 2014, 2017). This  $(1+z)$  term is included for the K-correction. Radio AGN in the COSMOS field are selected by applying this method to

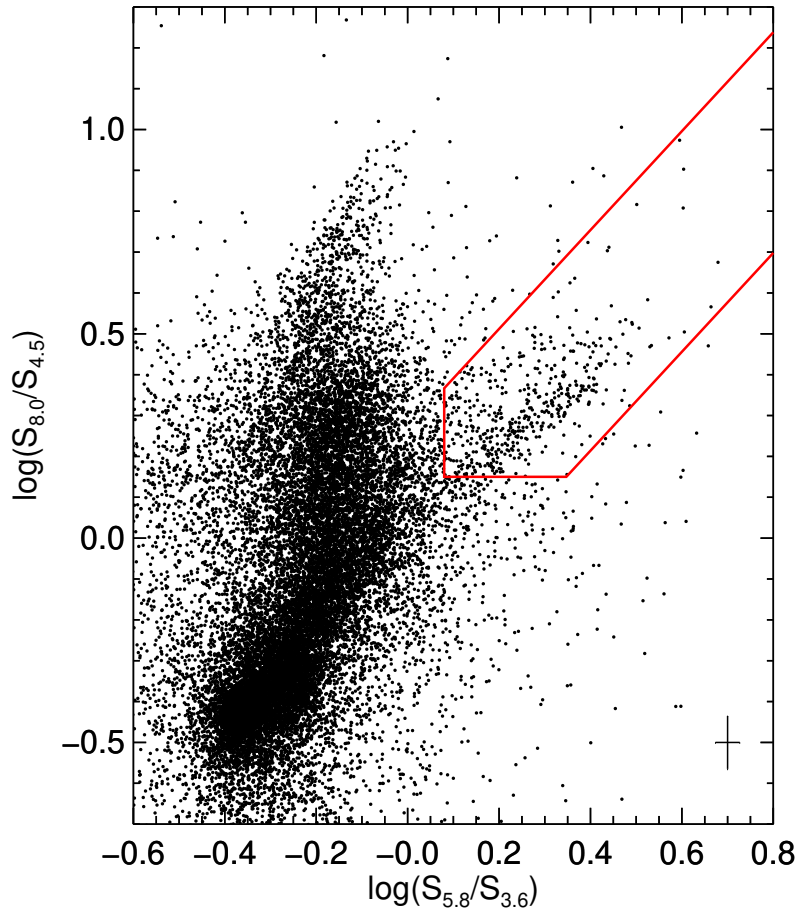


**Figure 2.1.** Mid infrared color-color diagram of the KMTNet detected sources in the COSMOS field. The x-axis is the ratio of 5.8  $\mu\text{m}$  and 3.6  $\mu\text{m}$  fluxes, while the y-axis shows the ratio of the 8.0  $\mu\text{m}$  and 4.5  $\mu\text{m}$  fluxes. Sources within the red solid lines are selected as AGN (Donley et al. 2012). The median error of the points is shown in the bottom-right corner.

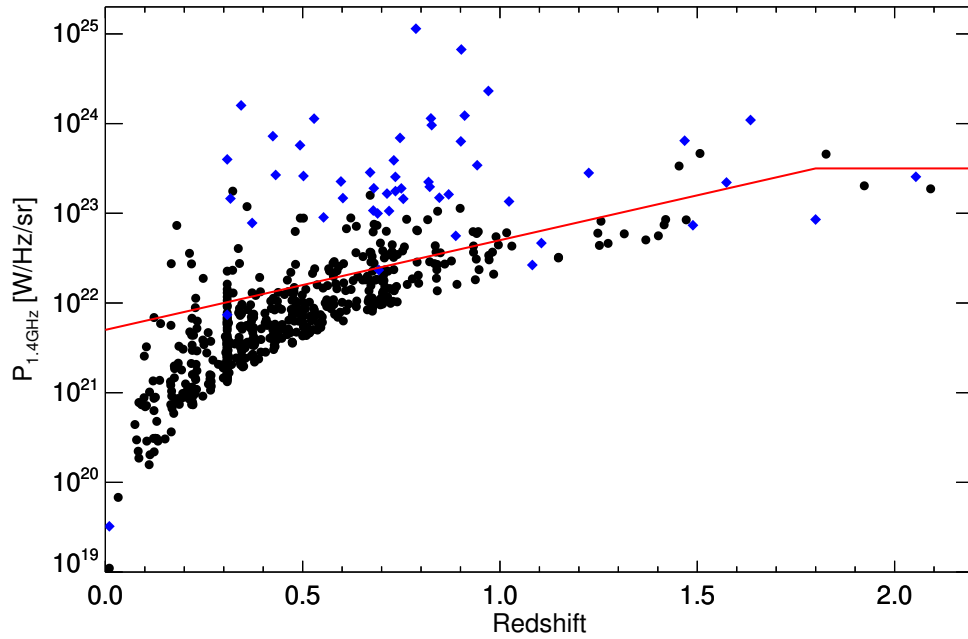


**Figure 2.2.** The distribution of 1.4GHz radio power (y-axis) and redshift (x-axis) of the KMTNet detected sources in the COSMOS field. Radio-loud sources are shown with blue diamonds, while radio-quiet sources are indicated with black circles. The red solid line is the radio power cut used for the radio selection of AGN. Sources above the red solid line are selected as radio AGN. The radio power uncertainties are smaller than symbol size.

the 1.4 GHz radio flux in the VLA-COSMOS catalog (Schinnerer et al. 2007) covering 2 deg<sup>2</sup> field of view. To calculate the radio power, we used the spectroscopic redshift catalog (Lilly et al. 2009, Damjanov et al. 2018) and photometric redshift catalog (Ilbert et al. 2009) of the COSMOS field by assuming isotropic radio emission. This selection yields 14-61 AGN, depending on the date of the observation and the filter. Figure 2.2 shows the radio power versus redshift of radio sources matched with the KMTNet detected sources, as well as the radio selection criteria defined by Equation (1). Furthermore, we calculated the radio loudness like

$$R_i = \log(F_{1.4\text{GHz}}/F_{i\text{-band}}) \quad (2.3)$$

where we classify radio-loud (quiet) sources as those where the radio loudness is larger (smaller) than 1 (Ivezic et al. 2002). The fraction of radio-loud sources is 30-60% in our radio AGN sample.

#### 2.4.4 SDSS DR7 quasars catalog

Type 1 AGN can be selected from optical colors and we use those AGN that are identified in the SDSS DR7 quasar catalog (Schneider et al. 2010). They are luminous ( $M_i < -22$ ), broad-line AGN for which physical parameters such as  $M_{BH}$  are available in the catalog. Furthermore, the quasar selection is not limited to the COSMOS field, and the SDSS type 1 quasars are also identified in the KMTNet field of view outside the COSMOS field. We identify 65-87 SDSS DR7 quasars in the KMTNet field of view, depending on the date of observation and the filter.

#### 2.4.5 Short summary on AGNs selected from different methods

Figure 2.3 shows the positions of selected AGN from the 2016 April data in  $R$  band. As shown in the figure, some AGN are selected by more than one selection method. 68, 151, 51, and 85 AGN are selected from the X-ray, MIR, radio, and SDSS quasar catalogs, respectively, in this particular case. Figure 2.4 shows the magnitude in  $R$  band versus

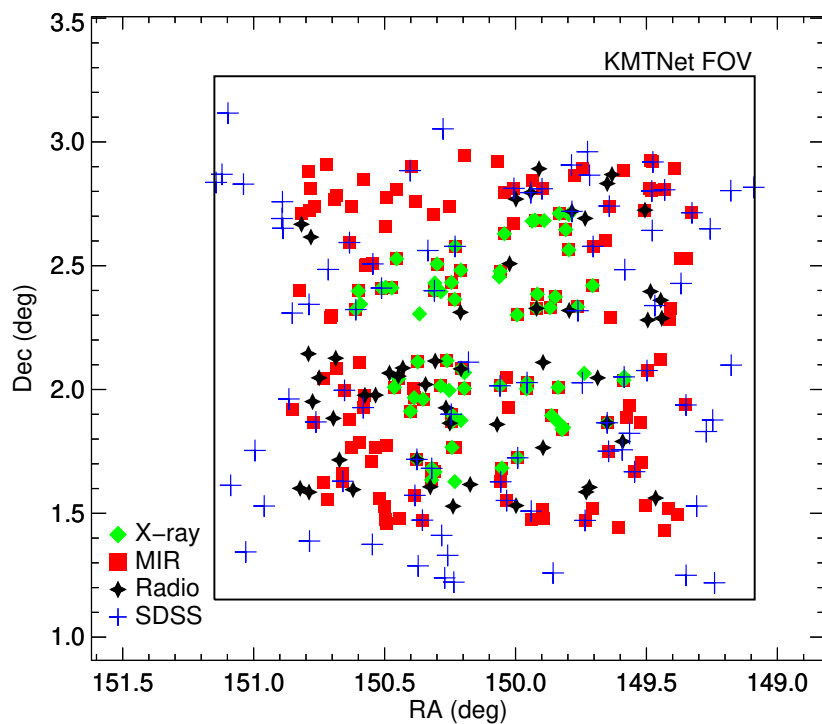


**Figure 2.3.** Positions of the selected AGNs from the 2016 April data in  $R$  band. Green diamonds, red squares, black stars, and blue crosses correspond to the X-ray selected AGNs, the MIR selected AGNs, the radio selected AGNs, and the SDSS quasars, respectively.

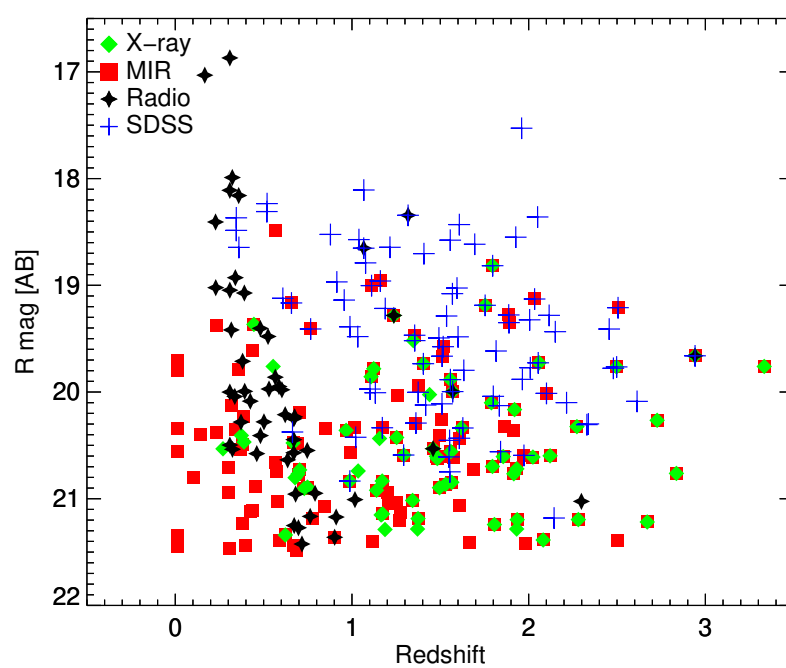


**Figure 2.4.** The apparent magnitude in  $R$  band and redshift of selected AGN from the 2016 April data. Green diamonds, red squares, black stars, and blue crosses correspond to X-ray selected AGN, MIR selected AGN, radio selected AGN, and matched SDSS quasars, respectively. The errors are smaller than the sizes of symbols.

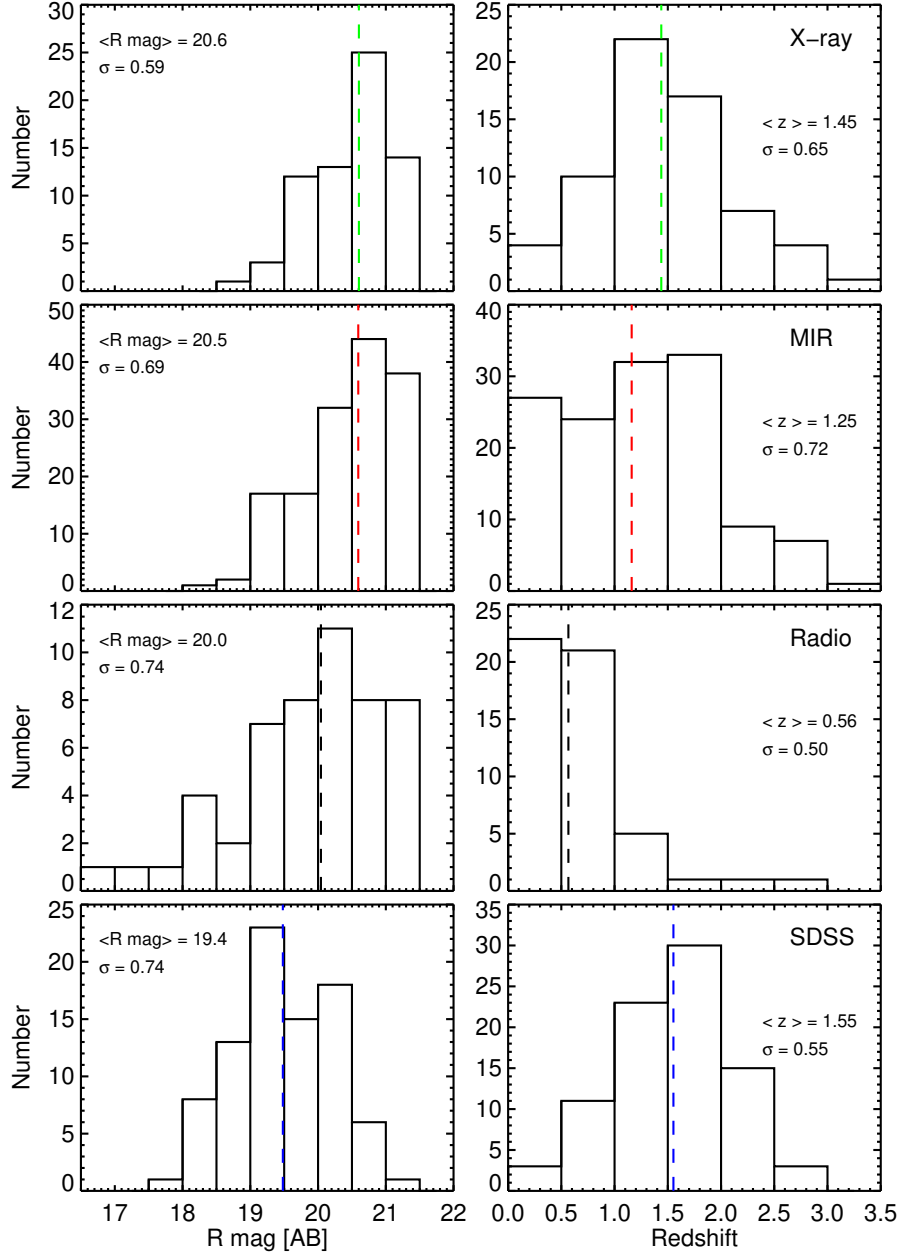


**Figure 2.5.** The apparent magnitude (left) and redshift (right) histogram of AGN from the 2016 April data in  $R$  band. The median value (the vertical dashed line) and the dispersion of the distribution is given in each panel. Also given are the AGN selection methods in each right panel.

the redshift of the selected AGN while Figure 2.5 shows the distribution of apparent magnitude (left) and redshift (right). The apparent magnitudes of radio selected AGN and SDSS quasars are brighter than MIR selected AGN and X-ray selected AGN. The median values of apparent magnitude are 20.6, 20.5, 20.0, and 19.4 for X-ray, MIR, radio, and SDSS, respectively. In the case of redshift, X-ray selected AGN and SDSS quasars have higher redshift than MIR selected AGN and radio selected AGN. The median values are 1.45, 1.25, 0.56, and 1.55 for X-ray, MIR, radio, and SDSS, respectively. The list of detected AGN is given in Table 2.5 of Appendix A, where we list 394 AGN that are detected in the KMTNet data at least once in one of the three observing runs and one filter.

## 2.5 Variability of AGN

Absolute photometry calibration is dependent on the photometry calibration error of the COSMOS catalog and can be uncertain by more than  $\sim 10^{-2}$  mag. For this reason, absolute calibration is attempted on images from one of the epochs with the best quality. The photometry from the absolute calibration is kept as a reference to judge the amount of variations in magnitude for data on other nights. To obtain the light curve with higher accuracy, we performed differential photometry for the selected AGN. First, we identified stars within the COSMOS field using parameters in SExtractor by selecting sources with CLASS\_STAR (stellarity) greater than 0.95, and FLAGS=0. To select non-variable stars only, we performed differential photometry for each selected star using  $\sim 20$  other bright ( $< 16$  mag) stars within 0.2 degree. The magnitude standard deviations of differential light-curves ( $\sigma_{LC}$ ) for all stars are calculated. Then, we chose stars within 3-sigma cut of  $\sigma_{LC}$  in each 0.25 magnitude bin as non-variable stars (Figure 2.6). A few thousands to ten thousand non-variable stars are selected in each band and each night.

Figure 2.6 shows an interesting trend where the  $\sigma_{LC}$  does not decrease below 0.003 mag even at very bright magnitudes ( $< 16$  mag). Seen in a different way, Figure 2.7 shows  $\sigma_{LC}$  versus  $\sigma_{phot}$ , the error from the photometry measurement. The trend seen in

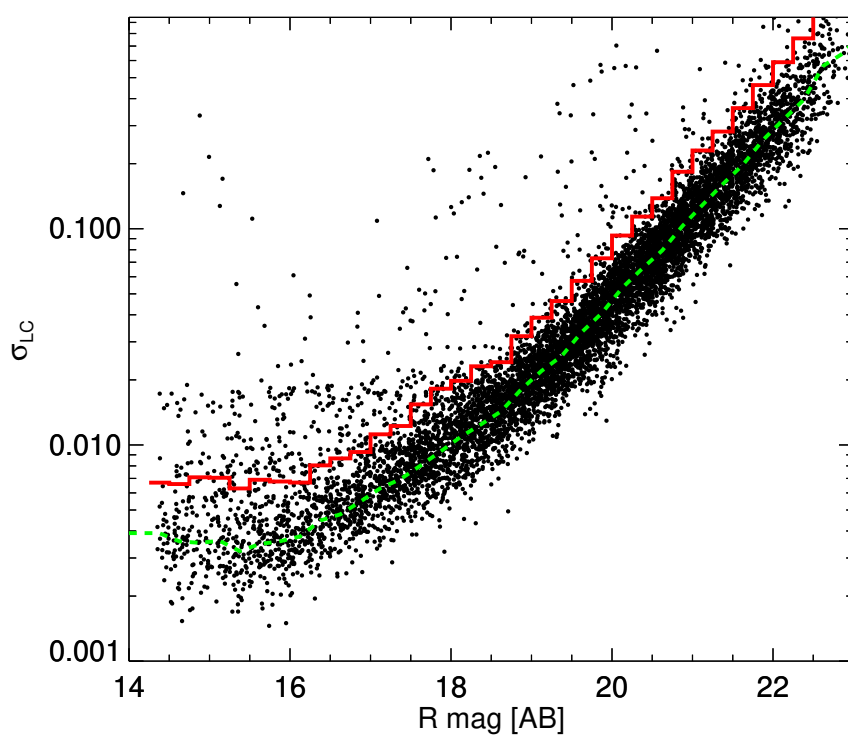


**Figure 2.6.** The standard deviation of the multi-epoch  $R$  band magnitudes for each star versus the mean  $R$  band magnitude of each star over the observed period. A red solid line is 3-sigma cut of  $\sigma_{LC}$  of stars in each 0.25 magnitude bin while a green dashed line is median value of  $\sigma_{LC}$ . Stars below this red solid line are selected as non-variable stars.

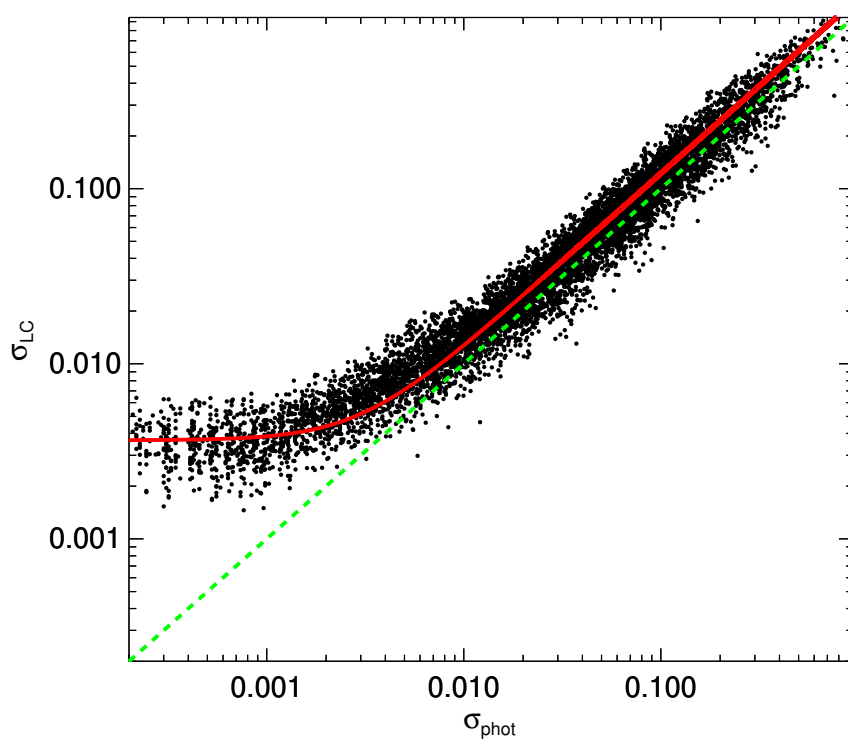


**Figure 2.7.** The standard deviation of the multi-epoch  $R$  band magnitudes for each star versus the mean photometric error of each star over the observed period. A green dashed line is the one-to-one line, and a red solid line is fitting result using Equation (4). It shows underestimation of photometric error.

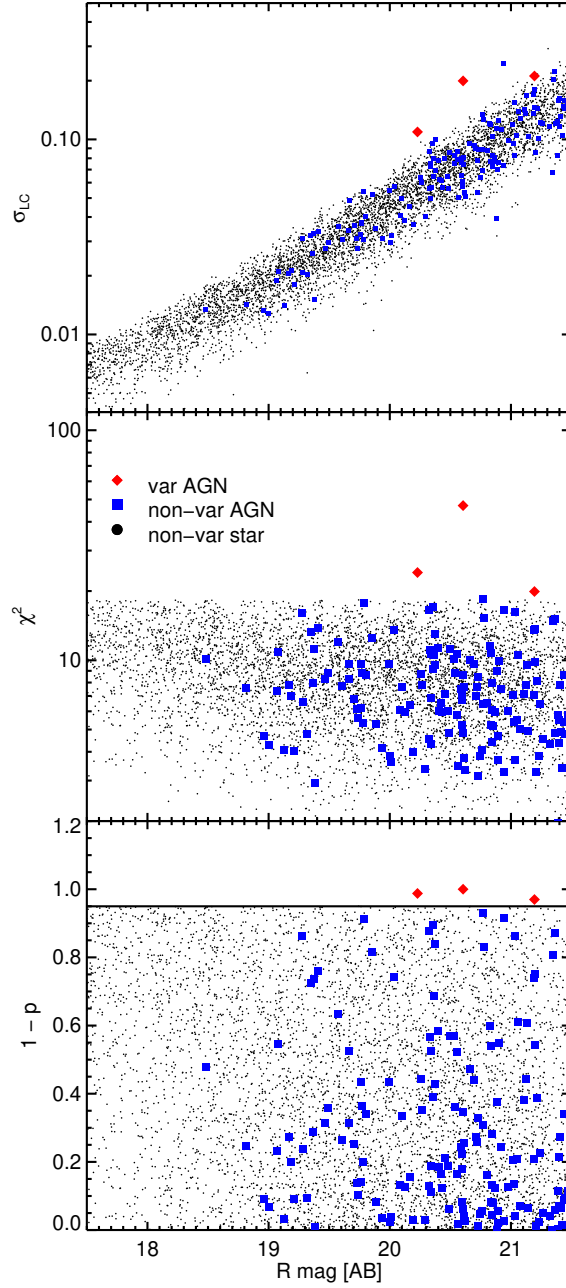


**Figure 2.8.**  $\sigma_{LC}$  (top),  $\chi^2$  (middle) and  $1-p$  (bottom) with their apparent magnitude of MIR selected AGN in  $R$  band of the 2016 April data (dof = 10 for the 11 epochs data). Red diamonds, blue squares, and black dots correspond to variable AGN, non-variable AGN, and non-variable stars, respectively. The  $\chi^2$  are calculated by Equation (5). A black horizontal line denotes  $1-p = 0.95$  and sources over this line are classified as variable AGN.

Figure 2.6 persists, i.e.,  $\sigma_{LC}$  staying above 0.003 mag even when  $\sigma_{phot}$  goes well below 0.003 mag. This trend suggests that there is a minimum photometric error possibly due to flat-fielding error, systematic uncertainties, frame-to-frame photometry variation, geometric distortion effect, and other effects. An accurate estimation of photometric error is crucial when we classify variable AGN in order to minimize the number of false positives. Therefore, we set  $\sigma_{int}$  as the minimum intrinsic error, below which we cannot reduce the photometry error in the KMTNet data. Another source of error is identified at large  $\sigma_{phot}$  ( $> 0.01$  mag) where  $\sigma_{int}$  is negligible. In this regime,  $\sigma_{phot}$  is found to be smaller than  $\sigma_{LC}$  by a factor of 1.2 to 1.4. We trace the cause of the difference to the re-sampling process in SWarp of sub-pixel shifted images for stacking that decreases background noise of the stacked image (Bertin et al. 2002). Note that a similar factor has been introduced in other AGN variability studies (e.g., Goyal et al. 2013b). Thus, we modeled the true photometry error,  $\sigma_{cal}$ , like

$$\sigma_{cal} = \sqrt{\sigma_{int}^2 + (\eta \times \sigma_{phot})^2} \quad (2.4)$$

where  $\eta$  is an underestimation factor and  $\sigma_{phot}$  is the mean photometric error of an object over all epochs. The intrinsic error and underestimation factor are estimated from each band and each night by fitting the  $\sigma_{LC}$  versus  $\sigma_{phot}$  relation as in Figure 2.7. The typical  $\sigma_{int}$  value is 0.002–0.005 and the underestimation factor ranges between 1.2 and 1.4.

After the error calibration, we constructed the light curves of AGN by differential photometry using the closest (within 0.2 degree)  $\sim 20$  non-variable reference stars brighter than 16 mag for each corresponding filter. To detect variability, we used the  $\chi^2$ -test (de Diego 2010, Villforth et al. 2010). The  $\chi^2$  value is calculated using the relation

$$\chi^2 = \sum_i \frac{(m_i - \langle m_i \rangle)^2}{(\sigma_{cal,i})^2} \quad (2.5)$$

Here,  $m_i$  denotes magnitude of each epoch,  $\langle m_i \rangle$  is average magnitude over all epochs, and  $\sigma_{cal,i}$  is calibrated photometric error of each epoch. The p-value is calculated from the  $\chi^2$ -distribution. AGN are classified as variable when  $1-p > 0.95$ , meaning that we reject the null hypothesis of non-variability at the 95% confidence level ( $\alpha = 0.05$ ). Figure 2.8 shows  $\sigma_{LC}$ ,  $\chi^2$  (degree of freedom, dof = 10) and  $1-p$  of AGN from the 2016 April data in  $R$  band. We applied the  $\chi^2$ -test for comparison stars to examine the validity of the  $\chi^2$ -test. Except for the 2015 March data, the results show that 5-7% of stars are classified as variable, which is expected according to our variability criterion. The 2015 March data shows  $\sim 12\%$  fraction of variable stars, but we attribute this to the bad weather conditions during the 2015 March run. We also employ the C-test (Jang & Miller 1997, Romero et al. 1999) as a alternative statistical test. The C statistic is defined as

$$C = \frac{\sigma_{mag}}{\langle \sigma_{cal,i} \rangle}, \quad (2.6)$$

where  $\langle \sigma_{cal,i} \rangle$  is the average photometric error over all the epochs. If the C value is greater than 1.95 (2.56), AGN can be classified as variable with 95% (99%) confidence level, assuming that the errors follow a Gaussian distribution. However, the  $\chi^2$ -test has an advantage that it uses photometric errors of each individual epoch unlike the C-test that uses the averaged photometric error. For that reason and since the C-test result is very similar to the  $\chi^2$ -test results, we mainly present the  $\chi^2$ -test results. The  $1-p$  and C-statistic values of the whole sample of 394 AGN are listed in Table 2.5.

## 2.6 Results

Using the  $\chi^2$ -test, we could differentiate variable AGN from non-variable AGN. Table 2.3 shows the number of detected and variable AGN with their fraction in the bracket. As can be seen in Table 2.3, the fractions of variable AGN do not significantly exceed the 5% level that we found for the comparison stars. The results of the C-test at 95% confidence level is very similar to the  $\chi^2$ -test results (not listed in Table 2.3). We can

conclude that many of the AGN that are classified as intra-night variable are unlikely to be truly intra-night variable.

Nevertheless, the probability that an AGN is truly variable becomes higher if the AGN is classified as variable in more than two data sets. If one AGN is classified as variable in two bands or nights at the 95% confidence level, then the expected probability of a false positive is only 0.25%. We identify eight AGN that are classified as intra-night variable in more than two bands or two nights both in the  $\chi^2$ -test and the C-test. We list these AGN in Table 2.4. The AGN name comes from their coordinate information in the KMTNet catalog (hhmmss.s+ddmmss) and their magnitudes are the mean magnitude over all observed epochs. The variability strength is defined by the error subtracted magnitude variation as shown in Equation (7) like

$$\begin{aligned}\sigma_{var} &= \sqrt{\sigma_{mag}^2 - \sigma_{cal}^2} & \text{if } \sigma_{mag} > \sigma_{cal} \\ \sigma_{var} &= -\sqrt{\sigma_{cal}^2 - \sigma_{mag}^2} & \text{if } \sigma_{mag} < \sigma_{cal}\end{aligned}\quad (2.7)$$

where  $\sigma_{mag}$  denotes the standard deviation of the differential light-curve and  $\sigma_{cal}$  is the mean calibrated photometric error. The variability strength of the variable AGN based on the  $\chi^2$ test is shown in bold. AGN that were not selected for being too faint (a), out of field of view (b), and contamination by other sources or noise (c) are marked in the table.

In Figure 2.9, we plotted the light-curves of the eight variable AGN. The AGN names are shown on the right side of the light-curve and the color denotes each band. Variable AGN are plotted with solid lines while non-variable AGN are plotted with dashed lines.

**100008.9+021440** This object is classified as a broad-line and obscured AGN in the Chandra-COSMOS identification catalog. The 2015 February data shows variability strength of 0.130 mag, 0.172 mag and 0.115 mag in  $B$ ,  $V$ , and  $R$  bands, respectively with 20.3 mag, 20.0 mag, and 19.4 mag in each band. Unfortunately, no usable data were obtained in 2015 March and 2016 April.

**095820.7+020213** This object is classified as a broad-line and unobscured AGN

Table 2.3. The number of detected and variable AGNs with their fraction in the bracket

	2015.02.18	2015.03.21	2016.04.08
X-ray selected AGN			
<i>B</i>	2/78 (2.6%)	0/47 (0%)	1/80 (1.3%)
<i>V</i>	2/85 (2.4%)		
<i>R</i>	2/90 (2.2%)	0/25 (0%)	3/68 (4.4%)
<i>I</i>	2/61 (3.3%)		
MIR selected AGN			
<i>B</i>	5/151 (3.3%)	1/91 (1.1%)	7/153 (4.6%)
<i>V</i>	6/169 (3.6%)		
<i>R</i>	5/174 (2.9%)	5/64 (7.8%)	3/151 (2.0%)
<i>I</i>	6/117 (5.1%)		
Radio selected AGN			
<i>B</i>	1/32 (3.1%)	0/14 (0%)	2/27 (7.4%)
<i>V</i>	3/47 (6.4%)		
<i>R</i>	4/61 (6.6%)	0/24 (0%)	4/51 (7.8%)
<i>I</i>	4/61 (6.6%)		
SDSS DR7 quasars			
<i>B</i>	4/80 (5.0%)	4/85 (4.7%)	7/87 (8.0%)
<i>V</i>	2/83 (2.4%)		
<i>R</i>	4/75 (5.3%)	4/65 (6.2%)	4/85 (4.7%)
<i>I</i>	3/72 (4.2%)		

Table 2.4. Information of eight variable AGNs

Name	Selection	Redshift	Class & log( $M_{\text{BH}}/M_{\odot}$ )	Band	Mag	$\sigma_{var}(\sigma_{cal})$	$\sigma_{var}(\sigma_{cal})$	$\sigma_{var}(\sigma_{cal})$
						15.02.18	15.03.21	16.04.08
100008.9+021440	X-ray &MIR	2.536 <sup>a</sup>	Broad-line Obscured Radio-quiet	<i>B</i>	20.3	<b>0.130</b> (0.039)	3	2
				<i>V</i>	20.0	<b>0.172</b> (0.038)		
				<i>R</i>	19.4	<b>0.115</b> (0.027)	3	2
				<i>I</i>	19.0	3		
095820.7+020213	X-ray &MIR	1.856 <sup>a</sup>	Broad-line Unobscured	<i>B</i>	20.8	-0.029 (0.077)	-0.100 (0.175)	<b>0.051</b> (0.054)
				<i>V</i>	21.0	-0.061 (0.115)		
				<i>R</i>	20.8	0.087 (0.142)	1	<b>0.172</b> (0.101)
				<i>I</i>	21.0	1		
100151.1+020032	X-ray &MIR	0.967 <sup>c</sup>	Broad-line Unobscured	<i>B</i>	20.7	3	-0.117 (0.130)	-0.045 (0.057)
				<i>V</i>	20.3	<b>0.097</b> (0.057)		
				<i>R</i>	20.3	<b>0.142</b> (0.064)	-0.169 (0.188)	-0.017 (0.068)
				<i>I</i>	20.0	0.101 (0.122)		
095834.0+024427	MIR &SDSS	1.887 <sup>b</sup>	Broad-line & 8.88 <sup>d</sup>	<i>B</i>	19.5	<b>0.025</b> (0.020)	-0.027 (0.047)	<b>0.034</b> (0.017)
				<i>V</i>	19.4	-0.019 (0.024)		
				<i>R</i>	19.3	0.010 (0.025)	-0.049 (0.084)	0.018 (0.025)
				<i>I</i>	18.9	0.027 (0.044)		
100021.7+020000	Radio	0.219 <sup>c</sup>	Radio-quiet & Early-type Galaxy	<i>B</i>	20.0	<b>0.278</b> (0.042)	2	2
				<i>V</i>	18.6	<b>0.190</b> (0.014)		
				<i>R</i>	17.8	3	2	2
				<i>I</i>	17.6	3		
100017.7+030524	SDSS	2.178 <sup>b</sup>	Broad-line & 8.38 <sup>d</sup>	<i>B</i>	20.6	<b>0.065</b> (0.046)	-0.029 (0.111)	2
				<i>V</i>	20.8	-0.019 (0.075)		
				<i>R</i>	20.7	<b>0.104</b> (0.087)	1	2
				<i>I</i>	20.1	-0.050 (0.098)		
100434.3+025011	SDSS	1.215 <sup>b</sup>	Broad-line & 8.94 <sup>d</sup>	<i>B</i>	18.7	3	3	<b>0.051</b> (0.011)
				<i>V</i>	18.4	<b>0.057</b> (0.011)		
				<i>R</i>	18.4	<b>0.063</b> (0.010)	3	<b>0.129</b> (0.017)
				<i>I</i>	18.0	3		
095621.6+024859	SDSS	0.956 <sup>b</sup>	Broad-line & 8.99 <sup>d</sup>	<i>B</i>	19.4	2	2	<b>0.081</b> (0.017)
				<i>V</i>		2		
				<i>R</i>	19.1	2	2	<b>0.222</b> (0.024)
				<i>I</i>		2		

Note. — 1: Too faint, 2: Out of field of view, 3: Contaminated

Note. — a: Civano et al. 2012, b: Schneider et al. 2010, c: Abolfathi et al. 2018, d: Shen et al. 2011

Note. — The variability strength of the variable AGN based on the  $\chi^2$  test is shown in bold.

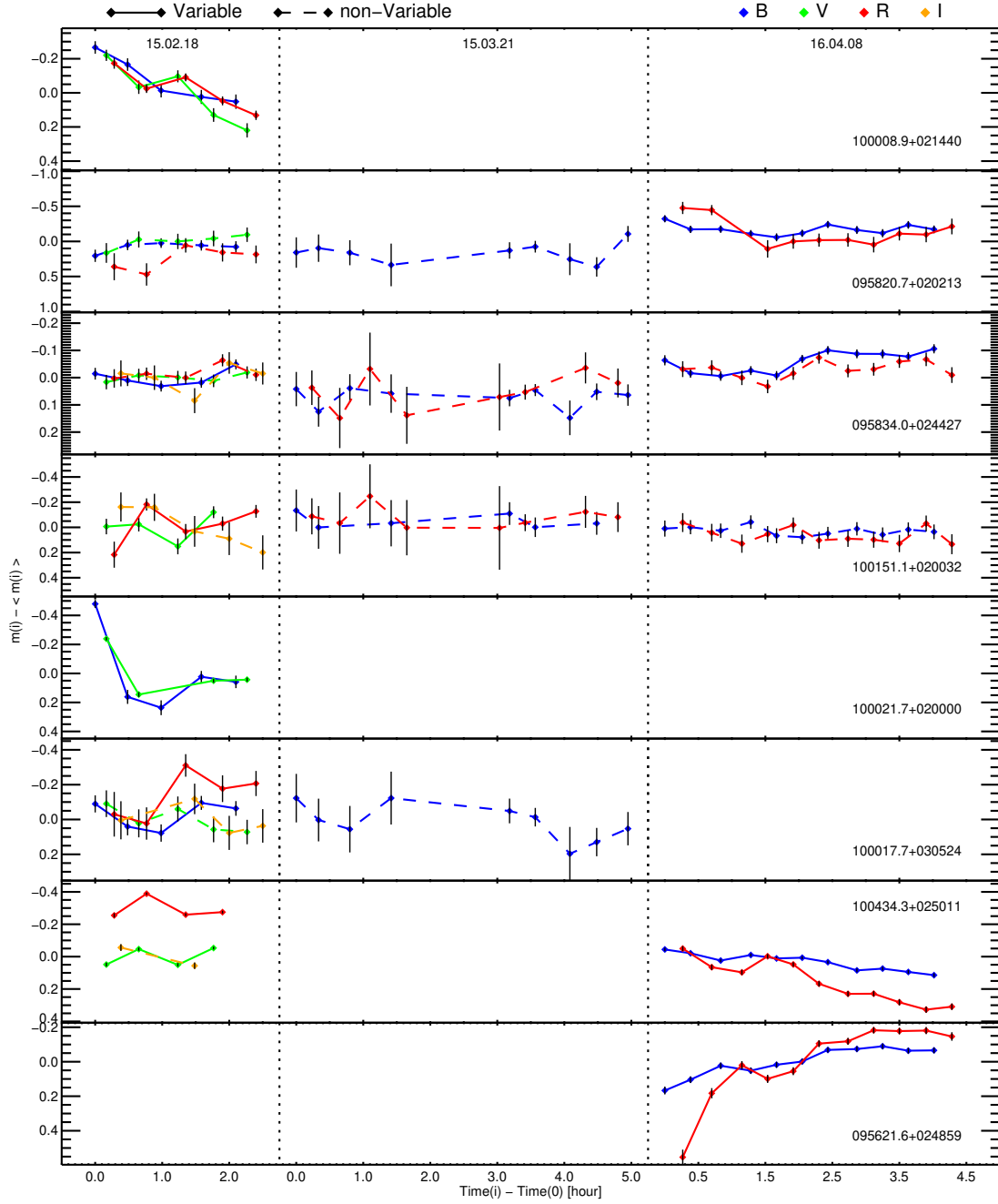


**Figure 2.9.** The light-curves of eight variable AGN. The name of AGN shown on the right side of each light-curve and the color denotes each band. Variable AGN are plotted as solid lines while non-variable AGN are plotted as dashed lines.

in the Chandra-COSMOS identification catalog. The variability of 0.05-0.17 mag is detected only in the 2016 April data, both in  $B$  and  $R$  bands.

**100151.1+020032** This is a X-ray and MIR-selected AGN which is classified as a broad-line and unobscured in the Chandra-COSMOS identification catalog. The variability is found only in the 2015 February data, with the  $\sigma_{var} \sim 0.1 - 0.14$  in  $V$  and  $R$  bands.

**095834.0+024427** A small amount of variability,  $\sim 0.03$  mag, is detected in  $B$  band in both the 2015 February and 2016 April data. This is a MIR-selected AGN which also appears in the SDSS quasar catalog.

**100021.7+020000** Radio-loud AGN with 20.0, and 18.6 magnitudes in  $B$  and  $V$  bands, respectively. This object is classified as variable in  $B$  and  $V$  bands with variability strength of 0.278 and 0.190 mag, respectively. However, the SDSS spectrum has the characteristics of early-type galaxy, not AGN. The SDSS image shows the morphology of an early-type galaxy too. The variability can arise from an increased nuclear activity or due to an unidentified systematic error in measuring the central variability of an extended source like this.

**100017.7+030524** SDSS quasar variable in  $B$  and  $R$  bands of the 2015 February data. The magnitudes are 20.6 and 20.7 in  $B$  and  $R$  bands with 0.065 and 0.104 mag variability strength, respectively.

**100434.3+025011** The brightest variable AGN in our sample. This SDSS quasar has apparent magnitudes of 18.7 and 18.4 in  $B$  and  $R$  bands, respectively. Variability is detected in both the 2015 February and 2016 April data with the strength of 0.06 to 0.13 magnitudes.

**095621.6+024859** This object is found to be variable in the 2016 April data, with the variability strengths of 0.08 and 0.22 in  $B$  and  $R$  bands, respectively.

## 2.7 Discussion and Conclusion

In our pilot study, we identified eight intra-night variable AGN out of 394 ( $\sim 2\%$ ). The smallness of the fraction can be due to the photometric error of the targets in

our sample which is in the range 0.01 to 0.1 mag. In previous studies, Gupta & Joshi (2005), Carini et al. (2007), and Goyal et al. (2013a), concluded that the INOV fraction of AGN with 12-19 magnitudes is 10-30%, but their photometric error is  $\sim 10^{-3}$  mag. In particular, Goyal et al. (2013a) show that peak-to-peak variabilities of most AGN are less than 0.05 mag. We compared the peak-to-peak variability and the variability strength used in our study and we find the peak-to-peak variability corresponds to about three times the variability strength. The minimum variability strength of the eight INOV AGN in our study is  $\sim 0.03$  mag (095834.0+024427), so we can detect a peak-to-peak variability of at least  $\sim 0.09$  mag. We checked with Goyal et al. (2013a) and find that the fraction of AGN with the peak-to-peak variability greater than 0.09 mag is 4.8%. This is roughly consistent with the 2% in our results, considering that most of AGN in this study have higher photometric uncertainty than 095834.0+024427. In addition, Webb & Malkan (2000), Carini et al. (2003), Klimek et al. (2004), Bachev et al. (2005), and Kumar et al. (2016) show no variability or very small fraction of variability with  $\sim 10^{-2}$  mag photometric error. However, when investigating INOV of a very small amplitude (0.01 or less), we caution that there can be intrinsic errors such as the one we discussed in Section 2.5. In our case, the intrinsic error amounts to 0.004 mag or so. As also discussed in Bachev et al. (2005), ignoring this effect could lead to spurious detection of INOV. For now, we conclude that the low fraction of INOV AGN indicates that the INOV amplitude is quite small if there is any – smaller than our photometric error.

Several possible INOV mechanisms have been suggested: (i) the accretion disk instability; (ii) the X-ray irradiation of an accretion disk; (iii) the variation in jet activity such as a weak blazar component (See Czerny et al. 2008). AGN with large  $M_{\text{BH}}$  are expected to show very weak INOV variability from the accretion disk instability (e.g., Bachev et al. (2005); Czerny et al. 2008), but some INOV AGN in our sample are found to have  $M_{\text{BH}}$  as massive as  $10^8 - 10^9 M_{\odot}$ . It will be interesting to see if there is a correlation between  $M_{\text{BH}}$  and the INOV variability as a way to support the accretion disk instability model. Otherwise, the accretion disk instabilities do not easily pro-

duce 0.1 mag level INOV observed in the 8 AGN. For the X-ray irradiation instability, the variability time-scale is predicted to be a week or longer for high  $M_{\text{BH}}$  ( $> 10^8 M_{\odot}$ ) AGN. Furthermore, strong irradiation is required, which is not compatible with general broad-band spectral shape of AGN (Czerny et al. 2008). Therefore, like the accretion disk instability model, the X-ray irradiation model faces a difficulty. This leaves the jet-related variability such as a weak blazar component as a plausible mechanism for the INOV of the 8 AGN. The small fraction of INOV AGN, however, suggests that this is not a common event.

We cross-matched the eight INOV AGN with longterm variability studies in the COSMOS field to determine whether there is a relation between short-term and long-term variability. De Cicco et al. (2015) used optical monitoring data from the VLT survey telescope to select AGN by variability. There are 5 months monitoring data covering the COSMOS field, which confirmed 67 AGN with variability. However, their list of variable AGN do not match with the eight variable AGN found in this study. Simm et al. (2015, 2016) used 4-years of the Pan-STARRS data to examine AGN variability. Among our eight variable sources, three (095820.7+020213, 095834.0+024427, and 100151.1+020032) AGN are matched with their samples. For these three AGN, year-scale variability is found in several bands. So far, the result is mixed whether the INOV AGN show long-term variability, and future investigation is necessary to reach to a firm conclusion.

The AGN long-term variability is attributed to the changes in accretion disk activities. A long-term variability of 0.1 mag over, say 30 days, can produce an INOV of about 0.003 mag. Detecting this kind of INOV can possibly be used to diagnose if an AGN is undergoing a long-term AGN variable activities. This kind of observation is beyond the scope of this study, but could be achieved with future observations with improved strategies and facilities.

There are two aspects where we can improve the study with the current instrument. One is to increase the exposure time to lower the photon noise, and another is to extend the observing period of the monitoring to catch intermittent AGN variation which was

reported in other studies. We are now performing a longer term, higher S/N monitoring study and we hope to report the new results in near future that are based on the improved observing strategy. A significant improvement in the INOV study sensitivity is also expected from future large, wide-field telescopes such as the Large Synoptic Survey Telescope (Juric et al. 2015).

**Table 2.5.** List of observed AGNs

Name	X	M	R	S	R mag	z	$R_i$	1-p (C value)							
								2015.02.18				2015.03.21		2016.04.08	
								B	V	R	I	B	R	B	R
095621.66+024859.9	x	x	x	o	19.1	0.95	-1	-99 (-99)	-99 (-99)	-99 (-99)	-99 (-99)	-99 (-99)	-99 (-99)	1.00 (7.23)	1.00 (11.7)
095642.33+020554.5	x	x	x	o	19.4	1.03	-1	0.34 (1.04)	0.78 (1.40)	-99 (-99)	-99 (-99)	0.15 (1.02)	0.30 (0.97)	0.19 (1.19)	0.01 (0.73)
095642.71+024812.7	x	x	x	o	19.7	2.00	-1	0.69 (1.53)	0.37 (1.17)	0.67 (1.40)	0.05 (0.66)	0.48 (1.12)	0.42 (0.79)	0.13 (1.12)	0.80 (1.53)
095657.63+011310.1	x	x	x	o	20.2	2.33	-1	0.31 (1.00)	0.94 (1.90)	0.41 (1.16)	0.07 (0.78)	0.31 (1.06)	0.25 (1.11)	0.06 (1.00)	0.79 (1.55)
095659.32+015236.2	x	x	x	o	20.6	1.55	-1	0.05 (0.62)	0.67 (1.40)	0.11 (0.74)	0.00 (0.37)	0.25 (1.23)	-99 (-99)	0.18 (1.24)	0.01 (0.74)
095701.59+023857.3	x	x	x	o	18.8	1.07	-1	0.37 (1.18)	0.20 (0.96)	0.18 (1.06)	0.56 (1.49)	0.64 (1.63)	0.12 (1.00)	0.21 (1.29)	0.00 (0.24)
095705.14+014949.5	x	x	x	o	20.0	1.13	-1	0.20 (0.93)	0.72 (1.63)	0.00 (0.40)	0.31 (1.08)	0.16 (1.38)	0.40 (1.09)	0.01 (0.77)	0.79 (1.53)
095714.02+013145.5	x	x	x	o	21.3	2.14	-1	0.08 (0.64)	-99 (-99)	-99 (-99)	-99 (-99)	-99 (-99)	-99 (-99)	0.03 (0.82)	0.31 (1.07)
095718.27+024250.2	x	o	x	o	19.5	1.49	-1	0.05 (0.67)	0.34 (1.01)	0.37 (1.15)	0.55 (1.34)	0.43 (0.94)	0.08 (1.06)	0.19 (1.22)	0.35 (1.21)
095722.92+023147.1	x	o	x	x	21.1	-99	-1	0.63 (1.39)	0.17 (0.88)	0.52 (1.31)	-99 (-99)	-99 (-99)	-99 (-99)	0.00 (0.73)	0.28 (1.19)
095723.69+011458.7	x	x	x	o	19.7	2.47	-1	0.25 (1.00)	0.89 (1.70)	0.88 (1.64)	-99 (-99)	0.52 (1.13)	0.22 (1.13)	0.04 (0.97)	0.45 (1.33)
095723.80+015615.3	x	o	x	o	20.0	1.37	-1	0.03 (0.61)	0.25 (0.93)	0.82 (1.46)	0.68 (1.50)	0.13 (1.21)	0.66 (1.22)	0.78 (1.74)	0.02 (0.75)
095724.37+023518.8	x	x	x	o	20.9	0.96	-99	0.26 (0.98)	0.01 (0.45)	0.02 (0.48)	0.99 (2.04)	-99 (-99)	-99 (-99)	0.11 (1.13)	-99 (-99)
095726.05+024501.2	x	o	x	x	20.1	-99	-99	0.31 (1.02)	0.98 (2.38)	0.57 (1.38)	-99 (-99)	0.38 (1.17)	-99 (-99)	-99 (-99)	-99 (-99)
095728.22+025002.4	x	o	x	x	19.7	-99	-99	0.38 (1.11)	0.48 (1.14)	0.11 (0.74)	0.99 (2.86)	0.00 (0.57)	0.12 (0.77)	0.01 (0.83)	-99 (-99)
095728.33+022542.1	x	x	x	o	19.3	1.53	-99	0.46 (1.11)	0.06 (0.69)	0.06 (0.62)	0.47 (1.33)	0.47 (0.94)	0.84 (1.75)	0.11 (1.12)	0.00 (0.73)
095728.58+023147.3	x	o	x	x	19.7	-99	-99	0.30 (1.02)	0.50 (1.17)	0.08 (0.65)	0.87 (1.94)	0.63 (1.54)	0.01 (0.56)	0.52 (1.57)	0.36 (1.16)
095731.52+012939.2	x	o	x	x	21.2	-99	-1	-99 (-99)	-99 (-99)	0.49 (1.17)	-99 (-99)	-99 (-99)	-99 (-99)	0.21 (1.15)	0.04 (0.95)

Note. — X = X-ray selected, M = MIR selected, R = Radio selected AGN, S = SDSS DR7 quasar

Note. — The value "-1" in  $R_i$  is source which position is out of the VLA field of view.

Name	X	M	R	S	R mag	z	$R_i$	1-p (C value)							
								2015.02.18				2015.03.21		2016.04.08	
								B	V	R	I	B	R	B	R
095732.02+024301.8	x	o	x	x	20.9	-99	-99	-99 (-99)	0.37 (1.12)	-99 (-99)	-99 (-99)	-99 (-99)	-99 (-99)	-99 (-99)	-99 (-99)
095734.40+025330.0	x	o	x	x	21.5	-99	-99	0.23 (0.93)	-99 (-99)	-99 (-99)	-99 (-99)	-99 (-99)	-99 (-99)	0.26 (1.28)	0.06 (0.85)
095735.07+020204.2	x	o	x	x	20.3	-99	-99	-99 (-99)	0.87 (1.54)	-99 (-99)	-99 (-99)	-99 (-99)	-99 (-99)	-99 (-99)	-99 (-99)
095738.04+021931.8	x	o	x	x	20.9	-99	-99	0.07 (0.59)	0.05 (0.63)	0.16 (0.85)	-99 (-99)	-99 (-99)	-99 (-99)	0.01 (0.88)	0.82 (1.51)
095738.52+021656.3	x	o	x	x	21.0	-99	-99	0.11 (0.70)	0.20 (0.85)	0.47 (1.13)	-99 (-99)	-99 (-99)	-99 (-99)	0.03 (1.01)	0.37 (1.26)
095740.02+013109.4	x	o	x	x	21.2	0.42	-99	-99 (-99)	-99 (-99)	0.47 (1.28)	-99 (-99)	-99 (-99)	-99 (-99)	-99 (-99)	0.44 (1.22)
095743.33+024823.8	x	o	x	o	20.2	1.36	-99	0.29 (1.01)	0.15 (0.78)	0.63 (1.26)	0.42 (1.19)	0.10 (1.13)	-99 (-99)	0.84 (1.88)	0.02 (0.79)
095743.80+012555.3	x	o	x	x	20.5	-99	-1	0.30 (1.01)	0.19 (0.87)	0.10 (0.65)	0.77 (1.47)	0.18 (0.92)	-99 (-99)	0.00 (0.59)	0.13 (0.99)
095745.96+021715.3	x	x	o	x	20.3	0.50	2.01	-99 (-99)	-99 (-99)	-99 (-99)	0.54 (1.43)	-99 (-99)	-99 (-99)	-99 (-99)	0.24 (1.01)
095745.98+022533.4	x	x	o	x	18.8	0.49	0.78	0.66 (1.43)	0.83 (1.66)	-99 (-99)	-99 (-99)	-99 (-99)	-99 (-99)	-99 (-99)	-99 (-99)
095746.70+020711.8	x	o	x	x	20.6	1.57	-99	-99 (-99)	-99 (-99)	-99 (-99)	-99 (-99)	-99 (-99)	-99 (-99)	0.51 (1.43)	0.04 (0.76)
095746.90+022137.9	x	x	o	x	18.9	0.34	0.95	0.48 (1.20)	0.01 (0.48)	0.17 (0.84)	0.43 (1.25)	-99 (-99)	0.15 (0.79)	0.95 (2.13)	0.13 (0.99)
095749.99+013354.2	x	o	x	o	19.9	2.01	-99	0.37 (1.10)	0.41 (1.06)	0.94 (2.44)	0.92 (2.02)	0.42 (0.98)	0.97 (1.54)	0.99 (3.09)	-99 (-99)
095751.59+013342.0	x	x	o	x	20.4	0.67	1.75	-99 (-99)	-99 (-99)	-99 (-99)	-99 (-99)	-99 (-99)	-99 (-99)	-99 (-99)	1.00 (3.56)
095752.32+022021.2	x	x	x	o	18.4	2.05	-99	0.32 (1.09)	0.24 (0.95)	0.00 (0.24)	0.55 (1.39)	0.08 (0.76)	-99 (-99)	0.33 (1.50)	0.62 (1.56)
095753.06+014114.5	x	o	x	x	21.2	1.81	-99	0.01 (0.54)	0.42 (1.02)	-99 (-99)	-99 (-99)	-99 (-99)	-99 (-99)	0.18 (1.06)	-99 (-99)
095754.10+025508.7	x	o	x	o	19.0	1.56	-1	0.67 (1.55)	0.35 (1.05)	0.51 (1.15)	0.98 (2.51)	0.13 (0.68)	0.02 (0.69)	0.05 (0.98)	0.54 (1.25)
095754.71+023832.9	x	o	x	o	19.3	1.60	-99	0.30 (1.02)	0.26 (0.97)	0.37 (1.08)	0.63 (1.45)	0.13 (0.85)	0.02 (0.54)	0.74 (1.85)	0.61 (1.52)
095755.08+024806.6	x	o	x	o	19.0	1.11	-99	0.11 (0.81)	0.01 (0.51)	0.78 (1.81)	0.30 (1.08)	0.32 (1.22)	0.05 (0.80)	0.51 (1.52)	0.06 (0.82)
095756.27+022344.8	x	x	o	x	19.4	0.48	0.94	-99 (-99)	0.00 (0.41)	0.94 (2.33)	0.60 (1.46)	-99 (-99)	0.72 (1.23)	0.29 (1.29)	0.05 (0.85)
095756.52+022717.3	x	x	o	x	21.7	0.73	2.21	-99 (-99)	-99 (-99)	-99 (-99)	0.00 (0.41)	-99 (-99)	-99 (-99)	-99 (-99)	-99 (-99)
095756.60+025530.1	x	o	x	x	20.8	-99	-1	0.09 (0.72)	0.01 (0.41)	0.00 (0.17)	0.09 (0.74)	-99 (-99)	-99 (-99)	0.16 (1.15)	0.07 (0.89)
095756.77+024841.0	x	o	x	x	20.9	1.68	-99	0.39 (1.16)	0.22 (0.92)	0.13 (0.67)	-99 (-99)	-99 (-99)	-99 (-99)	0.46 (1.47)	0.01 (0.70)
095757.48+014737.4	x	o	x	x	21.4	-99	-99	-99 (-99)	-99 (-99)	0.17 (0.86)	-99 (-99)	-99 (-99)	-99 (-99)	-99 (-99)	-99 (-99)
095758.41+021729.2	x	o	x	x	21.6	2.24	-99	0.16 (0.83)	0.64 (1.19)	-99 (-99)	-99 (-99)	-99 (-99)	-99 (-99)	-99 (-99)	-99 (-99)

Name	X	M	R	S	R mag	z	$R_i$	1-p (C value)							
								2015.02.18				2015.03.21		2016.04.08	
								B	V	R	I	B	R	B	R
095758.77+021650.4	x	x	o	x	19.0	0.30	0.71	-99 (-99)	0.95 (1.80)	0.40 (1.06)	0.24 (1.04)	-99 (-99)	-99 (-99)	-99 (-99)	0.90 (1.84)
095759.51+020436.1	x	o	x	o	19.1	2.03	-99	0.79 (1.58)	0.03 (0.57)	0.45 (1.11)	0.38 (1.28)	0.78 (1.81)	0.52 (1.57)	0.98 (2.32)	0.03 (0.80)
095800.78+013157.9	x	o	x	x	21.4	0.66	-99	-99 (-99)	-99 (-99)	-99 (-99)	-99 (-99)	-99 (-99)	-99 (-99)	-99 (-99)	0.08 (0.99)
095801.34+024328.0	x	o	o	x	20.9	0.57	0.84	-99 (-99)	-99 (-99)	0.73 (1.55)	0.04 (0.61)	-99 (-99)	-99 (-99)	-99 (-99)	0.13 (0.91)
095804.62+014213.6	x	o	x	x	21.3	0.01	-99	-99 (-99)	-99 (-99)	0.69 (1.54)	-99 (-99)	-99 (-99)	-99 (-99)	-99 (-99)	0.80 (1.49)
095805.76+025633.3	x	o	x	x	21.3	-99	-1	-99 (-99)	0.05 (0.62)	0.06 (0.72)	-99 (-99)	-99 (-99)	-99 (-99)	-99 (-99)	-99 (-99)
095805.85+015159.0	x	o	x	x	21.4	1.66	-99	0.48 (1.31)	0.00 (0.22)	0.09 (0.79)	-99 (-99)	-99 (-99)	-99 (-99)	0.00 (0.72)	0.06 (0.85)
095808.76+020001.1	o	x	x	x	18.7	-99	-99	0.49 (1.20)	0.12 (0.79)	0.50 (1.23)	0.23 (0.98)	0.53 (1.21)	0.29 (1.06)	0.63 (1.59)	-99 (-99)
095810.88+014005.2	x	o	x	o	20.0	2.10	-99	0.82 (1.64)	0.80 (1.40)	0.14 (0.86)	0.01 (0.50)	0.34 (1.14)	-99 (-99)	0.51 (1.52)	0.03 (0.81)
095814.25+013751.9	x	x	o	x	21.5	0.90	2.43	-99 (-99)	-99 (-99)	0.75 (1.64)	-99 (-99)	-99 (-99)	-99 (-99)	-99 (-99)	-99 (-99)
095814.86+013203.0	x	o	x	x	20.7	2.36	-99	0.04 (0.63)	0.41 (1.11)	0.87 (1.61)	-99 (-99)	0.22 (0.85)	-99 (-99)	0.17 (1.18)	-99 (-99)
095815.28+014738.7	x	o	x	x	21.8	1.83	-99	0.88 (1.80)	-99 (-99)	-99 (-99)	-99 (-99)	-99 (-99)	-99 (-99)	0.19 (1.35)	-99 (-99)
095815.50+015612.2	x	o	x	x	20.1	0.38	-99	0.55 (1.23)	0.07 (0.65)	0.30 (1.09)	0.67 (1.58)	-99 (-99)	0.45 (1.21)	0.06 (1.04)	0.98 (2.19)
095815.50+014922.9	x	o	x	o	19.9	1.50	1.05	-99 (-99)	-99 (-99)	-99 (-99)	-99 (-99)	-99 (-99)	-99 (-99)	0.52 (1.45)	0.94 (2.08)
095815.53+015840.6	o	o	x	x	21.1	1.67	-99	0.39 (1.09)	0.45 (1.13)	0.11 (0.80)	0.40 (1.16)	-99 (-99)	-99 (-99)	-99 (-99)	-99 (-99)
095818.23+015306.3	x	o	x	x	20.3	0.34	-99	0.19 (0.87)	0.39 (1.09)	0.86 (1.59)	0.62 (1.59)	-99 (-99)	-99 (-99)	-99 (-99)	0.89 (1.70)
095819.36+013530.6	x	o	x	x	21.6	0.06	-99	-99 (-99)	-99 (-99)	-99 (-99)	-99 (-99)	-99 (-99)	-99 (-99)	0.99 (2.72)	-99 (-99)
095819.88+022903.5	x	x	x	o	18.4	0.34	-99	-99 (-99)	-99 (-99)	-99 (-99)	-99 (-99)	-99 (-99)	-99 (-99)	0.97 (2.31)	0.49 (1.37)
095820.45+020304.1	o	o	x	o	19.7	1.35	-99	0.69 (1.36)	0.53 (1.38)	0.78 (1.52)	0.49 (1.37)	0.35 (1.15)	0.61 (1.05)	0.43 (1.45)	1.00 (3.42)
095820.78+020213.7	o	o	x	x	20.8	1.85	-99	0.30 (1.08)	0.21 (0.98)	0.73 (1.37)	-99 (-99)	0.60 (1.08)	-99 (-99)	0.95 (2.03)	1.00 (2.49)
095821.40+025259.0	x	o	x	x	20.0	0.31	-99	-99 (-99)	-99 (-99)	-99 (-99)	0.39 (1.23)	-99 (-99)	-99 (-99)	-99 (-99)	0.12 (0.88)
095821.66+024628.2	x	x	x	o	18.8	1.40	1.84	-99 (-99)	-99 (-99)	-99 (-99)	-99 (-99)	0.53 (1.27)	-99 (-99)	-99 (-99)	-99 (-99)
095821.82+014724.1	x	x	o	x	20.5	0.46	1.20	-99 (-99)	-99 (-99)	-99 (-99)	-99 (-99)	-99 (-99)	-99 (-99)	-99 (-99)	0.24 (1.25)
095822.08+012653.1	x	o	x	x	21.2	-99	-1	0.18 (0.85)	0.15 (0.68)	0.92 (1.75)	-99 (-99)	-99 (-99)	-99 (-99)	-99 (-99)	-99 (-99)
095822.19+014524.2	x	x	x	o	17.5	1.96	0.00	-99 (-99)	-99 (-99)	-99 (-99)	0.48 (1.51)	-99 (-99)	0.15 (0.89)	0.26 (1.86)	0.88 (2.07)

Name	X	M	R	S	R mag	z	$R_i$	1-p (C value)							
								2015.02.18				2015.03.21		2016.04.08	
								B	V	R	I	B	R	B	R
095823.74+011235.8	x	x	x	o	18.9	0.50	-1	-99 (-99)	0.82 (1.73)	-99 (-99)	-99 (-99)	-99 (-99)	-99 (-99)	-99 (-99)	-99 (-99)
095824.02+024916.0	x	x	o	x	18.4	0.34	2.19	0.02 (0.46)	0.05 (0.65)	0.79 (1.51)	0.71 (1.62)	-99 (-99)	-99 (-99)	0.47 (1.56)	-99 (-99)
095825.79+012628.6	x	o	x	x	20.9	-99	-1	0.65 (1.47)	0.24 (0.94)	0.69 (1.32)	0.99 (2.62)	-99 (-99)	-99 (-99)	0.32 (1.38)	0.12 (0.99)
095828.65+014407.8	x	x	o	x	20.6	0.59	1.65	-99 (-99)	0.01 (0.43)	0.32 (0.95)	0.07 (0.65)	-99 (-99)	-99 (-99)	-99 (-99)	-99 (-99)
095829.25+024418.0	x	o	x	x	20.2	1.15	-99	0.17 (0.88)	0.37 (1.07)	-99 (-99)	-99 (-99)	0.51 (1.22)	-99 (-99)	-99 (-99)	-99 (-99)
095831.55+025205.5	x	x	o	x	18.1	0.35	1.15	0.19 (0.89)	0.88 (1.78)	0.23 (1.08)	0.48 (1.33)	0.12 (1.11)	0.00 (0.51)	0.01 (0.86)	0.77 (1.63)
095832.46+023555.9	x	o	x	x	21.5	2.38	-99	-99 (-99)	0.17 (0.81)	-99 (-99)	-99 (-99)	-99 (-99)	-99 (-99)	-99 (-99)	-99 (-99)
095833.27+021720.4	x	o	x	x	20.5	0.23	-99	0.41 (1.07)	0.28 (1.00)	-99 (-99)	0.01 (0.50)	-99 (-99)	-99 (-99)	0.06 (0.99)	0.42 (1.25)
095834.05+024427.2	x	o	x	o	19.3	1.88	-99	0.96 (1.96)	0.09 (0.71)	0.65 (1.31)	0.64 (1.48)	0.17 (1.12)	0.17 (0.99)	1.00 (3.37)	0.86 (1.55)
095834.75+014502.4	x	o	x	o	19.3	1.88	-99	0.57 (1.35)	0.56 (1.29)	0.64 (1.27)	0.07 (0.75)	0.13 (0.91)	0.02 (0.63)	0.99 (2.31)	0.72 (1.44)
095835.91+024954.9	x	x	o	x	21.2	0.69	1.13	-99 (-99)	-99 (-99)	0.13 (0.85)	0.04 (0.67)	-99 (-99)	-99 (-99)	-99 (-99)	0.41 (1.29)
095835.98+015157.1	o	o	o	o	19.6	2.94	0.87	0.40 (1.06)	0.00 (0.20)	0.74 (1.56)	0.01 (0.50)	0.66 (1.10)	0.47 (1.25)	0.18 (1.24)	0.31 (1.15)
095837.36+023602.9	x	o	x	x	21.0	1.20	-99	-99 (-99)	-99 (-99)	0.85 (1.68)	-99 (-99)	-99 (-99)	-99 (-99)	-99 (-99)	0.20 (1.01)
095839.26+020506.8	o	o	x	x	20.1	1.22	-99	0.00 (0.28)	0.24 (0.87)	0.77 (1.43)	0.11 (0.82)	0.24 (0.98)	-99 (-99)	0.10 (1.07)	-99 (-99)
095840.02+021711.1	o	x	x	x	21.2	1.02	-99	0.01 (0.47)	0.90 (2.10)	0.19 (0.85)	-99 (-99)	-99 (-99)	-99 (-99)	-99 (-99)	-99 (-99)
095841.80+015318.2	o	x	x	x	20.1	1.78	-99	0.30 (1.08)	0.02 (0.53)	0.10 (0.82)	0.28 (0.99)	0.02 (0.87)	-99 (-99)	0.11 (1.09)	-99 (-99)
095844.73+020249.7	x	x	o	x	16.8	0.30	0.00	0.29 (1.26)	0.15 (0.92)	0.76 (2.56)	0.09 (1.10)	0.33 (1.54)	0.90 (1.90)	-99 (-99)	0.31 (2.00)
095844.94+014309.0	x	o	x	o	19.9	1.33	-99	-99 (-99)	-99 (-99)	-99 (-99)	-99 (-99)	0.64 (1.36)	0.35 (1.19)	0.31 (1.28)	-99 (-99)
095847.00+021552.3	o	o	x	x	20.8	0.55	0.91	-99 (-99)	-99 (-99)	0.14 (0.77)	0.76 (1.35)	-99 (-99)	-99 (-99)	-99 (-99)	-99 (-99)
095848.86+023441.2	x	o	x	o	20.5	1.54	-99	-99 (-99)	0.10 (0.68)	0.17 (0.81)	0.87 (1.84)	1.00 (4.44)	-99 (-99)	0.28 (1.23)	0.34 (1.14)
095849.03+013220.1	x	x	o	x	19.4	0.50	1.12	0.64 (1.39)	0.19 (0.94)	0.25 (1.07)	0.79 (1.60)	0.12 (0.80)	-99 (-99)	0.26 (1.18)	-99 (-99)
095849.40+022511.1	o	o	x	x	19.8	1.10	0.69	-99 (-99)	0.02 (0.45)	-99 (-99)	-99 (-99)	0.13 (1.09)	-99 (-99)	0.65 (1.62)	0.81 (1.54)
095849.50+013111.5	x	o	x	x	21.4	0.01	-99	-99 (-99)	-99 (-99)	0.64 (1.45)	-99 (-99)	-99 (-99)	-99 (-99)	-99 (-99)	0.27 (1.06)
095852.14+025156.6	x	o	x	o	18.7	1.40	-99	-99 (-99)	-99 (-99)	-99 (-99)	-99 (-99)	0.39 (1.32)	0.48 (1.23)	0.17 (1.23)	0.20 (0.96)
095852.26+013618.1	x	x	o	x	20.9	0.79	0.95	-99 (-99)	-99 (-99)	0.17 (1.09)	0.27 (1.05)	-99 (-99)	-99 (-99)	-99 (-99)	0.27 (1.00)

Name	X	M	R	S	R mag	z	$R_i$	1-p (C value)							
								2015.02.18				2015.03.21		2016.04.08	
								B	V	R	I	B	R	B	R
095854.03+025737.2	x	x	x	o	20.1	2.21	-1	0.98 (2.13)	0.88 (1.67)	0.26 (0.98)	0.91 (1.74)	0.24 (0.90)	0.47 (1.20)	0.25 (1.24)	0.00 (0.55)
095855.26+013510.1	x	x	o	x	20.2	0.62	1.33	0.02 (0.53)	0.65 (1.31)	0.61 (1.46)	0.13 (0.85)	-99 (-99)	0.04 (0.79)	0.55 (1.51)	0.80 (1.53)
095855.40+022037.3	x	o	x	x	19.5	0.38	0.25	0.24 (0.94)	0.05 (0.64)	0.27 (0.91)	0.83 (1.68)	0.00 (0.68)	-99 (-99)	-99 (-99)	-99 (-99)
095856.20+024127.9	x	x	o	x	21.2	0.91	2.46	-99 (-99)	-99 (-99)	0.58 (1.33)	-99 (-99)	-99 (-99)	-99 (-99)	-99 (-99)	0.17 (1.00)
095856.22+012816.8	x	o	x	o	20.2	1.55	-1	0.84 (1.69)	0.48 (1.17)	0.05 (0.58)	0.32 (1.14)	0.39 (1.20)	0.44 (0.83)	0.40 (1.51)	0.21 (1.33)
095857.03+020354.8	o	x	x	x	20.8	0.67	0.18	-99 (-99)	-99 (-99)	0.28 (1.11)	0.07 (0.81)	-99 (-99)	-99 (-99)	-99 (-99)	0.37 (1.25)
095857.24+022602.0	o	o	x	x	21.7	2.09	-99	-99 (-99)	-99 (-99)	-99 (-99)	-99 (-99)	-99 (-99)	-99 (-99)	0.07 (0.97)	-99 (-99)
095858.68+020139.2	o	o	x	o	19.4	2.45	-99	0.00 (0.33)	0.84 (1.69)	0.02 (0.59)	0.02 (0.60)	0.08 (0.91)	0.17 (0.79)	0.40 (1.48)	0.04 (0.74)
095858.93+025329.9	x	o	x	x	20.9	0.72	-99	-99 (-99)	-99 (-99)	0.07 (0.69)	-99 (-99)	-99 (-99)	-99 (-99)	0.03 (0.88)	0.55 (1.33)
095901.52+024740.6	x	x	o	x	19.2	0.49	1.89	-99 (-99)	0.30 (1.00)	-99 (-99)	-99 (-99)	-99 (-99)	-99 (-99)	-99 (-99)	-99 (-99)
095902.31+021520.3	o	x	x	x	21.0	-99	-99	-99 (-99)	-99 (-99)	0.27 (0.91)	0.26 (1.04)	-99 (-99)	-99 (-99)	-99 (-99)	-99 (-99)
095902.75+021906.5	o	x	x	o	18.4	0.34	0.09	0.27 (1.03)	0.01 (0.46)	0.18 (0.85)	0.87 (1.96)	0.13 (0.99)	0.03 (0.58)	0.34 (1.47)	0.06 (0.92)
095903.23+022003.0	o	o	x	x	20.9	1.13	-99	0.08 (0.66)	0.12 (0.78)	0.37 (1.15)	-99 (-99)	-99 (-99)	-99 (-99)	0.18 (1.24)	0.24 (1.15)
095905.12+021530.0	o	o	x	x	21.2	2.22	-99	-99 (-99)	0.21 (0.87)	0.03 (0.53)	-99 (-99)	-99 (-99)	-99 (-99)	-99 (-99)	-99 (-99)
095905.55+025145.1	x	o	x	x	19.6	0.43	-99	0.81 (1.54)	0.00 (0.40)	0.12 (0.72)	0.19 (0.94)	-99 (-99)	0.04 (1.12)	0.24 (1.29)	0.26 (1.09)
095906.64+023845.3	x	x	o	x	21.7	0.71	1.79	-99 (-99)	-99 (-99)	-99 (-99)	0.31 (1.04)	-99 (-99)	-99 (-99)	-99 (-99)	-99 (-99)
095908.32+024309.6	x	x	o	o	18.2	1.31	2.65	0.93 (2.23)	-99 (-99)	0.54 (1.31)	0.28 (1.08)	0.00 (0.57)	0.46 (1.57)	0.44 (1.52)	0.07 (0.91)
095908.69+025424.0	x	x	x	o	18.6	1.55	-99	0.73 (1.66)	0.31 (1.00)	0.05 (0.59)	0.80 (1.81)	0.13 (0.89)	0.27 (1.00)	0.03 (1.02)	0.30 (1.14)
095909.54+021916.5	o	o	x	x	20.1	0.37	-99	-99 (-99)	-99 (-99)	-99 (-99)	-99 (-99)	-99 (-99)	-99 (-99)	0.25 (1.27)	-99 (-99)
095910.82+021909.7	x	x	o	x	21.2	0.76	1.28	-99 (-99)	-99 (-99)	0.31 (0.95)	0.30 (1.08)	-99 (-99)	-99 (-99)	-99 (-99)	0.07 (0.99)
095911.08+023350.8	o	o	x	x	20.7	0.70	-99	0.09 (0.75)	0.46 (1.13)	0.28 (1.08)	0.48 (1.45)	0.04 (0.85)	-99 (-99)	0.07 (1.09)	0.32 (1.16)
095911.16+024224.0	o	x	x	x	21.3	-99	-99	-99 (-99)	-99 (-99)	0.18 (0.93)	-99 (-99)	-99 (-99)	-99 (-99)	-99 (-99)	0.99 (2.01)
095911.64+012603.1	x	o	x	x	21.8	-99	-1	0.07 (0.60)	-99 (-99)	-99 (-99)	-99 (-99)	-99 (-99)	-99 (-99)	0.05 (1.22)	-99 (-99)
095913.92+023844.6	o	o	x	x	21.3	2.08	-99	0.19 (0.90)	0.65 (1.30)	0.01 (0.42)	-99 (-99)	-99 (-99)	-99 (-99)	0.04 (0.90)	0.11 (0.86)
095916.05+015048.2	o	x	x	x	20.6	1.03	-99	-99 (-99)	-99 (-99)	0.62 (1.32)	0.84 (1.64)	-99 (-99)	-99 (-99)	0.06 (1.04)	0.41 (1.15)

Name	X	M	R	S	R mag	z	$R_i$	1-p (C value)							
								2015.02.18				2015.03.21		2016.04.08	
								B	V	R	I	B	R	B	R
095917.27+015019.2	o	o	x	x	20.9	1.34	-99	0.43 (1.17)	0.75 (1.53)	0.23 (0.81)	0.04 (0.63)	-99 (-99)	-99 (-99)	0.21 (1.37)	0.20 (1.14)
095919.82+024238.7	o	o	x	x	20.5	2.12	-99	0.13 (0.79)	0.82 (1.63)	0.86 (1.65)	0.23 (1.04)	0.07 (0.96)	-99 (-99)	0.01 (0.78)	0.08 (0.89)
095920.89+020031.9	o	o	x	x	20.6	1.48	-99	0.08 (0.71)	0.55 (1.20)	0.60 (1.38)	0.08 (0.69)	0.03 (0.56)	-99 (-99)	-99 (-99)	0.02 (0.75)
095920.91+015203.6	o	x	x	x	20.3	-99	-99	-99 (-99)	0.15 (0.88)	0.01 (0.50)	0.22 (0.98)	-99 (-99)	-99 (-99)	-99 (-99)	0.04 (0.89)
095923.55+022227.4	o	o	x	x	20.3	2.72	-99	0.03 (0.60)	0.85 (1.65)	0.57 (1.26)	0.76 (1.34)	0.00 (0.64)	-99 (-99)	0.43 (1.43)	0.35 (1.18)
095924.47+015954.4	o	o	x	o	18.3	1.23	-99	-99 (-99)	0.52 (1.24)	-99 (-99)	-99 (-99)	0.11 (0.82)	0.26 (0.73)	0.00 (0.69)	-99 (-99)
095925.55+011532.7	x	x	x	o	18.6	1.69	-1	0.56 (1.35)	0.59 (1.32)	0.57 (1.23)	0.10 (0.81)	0.57 (1.39)	0.62 (0.87)	0.08 (1.13)	0.17 (0.99)
095926.89+015341.5	o	o	x	x	19.3	0.44	0.16	0.07 (0.64)	0.10 (0.73)	0.67 (1.29)	0.04 (0.63)	-99 (-99)	0.56 (1.43)	0.08 (1.16)	0.28 (1.20)
095928.33+021950.6	o	o	x	x	20.6	1.47	-99	0.11 (0.77)	0.26 (0.91)	0.00 (0.17)	-99 (-99)	0.16 (0.92)	-99 (-99)	0.36 (1.35)	0.06 (0.83)
095928.45+015934.8	o	x	x	x	21.3	1.16	-99	0.04 (0.53)	-99 (-99)	0.16 (0.90)	-99 (-99)	-99 (-99)	-99 (-99)	0.08 (1.12)	-99 (-99)
095928.72+021738.6	o	o	x	x	21.5	3.34	0.99	-99 (-99)	-99 (-99)	0.18 (1.01)	-99 (-99)	-99 (-99)	-99 (-99)	-99 (-99)	-99 (-99)
095929.23+022844.8	x	x	o	x	21.6	0.73	1.85	-99 (-99)	-99 (-99)	0.64 (1.25)	0.71 (1.53)	-99 (-99)	-99 (-99)	-99 (-99)	-99 (-99)
095929.24+022034.4	o	o	x	x	21.7	1.73	-99	0.18 (0.82)	-99 (-99)	-99 (-99)	-99 (-99)	-99 (-99)	-99 (-99)	0.01 (0.83)	-99 (-99)
095929.33+021723.0	x	x	o	x	21.2	0.68	1.10	-99 (-99)	-99 (-99)	0.43 (1.29)	-99 (-99)	-99 (-99)	-99 (-99)	-99 (-99)	-99 (-99)
095930.20+024125.0	o	o	x	x	21.6	2.16	-99	0.25 (1.00)	0.16 (0.78)	0.37 (1.14)	-99 (-99)	-99 (-99)	-99 (-99)	-99 (-99)	-99 (-99)
095931.44+022703.1	o	x	x	x	21.2	1.31	0.81	0.39 (1.30)	0.53 (1.20)	0.14 (0.80)	-99 (-99)	-99 (-99)	-99 (-99)	-99 (-99)	-99 (-99)
095932.00+022048.4	o	o	x	x	21.5	1.02	-99	-99 (-99)	-99 (-99)	-99 (-99)	-99 (-99)	-99 (-99)	-99 (-99)	0.07 (0.98)	-99 (-99)
095933.73+024056.7	o	x	x	x	20.5	0.27	-99	0.51 (1.21)	0.10 (0.80)	0.55 (1.25)	0.09 (0.68)	-99 (-99)	-99 (-99)	0.26 (1.36)	0.15 (0.97)
095934.35+012849.4	x	o	x	x	20.7	-99	-1	0.63 (1.24)	-99 (-99)	-99 (-99)	0.43 (1.27)	-99 (-99)	-99 (-99)	0.32 (1.35)	0.59 (1.42)
095934.75+020633.8	x	x	o	x	21.2	0.67	1.09	-99 (-99)	-99 (-99)	0.07 (0.59)	-99 (-99)	-99 (-99)	-99 (-99)	-99 (-99)	0.39 (1.16)
095934.78+014553.9	x	x	o	x	19.9	0.53	0.72	-99 (-99)	0.05 (0.64)	0.29 (1.01)	0.94 (2.15)	-99 (-99)	0.00 (0.43)	-99 (-99)	0.21 (1.12)
095935.43+013100.0	x	o	x	x	20.7	1.49	-99	-99 (-99)	0.95 (1.51)	0.25 (0.96)	0.00 (0.36)	-99 (-99)	-99 (-99)	0.28 (1.36)	0.18 (1.08)
095935.50+020538.1	o	o	x	x	21.7	1.91	-99	0.24 (0.93)	-99 (-99)	-99 (-99)	-99 (-99)	-99 (-99)	-99 (-99)	0.08 (1.03)	-99 (-99)
095935.59+015100.4	x	x	o	x	21.0	0.63	1.02	-99 (-99)	-99 (-99)	0.01 (0.35)	-99 (-99)	-99 (-99)	-99 (-99)	-99 (-99)	-99 (-99)
095935.68+024839.2	x	o	x	o	20.4	1.97	-99	0.94 (1.97)	0.01 (0.48)	0.25 (1.06)	0.05 (0.71)	0.18 (1.16)	-99 (-99)	0.56 (1.56)	0.17 (0.96)

Name	X	M	R	S	R mag	z	$R_i$	1-p (C value)							
								2015.02.18				2015.03.21		2016.04.08	
								B	V	R	I	B	R	B	R
095938.28+020450.1	o	o	x	x	20.4	2.79	-99	0.10 (0.75)	0.14 (0.82)	-99 (-99)	-99 (-99)	-99 (-99)	-99 (-99)	-99 (-99)	-99 (-99)
095938.45+025329.4	x	x	o	x	19.0	0.22	0.92	0.19 (0.88)	0.47 (1.24)	0.47 (1.12)	0.67 (1.57)	-99 (-99)	-99 (-99)	-99 (-99)	0.08 (0.92)
095940.06+022306.8	o	o	x	x	19.7	1.12	-99	0.55 (1.22)	0.17 (0.82)	0.01 (0.52)	0.80 (1.84)	0.09 (0.77)	0.48 (1.40)	0.35 (1.35)	0.19 (0.99)
095940.74+021938.9	o	o	o	x	20.3	1.45	1.09	0.05 (0.64)	0.78 (1.53)	0.01 (0.48)	0.07 (0.80)	0.06 (1.00)	0.05 (0.64)	0.34 (1.40)	0.56 (1.29)
095941.41+015845.3	o	x	x	x	21.7	2.50	-99	-99 (-99)	-99 (-99)	-99 (-99)	-99 (-99)	-99 (-99)	-99 (-99)	0.00 (0.72)	-99 (-99)
095942.08+024103.3	o	o	x	x	20.5	1.79	0.63	0.35 (1.00)	0.70 (1.40)	0.20 (0.88)	0.75 (1.71)	0.15 (0.67)	-99 (-99)	0.01 (0.77)	0.43 (1.24)
095942.72+023206.5	x	x	o	x	21.1	0.67	1.00	-99 (-99)	-99 (-99)	0.11 (0.70)	0.02 (0.47)	-99 (-99)	-99 (-99)	-99 (-99)	-99 (-99)
095944.14+025037.7	x	o	x	x	21.4	1.11	-99	0.26 (1.01)	0.10 (0.81)	0.29 (0.89)	-99 (-99)	-99 (-99)	-99 (-99)	0.07 (1.11)	0.07 (0.79)
095944.79+024048.9	o	x	x	x	20.2	1.43	-99	0.37 (1.07)	0.81 (1.51)	0.60 (1.48)	-99 (-99)	0.02 (0.62)	-99 (-99)	0.47 (1.48)	0.15 (0.99)
095945.01+012828.8	x	o	x	x	20.6	-99	-1	0.12 (0.79)	0.45 (1.15)	0.00 (0.40)	-99 (-99)	-99 (-99)	-99 (-99)	0.48 (1.62)	0.22 (1.11)
095945.60+013032.2	x	o	x	o	20.0	1.10	-99	0.77 (1.55)	0.21 (0.83)	0.76 (1.55)	0.06 (0.72)	0.37 (1.25)	0.06 (0.78)	-99 (-99)	0.99 (2.57)
095946.02+024743.6	x	x	o	o	18.7	1.06	0.51	0.06 (0.68)	0.40 (1.12)	0.18 (0.89)	-99 (-99)	0.38 (1.38)	0.01 (0.58)	0.59 (1.70)	0.00 (0.68)
095946.36+023602.2	x	x	o	x	19.5	0.30	2.28	0.33 (1.06)	0.19 (0.91)	0.00 (0.38)	0.11 (0.79)	-99 (-99)	-99 (-99)	-99 (-99)	-99 (-99)
095946.93+022209.4	o	o	x	x	20.7	0.90	-99	0.67 (1.32)	0.25 (0.97)	0.20 (0.89)	-99 (-99)	0.41 (1.44)	-99 (-99)	-99 (-99)	-99 (-99)
095947.07+024806.8	x	x	o	x	21.4	0.60	2.00	-99 (-99)	-99 (-99)	-99 (-99)	0.16 (0.86)	-99 (-99)	-99 (-99)	-99 (-99)	-99 (-99)
095949.40+020141.0	o	o	x	o	19.2	1.75	-99	0.17 (0.87)	0.03 (0.57)	0.00 (0.36)	0.12 (0.84)	0.04 (0.65)	0.01 (0.53)	0.20 (1.28)	0.19 (1.12)
095949.85+020011.1	o	o	x	x	21.1	1.80	-99	0.46 (1.14)	0.71 (1.46)	0.02 (0.49)	-99 (-99)	-99 (-99)	-99 (-99)	0.13 (1.02)	0.22 (0.99)
095950.40+020156.7	o	x	x	x	20.8	1.95	-99	-99 (-99)	0.93 (2.28)	-99 (-99)	-99 (-99)	-99 (-99)	-99 (-99)	-99 (-99)	-99 (-99)
095951.39+014049.3	x	x	o	x	18.1	0.37	0.13	0.05 (0.57)	0.07 (0.69)	0.49 (1.21)	0.03 (0.62)	-99 (-99)	-99 (-99)	-99 (-99)	-99 (-99)
095954.24+022438.1	x	x	o	x	21.4	0.71	1.64	-99 (-99)	-99 (-99)	0.22 (0.97)	-99 (-99)	-99 (-99)	-99 (-99)	-99 (-99)	-99 (-99)
095954.78+013206.5	x	o	x	x	20.0	0.85	-99	0.99 (2.64)	0.81 (1.65)	-99 (-99)	-99 (-99)	-99 (-99)	-99 (-99)	-99 (-99)	-99 (-99)
095957.98+014327.4	o	o	x	o	20.2	1.62	-99	0.24 (0.85)	0.01 (0.43)	0.71 (1.52)	0.48 (1.25)	0.07 (0.91)	-99 (-99)	0.01 (0.77)	0.11 (0.91)
095958.47+021530.7	o	x	x	x	20.4	0.65	-99	0.42 (1.17)	-99 (-99)	-99 (-99)	-99 (-99)	-99 (-99)	-99 (-99)	-99 (-99)	-99 (-99)
095958.54+021805.3	o	o	x	x	20.1	1.78	-99	0.49 (1.24)	0.81 (1.77)	0.85 (1.40)	0.81 (1.94)	0.01 (0.64)	-99 (-99)	0.09 (1.06)	0.33 (1.18)
095959.50+013151.7	x	x	o	x	21.0	1.01	0.93	0.04 (0.55)	0.25 (1.03)	0.09 (0.65)	0.02 (0.56)	-99 (-99)	-99 (-99)	0.09 (0.97)	0.37 (1.26)

Name	X	M	R	S	R mag	z	$R_i$	1-p (C value)							
								2015.02.18				2015.03.21		2016.04.08	
								B	V	R	I	B	R	B	R
095959.63+024608.8	x	x	o	x	17.0	0.16	0.64	0.53 (1.38)	0.98 (2.66)	-99 (-99)	-99 (-99)	0.83 (1.44)	0.18 (0.96)	0.97 (2.37)	0.57 (2.13)
100001.45+024844.7	x	o	x	o	19.4	0.76	0.93	0.81 (1.68)	0.39 (1.08)	0.92 (1.68)	0.64 (1.47)	0.13 (1.00)	0.60 (1.08)	0.24 (1.32)	0.75 (1.51)
100001.76+024016.1	x	o	x	x	21.4	0.01	-99	-99 (-99)	-99 (-99)	0.25 (0.82)	-99 (-99)	-99 (-99)	-99 (-99)	0.02 (0.88)	0.09 (0.97)
100005.44+023029.2	x	x	o	x	20.6	0.74	1.97	-99 (-99)	0.01 (0.41)	0.19 (0.95)	0.07 (0.72)	-99 (-99)	-99 (-99)	-99 (-99)	0.58 (1.56)
100005.98+015453.4	x	o	o	x	21.2	0.94	1.10	-99 (-99)	-99 (-99)	0.01 (0.44)	0.04 (0.62)	-99 (-99)	-99 (-99)	-99 (-99)	-99 (-99)
100006.19+015535.1	x	o	x	x	21.5	0.68	-99	-99 (-99)	-99 (-99)	0.32 (1.07)	0.16 (1.00)	-99 (-99)	-99 (-99)	-99 (-99)	0.00 (0.40)
100007.35+024043.6	o	x	x	x	21.8	1.93	-99	0.13 (0.78)	-99 (-99)	-99 (-99)	-99 (-99)	-99 (-99)	-99 (-99)	-99 (-99)	-99 (-99)
100008.15+013306.5	x	o	x	o	20.4	1.17	-99	0.05 (0.64)	0.67 (1.31)	0.46 (1.29)	-99 (-99)	0.02 (0.89)	-99 (-99)	0.12 (1.09)	0.56 (1.31)
100008.43+020247.4	x	o	x	x	20.6	0.36	0.84	-99 (-99)	0.60 (1.42)	0.38 (0.98)	0.20 (0.86)	-99 (-99)	-99 (-99)	-99 (-99)	0.36 (1.05)
100008.93+021440.6	o	o	x	x	19.4	2.53	0.50	1.00 (4.04)	1.00 (5.37)	1.00 (5.18)	-99 (-99)	-99 (-99)	-99 (-99)	-99 (-99)	-99 (-99)
100009.97+024741.7	x	o	x	x	20.9	0.30	-99	0.95 (1.89)	0.54 (1.14)	0.55 (1.25)	0.85 (1.51)	-99 (-99)	-99 (-99)	-99 (-99)	0.02 (0.78)
100010.15+024141.4	x	x	o	x	18.1	0.21	0.92	-99 (-99)	0.55 (1.31)	-99 (-99)	-99 (-99)	-99 (-99)	-99 (-99)	-99 (-99)	-99 (-99)
100010.19+023745.2	o	o	x	x	20.5	1.55	-99	0.48 (1.13)	-99 (-99)	-99 (-99)	-99 (-99)	0.02 (0.78)	-99 (-99)	0.46 (1.43)	0.16 (1.06)
100012.44+014058.0	o	o	x	x	20.3	2.27	-99	0.16 (0.84)	0.06 (0.69)	0.91 (1.68)	0.14 (0.93)	0.02 (0.65)	-99 (-99)	0.09 (1.02)	0.87 (1.62)
100012.91+023522.8	o	x	x	o	18.5	0.69	-99	0.12 (0.86)	0.43 (1.17)	-99 (-99)	-99 (-99)	0.21 (1.10)	-99 (-99)	-99 (-99)	-99 (-99)
100013.53+013739.0	x	o	x	o	20.4	1.60	-99	0.11 (0.75)	0.01 (0.40)	0.27 (0.90)	-99 (-99)	-99 (-99)	-99 (-99)	0.00 (0.69)	0.12 (0.95)
100013.70+013034.6	x	o	x	x	20.0	0.31	-99	0.07 (0.64)	0.24 (0.91)	-99 (-99)	-99 (-99)	0.03 (0.76)	0.59 (1.53)	0.08 (1.04)	-99 (-99)
100014.09+022838.7	o	o	x	x	20.5	1.25	0.69	0.32 (1.04)	0.27 (1.03)	0.20 (0.97)	0.23 (0.89)	0.50 (1.25)	-99 (-99)	0.20 (1.24)	0.16 (1.06)
100014.14+020054.6	o	o	x	o	19.7	2.49	-99	0.78 (1.62)	0.12 (0.83)	0.02 (0.59)	0.01 (0.47)	0.38 (1.40)	0.77 (1.64)	0.00 (0.78)	0.43 (1.16)
100014.91+022718.0	o	x	x	x	21.0	0.73	-99	0.25 (1.08)	0.20 (0.85)	0.70 (1.43)	-99 (-99)	-99 (-99)	-99 (-99)	0.04 (1.04)	0.21 (1.02)
100016.11+025511.6	x	o	x	x	21.0	-99	-1	-99 (-99)	0.35 (0.99)	0.41 (1.26)	-99 (-99)	-99 (-99)	-99 (-99)	-99 (-99)	0.86 (1.46)
100016.29+015104.8	o	o	x	x	21.2	1.13	0.65	-99 (-99)	0.94 (1.76)	0.23 (1.14)	0.00 (0.30)	-99 (-99)	-99 (-99)	0.07 (1.10)	-99 (-99)
100016.83+015133.1	x	x	o	x	19.9	0.33	1.45	-99 (-99)	0.31 (0.96)	-99 (-99)	-99 (-99)	-99 (-99)	-99 (-99)	-99 (-99)	0.18 (1.08)
100017.53+020012.7	o	x	x	x	20.7	0.35	-99	0.24 (0.93)	0.24 (0.96)	0.62 (1.36)	1.00 (5.50)	-99 (-99)	-99 (-99)	-99 (-99)	-99 (-99)
100017.73+030525.0	x	x	x	o	20.7	2.17	-1	0.95 (2.01)	0.41 (1.10)	0.96 (1.83)	0.37 (0.86)	0.31 (1.28)	-99 (-99)	-99 (-99)	-99 (-99)

Name	X	M	R	S	R mag	z	$R_i$	1-p (C value)							
								2015.02.18				2015.03.21		2016.04.08	
								B	V	R	I	B	R	B	R
100021.78+020000.2	x	x	o	x	17.8	0.21	0.65	1.00 (7.85)	1.00 (13.8)	-99 (-99)	-99 (-99)	-99 (-99)	-99 (-99)	-99 (-99)	-99 (-99)
100040.09+024608.2	x	o	x	x	21.7	1.93	-99	-99 (-99)	-99 (-99)	-99 (-99)	-99 (-99)	-99 (-99)	-99 (-99)	0.05 (0.93)	-99 (-99)
100040.13+024751.5	x	o	x	x	21.6	0.57	-99	-99 (-99)	0.03 (0.54)	0.14 (0.86)	-99 (-99)	-99 (-99)	-99 (-99)	-99 (-99)	-99 (-99)
100041.16+020502.7	x	x	o	x	21.8	0.73	1.39	-99 (-99)	-99 (-99)	-99 (-99)	0.99 (2.21)	-99 (-99)	-99 (-99)	-99 (-99)	-99 (-99)
100041.56+013659.0	x	x	o	x	19.8	0.56	0.63	0.22 (0.88)	0.74 (1.47)	0.67 (1.39)	0.98 (2.24)	-99 (-99)	0.91 (1.43)	0.09 (1.07)	0.05 (1.00)
100043.15+020637.4	o	x	x	o	18.6	0.36	0.18	0.09 (0.71)	0.26 (0.97)	0.92 (1.94)	0.94 (2.13)	0.01 (0.75)	0.92 (1.97)	0.25 (1.26)	0.54 (1.38)
100043.64+014009.3	o	o	x	x	20.1	2.02	-99	-99 (-99)	-99 (-99)	-99 (-99)	-99 (-99)	0.04 (0.81)	-99 (-99)	0.02 (0.89)	-99 (-99)
100045.41+014712.7	x	x	o	x	21.4	0.81	1.79	-99 (-99)	-99 (-99)	0.25 (1.04)	-99 (-99)	-99 (-99)	-99 (-99)	-99 (-99)	-99 (-99)
100046.73+020404.5	o	x	x	x	19.8	0.55	-99	0.81 (1.46)	0.10 (0.67)	0.93 (2.14)	0.07 (0.68)	0.28 (1.10)	0.33 (0.95)	-99 (-99)	0.08 (0.84)
100046.89+025640.1	x	o	x	x	19.3	-99	-1	-99 (-99)	0.54 (1.23)	-99 (-99)	0.40 (1.20)	-99 (-99)	0.87 (0.91)	0.26 (1.26)	0.09 (0.94)
100046.94+020016.0	o	o	x	x	20.1	1.92	0.70	0.31 (1.03)	0.06 (0.64)	0.78 (1.61)	0.19 (0.88)	0.41 (1.39)	0.22 (0.56)	0.01 (0.84)	0.15 (1.00)
100048.82+015409.6	x	o	o	x	21.3	0.70	1.13	-99 (-99)	-99 (-99)	-99 (-99)	0.05 (0.65)	-99 (-99)	-99 (-99)	-99 (-99)	-99 (-99)
100049.59+014923.7	x	x	o	x	20.2	0.52	2.41	-99 (-99)	0.39 (0.93)	-99 (-99)	-99 (-99)	-99 (-99)	-99 (-99)	-99 (-99)	-99 (-99)
100049.91+020500.0	o	o	o	x	19.3	1.23	0.78	0.09 (0.71)	0.71 (1.43)	0.44 (1.07)	0.45 (1.28)	0.06 (1.02)	0.07 (0.86)	0.29 (1.23)	0.23 (1.05)
100049.97+015231.3	o	x	x	x	20.4	1.15	-99	0.84 (1.64)	0.02 (0.48)	0.71 (1.16)	-99 (-99)	0.05 (0.93)	-99 (-99)	0.01 (0.80)	0.13 (0.98)
100050.12+022855.0	o	o	x	x	19.7	3.33	-99	0.00 (0.33)	0.59 (1.35)	0.50 (1.29)	0.11 (0.82)	0.03 (0.64)	0.74 (1.32)	0.00 (0.81)	0.14 (1.01)
100050.16+022618.5	o	o	x	x	21.4	3.71	-99	-99 (-99)	-99 (-99)	0.98 (2.01)	-99 (-99)	-99 (-99)	-99 (-99)	-99 (-99)	-99 (-99)
100050.43+021842.0	x	x	o	x	21.3	0.71	1.09	-99 (-99)	-99 (-99)	0.10 (0.71)	0.00 (0.38)	-99 (-99)	-99 (-99)	-99 (-99)	0.14 (1.00)
100051.92+015919.5	o	o	x	x	21.6	2.24	-99	0.11 (0.70)	0.18 (0.83)	0.30 (1.05)	-99 (-99)	-99 (-99)	-99 (-99)	0.18 (1.25)	-99 (-99)
100054.50+021605.1	o	x	x	x	19.4	-99	-99	-99 (-99)	-99 (-99)	0.32 (1.07)	0.12 (0.85)	-99 (-99)	-99 (-99)	-99 (-99)	-99 (-99)
100054.79+014602.5	x	o	x	x	20.5	0.37	0.68	-99 (-99)	0.47 (1.32)	0.03 (0.61)	0.00 (0.38)	-99 (-99)	-99 (-99)	-99 (-99)	0.57 (1.38)
100055.39+023441.4	o	o	x	o	19.6	1.40	0.24	-99 (-99)	-99 (-99)	-99 (-99)	0.04 (0.63)	0.05 (1.06)	0.05 (0.87)	0.02 (0.92)	0.10 (0.92)
100055.63+022150.4	o	o	x	x	21.0	1.93	-99	0.88 (1.68)	0.50 (1.20)	0.14 (0.81)	-99 (-99)	0.12 (0.96)	-99 (-99)	0.03 (0.91)	0.25 (1.03)
100055.65+013740.8	o	x	x	x	20.5	0.38	-99	-99 (-99)	0.17 (0.75)	0.79 (1.71)	0.54 (1.33)	-99 (-99)	-99 (-99)	-99 (-99)	0.92 (1.75)
100056.54+011319.1	x	x	x	o	18.2	0.51	-1	0.18 (0.93)	0.32 (1.05)	0.23 (0.93)	0.98 (2.30)	0.88 (1.99)	0.01 (0.64)	0.85 (2.04)	0.56 (1.46)

Name	X	M	R	S	R mag	z	$R_i$	1-p (C value)							
								2015.02.18				2015.03.21		2016.04.08	
								B	V	R	I	B	R	B	R
100056.70+021720.8	o	o	x	x	21.5	2.07	0.77	0.77 (1.56)	0.91 (2.09)	-99 (-99)	-99 (-99)	-99 (-99)	-99 (-99)	0.68 (1.47)	-99 (-99)
100057.26+013142.7	x	x	o	x	19.1	0.39	0.54	0.38 (1.15)	0.88 (1.63)	0.93 (1.86)	0.39 (1.17)	-99 (-99)	-99 (-99)	0.59 (1.52)	0.01 (0.72)
100058.20+014559.0	o	o	x	x	21.3	0.62	0.76	-99 (-99)	-99 (-99)	-99 (-99)	0.02 (0.57)	-99 (-99)	-99 (-99)	-99 (-99)	0.00 (0.48)
100058.34+015208.8	o	o	x	x	20.7	2.02	-99	0.24 (1.03)	0.17 (0.90)	0.22 (0.94)	0.44 (1.14)	-99 (-99)	-99 (-99)	0.50 (1.58)	0.25 (1.08)
100058.71+022556.2	o	o	x	x	20.8	0.69	-99	0.79 (1.32)	-99 (-99)	0.84 (1.85)	0.55 (1.39)	-99 (-99)	-99 (-99)	0.49 (1.35)	0.92 (1.66)
100058.84+015400.3	o	o	x	o	19.9	1.55	-99	0.36 (1.03)	0.05 (0.61)	0.84 (1.82)	0.61 (1.48)	0.93 (2.26)	0.92 (1.57)	0.06 (1.04)	0.08 (0.96)
100100.21+015150.4	x	x	o	x	20.0	0.30	1.05	-99 (-99)	0.03 (0.58)	0.51 (1.14)	0.68 (1.51)	-99 (-99)	-99 (-99)	-99 (-99)	0.39 (1.15)
100100.31+024413.9	x	o	x	x	21.1	1.20	-99	0.43 (1.24)	-99 (-99)	-99 (-99)	-99 (-99)	-99 (-99)	-99 (-99)	0.08 (0.98)	0.91 (2.19)
100100.63+022910.8	x	o	x	x	20.7	1.54	-99	-99 (-99)	-99 (-99)	-99 (-99)	-99 (-99)	-99 (-99)	-99 (-99)	0.00 (0.57)	-99 (-99)
100100.82+015947.9	o	x	x	x	21.3	1.16	-99	-99 (-99)	-99 (-99)	-99 (-99)	-99 (-99)	-99 (-99)	-99 (-99)	0.94 (2.02)	0.09 (0.88)
100102.16+011948.5	x	x	x	o	19.5	2.15	-1	0.65 (1.44)	0.42 (1.12)	0.07 (0.74)	0.33 (1.04)	0.20 (1.41)	0.96 (1.65)	0.09 (1.04)	0.29 (1.13)
100102.81+020659.9	o	o	x	x	21.1	1.37	1.04	1.00 (4.83)	-99 (-99)	-99 (-99)	-99 (-99)	-99 (-99)	-99 (-99)	0.00 (0.86)	0.20 (1.13)
100103.74+015533.5	x	x	o	x	18.1	0.30	0.18	0.07 (0.68)	0.61 (1.32)	0.27 (0.99)	0.17 (0.98)	0.11 (1.18)	0.25 (1.28)	0.49 (1.56)	0.40 (1.34)
100104.86+011421.3	x	x	x	o	20.3	1.02	-1	0.11 (0.75)	0.51 (1.27)	0.38 (1.08)	0.35 (1.02)	0.51 (1.46)	-99 (-99)	0.09 (1.01)	0.30 (1.04)
100106.38+030309.8	x	x	x	o	19.0	0.60	-1	-99 (-99)	0.92 (1.71)	-99 (-99)	0.67 (1.57)	0.60 (1.15)	0.07 (0.53)	0.48 (1.53)	0.61 (1.44)
100106.92+015734.4	x	o	x	x	20.7	0.08	-99	0.09 (0.70)	0.62 (1.27)	-99 (-99)	0.69 (1.53)	-99 (-99)	-99 (-99)	-99 (-99)	-99 (-99)
100107.67+012439.2	x	x	x	o	19.6	1.63	-1	0.73 (1.52)	0.31 (1.01)	-99 (-99)	-99 (-99)	-99 (-99)	0.85 (1.60)	0.75 (1.73)	0.68 (1.40)
100108.36+022342.2	o	x	x	x	21.4	1.93	-99	0.62 (1.38)	0.22 (0.92)	-99 (-99)	-99 (-99)	-99 (-99)	-99 (-99)	0.47 (1.49)	0.13 (0.91)
100108.55+020052.5	o	o	x	x	21.1	2.67	-99	0.27 (1.00)	0.57 (1.17)	0.39 (1.19)	-99 (-99)	-99 (-99)	-99 (-99)	0.28 (1.15)	0.38 (1.18)
100110.19+023242.4	o	o	x	x	21.3	2.64	-99	-99 (-99)	0.01 (0.39)	-99 (-99)	-99 (-99)	-99 (-99)	-99 (-99)	-99 (-99)	-99 (-99)
100111.93+023024.9	o	o	x	x	21.0	1.49	-99	0.03 (0.55)	-99 (-99)	0.17 (0.89)	-99 (-99)	-99 (-99)	-99 (-99)	0.03 (0.96)	0.05 (0.85)
100112.28+014123.9	x	x	o	x	20.3	0.52	1.61	-99 (-99)	0.78 (1.56)	-99 (-99)	-99 (-99)	-99 (-99)	-99 (-99)	-99 (-99)	-99 (-99)
100113.58+020653.8	x	x	o	x	20.4	0.32	1.26	-99 (-99)	0.14 (0.75)	0.60 (1.34)	0.94 (2.32)	-99 (-99)	-99 (-99)	-99 (-99)	0.97 (1.71)
100113.84+014000.8	o	o	x	x	20.9	1.56	-99	0.09 (0.75)	0.13 (0.77)	0.14 (0.82)	-99 (-99)	-99 (-99)	-99 (-99)	0.23 (1.21)	0.04 (0.83)
100113.93+022548.3	o	x	x	x	20.4	0.37	-99	0.67 (1.66)	0.47 (1.21)	0.12 (0.68)	0.12 (0.86)	-99 (-99)	0.03 (0.58)	0.00 (0.72)	0.00 (0.71)

Name	X	M	R	S	R mag	z	$R_i$	1-p (C value)							
								2015.02.18				2015.03.21		2016.04.08	
								B	V	R	I	B	R	B	R
100114.14+015444.2	o	x	o	x	21.5	1.48	4.01	-99 (-99)	-99 (-99)	0.06 (0.60)	-99 (-99)	-99 (-99)	-99 (-99)	-99 (-99)	-99 (-99)
100114.29+022356.9	o	o	x	o	18.8	1.79	-99	0.54 (1.30)	0.84 (1.60)	0.01 (0.46)	0.41 (1.26)	0.25 (1.19)	0.08 (0.58)	0.64 (1.63)	0.24 (1.09)
100114.84+015840.6	o	o	x	x	21.5	2.34	-99	-99 (-99)	0.36 (1.04)	0.13 (0.78)	-99 (-99)	-99 (-99)	-99 (-99)	-99 (-99)	-99 (-99)
100114.96+014348.3	x	o	x	x	20.1	0.58	0.64	-99 (-99)	0.20 (0.82)	0.23 (0.86)	0.06 (0.67)	-99 (-99)	-99 (-99)	-99 (-99)	-99 (-99)
100115.38+024231.7	x	o	x	x	20.8	0.45	-99	-99 (-99)	-99 (-99)	0.04 (0.67)	0.92 (1.78)	-99 (-99)	-99 (-99)	-99 (-99)	0.00 (0.45)
100116.29+023607.6	o	x	x	x	20.9	0.95	-99	0.75 (1.45)	0.64 (1.24)	0.15 (0.87)	0.00 (0.21)	-99 (-99)	-99 (-99)	0.00 (0.65)	-99 (-99)
100116.79+014053.8	o	o	x	o	19.8	2.05	-99	0.91 (1.81)	0.52 (1.21)	0.25 (0.86)	0.52 (1.34)	0.85 (1.90)	0.33 (1.48)	0.41 (1.37)	0.13 (1.00)
100116.94+013804.2	o	o	x	x	20.8	0.74	-99	0.89 (1.76)	0.60 (1.28)	0.28 (1.02)	0.09 (0.80)	-99 (-99)	-99 (-99)	0.61 (1.49)	0.02 (0.77)
100118.10+013625.4	x	x	o	x	18.4	0.22	0.50	0.23 (0.99)	0.30 (1.02)	-99 (-99)	0.93 (2.09)	0.57 (1.07)	0.12 (0.92)	0.51 (1.48)	0.60 (1.50)
100118.58+022739.3	o	o	x	x	20.1	1.04	0.84	-99 (-99)	0.21 (0.85)	-99 (-99)	-99 (-99)	-99 (-99)	-99 (-99)	-99 (-99)	-99 (-99)
100120.25+020341.2	o	o	x	x	20.0	0.90	-99	0.70 (1.43)	0.00 (0.38)	0.75 (1.63)	0.06 (0.73)	0.68 (1.98)	0.24 (0.89)	-99 (-99)	-99 (-99)
100120.26+023341.4	o	o	x	o	19.9	1.83	-99	0.18 (0.92)	0.81 (1.60)	0.14 (0.78)	0.03 (0.64)	0.00 (0.56)	0.20 (0.99)	0.00 (0.67)	0.41 (1.34)
100122.46+020112.5	x	x	o	x	20.1	0.42	2.52	-99 (-99)	-99 (-99)	-99 (-99)	0.74 (1.62)	-99 (-99)	-99 (-99)	-99 (-99)	0.33 (1.09)
100124.10+024936.4	x	x	o	x	21.7	0.82	2.52	-99 (-99)	-99 (-99)	-99 (-99)	0.19 (0.96)	-99 (-99)	-99 (-99)	-99 (-99)	-99 (-99)
100124.74+015738.8	o	o	x	x	21.2	1.17	-99	-99 (-99)	0.33 (0.98)	0.05 (0.61)	-99 (-99)	-99 (-99)	-99 (-99)	0.31 (1.50)	0.06 (0.89)
100124.86+022031.9	o	x	x	x	20.5	1.70	-99	-99 (-99)	-99 (-99)	-99 (-99)	-99 (-99)	0.01 (0.67)	-99 (-99)	0.35 (1.37)	-99 (-99)
100125.30+012820.3	x	o	x	o	20.0	2.61	-1	0.30 (0.98)	0.70 (1.60)	0.68 (1.59)	0.38 (1.19)	0.63 (1.36)	0.00 (0.44)	0.00 (0.73)	0.13 (0.96)
100128.00+021819.4	o	x	x	x	21.3	1.18	-99	-99 (-99)	-99 (-99)	-99 (-99)	-99 (-99)	-99 (-99)	-99 (-99)	0.19 (1.21)	0.27 (0.97)
100129.19+011715.9	x	x	x	o	18.5	1.60	-1	0.02 (0.52)	0.68 (1.35)	0.58 (1.45)	0.03 (0.64)	0.23 (1.32)	0.23 (0.98)	0.97 (2.26)	0.05 (0.88)
100129.67+020643.3	o	o	x	x	20.5	1.91	-99	0.84 (1.66)	0.61 (1.41)	0.09 (0.62)	-99 (-99)	-99 (-99)	-99 (-99)	-99 (-99)	0.30 (1.08)
100130.38+014304.4	o	o	o	o	20.1	1.56	0.83	0.47 (1.21)	0.46 (1.17)	0.81 (1.71)	0.08 (0.73)	0.10 (0.85)	-99 (-99)	0.14 (1.14)	0.43 (1.35)
100131.67+024530.1	x	o	x	x	21.4	0.58	-99	0.01 (0.42)	-99 (-99)	0.94 (2.19)	-99 (-99)	-99 (-99)	-99 (-99)	0.71 (1.56)	0.00 (0.56)
100132.15+013420.8	x	o	x	o	19.4	1.35	-99	0.00 (0.41)	0.02 (0.54)	0.08 (0.69)	0.23 (0.99)	0.11 (1.02)	0.58 (1.24)	0.97 (2.16)	0.31 (1.15)
100132.82+015800.0	o	o	x	x	20.8	1.53	-99	0.00 (0.32)	0.12 (0.81)	0.41 (1.18)	0.38 (1.25)	-99 (-99)	-99 (-99)	0.00 (0.77)	0.12 (0.93)
100133.48+020017.4	x	o	x	x	20.8	0.10	0.56	-99 (-99)	-99 (-99)	0.00 (0.29)	0.98 (1.79)	-99 (-99)	-99 (-99)	-99 (-99)	0.16 (1.06)

Name	X	M	R	S	R mag	z	$R_i$	1-p (C value)							
								2015.02.18				2015.03.21		2016.04.08	
								B	V	R	I	B	R	B	R
100135.45+025405.9	x	o	x	x	20.6	0.99	-99	0.44 (1.14)	0.07 (0.70)	0.37 (1.29)	0.78 (1.43)	-99 (-99)	-99 (-99)	0.07 (1.03)	0.01 (0.76)
100136.24+015443.1	o	o	x	x	20.9	2.28	-99	-99 (-99)	0.02 (0.43)	0.19 (0.82)	0.15 (1.04)	-99 (-99)	-99 (-99)	0.67 (1.56)	0.54 (1.26)
100136.46+022641.9	x	x	o	x	16.8	0.12	0.32	0.22 (1.05)	0.45 (1.41)	-99 (-99)	0.80 (2.62)	0.75 (1.45)	0.21 (1.26)	-99 (-99)	-99 (-99)
100136.50+025303.6	x	x	x	o	19.2	2.11	-99	0.02 (0.49)	0.11 (0.76)	0.38 (0.99)	0.47 (1.32)	0.00 (0.46)	0.08 (0.62)	-99 (-99)	0.87 (1.85)
100137.21+021612.5	o	o	x	x	20.6	1.66	-99	-99 (-99)	0.66 (1.32)	0.92 (1.85)	0.95 (1.92)	-99 (-99)	-99 (-99)	-99 (-99)	-99 (-99)
100141.03+015903.9	x	x	o	x	18.5	0.32	0.70	0.09 (0.66)	0.93 (1.93)	0.36 (1.14)	0.56 (1.43)	-99 (-99)	0.78 (2.05)	-99 (-99)	-99 (-99)
100143.04+014932.1	o	o	x	x	21.9	2.08	-99	-99 (-99)	-99 (-99)	-99 (-99)	-99 (-99)	-99 (-99)	-99 (-99)	0.02 (0.81)	-99 (-99)
100143.23+020512.8	x	x	o	x	20.6	0.67	1.03	0.14 (0.74)	0.66 (1.35)	0.95 (2.11)	0.90 (1.73)	-99 (-99)	-99 (-99)	0.16 (1.05)	0.45 (1.35)
100145.16+022457.0	x	x	x	o	20.7	2.03	-99	-99 (-99)	-99 (-99)	-99 (-99)	-99 (-99)	0.16 (1.01)	-99 (-99)	-99 (-99)	-99 (-99)
100146.05+012839.7	x	o	x	x	21.4	-99	-1	-99 (-99)	-99 (-99)	-99 (-99)	-99 (-99)	-99 (-99)	-99 (-99)	-99 (-99)	0.04 (0.80)
100146.49+020256.8	o	o	x	x	20.2	0.66	-99	0.85 (1.82)	0.84 (1.51)	0.69 (1.44)	0.45 (1.36)	0.03 (0.67)	-99 (-99)	-99 (-99)	-99 (-99)
100147.04+020236.6	o	o	x	x	20.8	1.17	-99	0.34 (0.93)	0.61 (1.24)	0.30 (0.98)	0.93 (1.82)	-99 (-99)	-99 (-99)	-99 (-99)	0.08 (0.88)
100147.29+015258.3	x	x	o	x	20.6	0.67	1.36	-99 (-99)	-99 (-99)	0.11 (0.77)	-99 (-99)	-99 (-99)	-99 (-99)	-99 (-99)	-99 (-99)
100147.35+020314.3	x	x	o	x	18.0	0.32	1.18	-99 (-99)	-99 (-99)	0.80 (1.91)	0.32 (1.26)	-99 (-99)	0.59 (1.32)	-99 (-99)	0.97 (2.10)
100148.86+023140.5	o	o	x	x	21.2	1.93	-99	0.31 (0.98)	0.40 (1.07)	0.13 (0.76)	-99 (-99)	-99 (-99)	-99 (-99)	0.33 (1.29)	0.75 (1.42)
100149.00+024821.7	x	o	x	x	20.3	1.50	-99	-99 (-99)	-99 (-99)	-99 (-99)	-99 (-99)	0.52 (1.62)	0.18 (0.92)	0.36 (1.38)	0.44 (1.20)
100149.84+020344.9	o	o	x	x	21.2	2.37	-99	-99 (-99)	-99 (-99)	0.08 (0.57)	-99 (-99)	-99 (-99)	-99 (-99)	-99 (-99)	-99 (-99)
100150.67+022552.2	x	o	x	x	20.2	1.28	-99	0.41 (1.15)	0.19 (0.91)	0.37 (1.05)	0.12 (0.85)	0.11 (1.06)	-99 (-99)	-99 (-99)	-99 (-99)
100151.12+020032.6	o	o	x	x	20.3	0.96	-99	-99 (-99)	0.98 (2.27)	0.99 (2.88)	0.77 (1.64)	-99 (-99)	0.00 (0.54)	0.03 (0.90)	0.39 (1.19)
100153.29+022436.8	o	o	x	x	20.4	0.66	0.22	-99 (-99)	-99 (-99)	0.79 (1.63)	0.14 (0.89)	-99 (-99)	-99 (-99)	0.12 (1.11)	0.18 (1.01)
100153.71+015427.3	x	x	o	x	20.6	0.56	0.98	-99 (-99)	-99 (-99)	-99 (-99)	0.48 (1.16)	-99 (-99)	-99 (-99)	-99 (-99)	-99 (-99)
100154.40+024236.5	x	o	x	x	20.8	1.51	-99	-99 (-99)	0.28 (0.95)	-99 (-99)	-99 (-99)	-99 (-99)	-99 (-99)	-99 (-99)	-99 (-99)
100154.51+021507.8	x	x	o	x	20.4	0.78	0.90	-99 (-99)	-99 (-99)	1.00 (4.17)	-99 (-99)	-99 (-99)	-99 (-99)	-99 (-99)	-99 (-99)
100155.52+020358.6	x	x	o	x	20.5	0.30	1.15	-99 (-99)	-99 (-99)	0.83 (1.58)	0.74 (1.69)	-99 (-99)	-99 (-99)	-99 (-99)	0.33 (1.23)
100155.60+021623.4	o	o	x	x	20.7	1.43	-99	0.38 (0.97)	0.09 (0.75)	0.05 (0.67)	-99 (-99)	-99 (-99)	-99 (-99)	-99 (-99)	-99 (-99)

Name	X	M	R	S	R mag	z	$R_i$	1-p (C value)							
								2015.02.18				2015.03.21		2016.04.08	
								B	V	R	I	B	R	B	R
100157.78+024631.7	x	o	x	x	20.3	0.84	-99	-99 (-99)	0.78 (1.50)	0.93 (1.72)	0.01 (0.42)	0.02 (0.57)	0.21 (0.90)	0.10 (1.11)	0.18 (0.99)
100158.00+014621.4	x	o	x	x	21.1	0.84	-99	-99 (-99)	-99 (-99)	0.34 (0.94)	0.14 (0.81)	-99 (-99)	-99 (-99)	-99 (-99)	0.07 (1.18)
100158.19+012735.6	x	o	x	x	19.1	-99	-1	0.33 (1.07)	0.67 (1.37)	0.72 (1.69)	0.35 (1.19)	0.48 (1.36)	0.01 (0.53)	0.15 (1.17)	0.23 (1.13)
100158.95+022445.3	o	x	x	x	21.4	1.37	0.67	-99 (-99)	-99 (-99)	-99 (-99)	-99 (-99)	-99 (-99)	-99 (-99)	0.73 (1.73)	0.19 (1.18)
100159.21+012828.6	x	o	x	x	20.4	-99	-1	0.45 (1.21)	0.00 (0.41)	-99 (-99)	0.22 (0.98)	-99 (-99)	-99 (-99)	-99 (-99)	0.83 (1.72)
100159.43+023935.7	x	o	x	x	19.9	1.37	-99	0.37 (1.13)	0.92 (1.79)	0.98 (2.33)	0.02 (0.52)	0.02 (0.80)	0.56 (1.50)	0.61 (1.57)	0.03 (0.82)
100159.79+022641.7	o	o	x	x	19.2	2.03	-99	-99 (-99)	0.24 (0.94)	0.53 (1.18)	0.05 (0.63)	0.53 (1.22)	-99 (-99)	-99 (-99)	-99 (-99)
100159.86+013135.3	x	o	x	x	21.4	0.30	-99	0.12 (0.76)	0.13 (0.76)	-99 (-99)	-99 (-99)	-99 (-99)	-99 (-99)	-99 (-99)	0.11 (1.00)
100201.52+020329.4	o	o	x	o	18.2	2.02	-99	0.73 (1.66)	0.97 (2.17)	-99 (-99)	-99 (-99)	0.80 (1.65)	0.58 (1.05)	0.21 (1.16)	-99 (-99)
100202.23+024157.8	x	o	x	x	21.2	1.53	-99	0.14 (0.78)	-99 (-99)	0.36 (0.99)	-99 (-99)	-99 (-99)	-99 (-99)	0.39 (1.38)	-99 (-99)
100202.78+022434.6	o	o	x	o	20.8	0.98	-99	-99 (-99)	-99 (-99)	0.69 (1.53)	-99 (-99)	0.24 (1.21)	-99 (-99)	0.00 (0.85)	0.54 (1.29)
100204.67+013339.6	x	o	x	x	20.3	1.01	-99	-99 (-99)	0.25 (0.86)	0.49 (1.40)	-99 (-99)	-99 (-99)	-99 (-99)	0.63 (1.56)	0.56 (1.33)
100208.27+015838.8	x	x	o	x	21.0	0.68	1.18	-99 (-99)	-99 (-99)	-99 (-99)	-99 (-99)	-99 (-99)	-99 (-99)	-99 (-99)	0.08 (0.88)
100208.55+014553.7	x	o	x	x	21.5	1.98	-99	-99 (-99)	-99 (-99)	-99 (-99)	-99 (-99)	-99 (-99)	-99 (-99)	0.03 (0.92)	0.01 (0.70)
100210.72+023026.2	x	o	x	o	19.0	1.16	-99	0.13 (0.90)	0.20 (0.84)	0.00 (0.42)	0.78 (1.70)	0.06 (0.65)	0.02 (0.70)	0.02 (0.88)	0.08 (0.87)
100211.16+012228.4	x	x	x	o	19.6	1.81	-1	0.64 (1.40)	0.06 (0.70)	0.87 (1.55)	0.71 (1.82)	0.29 (0.93)	0.07 (0.90)	0.01 (0.81)	0.27 (1.17)
100212.11+014232.4	x	o	x	x	20.1	0.70	0.37	0.92 (2.08)	0.84 (1.55)	0.03 (0.52)	0.11 (0.86)	0.29 (1.13)	0.05 (0.32)	0.04 (0.98)	0.03 (0.79)
100216.15+023013.0	x	o	x	x	21.2	0.37	0.88	-99 (-99)	-99 (-99)	0.38 (0.92)	0.56 (1.46)	-99 (-99)	-99 (-99)	-99 (-99)	0.02 (0.77)
100217.42+022959.8	x	o	x	x	20.6	0.30	-99	0.08 (0.68)	0.54 (1.27)	0.82 (1.71)	-99 (-99)	-99 (-99)	-99 (-99)	0.29 (1.40)	0.27 (1.12)
100217.97+015836.4	x	o	o	x	21.2	0.90	3.39	0.01 (0.42)	0.93 (1.61)	0.95 (1.83)	-99 (-99)	-99 (-99)	-99 (-99)	0.06 (0.94)	0.87 (1.53)
100218.31+022804.3	x	x	o	x	20.7	0.55	1.52	-99 (-99)	-99 (-99)	-99 (-99)	0.78 (1.81)	-99 (-99)	-99 (-99)	-99 (-99)	-99 (-99)
100219.43+025049.6	x	o	x	x	20.5	0.69	-99	0.04 (0.62)	0.20 (0.80)	0.32 (1.16)	0.72 (1.54)	-99 (-99)	-99 (-99)	0.15 (1.26)	0.06 (0.90)
100219.50+015537.1	x	o	x	o	19.6	1.51	-99	0.17 (0.82)	0.09 (0.71)	0.35 (1.05)	0.56 (1.26)	0.29 (1.38)	0.95 (1.47)	0.02 (0.84)	0.52 (1.61)
100221.95+022041.9	o	x	x	x	19.8	-99	-99	-99 (-99)	0.27 (1.02)	0.94 (1.92)	-99 (-99)	-99 (-99)	0.38 (1.18)	0.42 (1.25)	0.23 (1.03)
100222.98+020640.1	x	o	x	x	21.2	0.43	-99	-99 (-99)	-99 (-99)	0.53 (1.24)	-99 (-99)	-99 (-99)	-99 (-99)	-99 (-99)	0.38 (1.22)

Name	X	M	R	S	R mag	z	$R_i$	1-p (C value)							
								2015.02.18				2015.03.21		2016.04.08	
								B	V	R	I	B	R	B	R
100223.05+014715.0	x	o	x	x	21.1	1.25	-99	0.09 (0.66)	0.71 (1.41)	0.59 (1.62)	-99 (-99)	-99 (-99)	-99 (-99)	-99 (-99)	0.04 (0.82)
100223.93+022353.6	o	o	x	x	20.5	2.83	-99	-99 (-99)	0.02 (0.45)	0.05 (0.54)	0.65 (1.47)	-99 (-99)	-99 (-99)	0.22 (1.19)	0.05 (0.85)
100226.11+024610.9	x	o	x	x	19.9	0.29	-99	0.17 (0.83)	0.49 (1.19)	0.20 (0.84)	0.18 (0.98)	0.02 (0.65)	0.01 (0.75)	0.61 (1.56)	-99 (-99)
100226.33+021923.2	o	o	x	o	20.5	1.29	-99	0.33 (1.11)	0.00 (0.43)	0.94 (1.67)	0.13 (0.87)	-99 (-99)	-99 (-99)	0.26 (1.23)	0.24 (1.16)
100226.94+015939.9	x	o	x	x	21.7	1.46	-99	-99 (-99)	-99 (-99)	-99 (-99)	-99 (-99)	-99 (-99)	-99 (-99)	0.22 (1.32)	-99 (-99)
100228.92+013544.4	x	x	o	x	20.0	0.58	0.94	-99 (-99)	-99 (-99)	-99 (-99)	0.11 (0.81)	-99 (-99)	-99 (-99)	-99 (-99)	0.57 (1.30)
100229.02+010858.4	x	x	x	o	19.5	0.68	-1	0.28 (0.99)	-99 (-99)	-99 (-99)	-99 (-99)	0.82 (1.53)	0.88 (2.02)	0.18 (1.04)	-99 (-99)
100229.89+023225.2	x	o	o	x	19.4	0.44	1.70	-99 (-99)	0.40 (1.23)	0.01 (0.44)	0.96 (2.25)	-99 (-99)	0.01 (0.61)	-99 (-99)	-99 (-99)
100230.14+024212.7	x	x	o	x	18.2	0.21	1.07	0.53 (1.23)	-99 (-99)	-99 (-99)	0.99 (3.37)	0.47 (1.06)	0.73 (1.47)	0.02 (0.89)	-99 (-99)
100230.17+014555.7	x	o	x	x	21.2	0.77	-99	-99 (-99)	-99 (-99)	0.20 (0.72)	-99 (-99)	-99 (-99)	-99 (-99)	0.05 (1.02)	0.74 (1.27)
100230.64+024427.7	x	o	x	x	20.0	0.36	0.56	0.49 (1.10)	0.08 (0.71)	0.30 (1.03)	0.48 (1.27)	0.00 (0.56)	0.65 (1.21)	0.20 (1.14)	0.91 (1.65)
100231.85+015242.5	x	o	x	x	21.2	-99	0.69	-99 (-99)	-99 (-99)	-99 (-99)	-99 (-99)	-99 (-99)	-99 (-99)	-99 (-99)	0.96 (1.70)
100232.13+023537.4	x	o	x	o	19.1	0.65	0.13	0.40 (1.17)	0.64 (1.28)	0.39 (1.11)	0.13 (0.86)	0.37 (1.48)	0.16 (0.76)	0.67 (1.66)	0.27 (1.11)
100232.48+023859.7	x	o	x	x	20.9	0.56	-99	0.69 (1.39)	0.20 (0.84)	0.02 (0.42)	-99 (-99)	-99 (-99)	-99 (-99)	-99 (-99)	-99 (-99)
100236.70+015948.8	x	o	x	o	19.6	1.51	-99	0.08 (0.78)	0.54 (1.22)	0.21 (0.94)	0.62 (1.34)	0.20 (0.97)	0.58 (0.96)	0.84 (1.92)	0.63 (1.32)
100238.25+013746.8	x	o	x	o	19.2	2.50	-99	0.24 (0.98)	0.35 (1.06)	-99 (-99)	-99 (-99)	0.80 (1.85)	-99 (-99)	0.88 (2.00)	0.09 (0.88)
100238.61+015831.2	x	o	x	x	21.2	1.85	-99	0.46 (1.16)	0.28 (1.00)	-99 (-99)	-99 (-99)	-99 (-99)	-99 (-99)	-99 (-99)	-99 (-99)
100238.70+013936.6	x	o	x	x	20.7	0.57	-99	-99 (-99)	-99 (-99)	-99 (-99)	-99 (-99)	-99 (-99)	-99 (-99)	0.27 (1.22)	0.04 (0.80)
100241.34+014256.6	x	x	o	x	20.6	0.63	1.22	-99 (-99)	-99 (-99)	0.26 (0.93)	0.14 (0.90)	-99 (-99)	-99 (-99)	-99 (-99)	0.15 (0.98)
100241.43+013309.2	x	o	x	x	21.4	0.21	-99	0.62 (1.43)	-99 (-99)	0.23 (0.98)	-99 (-99)	-99 (-99)	-99 (-99)	-99 (-99)	-99 (-99)
100243.70+024707.9	x	o	x	x	19.7	0.01	-99	-99 (-99)	0.16 (0.82)	-99 (-99)	-99 (-99)	-99 (-99)	-99 (-99)	0.18 (1.17)	0.25 (1.20)
100243.85+020502.6	x	o	x	x	20.9	0.57	-99	0.00 (0.31)	0.20 (0.90)	0.43 (1.25)	-99 (-99)	-99 (-99)	-99 (-99)	0.00 (0.69)	0.47 (1.22)
100244.74+020735.0	x	x	o	x	20.2	0.67	1.39	-99 (-99)	-99 (-99)	-99 (-99)	-99 (-99)	-99 (-99)	-99 (-99)	0.77 (1.49)	0.27 (1.19)
100246.34+024609.7	x	o	x	x	19.4	0.23	-99	0.22 (0.93)	-99 (-99)	0.35 (1.26)	0.00 (0.48)	0.52 (1.04)	0.18 (1.09)	0.00 (0.81)	0.00 (0.67)
100246.93+015301.2	x	x	o	x	19.5	0.52	0.54	-99 (-99)	0.26 (0.90)	-99 (-99)	-99 (-99)	-99 (-99)	-99 (-99)	0.32 (1.37)	0.59 (1.51)

Name	X	M	R	S	R mag	z	$R_i$	1-p (C value)							
								2015.02.18				2015.03.21		2016.04.08	
								B	V	R	I	B	R	B	R
100247.00+024538.7	x	x	o	x	20.8	0.47	1.10	-99 (-99)	-99 (-99)	0.48 (1.26)	0.89 (1.88)	-99 (-99)	-99 (-99)	-99 (-99)	-99 (-99)
100249.00+021750.7	x	o	x	x	21.5	2.50	-99	-99 (-99)	0.92 (1.46)	-99 (-99)	-99 (-99)	-99 (-99)	-99 (-99)	-99 (-99)	0.21 (1.08)
100249.32+023746.6	x	o	x	x	19.9	0.01	2.24	0.50 (1.21)	-99 (-99)	-99 (-99)	-99 (-99)	0.04 (0.77)	0.37 (1.36)	0.06 (1.00)	-99 (-99)
100249.92+021732.4	x	o	x	x	21.0	1.60	-99	0.24 (0.87)	0.89 (1.72)	0.65 (1.12)	-99 (-99)	-99 (-99)	-99 (-99)	-99 (-99)	0.61 (1.34)
100251.62+022905.4	x	o	x	o	19.3	2.00	-99	0.40 (1.18)	0.71 (1.45)	0.28 (0.93)	0.10 (0.79)	0.40 (1.41)	0.67 (1.29)	0.26 (1.27)	0.64 (1.55)
100252.34+013319.7	x	o	x	x	21.2	1.27	-99	-99 (-99)	0.99 (2.27)	0.41 (0.98)	-99 (-99)	-99 (-99)	-99 (-99)	-99 (-99)	0.60 (1.43)
100252.87+025426.9	x	o	x	x	19.9	0.01	-99	0.81 (1.78)	0.45 (1.06)	0.09 (0.76)	0.87 (1.72)	0.23 (1.04)	0.07 (0.96)	0.15 (1.17)	0.34 (1.24)
100252.96+024137.0	x	o	x	x	19.9	0.02	-99	-99 (-99)	0.87 (1.66)	0.49 (1.14)	0.72 (1.50)	0.39 (1.26)	0.96 (1.43)	0.31 (1.27)	-99 (-99)
100255.80+020242.0	x	o	x	x	21.2	1.26	-99	0.57 (1.31)	-99 (-99)	0.59 (1.22)	-99 (-99)	-99 (-99)	-99 (-99)	0.63 (1.42)	0.01 (0.72)
100255.89+013730.5	x	o	x	x	20.3	1.91	-99	0.84 (1.58)	0.18 (0.89)	0.79 (1.36)	0.65 (1.38)	0.45 (1.18)	0.15 (1.15)	0.03 (0.94)	0.68 (1.40)
100258.96+022724.9	x	o	x	x	21.1	1.09	-99	-99 (-99)	0.45 (1.04)	-99 (-99)	-99 (-99)	-99 (-99)	-99 (-99)	-99 (-99)	-99 (-99)
100259.94+020249.5	x	x	o	x	20.0	0.60	0.74	0.66 (1.51)	0.00 (0.36)	0.99 (2.79)	0.79 (1.66)	-99 (-99)	0.26 (0.83)	0.05 (0.94)	0.00 (0.61)
100302.93+015208.6	x	o	x	o	20.1	1.79	-99	0.08 (0.75)	0.18 (0.87)	0.43 (1.21)	0.30 (1.13)	0.05 (0.76)	0.96 (1.38)	0.03 (0.86)	0.00 (0.44)
100303.48+022632.0	x	o	x	x	21.2	0.69	-99	-99 (-99)	-99 (-99)	0.81 (1.61)	-99 (-99)	-99 (-99)	-99 (-99)	-99 (-99)	-99 (-99)
100304.18+024420.5	x	o	x	x	20.2	1.86	-99	0.89 (1.80)	0.35 (0.95)	-99 (-99)	-99 (-99)	0.64 (1.04)	0.41 (1.26)	0.88 (2.08)	0.12 (0.99)
100304.72+013351.6	x	x	o	x	21.4	0.94	1.13	-99 (-99)	-99 (-99)	0.46 (0.95)	-99 (-99)	-99 (-99)	-99 (-99)	-99 (-99)	-99 (-99)
100305.08+015156.4	x	o	x	x	20.5	0.14	-99	0.10 (0.76)	0.57 (1.25)	0.16 (0.81)	0.78 (1.61)	-99 (-99)	-99 (-99)	0.06 (1.06)	0.58 (1.31)
100305.98+015704.1	x	x	o	x	19.7	0.38	0.73	0.27 (0.98)	0.02 (0.51)	0.08 (0.67)	0.87 (1.85)	-99 (-99)	0.21 (1.30)	0.81 (1.68)	0.74 (1.74)
100307.48+023655.9	x	x	o	x	19.4	0.31	1.90	0.58 (1.35)	0.61 (1.34)	0.43 (1.36)	0.07 (0.75)	-99 (-99)	0.89 (1.91)	0.09 (1.08)	0.09 (0.94)
100308.22+024837.7	x	o	x	x	20.1	1.25	-99	0.31 (0.95)	0.54 (1.32)	0.15 (0.74)	-99 (-99)	0.96 (1.80)	0.91 (1.34)	-99 (-99)	0.74 (1.35)
100308.58+024323.0	x	o	x	x	20.6	0.01	-99	0.91 (1.78)	0.47 (1.12)	0.90 (1.52)	-99 (-99)	0.65 (1.28)	-99 (-99)	0.02 (0.92)	0.52 (1.30)
100308.79+012316.5	x	x	x	o	20.3	2.32	-1	0.92 (1.86)	0.89 (1.94)	0.98 (2.38)	0.49 (1.27)	-99 (-99)	-99 (-99)	0.87 (2.03)	0.29 (1.15)
100309.21+013507.5	x	x	o	x	20.3	0.37	1.80	-99 (-99)	0.38 (1.04)	0.82 (1.79)	0.44 (1.31)	-99 (-99)	-99 (-99)	-99 (-99)	0.93 (1.68)
100309.21+022038.3	x	x	x	o	19.9	1.96	-99	0.95 (1.81)	0.83 (1.74)	0.51 (1.16)	-99 (-99)	0.18 (1.23)	0.71 (1.22)	0.17 (1.19)	0.78 (1.50)
100309.55+025248.7	x	o	x	x	21.4	0.39	-99	-99 (-99)	0.38 (1.05)	0.82 (1.48)	-99 (-99)	-99 (-99)	-99 (-99)	-99 (-99)	0.34 (1.05)

Name	X	M	R	S	R mag	z	$R_i$	1-p (C value)							
								2015.02.18				2015.03.21		2016.04.08	
								B	V	R	I	B	R	B	R
100309.75+020838.9	x	x	o	x	19.9	0.39	0.77	-99 (-99)	-99 (-99)	-99 (-99)	-99 (-99)	-99 (-99)	-99 (-99)	-99 (-99)	1.00 (7.40)
100315.02+013354.8	x	o	x	x	21.6	0.68	-99	-99 (-99)	-99 (-99)	0.90 (1.41)	-99 (-99)	-99 (-99)	-99 (-99)	-99 (-99)	-99 (-99)
100316.12+024002.7	x	x	o	x	20.5	0.48	1.06	-99 (-99)	0.17 (0.85)	0.21 (0.92)	0.90 (1.96)	-99 (-99)	-99 (-99)	-99 (-99)	0.64 (1.49)
100316.27+024237.4	x	o	x	x	18.5	0.56	-99	0.19 (0.90)	0.84 (1.79)	0.56 (1.25)	0.39 (1.22)	0.86 (1.73)	0.89 (1.53)	0.13 (1.13)	0.47 (1.34)
100316.36+014223.7	x	o	x	x	21.5	1.72	-99	0.26 (0.99)	0.20 (0.89)	0.04 (0.66)	-99 (-99)	-99 (-99)	-99 (-99)	0.16 (1.16)	-99 (-99)
100317.38+013602.9	x	x	o	x	20.2	0.67	0.72	0.43 (1.30)	0.26 (0.96)	0.14 (0.77)	0.29 (1.07)	-99 (-99)	0.46 (1.16)	0.58 (1.49)	0.08 (0.88)
100317.94+022355.6	x	o	x	x	20.2	0.01	-99	0.88 (1.81)	0.10 (0.76)	0.87 (1.56)	0.93 (2.15)	0.14 (0.97)	0.99 (1.33)	0.29 (1.30)	0.52 (1.37)
100319.81+012719.1	x	o	x	x	21.8	-99	-1	-99 (-99)	0.20 (0.83)	-99 (-99)	-99 (-99)	-99 (-99)	-99 (-99)	-99 (-99)	-99 (-99)
100320.06+022042.9	x	o	x	x	21.7	-99	-99	0.00 (0.35)	-99 (-99)	-99 (-99)	-99 (-99)	-99 (-99)	-99 (-99)	-99 (-99)	-99 (-99)
100323.93+015503.8	x	o	x	x	19.4	-99	-99	0.68 (1.39)	0.83 (1.67)	0.56 (1.42)	0.12 (0.88)	0.23 (0.87)	0.64 (1.72)	0.21 (1.26)	0.73 (1.48)
100324.57+021831.3	x	x	x	o	18.2	0.51	-99	0.68 (1.74)	0.56 (1.32)	0.42 (1.16)	0.16 (0.95)	0.18 (0.88)	0.96 (1.67)	0.91 (2.30)	0.15 (1.16)
100327.68+015742.4	x	x	x	o	18.2	1.06	-99	0.70 (1.59)	0.31 (1.08)	0.40 (1.10)	0.81 (1.79)	0.66 (1.48)	0.39 (1.16)	0.68 (1.84)	0.44 (1.34)
100328.50+022018.7	x	o	x	x	21.3	-99	-99	-99 (-99)	-99 (-99)	0.01 (0.49)	0.32 (1.06)	-99 (-99)	-99 (-99)	-99 (-99)	-99 (-99)
100333.05+023904.4	x	x	x	o	20.4	0.66	-1	-99 (-99)	0.34 (1.03)	0.22 (0.92)	0.67 (1.43)	0.24 (1.08)	-99 (-99)	0.25 (1.28)	0.40 (1.13)
100333.57+024530.5	x	x	x	o	18.6	1.92	-1	0.91 (2.01)	0.14 (0.79)	0.51 (1.30)	0.71 (1.61)	0.24 (0.89)	0.41 (1.10)	0.77 (2.10)	0.69 (1.47)
100333.99+024126.3	x	x	x	o	19.3	0.98	-1	0.38 (1.12)	0.27 (0.96)	0.40 (1.18)	0.00 (0.45)	0.73 (1.80)	0.84 (1.86)	0.13 (1.13)	0.16 (1.01)
100350.28+013145.8	x	x	x	o	19.2	1.18	-1	0.55 (1.26)	0.05 (0.62)	0.01 (0.50)	0.15 (0.90)	0.99 (2.31)	-99 (-99)	0.11 (1.12)	0.21 (1.07)
100357.18+022638.9	x	x	x	o	18.7	1.48	-1	0.02 (0.56)	0.71 (1.38)	-99 (-99)	-99 (-99)	0.06 (0.90)	-99 (-99)	0.76 (1.81)	-99 (-99)
100358.73+014513.6	x	x	x	o	20.1	1.41	-1	0.17 (0.86)	0.02 (0.52)	0.44 (1.07)	0.16 (0.89)	0.26 (1.15)	-99 (-99)	0.63 (1.54)	0.00 (0.61)
100407.21+012039.0	x	x	x	o	20.6	1.84	-1	0.13 (0.82)	0.71 (1.37)	0.83 (1.39)	0.19 (0.96)	0.97 (1.96)	-99 (-99)	-99 (-99)	0.93 (1.68)
100409.29+024946.4	x	x	x	o	19.1	1.59	-1	-99 (-99)	-99 (-99)	-99 (-99)	-99 (-99)	-99 (-99)	0.32 (0.99)	0.00 (0.81)	0.50 (1.30)
100421.02+013647.4	x	x	x	o	18.5	1.03	-1	0.25 (1.04)	0.75 (1.49)	0.99 (2.72)	0.00 (0.39)	0.91 (2.05)	0.20 (1.05)	0.52 (1.55)	0.31 (1.19)
100423.49+030658.9	x	x	x	o	19.0	0.91	-1	0.05 (0.64)	0.08 (0.68)	0.02 (0.50)	0.19 (1.01)	0.57 (1.13)	0.49 (0.99)	0.33 (1.37)	0.31 (1.16)
100429.00+025209.2	x	x	x	o	18.5	0.87	-1	0.07 (0.69)	0.54 (1.29)	-99 (-99)	0.00 (0.48)	0.07 (0.58)	0.31 (1.24)	0.20 (1.17)	0.50 (1.40)
100434.37+025011.0	x	x	x	o	18.4	1.21	-1	-99 (-99)	1.00 (6.45)	1.00 (7.94)	-99 (-99)	1.00 (4.99)	-99 (-99)	1.00 (7.39)	1.00 (10.0)

## Chapter 3

# Medium-band Photometry

# Reverberation Mapping of

# Nearby Active Galactic Nuclei<sup>†</sup>

### 3.1 Introduction

Reverberation mapping (RM) is known to be an important way to investigate the structure and kinematics of the broad-line region (BLR) around the central supermassive black holes of the active galactic nuclei (AGNs; Blandford & McKee 1982; Peterson 1993). According to the AGN unification model (Antonucci 1993; Urry & Padovani 1995; Peterson 1997), the accretion disk around the central black hole is responsible for the thermal continuum emission in the ultraviolet and optical. On the other hand, the broad emission lines (BEL) arise from the recombination in clouds that are sufficiently far from the central engine (light days to years), and these clouds are called the BLR clouds. When the accretion disk activity varies due to a reason (e.g., increased amount of infalling gas), it takes time for the effect to reach BLR, and hence a time lag in the variation between the continuum and the BEL occurs. Then, the time lag can tell us

---

<sup>†</sup>This chapter is a revised version of the article published in *The Astrophysical Journal* in October 2019 (Kim et al. 2019b).

the distance between the central accretion disk to BLR. Once the BLR size is determined, the masses of the supermassive black holes can be measured from the size and the velocity width of the BEL. RM studies have enabled black hole mass ( $M_{\text{BH}}$ ) measurements for hundreds of AGNs. From such studies, the correlation between the BLR size and the continuum luminosity has been established, which then resulted in  $M_{\text{BH}}$  estimates for hundreds of thousands of AGNs (Kaspi et al. 2000, 2005, 2007; Peterson et al. 2004; Bentz et al. 2006, 2009, 2010, 2013; Denney et al. 2010; Kim et al. 2010, 2015; Grier et al. 2012, 2017; Du et al. 2014, 2015, 2016, 2018; Barth et al. 2015; Hu et al. 2015; Jun et al. 2015; Shen et al. 2016; Fausnaugh et al. 2017; Li et al. 2017; Lira et al. 2018).

The common way of performing RM is to do a long term spectroscopic monitoring. Through the spectroscopy, one measures the velocity width and the line intensity variation directly from the observed spectra that are taken over the course of months to years. Then, the time lag of the continuum and the line intensity can be directly inferred. However, spectroscopic RM requires an extensive amount of observing time of 1-3 m telescopes (Kaspi et al. 2000; Bentz et al. 2009; Shen et al. 2016), and therefore it is difficult to perform on a large number of AGNs ( $> 100$ ).

To overcome the shortcomings of the spectroscopic RM, purely photometric RM has successfully been performed adopting broad-bands only or a combination of broad-, medium-, and narrow-bands (Haas et al. 2011; Pozo Nuñez et al. 2012, 2013, 2015; Chelouche & Daniel 2012; Chelouche et al. 2012; Edri et al. 2012; Hernitschek et al. 2015; Jiang et al. 2016; Zu et al. 2016; Zhang et al. 2018). Such a technique opens up a possibility of performing the RM of more than thousands of AGNs at once, even using a moderately sized telescopes. In its simplest form, the photometric RM uses two bands or more. One covers the wavelength where a BEL is located, and another covers the wavelength where no strong emission line exists. For example, Haas et al. (2011); Pozo Nuñez et al. (2012, 2013, 2015) observed a few AGNs using sets of a broad-band and a narrow-band. The broad-band is for the continuum flux and the narrow-band traces the BEL. Their time lag measurements agree with results from spectroscopic RM. The

use of the narrow-band is advantageous for increasing signal-to-noise ratio (S/N) from an emission line, but a narrow-band can cover a very limited redshift range of the AGN emission lines.

On the other hand, RM with broad-band filters can cover an emission line over a wide range of redshifts. The broad-band based RM has been tried on a few AGNs initially (Chelouche & Daniel 2012; Chelouche et al. 2012; Edri et al. 2012; Zu et al. 2016), and more recently to a few hundred quasars in the Sloan Digital Sky Survey (SDSS) Stripe 82 field with  $\sim 60$  epochs over a  $\sim 10$  year period (Hernitschek et al. 2015). One problem of the broad-band RM approach is that broad-bands are often too broad to observe only the continuum without contamination by a BEL. Also, the emission lines are often too narrow in comparison to the width of the broad-band filter, and the contrast between the continuum and the line is difficult to measure. Zhang et al. (2018) show that the line flux to continuum flux ratio should be 6 % or larger for the broad-band RM to be effective. To overcome these problems, Jiang et al. (2016) used a combination of broad-band and medium-band with the band widths of 180-264 Å which are several times narrower than typical broad-band filter widths. They observed 13 AGNs at  $z = 0.2-0.4$ , and detected time lags in 6 AGNs. The results agree with the BLR size-luminosity relation.

The above examples show the usefulness of a broad-band or medium-band RM approach. However, purely medium-band based RM with multiple medium-bands can be even more powerful. Multiple medium-bands can cover multiple BELs over a wide range of redshifts (Kim et al. 2019a). The medium-bands can limit contamination from BELs while sampling a fair amount of continuum flux to trace the continuum variation accurately. The medium-band is matched reasonably well with FWHMs of typical BELs. For example, for an  $H\alpha$  with  $\text{FWHM} = 3000 \text{ km s}^{-1}$  at  $z = 0.3$ , the observed line width corresponds to 85 Å, comparable to a medium-band width within a factor of a few, which is helpful for increasing the line flux to continuum ratio. The use of a medium-band also opens a possibility of using small telescopes for AGN RM.

To verify the usefulness of the medium-band photometric RM through a comparison

with spectroscopic RM results, we used three medium-bands on a 0.43m telescope to monitor five nearby AGNs that have been studied previously with spectroscopic RM. In Section 3.2, we describe the target AGNs, the system used for the observation, and the observation campaign. Section 3.3 explains the analysis of the data and the light-curve analysis. We estimate the AGN variability based on the light curve in Section 3.4. In Section 3.5, we present the time lag measurements and how they compare with previous works. Finally, we end the chapter with discussion for future prospects and the conclusion of this study.

## 3.2 Sample and Observation

For the medium-band photometric RM, we used the Lee Sang Gak Telescope (LSGT; Im et al. 2015) and its imaging camera, SNUCAM-II (Choi & Im 2017). LSGT is a 0.43 m diameter telescope located at the Siding Spring Observatory (SSO). The SNUCAM-II camera has a suite of  $\sim 50.0$  nm width medium-bands covering the wavelength range of 400 to 1050 nm.

For our targets, we selected AGNs that have been studied using the  $H\alpha$  emission line for RM at low redshifts ( $z < 0.02$ ), since  $H\alpha$  is the strongest emission line and easy to monitor with the small telescope. Additionally, we imposed a requirement that the time lag is less than 2 weeks so that we can obtain results from several months of monitoring campaign. With the above criteria, we select five nearby AGNs, Mrk 1310, NGC 4593, NGC 4748, NGC 6814, and NGC 7469 from Peterson et al. (2004, 2014) and Bentz et al. (2010). Table 3.1 shows the basic properties of our target AGNs, along with the observation summary for each target.

We observed these targets using three medium-bands,  $m625$  (596.2-658.7 nm),  $m675$  (643.3-712.0 nm), and  $m725$  (693.6-754.8 nm). Figure 3.1 shows the filter transmission curves of these medium-band filters. As shown in the figure,  $m675$  covers the  $H\alpha$  emission line and the others cover the continuum. We took five frames of 5 minutes exposure time in each band at each epoch. We tried to observe the targets every night. One day cadence observation was possible for patches of extended periods, but because of the

Table 3.1. List of the monitored AGNs

Name	R.A.	Decl.	$V$ mag	Redshift	Epochs	Obs Start-End
Mrk 1310	12:01:14.3	-03:40:41.1	15.89 <sup>a</sup>	0.019	28	2017.05.02-07.24
NGC 4593	12:39:39.5	-05:20:39.2	13.15 <sup>a</sup>	0.008	29	2017.04.30-08.07
NGC 4748	12:52:12.5	-13:24:52.8	14.03 <sup>a</sup>	0.014	33	2017.05.15-08.15
NGC 6814	19:42:40.6	-10:19:25.5	14.21 <sup>a</sup>	0.005	53	2017.05.04-09.10
NGC 7469	23:03:15.7	+08:52:25.3	12.34 <sup>b</sup>	0.016	32	2017.05.11-09.02

<sup>a</sup>Véron-Cetty & Véron (2010)

<sup>b</sup>Gil de Paz et al. (2007)

weather condition and the Moon distance restriction, the average observational cadence was about 3 days. Typical seeing was  $2''$  to  $4''$  and poor weather condition made it worse to be  $\sim 5''$ .

The basic data reduction procedure (bias subtraction, dark subtraction, and flat-fielding) was performed with an automatic pipeline as soon as the data were taken. Astrometric solution was found using the Astrometry.net software (Lang et al. 2010), which returned astrometric solutions to a  $0''.34$  rms accuracy. Then, we used the SWarp software (Bertin et al. 2002) to combine the five images of 5 minutes exposure to make a single epoch image.

### 3.3 Medium-band Photometry and Light Curve

When comparing aperture photometry results at different epochs, difference in seeing conditions systematically biases the photometry result. Therefore, we convolved all the epoch images with a Gaussian kernel to make them to have a common seeing FWHM =  $3''.8$  to  $5''.3$  (object-dependent). To exact the flux of the central AGNs, SExtractor (Bertin & Arnouts 1996) was used with a  $12''$  diameter aperture which corresponds to 2-3 times of the seeing FWHM of the convolved images. Figure 3.2 shows the images of

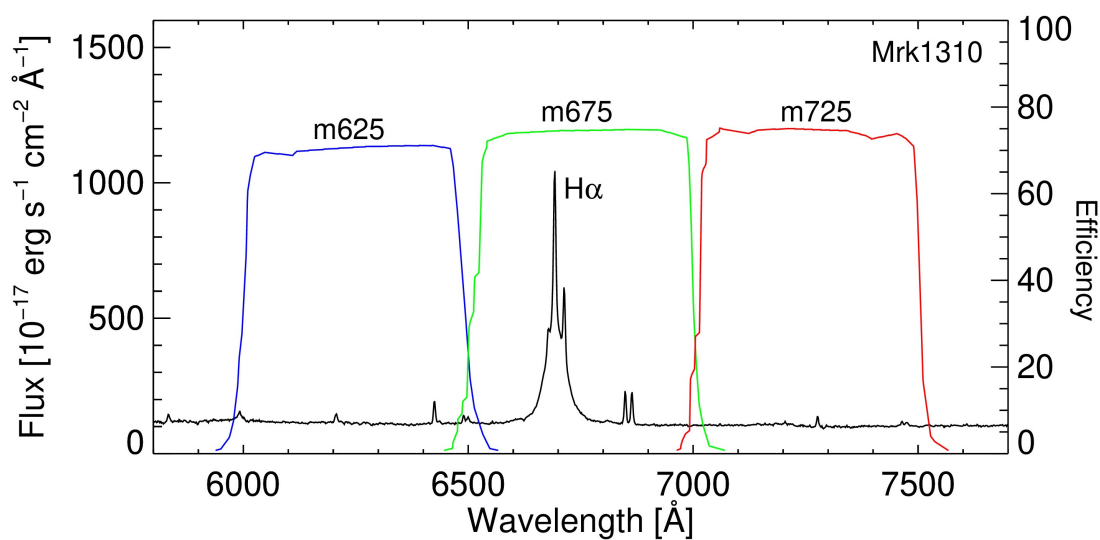


**Figure 3.1.** SDSS spectrum of Mrk 1310 and transmission curves of the medium-band filters used in this study. As shown here, *m675* covers the H $\alpha$  emission line and the others cover the continuum.



**Figure 3.2.** The images of the five AGNs in  $m675$ . The red circle indicates the  $12''$  aperture that we used to measure the AGN flux.

the five AGNs, and the size of the aperture, demonstrating that the aperture excludes most of the host galaxy light.

For the photometric calibration, we used magnitudes of stars in the AAVSO Photometric All-Sky Survey (APASS) catalog (Henden et al. 2016). However, the APASS catalog provides  $B$ ,  $V$ ,  $g$ ,  $r$ , and  $i$  magnitudes only. To obtain the photometry zero-point of each medium-band image, we first identified photometric reference stars from the APASS catalog as stars that are brighter than 15 mag in each broad-band and within  $10'$  away from the target AGN. Then, we searched for the stellar spectral energy distribution (SED) template among the stellar SED templates of Gunn & Stryker (1983) that best fits the five broad-band magnitudes of each photometry reference star. Only the SEDs that return the reduced  $\chi^2$  values less than 10 are adopted to derive the medium-band photometry zero-points. Then, applying the transmission curve of each medium-band, we calculated synthetic medium-band magnitudes of the selected stars, and used them for measuring magnitude zero-points (see also Choi & Im 2017 for more details on this procedure). Typically, 10-70 stars were used to derive the photometric zero-points in each band. The zero-point errors were derived from the rms dispersion of the zero-points from these stars, and a typical zero-point error is found to be 0.01 mag. To verify that the derived medium-band photometry traces the emission line feature in the spectrum well, we compared the photometric result with available spectra of our targets. Figure 3.3 shows the spectra of NGC 7469 (Kim et al. 1995) and Mrk 1310 (Abolfathi et al. 2018) along with the medium-band photometry data points. For the medium-band photometry in this case, we used a  $3''$  diameter aperture to be consis-

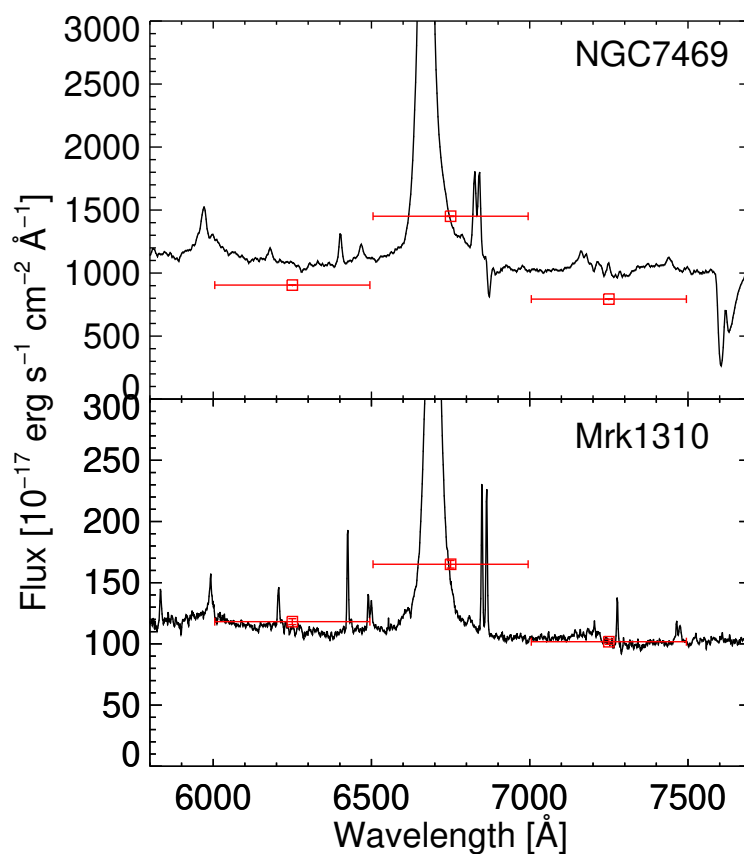


**Figure 3.3.** Comparison between the spectra and the medium-band photometry (squares with error bars) of NGC 7469 and Mrk 1310. The horizontal line of each point shows the width of the medium-band filter.

tent with the aperture size of the SDSS spectrum (for Mrk 1310) or be close to the spatial extraction window of the long-slit spectrum (for NGC 7469). As in the figure, the medium-band photometry traces well the spectral shape around  $H\alpha$  for both Mrk 1310 and NGC 7469. There is a small constant offset between the medium-band data and the spectrum for NGC 7469, but this can be attributed to the long term variability of the AGN or a mismatch in the aperture between the medium-band and the long-slit spectrum.

We employed differential photometry to construct the light curve (Kim et al. 2018). For this, bright stars ( $< 15$  mag in all the medium-bands) that are not near the edge of the image are selected as comparison stars. After differential photometry between the comparison stars, those with a relatively large magnitude variation ( $> 0.01$  mag) are removed from the list of the comparison stars. By subtracting the light curves of the AGNs from the light curves of the comparison stars, differential light curves of each AGN are obtained. For the continuum flux at  $m675$ , we simply take the average of the  $m625$  and  $m725$  fluxes. Then, the  $H\alpha$  flux is obtained by subtracting the continuum flux from the observed  $m675$  flux. The continuum and the emission line light curves are shown in Figures 3.4 and 3.5 for all the target AGNs and a comparison star. The flux scale of the light curve is set to be the flux at the first epoch of the observation. In Table 3.2, we provide light curves of five AGNs in machine-readable format.

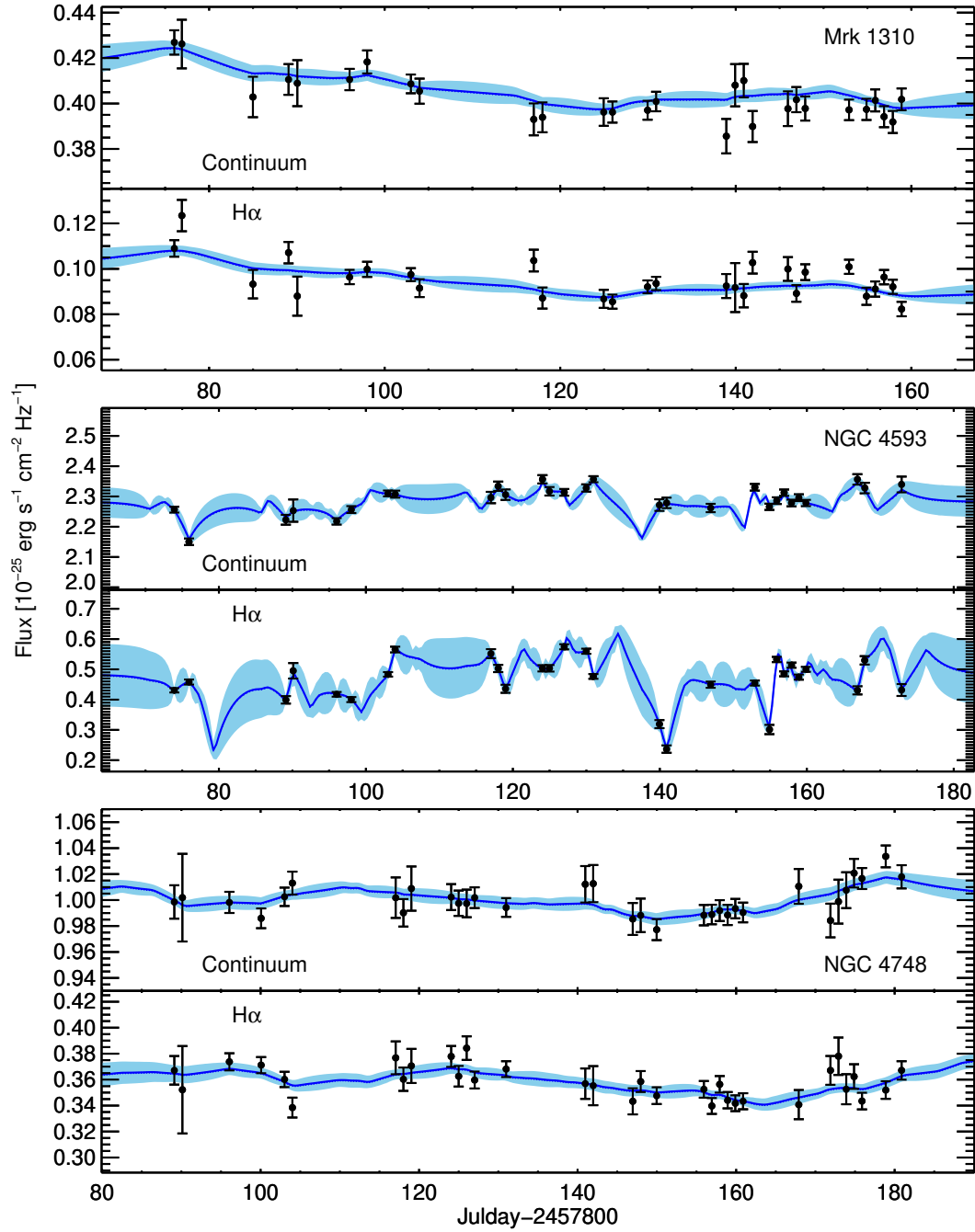


**Figure 3.4.** The continuum (upper panel) and the H $\alpha$  emission line (lower panel) light curves of five AGNs and of a sample comparison star (the black squares and the error bars). The blue solid lines are the best-fit light curves from JAVELIN, and the filled regions are the uncertainties of the best-fit light curves.

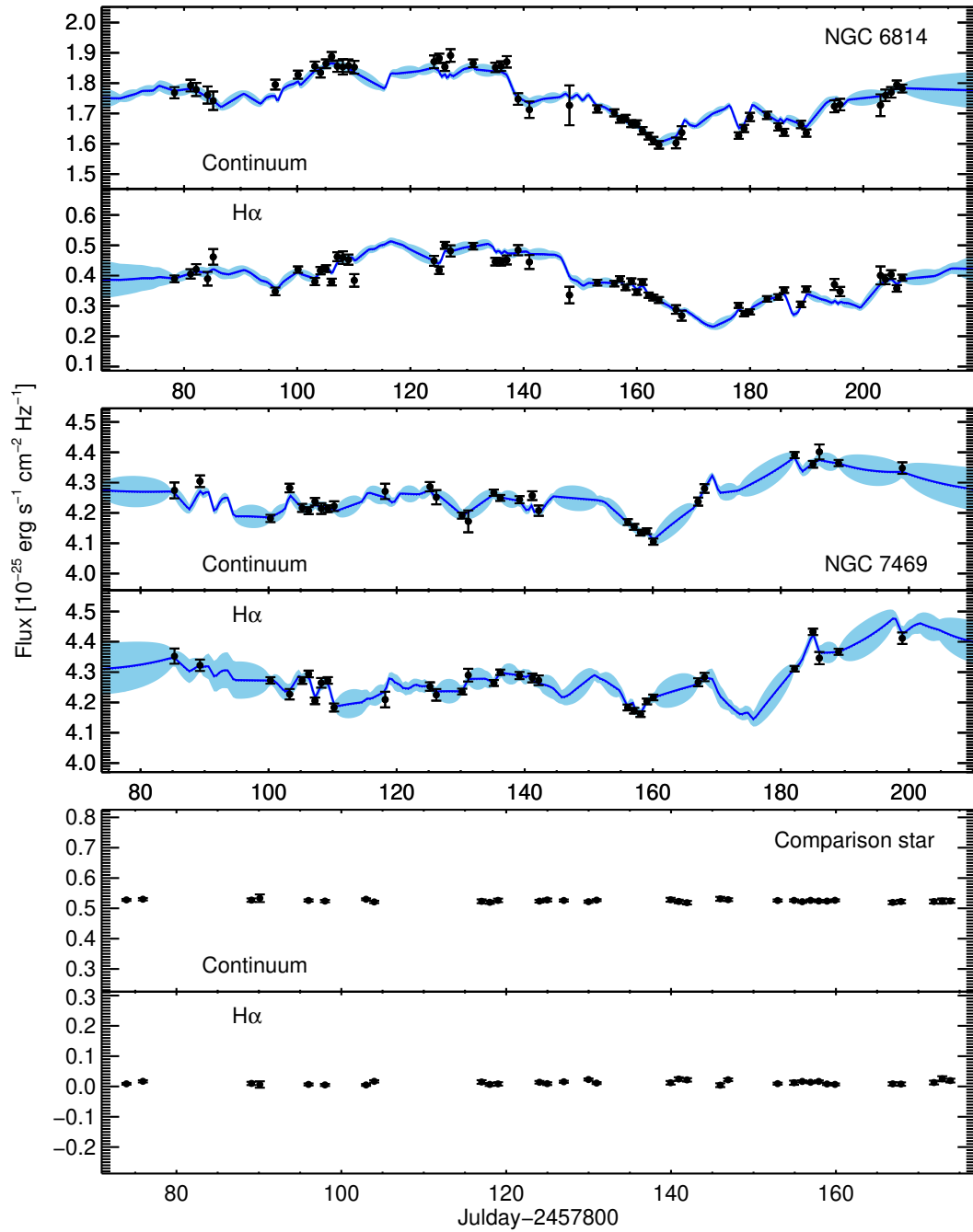


Figure 3.5. Continued of Figure 3.4

Table 3.2. The continuum and the H $\alpha$  emission line light curve of five nearby AGNs

Name (1)	MJD (2)	$m_{625}$ (3)	$m_{675}$ (4)	$m_{725}$ (5)	Continuum flux (6)	H $\alpha$ flux (7)
Mrk 1310	57875.5431	$15.0886 \pm 0.0079$	$14.7209 \pm 0.0062$	$14.8894 \pm 0.0085$	$0.4269 \pm 0.0053$	$0.1090 \pm 0.0036$
Mrk 1310	57876.3990	$15.0775 \pm 0.0165$	$14.6971 \pm 0.0116$	$14.9046 \pm 0.0170$	$0.4262 \pm 0.0107$	$0.1234 \pm 0.0069$
Mrk 1310	57884.4938	$15.1511 \pm 0.0153$	$14.8072 \pm 0.0115$	$14.9636 \pm 0.0138$	$0.4029 \pm 0.0089$	$0.0933 \pm 0.0063$
Mrk 1310	57888.5552	$15.1283 \pm 0.0110$	$14.7662 \pm 0.0083$	$14.9526 \pm 0.0106$	$0.4106 \pm 0.0068$	$0.1071 \pm 0.0047$
Mrk 1310	57889.5500	$15.1502 \pm 0.0107$	$14.8038 \pm 0.0156$	$14.9385 \pm 0.0192$	$0.4089 \pm 0.0101$	$0.0880 \pm 0.0086$
Mrk 1310	57895.5087	$15.1533 \pm 0.0073$	$14.7871 \pm 0.0057$	$14.9342 \pm 0.0077$	$0.4106 \pm 0.0047$	$0.0964 \pm 0.0031$
Mrk 1310	57897.5066	$15.1252 \pm 0.0079$	$14.7683 \pm 0.0059$	$14.9205 \pm 0.0080$	$0.4183 \pm 0.0051$	$0.0998 \pm 0.0033$
Mrk 1310	57902.4880	$15.1475 \pm 0.0065$	$14.7925 \pm 0.0051$	$14.9474 \pm 0.0067$	$0.4086 \pm 0.0041$	$0.0975 \pm 0.0028$
Mrk 1310	57903.4760	$15.1449 \pm 0.0089$	$14.8053 \pm 0.0073$	$14.9566 \pm 0.0092$	$0.4054 \pm 0.0055$	$0.0915 \pm 0.0039$
Mrk 1310	57916.4870	$15.1930 \pm 0.0121$	$14.8115 \pm 0.0089$	$14.9857 \pm 0.0117$	$0.3930 \pm 0.0070$	$0.1036 \pm 0.0048$
Mrk 1310	57917.4810	$15.1889 \pm 0.0116$	$14.8477 \pm 0.0088$	$14.9938 \pm 0.0111$	$0.3939 \pm 0.0066$	$0.0871 \pm 0.0046$
Mrk 1310	57924.4530	$15.1718 \pm 0.0097$	$14.8435 \pm 0.0075$	$14.9927 \pm 0.0103$	$0.3962 \pm 0.0061$	$0.0868 \pm 0.0040$
Mrk 1310	57925.4550	$15.1826 \pm 0.0077$	$14.8462 \pm 0.0060$	$14.9711 \pm 0.0082$	$0.3962 \pm 0.0047$	$0.0855 \pm 0.0031$
Mrk 1310	57929.4550	$15.1677 \pm 0.0069$	$14.8320 \pm 0.0053$	$14.9879 \pm 0.0069$	$0.3970 \pm 0.0042$	$0.0921 \pm 0.0028$
Mrk 1310	57930.4270	$15.1688 \pm 0.0071$	$14.8205 \pm 0.0055$	$14.9691 \pm 0.0071$	$0.4009 \pm 0.0043$	$0.0936 \pm 0.0029$
Mrk 1310	57938.4240	$15.1895 \pm 0.0132$	$14.8524 \pm 0.0100$	$15.0166 \pm 0.0126$	$0.3856 \pm 0.0076$	$0.0924 \pm 0.0053$
Mrk 1310	57939.4280	$15.1601 \pm 0.0146$	$14.8167 \pm 0.0203$	$14.9402 \pm 0.0153$	$0.4080 \pm 0.0093$	$0.0918 \pm 0.0108$
Mrk 1310	57940.4140	$15.1518 \pm 0.0123$	$14.8129 \pm 0.0095$	$14.9420 \pm 0.0117$	$0.4101 \pm 0.0074$	$0.0882 \pm 0.0051$

Table 3.2 (cont'd)

Name (1)	MJD (2)	$m_{625}$ (3)	$m_{675}$ (4)	$m_{725}$ (5)	Continuum flux (6)	H $\alpha$ flux (7)
Mrk 1310	57941.4180	15.1933 $\pm$ 0.0120	14.8246 $\pm$ 0.0089	14.9981 $\pm$ 0.0110	0.3899 $\pm$ 0.0068	0.1027 $\pm$ 0.0048
Mrk 1310	57945.4420	15.1611 $\pm$ 0.0129	14.8120 $\pm$ 0.0097	14.9776 $\pm$ 0.0126	0.3977 $\pm$ 0.0076	0.0999 $\pm$ 0.0052
Mrk 1310	57946.4080	15.1755 $\pm$ 0.0087	14.8289 $\pm$ 0.0069	14.9570 $\pm$ 0.0093	0.4017 $\pm$ 0.0055	0.0892 $\pm$ 0.0037
Mrk 1310	57947.4130	15.1499 $\pm$ 0.0080	14.8159 $\pm$ 0.0064	15.0017 $\pm$ 0.0094	0.3978 $\pm$ 0.0053	0.0985 $\pm$ 0.0035
Mrk 1310	57952.4030	15.1759 $\pm$ 0.0076	14.8116 $\pm$ 0.0056	14.9831 $\pm$ 0.0075	0.3972 $\pm$ 0.0046	0.1009 $\pm$ 0.0031
Mrk 1310	57954.3900	15.1727 $\pm$ 0.0075	14.8342 $\pm$ 0.0070	14.9840 $\pm$ 0.0079	0.3974 $\pm$ 0.0047	0.0879 $\pm$ 0.0038
Mrk 1310	57955.3910	15.1653 $\pm$ 0.0082	14.8206 $\pm$ 0.0063	14.9666 $\pm$ 0.0079	0.4014 $\pm$ 0.0048	0.0911 $\pm$ 0.0034
Mrk 1310	57956.3930	15.1753 $\pm$ 0.0078	14.8308 $\pm$ 0.0059	14.9902 $\pm$ 0.0079	0.3942 $\pm$ 0.0046	0.0963 $\pm$ 0.0032
Mrk 1310	57957.3900	15.1626 $\pm$ 0.0080	14.8443 $\pm$ 0.0060	15.0168 $\pm$ 0.0088	0.3919 $\pm$ 0.0049	0.0921 $\pm$ 0.0031
Mrk 1310	57958.3910	15.1515 $\pm$ 0.0076	14.8454 $\pm$ 0.0059	14.9812 $\pm$ 0.0081	0.4018 $\pm$ 0.0048	0.0823 $\pm$ 0.0032
NGC 4593	57873.4316	13.3852 $\pm$ 0.0025	13.0296 $\pm$ 0.0023	13.1081 $\pm$ 0.0028	2.2565 $\pm$ 0.0097	0.4308 $\pm$ 0.0072
NGC 4593	57875.4299	13.4928 $\pm$ 0.0029	13.0708 $\pm$ 0.0028	13.1466 $\pm$ 0.0033	2.1505 $\pm$ 0.0110	0.4581 $\pm$ 0.0083
NGC 4593	57888.6038	13.4028 $\pm$ 0.0044	13.0724 $\pm$ 0.0041	13.1298 $\pm$ 0.0047	2.2231 $\pm$ 0.0164	0.3993 $\pm$ 0.0123
NGC 4593	57889.6146	13.3999 $\pm$ 0.0100	12.9973 $\pm$ 0.0082	13.1010 $\pm$ 0.0101	2.2533 $\pm$ 0.0367	0.4952 $\pm$ 0.0256
NGC 4593	57895.5219	13.4173 $\pm$ 0.0027	13.0554 $\pm$ 0.0026	13.1241 $\pm$ 0.0031	2.2180 $\pm$ 0.0106	0.4175 $\pm$ 0.0078
NGC 4593	57897.5198	13.3688 $\pm$ 0.0029	13.0389 $\pm$ 0.0028	13.1269 $\pm$ 0.0033	2.2567 $\pm$ 0.0114	0.4002 $\pm$ 0.0083
NGC 4593	57902.5000	13.3422 $\pm$ 0.0023	12.9799 $\pm$ 0.0023	13.0953 $\pm$ 0.0026	2.3100 $\pm$ 0.0096	0.4834 $\pm$ 0.0075
NGC 4593	57903.4910	13.3573 $\pm$ 0.0026	12.9519 $\pm$ 0.0028	13.0807 $\pm$ 0.0033	2.3076 $\pm$ 0.0117	0.5653 $\pm$ 0.0094

Table 3.2 (cont'd)

Name (1)	MJD (2)	$m_{625}$ (3)	$m_{675}$ (4)	$m_{725}$ (5)	Continuum flux (6)	H $\alpha$ flux (7)
NGC 4593	57916.5130	$13.3394 \pm 0.0047$	$12.9568 \pm 0.0045$	$13.1372 \pm 0.0052$	$2.2964 \pm 0.0188$	$0.5519 \pm 0.0149$
NGC 4593	57917.5060	$13.3401 \pm 0.0040$	$12.9771 \pm 0.0036$	$13.0852 \pm 0.0040$	$2.3337 \pm 0.0153$	$0.5030 \pm 0.0121$
NGC 4593	57918.5120	$13.3736 \pm 0.0042$	$13.0326 \pm 0.0042$	$13.0923 \pm 0.0048$	$2.3058 \pm 0.0173$	$0.4359 \pm 0.0134$
NGC 4593	57923.5330	$13.3185 \pm 0.0033$	$12.9549 \pm 0.0031$	$13.0688 \pm 0.0037$	$2.3565 \pm 0.0138$	$0.5034 \pm 0.0104$
NGC 4593	57924.4800	$13.3317 \pm 0.0034$	$12.9735 \pm 0.0033$	$13.0971 \pm 0.0039$	$2.3172 \pm 0.0140$	$0.5035 \pm 0.0109$
NGC 4593	57926.4890	$13.3236 \pm 0.0026$	$12.9360 \pm 0.0025$	$13.1139 \pm 0.0031$	$2.3136 \pm 0.0110$	$0.5745 \pm 0.0084$
NGC 4593	57929.4830	$13.3550 \pm 0.0026$	$12.9355 \pm 0.0025$	$13.0885 \pm 0.0034$	$2.3279 \pm 0.0120$	$0.5597 \pm 0.0084$
NGC 4593	57930.4670	$13.3284 \pm 0.0025$	$12.9646 \pm 0.0024$	$13.0489 \pm 0.0027$	$2.3568 \pm 0.0100$	$0.4766 \pm 0.0078$
NGC 4593	57939.4410	$13.3897 \pm 0.0046$	$13.0957 \pm 0.0045$	$13.0907 \pm 0.0054$	$2.2715 \pm 0.0191$	$0.3191 \pm 0.0133$
NGC 4593	57940.4260	$13.3615 \pm 0.0046$	$13.1596 \pm 0.0042$	$13.1016 \pm 0.0047$	$2.2788 \pm 0.0172$	$0.2367 \pm 0.0123$
NGC 4593	57946.4210	$13.3906 \pm 0.0032$	$13.0165 \pm 0.0033$	$13.1135 \pm 0.0041$	$2.2619 \pm 0.0139$	$0.4493 \pm 0.0103$
NGC 4593	57952.4290	$13.3522 \pm 0.0026$	$12.9846 \pm 0.0025$	$13.0614 \pm 0.0030$	$2.3303 \pm 0.0110$	$0.4547 \pm 0.0082$
NGC 4593	57954.4170	$13.3917 \pm 0.0027$	$13.1020 \pm 0.0052$	$13.1134 \pm 0.0029$	$2.2660 \pm 0.0103$	$0.3014 \pm 0.0153$
NGC 4593	57955.4170	$13.3614 \pm 0.0029$	$12.9711 \pm 0.0027$	$13.1165 \pm 0.0030$	$2.2860 \pm 0.0110$	$0.5325 \pm 0.0086$
NGC 4593	57956.4220	$13.3642 \pm 0.0026$	$12.9761 \pm 0.0025$	$13.0709 \pm 0.0029$	$2.3125 \pm 0.0104$	$0.4851 \pm 0.0081$
NGC 4593	57957.4160	$13.3343 \pm 0.0029$	$12.9667 \pm 0.0027$	$13.1196 \pm 0.0032$	$2.2785 \pm 0.0110$	$0.5137 \pm 0.0084$
NGC 4593	57958.4170	$13.3703 \pm 0.0026$	$12.9907 \pm 0.0026$	$13.0893 \pm 0.0031$	$2.2959 \pm 0.0111$	$0.4744 \pm 0.0083$
NGC 4593	57959.3870	$13.3561 \pm 0.0025$	$12.9923 \pm 0.0025$	$13.1261 \pm 0.0029$	$2.2784 \pm 0.0103$	$0.5000 \pm 0.0080$

Table 3.2 (cont'd)

Name (1)	MJD (2)	$m_{625}$ (3)	$m_{675}$ (4)	$m_{725}$ (5)	Continuum flux (6)	H $\alpha$ flux (7)
NGC 4593	57966.3870	13.3227 $\pm$ 0.0043	13.0008 $\pm$ 0.0042	13.0470 $\pm$ 0.0047	2.3563 $\pm$ 0.0173	0.4307 $\pm$ 0.0134
NGC 4593	57967.3910	13.3286 $\pm$ 0.0044	12.9376 $\pm$ 0.0043	13.0610 $\pm$ 0.0050	2.3279 $\pm$ 0.0174	0.5297 $\pm$ 0.0138
NGC 4593	57972.4030	13.3269 $\pm$ 0.0068	12.9801 $\pm$ 0.0061	13.0711 $\pm$ 0.0069	2.3396 $\pm$ 0.0260	0.4318 $\pm$ 0.0197
NGC 4748	57888.6177	14.2408 $\pm$ 0.0078	13.7317 $\pm$ 0.0070	13.9573 $\pm$ 0.0081	0.9985 $\pm$ 0.0128	0.3671 $\pm$ 0.0110
NGC 4748	57889.6330	14.2498 $\pm$ 0.0196	13.7450 $\pm$ 0.0220	13.9449 $\pm$ 0.0216	1.0019 $\pm$ 0.0338	0.3522 $\pm$ 0.0337
NGC 4748	57895.5594	14.2332 $\pm$ 0.0046	13.7238 $\pm$ 0.0042	13.9688 $\pm$ 0.0053	0.9982 $\pm$ 0.0081	0.3737 $\pm$ 0.0066
NGC 4748	57899.5660	14.2530 $\pm$ 0.0044	13.7397 $\pm$ 0.0040	13.9784 $\pm$ 0.0049	0.9859 $\pm$ 0.0076	0.3711 $\pm$ 0.0062
NGC 4748	57902.5190	14.2299 $\pm$ 0.0040	13.7345 $\pm$ 0.0037	13.9639 $\pm$ 0.0045	1.0025 $\pm$ 0.0071	0.3601 $\pm$ 0.0059
NGC 4748	57903.5130	14.2038 $\pm$ 0.0052	13.7407 $\pm$ 0.0049	13.9525 $\pm$ 0.0057	1.0131 $\pm$ 0.0089	0.3384 $\pm$ 0.0077
NGC 4748	57916.5470	14.2216 $\pm$ 0.0094	13.7218 $\pm$ 0.0080	13.9664 $\pm$ 0.0100	1.0018 $\pm$ 0.0156	0.3768 $\pm$ 0.0127
NGC 4748	57917.5190	14.2453 $\pm$ 0.0065	13.7448 $\pm$ 0.0058	13.9762 $\pm$ 0.0068	0.9902 $\pm$ 0.0106	0.3603 $\pm$ 0.0090
NGC 4748	57918.5240	14.2174 $\pm$ 0.0087	13.7202 $\pm$ 0.0083	13.9576 $\pm$ 0.0114	1.0088 $\pm$ 0.0170	0.3705 $\pm$ 0.0131
NGC 4748	57923.5480	14.2258 $\pm$ 0.0057	13.7208 $\pm$ 0.0051	13.9567 $\pm$ 0.0066	1.0023 $\pm$ 0.0100	0.3778 $\pm$ 0.0080
NGC 4748	57924.4920	14.2396 $\pm$ 0.0058	13.7350 $\pm$ 0.0051	13.9670 $\pm$ 0.0062	0.9976 $\pm$ 0.0097	0.3626 $\pm$ 0.0080
NGC 4748	57925.4970	14.2349 $\pm$ 0.0056	13.7176 $\pm$ 0.0061	13.9657 $\pm$ 0.0077	0.9974 $\pm$ 0.0106	0.3842 $\pm$ 0.0091
NGC 4748	57926.5070	14.2326 $\pm$ 0.0046	13.7345 $\pm$ 0.0041	13.9626 $\pm$ 0.0052	1.0018 $\pm$ 0.0080	0.3597 $\pm$ 0.0065
NGC 4748	57930.4800	14.2387 $\pm$ 0.0043	13.7351 $\pm$ 0.0039	13.9670 $\pm$ 0.0047	0.9943 $\pm$ 0.0072	0.3681 $\pm$ 0.0061
NGC 4748	57940.4670	14.2315 $\pm$ 0.0083	13.7305 $\pm$ 0.0073	13.9452 $\pm$ 0.0087	1.0121 $\pm$ 0.0140	0.3569 $\pm$ 0.0117

Table 3.2 (cont'd)

Name (1)	MJD (2)	$m_{625}$ (3)	$m_{675}$ (4)	$m_{725}$ (5)	Continuum flux (6)	H $\alpha$ flux (7)
NGC 4748	57941.4690	14.2254 $\pm$ 0.0086	13.7329 $\pm$ 0.0095	13.9489 $\pm$ 0.0088	1.0127 $\pm$ 0.0143	0.3553 $\pm$ 0.0151
NGC 4748	57946.4600	14.2508 $\pm$ 0.0077	13.7590 $\pm$ 0.0066	13.9821 $\pm$ 0.0079	0.9854 $\pm$ 0.0123	0.3433 $\pm$ 0.0101
NGC 4748	57947.4580	14.2418 $\pm$ 0.0052	13.7475 $\pm$ 0.0052	13.9804 $\pm$ 0.0094	0.9882 $\pm$ 0.0129	0.3585 $\pm$ 0.0081
NGC 4748	57949.4760	14.2653 $\pm$ 0.0048	13.7650 $\pm$ 0.0042	13.9870 $\pm$ 0.0054	0.9772 $\pm$ 0.0081	0.3476 $\pm$ 0.0064
NGC 4748	57955.4290	14.2497 $\pm$ 0.0047	13.7507 $\pm$ 0.0042	13.9772 $\pm$ 0.0051	0.9884 $\pm$ 0.0078	0.3525 $\pm$ 0.0064
NGC 4748	57956.4360	14.2517 $\pm$ 0.0045	13.7683 $\pm$ 0.0041	13.9798 $\pm$ 0.0050	0.9889 $\pm$ 0.0075	0.3397 $\pm$ 0.0061
NGC 4748	57957.4280	14.2504 $\pm$ 0.0047	13.7451 $\pm$ 0.0043	13.9652 $\pm$ 0.0054	0.9919 $\pm$ 0.0080	0.3563 $\pm$ 0.0064
NGC 4748	57958.4290	14.2423 $\pm$ 0.0045	13.7591 $\pm$ 0.0041	13.9861 $\pm$ 0.0051	0.9885 $\pm$ 0.0077	0.3441 $\pm$ 0.0063
NGC 4748	57959.4000	14.2423 $\pm$ 0.0043	13.7586 $\pm$ 0.0040	13.9739 $\pm$ 0.0048	0.9934 $\pm$ 0.0075	0.3418 $\pm$ 0.0061
NGC 4748	57960.3740	14.2551 $\pm$ 0.0044	13.7598 $\pm$ 0.0040	13.9735 $\pm$ 0.0048	0.9904 $\pm$ 0.0076	0.3434 $\pm$ 0.0062
NGC 4748	57967.4030	14.2230 $\pm$ 0.0083	13.7381 $\pm$ 0.0077	13.9468 $\pm$ 0.0089	1.0106 $\pm$ 0.0134	0.3407 $\pm$ 0.0112
NGC 4748	57971.4030	14.2412 $\pm$ 0.0083	13.7429 $\pm$ 0.0071	13.9856 $\pm$ 0.0082	0.9842 $\pm$ 0.0130	0.3671 $\pm$ 0.0111
NGC 4748	57972.4150	14.2262 $\pm$ 0.0110	13.7240 $\pm$ 0.0090	13.9683 $\pm$ 0.0102	0.9988 $\pm$ 0.0169	0.3780 $\pm$ 0.0144
NGC 4748	57973.3920	14.2193 $\pm$ 0.0085	13.7359 $\pm$ 0.0073	13.9612 $\pm$ 0.0084	1.0076 $\pm$ 0.0138	0.3526 $\pm$ 0.0116
NGC 4748	57974.3820	14.2045 $\pm$ 0.0064	13.7182 $\pm$ 0.0060	13.9445 $\pm$ 0.0069	1.0207 $\pm$ 0.0110	0.3623 $\pm$ 0.0095
NGC 4748	57975.3810	14.2072 $\pm$ 0.0047	13.7351 $\pm$ 0.0041	13.9524 $\pm$ 0.0050	1.0166 $\pm$ 0.0081	0.3435 $\pm$ 0.0064
NGC 4748	57978.3810	14.1913 $\pm$ 0.0047	13.7160 $\pm$ 0.0043	13.9241 $\pm$ 0.0052	1.0336 $\pm$ 0.0084	0.3520 $\pm$ 0.0068
NGC 4748	57980.3790	14.2052 $\pm$ 0.0050	13.7132 $\pm$ 0.0045	13.9427 $\pm$ 0.0056	1.0179 $\pm$ 0.0089	0.3671 $\pm$ 0.0071

Table 3.2 (cont'd)

Name (1)	MJD (2)	$m_{625}$ (3)	$m_{675}$ (4)	$m_{725}$ (5)	Continuum flux (6)	H $\alpha$ flux (7)
NGC 6814	57877.8087	$13.6778 \pm 0.0046$	$13.2848 \pm 0.0045$	$13.1373 \pm 0.0083$	$1.7685 \pm 0.0185$	$0.3894 \pm 0.0111$
NGC 6814	57880.6507	$13.6762 \pm 0.0071$	$13.2548 \pm 0.0061$	$13.1116 \pm 0.0073$	$1.7919 \pm 0.0193$	$0.4056 \pm 0.0153$
NGC 6814	57881.6483	$13.6697 \pm 0.0078$	$13.2482 \pm 0.0068$	$13.1260 \pm 0.0083$	$1.7791 \pm 0.0216$	$0.4207 \pm 0.0173$
NGC 6814	57883.6562	$13.6695 \pm 0.0106$	$13.2784 \pm 0.0091$	$13.1495 \pm 0.0107$	$1.7609 \pm 0.0283$	$0.3898 \pm 0.0225$
NGC 6814	57884.6535	$13.7186 \pm 0.0112$	$13.2532 \pm 0.0102$	$13.1418 \pm 0.0120$	$1.7420 \pm 0.0305$	$0.4617 \pm 0.0258$
NGC 6814	57895.6163	$13.6852 \pm 0.0052$	$13.2874 \pm 0.0050$	$13.1052 \pm 0.0065$	$1.7951 \pm 0.0162$	$0.3479 \pm 0.0126$
NGC 6814	57899.6330	$13.6361 \pm 0.0042$	$13.2294 \pm 0.0040$	$13.1041 \pm 0.0053$	$1.8278 \pm 0.0135$	$0.4197 \pm 0.0105$
NGC 6814	57902.6080	$13.6240 \pm 0.0048$	$13.2413 \pm 0.0046$	$13.0822 \pm 0.0059$	$1.8557 \pm 0.0153$	$0.3804 \pm 0.0119$
NGC 6814	57903.6080	$13.6486 \pm 0.0049$	$13.2324 \pm 0.0046$	$13.0909 \pm 0.0063$	$1.8347 \pm 0.0159$	$0.4164 \pm 0.0121$
NGC 6814	57904.5760	$13.5982 \pm 0.0049$	$13.2096 \pm 0.0042$	$13.0909 \pm 0.0054$	$1.8639 \pm 0.0145$	$0.4232 \pm 0.0112$
NGC 6814	57905.5770	$13.6169 \pm 0.0047$	$13.2153 \pm 0.0041$	$13.0538 \pm 0.0057$	$1.8877 \pm 0.0152$	$0.3789 \pm 0.0109$
NGC 6814	57906.5770	$13.6286 \pm 0.0066$	$13.1909 \pm 0.0055$	$13.0808 \pm 0.0068$	$1.8560 \pm 0.0186$	$0.4623 \pm 0.0147$
NGC 6814	57907.5470	$13.6229 \pm 0.0086$	$13.1939 \pm 0.0077$	$13.0842 \pm 0.0093$	$1.8536 \pm 0.0252$	$0.4595 \pm 0.0208$
NGC 6814	57908.5510	$13.6302 \pm 0.0073$	$13.1926 \pm 0.0063$	$13.0783 \pm 0.0074$	$1.8574 \pm 0.0206$	$0.4526 \pm 0.0167$
NGC 6814	57909.5740	$13.6072 \pm 0.0080$	$13.2395 \pm 0.0083$	$13.0962 \pm 0.0073$	$1.8524 \pm 0.0211$	$0.3842 \pm 0.0207$
NGC 6814	57923.6600	$13.6157 \pm 0.0069$	$13.1964 \pm 0.0060$	$13.0752 \pm 0.0078$	$1.8705 \pm 0.0211$	$0.4489 \pm 0.0164$
NGC 6814	57924.5820	$13.6167 \pm 0.0050$	$13.2077 \pm 0.0045$	$13.0601 \pm 0.0058$	$1.8817 \pm 0.0155$	$0.4177 \pm 0.0122$
NGC 6814	57925.5850	$13.6163 \pm 0.0044$	$13.1729 \pm 0.0041$	$13.0891 \pm 0.0054$	$1.8540 \pm 0.0138$	$0.4999 \pm 0.0113$

Table 3.2 (cont'd)

Name (1)	MJD (2)	$m_{625}$ (3)	$m_{675}$ (4)	$m_{725}$ (5)	Continuum flux (6)	H $\alpha$ flux (7)
NGC 6814	57926.5800	13.5860 $\pm$ 0.0042	13.1666 $\pm$ 0.0066	13.0722 $\pm$ 0.0089	1.8915 $\pm$ 0.0208	0.4813 $\pm$ 0.0183
NGC 6814	57930.5620	13.6237 $\pm$ 0.0041	13.1702 $\pm$ 0.0040	13.0740 $\pm$ 0.0049	1.8653 $\pm$ 0.0129	0.4971 $\pm$ 0.0109
NGC 6814	57934.4960	13.6385 $\pm$ 0.0052	13.2024 $\pm$ 0.0048	13.0758 $\pm$ 0.0059	1.8518 $\pm$ 0.0156	0.4460 $\pm$ 0.0126
NGC 6814	57935.5150	13.6239 $\pm$ 0.0052	13.1970 $\pm$ 0.0046	13.0810 $\pm$ 0.0060	1.8561 $\pm$ 0.0159	0.4455 $\pm$ 0.0123
NGC 6814	57936.5150	13.6031 $\pm$ 0.0066	13.1906 $\pm$ 0.0055	13.0787 $\pm$ 0.0067	1.8703 $\pm$ 0.0188	0.4518 $\pm$ 0.0148
NGC 6814	57938.5140	13.7032 $\pm$ 0.0068	13.2381 $\pm$ 0.0064	13.1458 $\pm$ 0.0075	1.7477 $\pm$ 0.0191	0.4841 $\pm$ 0.0167
NGC 6814	57940.5070	13.7362 $\pm$ 0.0100	13.2935 $\pm$ 0.0092	13.1624 $\pm$ 0.0109	1.7125 $\pm$ 0.0271	0.4450 $\pm$ 0.0230
NGC 6814	57947.5900	13.6977 $\pm$ 0.0299	13.3246 $\pm$ 0.0115	13.1720 $\pm$ 0.0208	1.7269 $\pm$ 0.0657	0.3360 $\pm$ 0.0272
NGC 6814	57952.5170	13.7188 $\pm$ 0.0041	13.3124 $\pm$ 0.0039	13.1683 $\pm$ 0.0050	1.7150 $\pm$ 0.0120	0.3767 $\pm$ 0.0095
NGC 6814	57955.5190	13.7475 $\pm$ 0.0042	13.3242 $\pm$ 0.0038	13.1674 $\pm$ 0.0048	1.7021 $\pm$ 0.0117	0.3737 $\pm$ 0.0092
NGC 6814	57956.5250	13.7569 $\pm$ 0.0041	13.3286 $\pm$ 0.0039	13.1826 $\pm$ 0.0047	1.6808 $\pm$ 0.0112	0.3890 $\pm$ 0.0093
NGC 6814	57957.5190	13.7253 $\pm$ 0.0047	13.3420 $\pm$ 0.0039	13.1982 $\pm$ 0.0046	1.6838 $\pm$ 0.0116	0.3612 $\pm$ 0.0092
NGC 6814	57958.5190	13.7795 $\pm$ 0.0041	13.3414 $\pm$ 0.0039	13.1880 $\pm$ 0.0048	1.6663 $\pm$ 0.0114	0.3817 $\pm$ 0.0091
NGC 6814	57959.4960	13.7742 $\pm$ 0.0042	13.3633 $\pm$ 0.0038	13.1910 $\pm$ 0.0049	1.6657 $\pm$ 0.0115	0.3457 $\pm$ 0.0089
NGC 6814	57960.4810	13.7903 $\pm$ 0.0042	13.3572 $\pm$ 0.0040	13.2033 $\pm$ 0.0053	1.6430 $\pm$ 0.0121	0.3787 $\pm$ 0.0094
NGC 6814	57961.5830	13.8055 $\pm$ 0.0042	13.3926 $\pm$ 0.0038	13.2172 $\pm$ 0.0049	1.6254 $\pm$ 0.0113	0.3355 $\pm$ 0.0087
NGC 6814	57962.4100	13.7994 $\pm$ 0.0049	13.4089 $\pm$ 0.0042	13.2340 $\pm$ 0.0052	1.6105 $\pm$ 0.0123	0.3277 $\pm$ 0.0095
NGC 6814	57963.4010	13.8121 $\pm$ 0.0051	13.4222 $\pm$ 0.0045	13.2415 $\pm$ 0.0055	1.5968 $\pm$ 0.0127	0.3195 $\pm$ 0.0098

Table 3.2 (cont'd)

Name (1)	MJD (2)	$m_{625}$ (3)	$m_{675}$ (4)	$m_{725}$ (5)	Continuum flux (6)	H $\alpha$ flux (7)
NGC 6814	57966.4140	13.7980 $\pm$ 0.0077	13.4438 $\pm$ 0.0069	13.2470 $\pm$ 0.0075	1.6029 $\pm$ 0.0178	0.2883 $\pm$ 0.0142
NGC 6814	57967.4240	13.7877 $\pm$ 0.0086	13.4366 $\pm$ 0.0078	13.2144 $\pm$ 0.0090	1.6369 $\pm$ 0.0213	0.2679 $\pm$ 0.0165
NGC 6814	57977.4760	13.8009 $\pm$ 0.0040	13.4108 $\pm$ 0.0038	13.2165 $\pm$ 0.0047	1.6270 $\pm$ 0.0108	0.3019 $\pm$ 0.0085
NGC 6814	57978.4340	13.7584 $\pm$ 0.0046	13.4160 $\pm$ 0.0041	13.2198 $\pm$ 0.0050	1.6504 $\pm$ 0.0119	0.2747 $\pm$ 0.0090
NGC 6814	57979.4670	13.7789 $\pm$ 0.0051	13.4052 $\pm$ 0.0039	13.1744 $\pm$ 0.0056	1.6884 $\pm$ 0.0136	0.2806 $\pm$ 0.0087
NGC 6814	57982.5060	13.7411 $\pm$ 0.0040	13.3615 $\pm$ 0.0039	13.1784 $\pm$ 0.0051	1.6938 $\pm$ 0.0119	0.3232 $\pm$ 0.0092
NGC 6814	57984.5030	13.7623 $\pm$ 0.0043	13.3791 $\pm$ 0.0040	13.2052 $\pm$ 0.0053	1.6558 $\pm$ 0.0123	0.3294 $\pm$ 0.0092
NGC 6814	57985.5060	13.7784 $\pm$ 0.0043	13.3753 $\pm$ 0.0040	13.2178 $\pm$ 0.0050	1.6377 $\pm$ 0.0116	0.3521 $\pm$ 0.0091
NGC 6814	57988.5030	13.7704 $\pm$ 0.0044	13.3925 $\pm$ 0.0041	13.1920 $\pm$ 0.0051	1.6639 $\pm$ 0.0122	0.3049 $\pm$ 0.0093
NGC 6814	57989.4350	13.7832 $\pm$ 0.0043	13.3742 $\pm$ 0.0041	13.2168 $\pm$ 0.0053	1.6355 $\pm$ 0.0120	0.3553 $\pm$ 0.0093
NGC 6814	57994.4080	13.7125 $\pm$ 0.0087	13.3149 $\pm$ 0.0075	13.1655 $\pm$ 0.0067	1.7236 $\pm$ 0.0197	0.3710 $\pm$ 0.0183
NGC 6814	57995.4070	13.7179 $\pm$ 0.0067	13.3283 $\pm$ 0.0064	13.1582 $\pm$ 0.0077	1.7293 $\pm$ 0.0191	0.3474 $\pm$ 0.0153
NGC 6814	58002.5380	13.7282 $\pm$ 0.0129	13.2936 $\pm$ 0.0119	13.1469 $\pm$ 0.0143	1.7273 $\pm$ 0.0359	0.4006 $\pm$ 0.0297
NGC 6814	58003.4120	13.7040 $\pm$ 0.0068	13.2854 $\pm$ 0.0062	13.1356 $\pm$ 0.0073	1.7597 $\pm$ 0.0189	0.3871 $\pm$ 0.0154
NGC 6814	58004.4270	13.6888 $\pm$ 0.0055	13.2669 $\pm$ 0.0059	13.1287 $\pm$ 0.0071	1.7697 $\pm$ 0.0172	0.4034 $\pm$ 0.0142
NGC 6814	58005.4240	13.6725 $\pm$ 0.0048	13.2887 $\pm$ 0.0043	13.1145 $\pm$ 0.0055	1.7945 $\pm$ 0.0141	0.3578 $\pm$ 0.0107
NGC 6814	58006.3940	13.6764 $\pm$ 0.0042	13.2739 $\pm$ 0.0040	13.1256 $\pm$ 0.0051	1.7825 $\pm$ 0.0129	0.3929 $\pm$ 0.0101
NGC 7469	57884.7958	13.2087 $\pm$ 0.0039	11.7055 $\pm$ 0.0027	12.0806 $\pm$ 0.0036	4.2743 $\pm$ 0.0262	4.3526 $\pm$ 0.0250

Table 3.2 (cont'd)

Name (1)	MJD (2)	$m_{625}$ (3)	$m_{675}$ (4)	$m_{725}$ (5)	Continuum flux (6)	H $\alpha$ flux (7)
NGC 7469	57888.7816	$13.1955 \pm 0.0027$	$11.7026 \pm 0.0019$	$12.0745 \pm 0.0026$	$4.3045 \pm 0.0194$	$4.3226 \pm 0.0188$
NGC 7469	57899.7870	$13.2399 \pm 0.0015$	$11.7251 \pm 0.0011$	$12.1030 \pm 0.0016$	$4.1820 \pm 0.0119$	$4.2728 \pm 0.0106$
NGC 7469	57902.7830	$13.2204 \pm 0.0020$	$11.7180 \pm 0.0018$	$12.0741 \pm 0.0020$	$4.2821 \pm 0.0142$	$4.2272 \pm 0.0173$
NGC 7469	57904.7390	$13.2321 \pm 0.0016$	$11.7233 \pm 0.0012$	$12.0951 \pm 0.0018$	$4.2165 \pm 0.0131$	$4.2725 \pm 0.0113$
NGC 7469	57905.7430	$13.2246 \pm 0.0016$	$11.7211 \pm 0.0011$	$12.0975 \pm 0.0016$	$4.2076 \pm 0.0116$	$4.2940 \pm 0.0110$
NGC 7469	57906.7450	$13.2247 \pm 0.0016$	$11.7297 \pm 0.0011$	$12.0893 \pm 0.0017$	$4.2372 \pm 0.0123$	$4.2052 \pm 0.0109$
NGC 7469	57907.7330	$13.2254 \pm 0.0022$	$11.7252 \pm 0.0017$	$12.0942 \pm 0.0024$	$4.2143 \pm 0.0178$	$4.2645 \pm 0.0159$
NGC 7469	57908.7350	$13.2226 \pm 0.0016$	$11.7230 \pm 0.0011$	$12.0963 \pm 0.0016$	$4.2141 \pm 0.0114$	$4.2725 \pm 0.0110$
NGC 7469	57909.7370	$13.2247 \pm 0.0020$	$11.7298 \pm 0.0014$	$12.0876 \pm 0.0023$	$4.2223 \pm 0.0161$	$4.1833 \pm 0.0132$
NGC 7469	57917.6970	$13.2163 \pm 0.0036$	$11.7212 \pm 0.0028$	$12.0790 \pm 0.0034$	$4.2711 \pm 0.0253$	$4.2095 \pm 0.0258$
NGC 7469	57924.6970	$13.2093 \pm 0.0021$	$11.7109 \pm 0.0015$	$12.0702 \pm 0.0022$	$4.2865 \pm 0.0153$	$4.2525 \pm 0.0139$
NGC 7469	57925.6950	$13.2141 \pm 0.0028$	$11.7220 \pm 0.0021$	$12.0839 \pm 0.0035$	$4.2518 \pm 0.0234$	$4.2250 \pm 0.0192$
NGC 7469	57929.7170	$13.2273 \pm 0.0014$	$11.7312 \pm 0.0010$	$12.1037 \pm 0.0013$	$4.1915 \pm 0.0099$	$4.2359 \pm 0.0095$
NGC 7469	57930.6910	$13.2184 \pm 0.0082$	$11.7276 \pm 0.0022$	$12.1169 \pm 0.0044$	$4.1723 \pm 0.0361$	$4.2899 \pm 0.0210$
NGC 7469	57934.6690	$13.2140 \pm 0.0014$	$11.7161 \pm 0.0011$	$12.0796 \pm 0.0015$	$4.2666 \pm 0.0106$	$4.2642 \pm 0.0098$
NGC 7469	57935.6910	$13.2139 \pm 0.0013$	$11.7123 \pm 0.0010$	$12.0854 \pm 0.0013$	$4.2497 \pm 0.0098$	$4.2993 \pm 0.0089$
NGC 7469	57938.6850	$13.2172 \pm 0.0017$	$11.7178 \pm 0.0012$	$12.0883 \pm 0.0016$	$4.2437 \pm 0.0118$	$4.2888 \pm 0.0119$
NGC 7469	57940.6810	$13.2213 \pm 0.0021$	$11.7138 \pm 0.0015$	$12.0829 \pm 0.0019$	$4.2569 \pm 0.0144$	$4.2809 \pm 0.0146$

Table 3.2 (cont'd)

Name (1)	MJD (2)	$m_{625}$ (3)	$m_{675}$ (4)	$m_{725}$ (5)	Continuum flux (6)	H $\alpha$ flux (7)
NGC 7469	57941.6880	$13.2381 \pm 0.0027$	$11.7220 \pm 0.0017$	$12.0964 \pm 0.0023$	$4.2076 \pm 0.0170$	$4.2730 \pm 0.0160$
NGC 7469	57955.5940	$13.2407 \pm 0.0014$	$11.7405 \pm 0.0011$	$12.1039 \pm 0.0014$	$4.1698 \pm 0.0099$	$4.1834 \pm 0.0096$
NGC 7469	57956.5980	$13.2497 \pm 0.0014$	$11.7435 \pm 0.0010$	$12.1085 \pm 0.0013$	$4.1540 \pm 0.0097$	$4.1728 \pm 0.0093$
NGC 7469	57957.5920	$13.2496 \pm 0.0014$	$11.7485 \pm 0.0010$	$12.1173 \pm 0.0013$	$4.1350 \pm 0.0095$	$4.1615 \pm 0.0092$
NGC 7469	57958.5950	$13.2537 \pm 0.0014$	$11.7420 \pm 0.0010$	$12.1172 \pm 0.0013$	$4.1399 \pm 0.0097$	$4.2032 \pm 0.0094$
NGC 7469	57959.5990	$13.2566 \pm 0.0014$	$11.7467 \pm 0.0010$	$12.1250 \pm 0.0014$	$4.1053 \pm 0.0103$	$4.2164 \pm 0.0094$
NGC 7469	57966.5880	$13.2085 \pm 0.0019$	$11.7208 \pm 0.0014$	$12.0933 \pm 0.0018$	$4.2374 \pm 0.0134$	$4.2665 \pm 0.0134$
NGC 7469	57967.5920	$13.1957 \pm 0.0022$	$11.7117 \pm 0.0015$	$12.0802 \pm 0.0020$	$4.2807 \pm 0.0143$	$4.2838 \pm 0.0138$
NGC 7469	57981.6420	$13.1721 \pm 0.0013$	$11.6939 \pm 0.0010$	$12.0494 \pm 0.0013$	$4.3907 \pm 0.0102$	$4.3112 \pm 0.0091$
NGC 7469	57984.5310	$13.1701 \pm 0.0014$	$11.6820 \pm 0.0011$	$12.0600 \pm 0.0015$	$4.3605 \pm 0.0111$	$4.4329 \pm 0.0104$
NGC 7469	57985.5320	$13.1446 \pm 0.0017$	$11.6860 \pm 0.0020$	$12.0578 \pm 0.0034$	$4.4013 \pm 0.0248$	$4.3462 \pm 0.0203$
NGC 7469	57988.5300	$13.1761 \pm 0.0013$	$11.6903 \pm 0.0010$	$12.0579 \pm 0.0013$	$4.3645 \pm 0.0103$	$4.3670 \pm 0.0100$
NGC 7469	57998.4810	$13.1875 \pm 0.0028$	$11.6912 \pm 0.0020$	$12.0633 \pm 0.0026$	$4.3480 \pm 0.0191$	$4.4119 \pm 0.0191$

Note. — (1) AGN name, (2) Modified Julian Date of observation, (3)-(5) AB mag, (6) the 675 nm continuum flux in  $10^{-25}$  erg s $^{-1}$  cm $^{-2}$  Hz $^{-1}$  (observed frame) and its error, (7) H $\alpha$  flux in  $10^{-25}$  erg s $^{-1}$  cm $^{-2}$  Hz $^{-1}$  (observed frame) and its error

### 3.4 AGN Variability

We examined the variability of the five AGNs to make sure that they were variable during our observation period. This was done by the  $\chi^2$  test (Kim et al. 2018). Here, the  $\chi^2$  value is defined as

$$\chi^2 = \sum_i \frac{(m_i - \langle m_i \rangle)^2}{(\sigma_i)^2} \quad (3.1)$$

where  $i$  denotes each epoch,  $m_i$  and  $\sigma_i$  are the magnitude and its error at the epoch  $i$ , and  $\langle m_i \rangle$  is the magnitude averaged over all the epochs. The results of the  $\chi^2$ -test, the excess variability (given by  $\sqrt{m_{rms}^2 - \langle \sigma_i \rangle^2}$ , where  $m_{rms}$  is the rms of the light-curve magnitudes and  $\langle \sigma_i \rangle$  is the average magnitude error over all the epochs), and the peak-to-peak (p-to-p) variability in each band are given in Table 3.3. In the table, the reduced  $\chi^2$  is indicated, which is  $\chi^2$  divided by the degree of freedom (the number of data points minus 1). The  $\chi^2$ -test result shows that all of the AGNs are variable in all of the three medium-band filters at 99.9% confidence level.

### 3.5 Result: Medium-band Based Time Lags

We used two different ways to measure the time lag between the continuum and the H $\alpha$  emission line light curves of the AGNs, the JAVELIN software (Zu et al. 2011, 2016), and the discrete correlation function (DCF; Edelson & Krolik 1988). The JAVELIN software models the continuum light curve using damped random walk (Kelly et al. 2009) for AGN variability. Then, the continuum light curve is scaled, smoothed and displaced in time and flux to the emission line light curve to find the best-fitting time lag. This procedure is repeated at least 10,000 times by the Markov chain Monte Carlo method to derive many plausible time lags. From the time lag distribution, we identify the time lag that gives the peak value of the distribution as the most probable time lag. The time lag  $1\sigma$  limits are determined to be the upper and lower limits from the most probable time lag value that encompasses 68% of the time lag distribution. The best-fit light curves for the most probable time lag from JAVELIN are plotted in Figures 3.4 and 3.5, along with the observed light curves. Also, the lower panels of Figure 3.6 show

the time lag distribution from JAVELIN for each target with a 0.2 day bin. The peak value of the distribution is normalized to 1.

Another method we tried is DCF, which is developed for analyzing unevenly sampled time-series data. For the DCF analysis, we assumed that the time lag to be 0-50 days, adopting a prior information on the expected time lag. Similarly to the JAVELIN case, many trials are made to search for time lags. The result of the DCF analysis is plotted in the upper panels of Figure 3.6 for the calculation using a 1 day interval.

Note that we did not detrend the light curve for the above analyses (Welsh 1999; Grier et al. 2008; Peterson et al. 2014), because the long term variation of our light curves is rather modest.

We find that the measured time lag from two different methods are broadly consistent with each other. However, the JAVELIN results show much clearer peaks than the DCF results. Therefore, we adopt the result from the JAVELIN measurements as the time lag of the  $H\alpha$  emission line. In Table 3.3 and Figure 3.7, we compare our results with the time lags from previous studies. Also, correlation coefficient between the two time lag measurements is calculated as 0.93, which means our results and the previous results are consistent with each other. Details on the time lag of each target are described below.

**Mrk 1310:** It has the shortest time lag among five targets. The peak of the DCF is 1 day and the JAVELIN result shows a broad lag distribution. Ignoring the weak second peak and using the lag distribution less than 18 days we find the time lag of  $1.5^{+8.2}_{-3.3}$  days. The large error is not surprising, considering our average sampling interval of 3 days. In comparison, Bentz et al. (2010) find the time lag between  $H\alpha$  and the  $V$ -band continuum is  $4.5^{+0.7}_{-0.6}$  days. Their time lag result with respect to  $B$ -band continuum is also of order of  $4.6^{+0.7}_{-0.6}$  days. Our time lag is consistent with the Bentz et al. (2010) result within error.

**NGC 4593:** For NGC 4593, the DCF shows a peak at 3 days. Similarly, the JAVELIN lag distribution shows a narrow peak at  $3.3^{+0.4}_{-0.2}$  days with the very sharp distribution. Peterson et al. (2004) found a time lag of  $3.2^{+5.6}_{-4.1}$  days, in agreement with

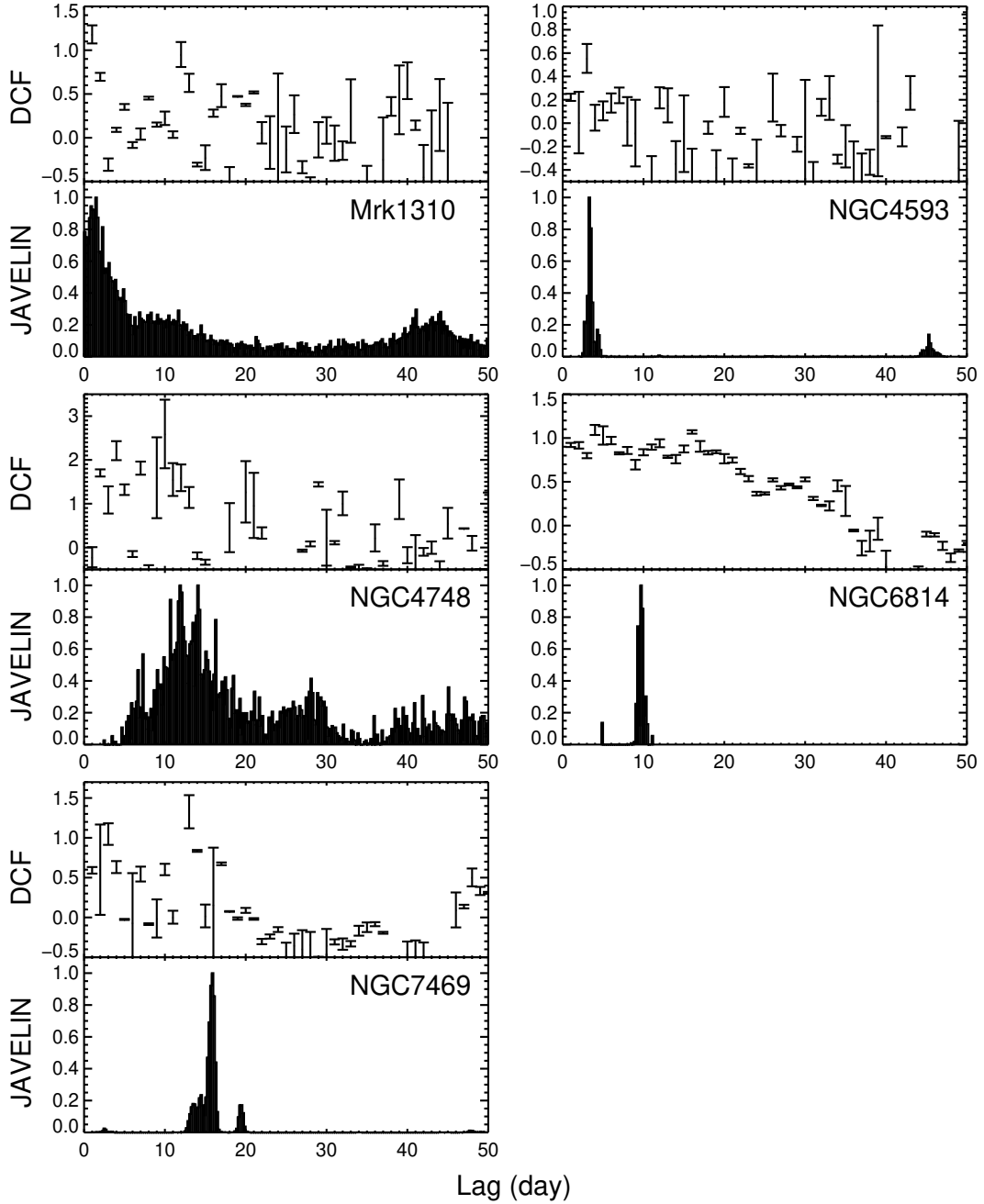


**Figure 3.6.** Time lag measurement results for the five AGNs in our sample. Upper panels show the DCF values from the DCF analysis, and the lower panels are for the time lag distribution from the JAVELIN analysis.

our result. Along with NGC 6814, this object shows the strongest variability among our sample, and we believe that this is why the JAVELIN distribution has a narrow peak.

**NGC 4748:** The peak value in the DCF of NGC 4748 is 10 days. From the JAVELIN analysis, we find  $11.9^{+5.3}_{-2.6}$  days using the time lag distribution from 0.05 to 22.0 days. It shows the smallest magnitude variations among five AGNs. Contrary to the result of NGC 4593, the small variability makes the time lag uncertainty larger (discussed in Section 3.6). However, the result is consistent within uncertainty with the previous measurement of  $10.8^{+3.1}_{-3.1}$  days by Bentz et al. (2010).

**NGC 6814:** Unlike others, the DCF of NGC 6814 shows a clear trend, but a peak seems not to be defined well with a double peak at 4 days and 16 days. On the other hand, JAVELIN lag distribution is sharp with a peak at  $9.7^{+0.4}_{-0.4}$  days. It is close to the mean value of double peak in DCF. The time lag of NGC 6814 from Bentz et al. (2010) is  $9.6^{+2.2}_{-1.7}$  days, in an excellent agreement with our result. Like NGC 4593, the small error in the time lag peak reflects the strongest variation of the light curve (0.06 mag, excess variability).

**NGC 7469:** The DCF peaks at 13 days and the JAVELIN result shows  $15.9^{+0.3}_{-1.7}$  days time lag. Conflicting time lag measurements are presented in previous studies, with  $4.9^{+1.7}_{-1.3}$  days time lag of H $\alpha$  emission line (Peterson et al. 2004), and  $10.9^{+3.5}_{-1.3}$  days using H $\beta$  emission line in a more recent study by Peterson et al. (2014). We note that the H $\alpha$  time lag from our analysis is significantly larger than the values in previous works (Peterson et al. 2014; Shapovalova et al. 2017). However, considering that the general trend of the H $\alpha$  and H $\beta$  time lag ratio of  $\tau(\text{H}\alpha):\tau(\text{H}\beta)=1.54:1.00$  (Bentz et al. 2010), our result is in agreement with the Peterson et al. (2014) result. Taking our value and the mass estimators of Peterson et al. (2014) and Jun et al. (2015), the  $M_{\text{BH}}$  estimate from H $\alpha$  is about  $4 \times 10^6 M_{\odot}$ . This value agrees well with the most recent H $\beta$ -based  $M_{\text{BH}}$  (Table 3.3; Peterson et al. 2014). Despite of the small variation of 0.01 mag (excess variability), the time lag measurement has a small error of  $\sim 12\%$ , comparable to the time lag error of NGC 4593 and NGC 6814, both of which have much larger

excess variability of  $\sim 0.06$  mag. This can be attributed to the fact that NGC 7469 is several times brighter than NGC 4593 and NGC 6814, and thus has the light curve with higher S/N.

Table 3.3. Variability and time lag of monitored AGNs.

Name	Excess Variability [mag]			p-to-p Variability [mag]			Reduced $\chi^2$			Time Lag [day]		Reference
	<i>m</i> 625	<i>m</i> 675	<i>m</i> 725	<i>m</i> 625	<i>m</i> 675	<i>m</i> 725	<i>m</i> 625	<i>m</i> 675	<i>m</i> 725	This Study	Previous Study	
Mrk 1310	0.03	0.04	0.03	0.12	0.16	0.13	7.4	23.1	10.6	$1.5^{+8.2}_{-3.3}$	$4.5^{+0.7}_{-0.6}$	2
NGC 4593	0.04	0.06	0.03	0.17	0.22	0.10	141.1	257.6	57.3	$3.3^{+0.4}_{-0.2}$	$3.2^{+5.6}_{-4.1}$	1
NGC 4748	0.02	0.01	0.01	0.07	0.06	0.06	11.3	10.3	6.1	$11.9^{+5.3}_{-2.6}$	$10.8^{+3.1}_{-3.1}$	2
NGC 6814	0.07	0.08	0.05	0.23	0.28	0.19	191.8	294.3	91.6	$9.7^{+0.4}_{-0.4}$	$9.6^{+2.2}_{-1.7}$	2
NGC 7469	0.03	0.02	0.02	0.11	0.07	0.08	289.1	232.4	143.5	$15.9^{+0.3}_{-1.7}$	$4.6^{+1.7}_{-1.3}$	1
											$10.9^{+3.5}_{-1.3}$ (H $\beta$ )	3

Note. — References. (1) Peterson et al. 2004; (2) Bentz et al. 2010; (3) Peterson et al. 2014

### 3.6 Discussion: Implications for future medium-band RM study

The detailed examination of each target in the previous section shows that the accuracy of time lag measurement correlates with the amount of variability as well as S/N, relative cadence, and the number of data points. Obviously, high S/N measurements allow us to examine the time variability better by providing high accuracy photometry. It is easier to catch the variability for highly variable sources, so the time lag accuracy must be improved with the amount of variability. Finally, the number of data points for a given time lag matters, as denser sampling of the light curve can help to understand the overall trend of the variability even if the photometry accuracy is less than the variability. Therefore, we suggest that the product of S/N, the excess variability, and the time lag ( $t_{\text{lag}}$ ) divided by the average time spacing of the observation ( $\Delta t$ ) as a proxy of the time lag measurement accuracy. In Figure 3.8, we show how the time lag uncertainty changes with the product of the excess variability, the average S/N, and  $t_{\text{lag}}/\Delta t$ . Here, the S/N is the average of the measured flux divided by the average of the flux errors.

For a medium-band survey with a photometric accuracy of 10%, the excess variability of 0.03 mag, and 1 week cadence for an AGN of a 1 year time lag (i.e.,  $t_{\text{lag}}/\Delta t = 52$ ), Figure 3.8 shows that the time lag uncertainty is about 10%. With this result at hand, we can expect how powerful the medium-band RM can be if one uses a dedicated wide-field telescope. For example, a wide-field imaging telescope such as KMTNet (Kim et al. 2016a) can observe 4 deg<sup>2</sup> of the sky at once. If the KMTNet 1.6m telescope is equipped with a suite of medium-band filters similar to those on SNUCAM-II (Choi & Im 2017) or SQUEAN (Kim et al. 2016b), we expect to be able to reach 22 AB mag ( $10\sigma$ ) at  $m675$  with an exposure time of 6 minutes. There are about 300 AGNs at  $i < 22$  AB mag (Richards et al. 2006) in a single KMTNet field of view. An observation with a set of 8 medium-band filters over 400 - 800 nm (e.g., see Choi & Im 2017) can cover BELs of AGNs at various redshifts (e.g., H $\alpha$  at  $0 < z < 0.22$ , H $\beta$  at  $0 < z < 0.65$ ,

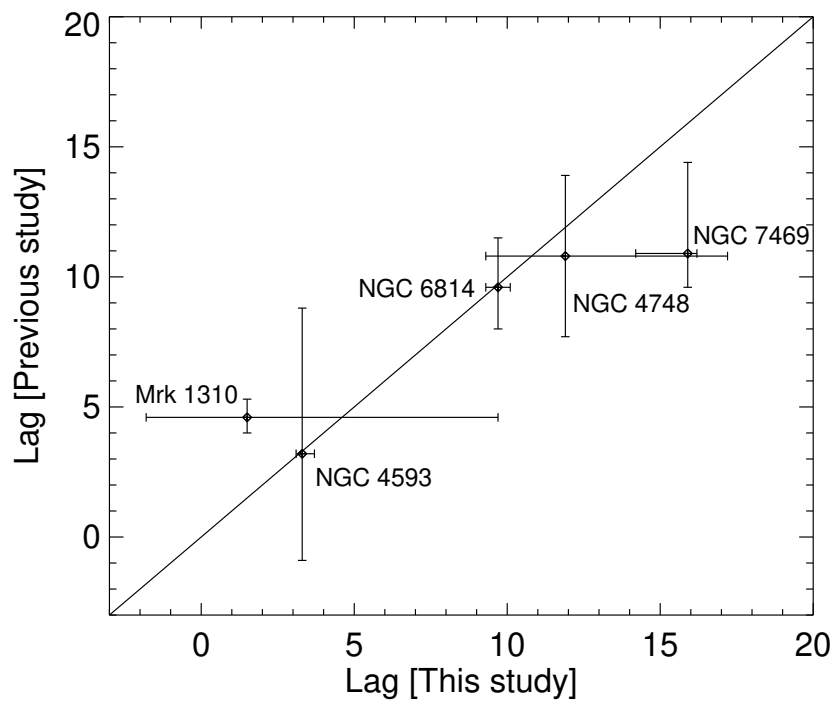


**Figure 3.7.** Comparison of the time lag results between this study and previous studies. The calculated correlation coefficient of the two time lag measurements is 0.93, meaning that our results and the previous results agree well with each other.

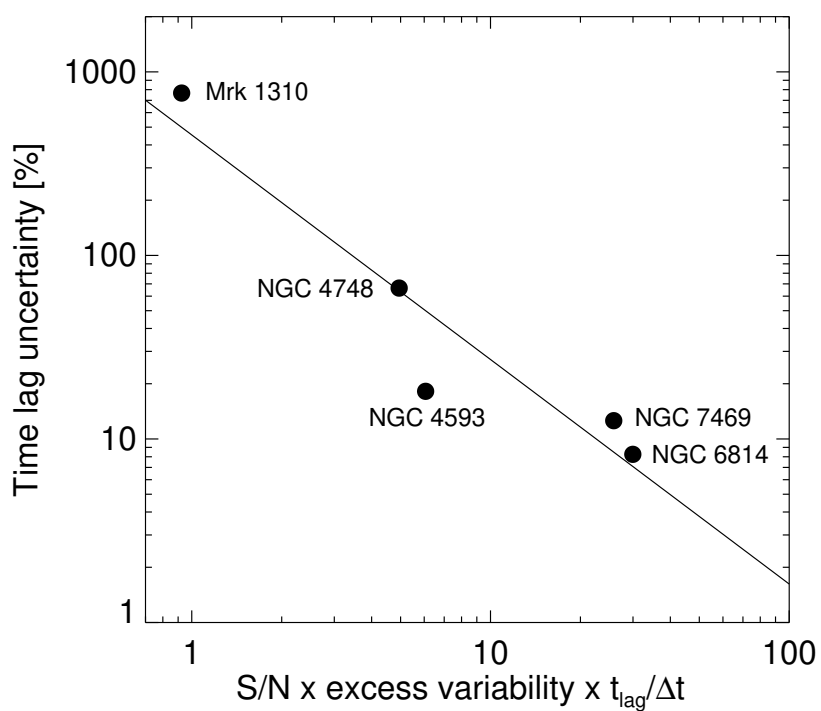


**Figure 3.8.** A plot showing how the time lag uncertainty decreases with  $S/N \times \text{excess variability} \times t_{\text{lag}}/\Delta t$ . The solid line is the fitting result with a slope of -1.22. This shows that the time lag uncertainty is inversely proportional to the  $S/N$ , variability, and  $t_{\text{lag}}/\Delta t$ .

MgII at  $0.43 < z < 1.86$ , and CIV at  $1.6 < z < 4.1$ ), and would take about one hour to complete multi-band imaging of a single field. Therefore, over one night of observation ( $\sim 10$  hrs), a wide-field telescope like KMTNet can detect 3000 AGNs in eight medium-bands. If we perform a multi-year, one week cadence RM campaign with such a facility, medium-band RM mapping monitoring observation is possible for  $\sim 21,000$  AGNs, a substantial increase in the sample size over previous RM studies. We expect to be able to study both low redshift, low luminosity AGNs with short time lags, and high redshift, high luminosity AGNs with long time lags. Since there is a correlation between the AGN luminosity and the time lag, the time lag of 1 week sets the lower limit on the AGN luminosity for the RM to be  $L_{bol} = 5 \times 10^{43}$  erg/s. The upper limit on the AGN luminosity will be defined by the length of the monitoring observation as well as the redshift due to time dilation effect. If we adopt a 5 year period monitoring, we can do RM mapping for  $L_{bol} = 1.5 \times 10^{48}$  erg/s at  $z = 0$  or  $L_{bol} = 7 \times 10^{46}$  erg/s at  $z = 4$ . If we change the monitoring period to 15 years, then the  $L_{bol}$  upper limit can increase. The amount of the AGN variability is anti-correlated with the  $L_{bol}$ . AGNs with  $L_{bol} \sim 10^{47}$  erg/s at  $1 < z < 2$  with  $\Delta t \sim$  months to years are known to have 0.03 mag variability in  $g$ -band (Simm et al. 2016), so this roughly sets the upper limit of the  $L_{bol}$  of AGNs for this RM study.

### 3.7 Summary

In this Chapter, we present the RM results of five AGNs using medium-bands. They are observed over 3-5 months with LSGT, a 0.43m telescope at SSO, and three medium-bands for tracing continuum and H $\alpha$  emission line. All the targets are found to be variable, and the continuum-BEL time lags are calculated. The results show that the time lags from medium-band and spectroscopy agree well within error, and the time lag measurement is possible to 10% accuracy for objects with 0.03 mag excess variability and S/N=10 for each epoch measurement. Therefore, medium-band photometry is effective to study BLR size. This shows a promise for a dedicated 1 m class, wide-field telescope to perform RM study of tens of thousands AGNs down to  $i \sim 22$  mag.

Medium-band observations would also open doors to amateur astronomers or institutions with small telescopes performing unique science of the RM study.

## Chapter 4

# Reverberation Mapping of Six PG Quasars with Medium-band Photometry

### 4.1 Introduction

Reverberation mapping (RM; Blandford & McKee 1982; Peterson 1993) is a technique that has been widely used to measure the masses of the central supermassive black holes in active galactic nuclei (AGNs). The variability is one of the representing properties of AGN (Ulrich et al. 1997). When the continuum from the accretion disk reaches to the broad-line region (BLR), photoionization and recombination processes make the broad emission lines (BELs). Here, if the continuum shows variability, then the BEL will be observed to be variable. Because of the distance from the accretion disk to the BLR, the time lag between the continuum and BEL light-curves can be observed as a tracer of the BLR size. By combining the BLR size and the BEL velocity width, the black hole mass ( $M_{\text{BH}}$ ) can be measured. For decades, many studies performed not only for measuring black hole masses, but also have found a correlation between the BLR size and the AGN luminosity for hundreds of AGNs (Kaspi et al. 2000, 2005, 2007; Peterson et al. 2004; Bentz et al. 2006, 2009, 2010, 2013; Denney et al. 2010; Kim et al. 2010,

2015; Grier et al. 2012, 2017, 2019; Du et al. 2014, 2015, 2016, 2018; Barth et al. 2015; Hu et al. 2015; Jun et al. 2015; Shen et al. 2016; Fausnaugh et al. 2017; Li et al. 2017; Lira et al. 2018). However, recent studies show that the time lags are under-estimated in the BLR size and the AGN luminosity plane than those in the previous studies (Du et al. 2016; Grier et al. 2017), making it necessary to study a large number of AGNs.

The RM studies have difficulties in several ways. It needs spectroscopic monitoring for months to years that is high cost and time consuming more than photometric one and makes it hard to increase RM samples in the previous studies. Moreover, according to the BLR size and the AGN luminosity relation, the time lag should logarithmically increase in higher luminosity spanning hundreds of days. Then, very long term monitoring, at least a few years, is inevitable and it is a result of only a few RM studies for AGNs in high luminosity  $> 10^{45} \text{ erg/s}$ . The last thing is the AGN variability, which is reported to have an anti-correlation with the AGN luminosity (Hook et al. 1994; Giveon et al. 1999; Simm et al. 2016) making it difficult to perform the RM in higher luminosity.

The limitations of RM can be solved by increasing the AGN samples. If the photometric RM rather than the spectroscopic one can be established, we can dramatically increase the sample size of RM with large field of view telescopes (Kim et al. 2019b). A few studies have tried photometric RM obtaining successful results. The photometric RM uses the sets of broad-band filters one of which covers the continuum and the other covers the BEL (Chelouche & Daniel 2012; Chelouche et al. 2012; Edri et al. 2012; Hernitschek et al. 2015; Zu et al. 2016). However, the band width of the broad-band is too wide to trace the continuum and the BEL because of the contaminations of each other. The uncertainty of the time lag becomes much higher than the spectroscopic RM. Another kind of studies performed the photometric RM with the broad-band (for the continuum) and a narrow-band (for BEL) combination (Haas et al. 2011; Pozo Nuñez et al. 2012, 2013, 2015). As a result, it shows comparable uncertainty of the time lag with the spectroscopic RM. Despite the fine uncertainty, the narrow-band is too narrow to be employed for AGNs at various redshifts, thus hard to increase the AGN samples.

Therefore, RM with the broad-band or the narrow-band filters needs to be changed to another filter system to study large AGN samples with smaller uncertainty. For this reason, Jiang et al. (2016) used  $\sim 20$  nm medium-bands for BEL and the broad-band for the continuum to study 13 AGNs and successfully found time lags for 6 AGNs. Also, their result agrees with the BLR size and AGN luminosity relation from previous studies. Furthermore, Kim et al. (2019b) monitored five AGNs for 3 - 5 months, which targets are already studied by the spectroscopic RM, only with medium-bands (bandwidth  $\sim 50$  nm) for both the continuum and the BEL. The result shows 1.5 – 15.9 days of time lags that is consistent with the spectroscopic RM results. This study increased the possibility of the photometric RM with the medium-band filters.

As an attempt to expand the study of Kim et al. (2019b), we report the results of photometric RM for six quasars which are expected to have longer time lags (weeks to months) than those in Kim et al. (2019b) of days to weeks, using medium-bands installed on a 0.43 m telescope. In Section 4.2, we describe our AGN sample and observations. Section 4.3 deals with the construction of the light-curves and Section 4.4 presents the AGN variability in both continuum and BEL. Section 4.5 reports the measured time lags as a result. We will discuss the results in Section 4.6.

## 4.2 Data

### 4.2.1 Sample selection

In this study, we used the Lee Sang Gak Telescope (LSGT; Im et al. 2015) which is a 0.43 m telescope at Siding Spring Observatory (SSO). We selected targets from the Palomar-Green (PG) quasar catalog (Schmidt & Green 1983; Green et al. 1986; Boroson & Green 1992) that are bright enough ( $B < 17$  mag) to be observed with the small telescope, and observable from the southern hemisphere for an extensive period ( $> 6$  months per year). We limited the declination of the targets to be  $< +5$  deg so that they can be observed at SSO. Also, we removed PG quasars whose RM results are found in previous studies (Kaspi et al. 2000; Grier et al. 2012; Park et al. 2017). One

quasar was excluded because the demise of BEL was reported in (Sulentic et al. 2000), and this gives 11 PG quasars to study. For the RM study, AGNs should be variable during the monitoring period to find the time lag. We examined the light curves of 11 quasars using archive data of the Catalina Real-time Transient Survey (CRTS; Drake et al. 2009) and compared the standard deviations of magnitudes from multiple epochs with the mean photometric errors to measure their variabilities. Two AGNs showed small variability of 0.06 mag (standard deviation) which is similar to the average of the photometric uncertainties, and they were removed from the target list. Finally, we selected 9 PG quasars as monitoring targets. However, from now on, we focus on RM results of 6 PG quasars in this Chapter which are expected to have time lags of,  $< 150$  days in the observed frame from the BLR size and the AGN luminosity relation in Bentz et al. (2013).

Table 4.1. List of the monitored AGNs

Name	R.A. [hh:mm:ss]	Decl. [dd:mm:ss]	$m_{525}^a$ [mag]	Redshift	Epochs	Cadence <sup>b</sup> [days]	Monitoring Start-End	$\log \lambda L_{\lambda, 5100}$ [erg/s]	Expected Time Lag [days]
PG 0157+001	01:59:50.21	+00:23:40.6	15.6	0.16	114	7.1 (4.8)	2018.06.21 - 2020.09.12	44.781 <sup>c</sup>	88.3
PG 1011-040	10:14:20.68	-04:18:40.3	15.2	0.058	60	12.7 (6.8)	2018.05.28 - 2020.06.29	43.632 <sup>d</sup>	13.0
PG 1126-041	11:29:16.66	-04:24:07.5	14.8	0.062	64	11.8 (6.7)	2018.06.06 - 2020.07.01	43.819 <sup>d</sup>	17.5
PG 1435-067	14:38:16.16	-06:58:20.5	15.9	0.13	77	9.7 (5.5)	2018.05.23 - 2020.06.08	44.388 <sup>d</sup>	46.0
PG 2304+042	23:07:02.91	+04:32:57.2	15.1	0.042	88	9.6 (5.6)	2018.05.24 - 2020.09.12	43.592 <sup>d</sup>	12.0
PG 2349-014	23:51:56.12	-01:09:13.3	16.2	0.17	110	7.0 (4.8)	2018.07.09 - 2020.09.12	44.768 <sup>c</sup>	87.2

<sup>a</sup> $m_{525}$  magnitude averaged over all epoch.

<sup>b</sup>mean cadence over all epoch. The numbers in the parentheses are the mean cadence during contiguous observing seasons.

<sup>c</sup>Shen et al. 2011

<sup>d</sup>Lani et al. 2017

### 4.2.2 Observation

LSGT has medium-band filters covering wavelengths from 400 to 1050 nm with a band width of  $\sim 50$  nm (Choi & Im 2017). The names of the filters are designated as ‘m’ and followed by the central wavelength of each filter. For example, a filter named *m575* has the central wavelength at 575 nm with  $\sim 50$  nm band width. We monitored H $\beta$  and H $\gamma$  emission lines using three consecutive medium-bands, which are designated as band1, band2, and band3 from short to long wavelength. Then, band1, band2, and band3 trace H $\gamma$ , H $\beta$ , and the continuum, respectively (Figure 4.1). We took three frames for each band with three minutes exposure time per frame for an epoch. The targets were planned to be observed every night by the remote observation system, however, the weather condition and the Moon phase made the observation cadence to be 4.8 - 6.8 days. The total observation period (from the start to the end of the run) is 747 - 842 days with 60 - 114 epochs for these targets. During these periods, the observations were stopped for a period of about 150 days each year due to the visibility of the target. We denote the period of the observing season when the monitoring was possible as  $t_{obs}$ . Therefore,  $t_{obs}$  is about 210 days. After  $t_{obs}$ , the monitoring is stopped for 150 days, and the monitoring is resumed for another  $t_{obs}$  period and so on. For the observations, the seeing condition varied from 2''0 to 5''0. We summarize the sample and the observation in Table 4.1.

## 4.3 Photometry

The bias subtraction, dark subtraction, and flat-fielding were done by an automatic pipeline right after the observations as described in Kim et al. (2019b). We derived the astrometric solutions using Astrometry.net (Lang et al. 2010) using bright stars around the targets ( $< 15$  arcmin) as photometry references, finding an rms accuracy of  $\sim 0''.3$ . SWarp (Bertin et al. 2002) was used to combine three frames (total 9 minutes exposure time) to a single epoch to increase S/N of each epoch data.

To measure fluxes, we followed the same photometry process with Kim et al.

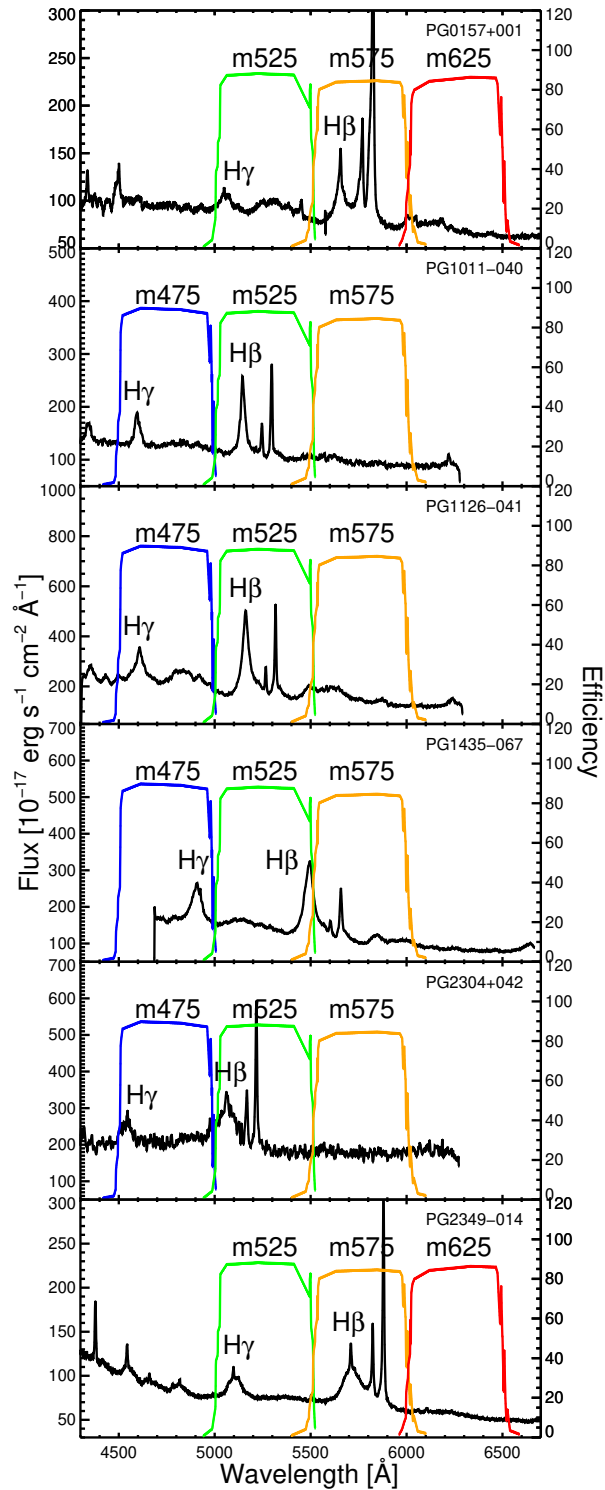


**Figure 4.1.** The medium-band filter transmission curves on the spectra six targets show how these filters sample the continuum, H $\beta$ , and H $\gamma$  emission lines. The spectra of PG 0159+001 and PG 2349-014 are from Abolfathi et al. (2018) and the others are from Boroson & Green (1992).

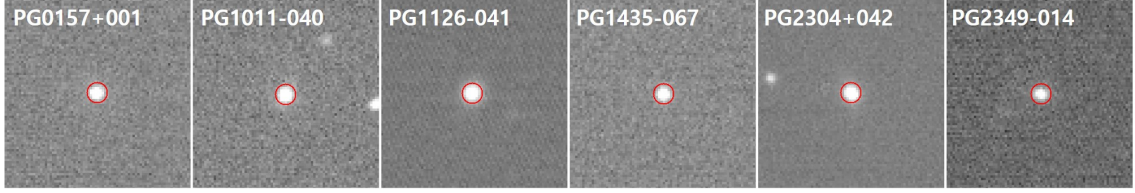


**Figure 4.2.** The first epoch image of the six AGNs in the central medium-band which traces  $H\beta$  emission line. The red circle is  $8''$  diameter aperture used for photometry.

(2019b). To avoid systematic biases from different seeing conditions in aperture photometry, we employed the image convolution. All the images were convolved with a Gaussian kernel to have similar seeing conditions ( $4''$  -  $6''$ ) over all epochs. We used  $8''$  diameter aperture magnitude from SExtractor (Bertin & Arnouts 1996) to extract flux of AGNs and objects in the fields. The aperture size is approximately 1.5 times the seeing FWHM of convolved images which is expected to maximize the signal to noise ratio. Figure 4.2 shows the first epoch image of the six AGNs in central medium-band (band2) with the aperture size in red circle.

To measure the magnitude zero-points, we used the AAVSO Photometric All-Sky Survey (APASS) catalog (Henden et al. 2016). First, we downloaded the APASS catalog with sources within  $10'$  distance from the target AGN. Because the catalog only includes broad-band magnitudes, we needed to derive medium-band magnitudes. We matched the  $B$ ,  $V$ ,  $g$ ,  $r$ , and  $i$  magnitudes in the catalog with the stellar spectral energy distribution (SED) templates of Gunn & Stryker (1983) and selected sources with the minimum reduced  $\chi^2$  as the best fit SED of the reference star. Then, we convolved the best fit SEDs with transmission curves of each medium-band to get the medium-band magnitudes of the reference star. The zero-point was derived for each reference star, and the zero-points were averaged to provide the magnitude zero-points of each image. The number of the reference stars are 10 - 30 and the rms errors of the zero-points are 0.01 - 0.05 mag.

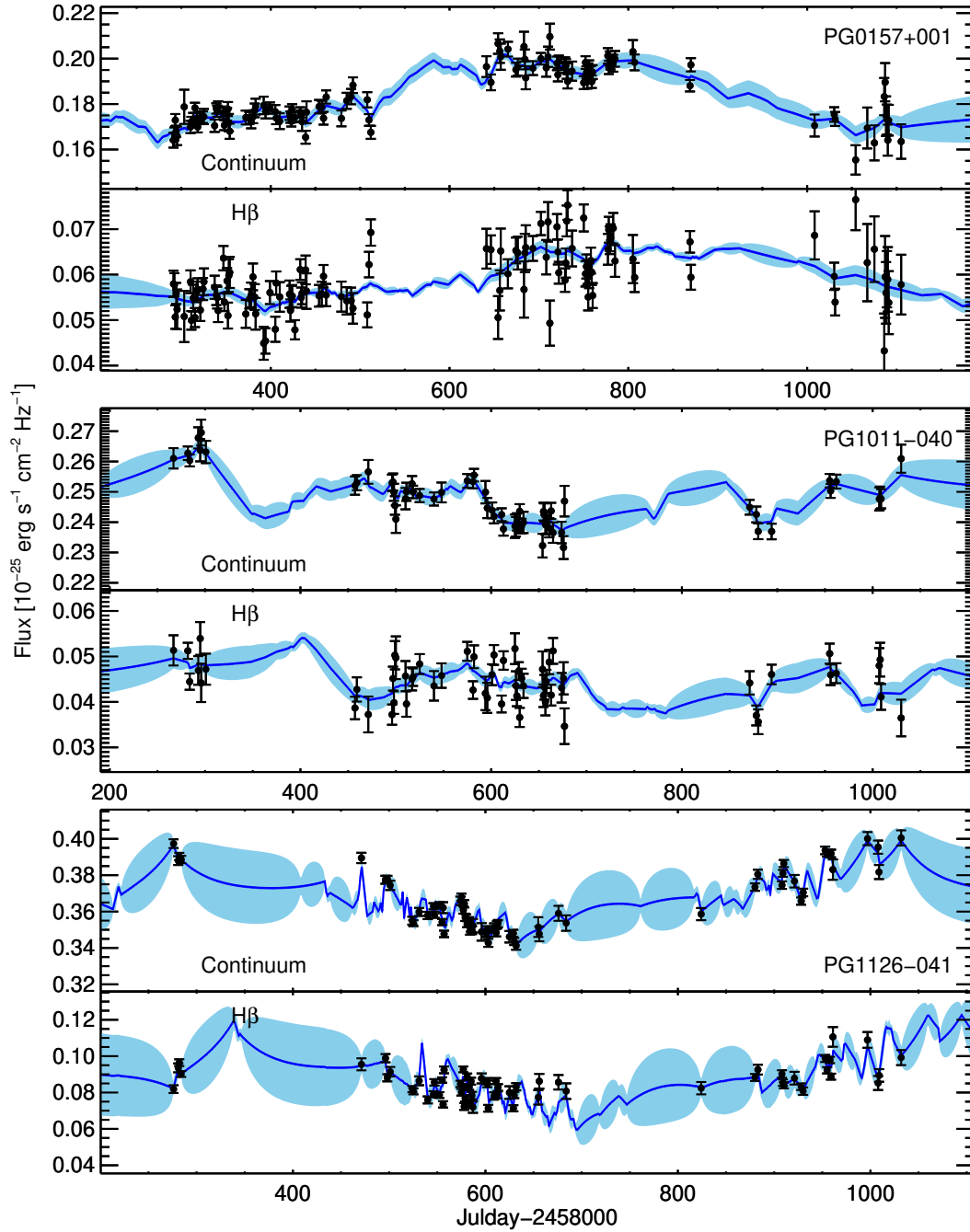
We used differential photometry to trace temporal flux variations more accurately (Kim et al. 2018). We selected comparison stars which are bright ( $< 17$  mag) and

Table 4.2. Variability of targets

Name	Excess Variability [mag]			p-to-p Variability [mag]			Reduced $\chi^2$		
	band1	band2	band3	band1	band2	band3	band1	band2	band3
PG 0157+001	0.08	0.07	0.08	0.34	0.24	0.34	39.1	32.1	21.8
PG 1011-040	0.05	0.04	0.04	0.22	0.17	0.17	23.9	18.4	14.6
PG 1126-041	0.06	0.05	0.05	0.19	0.22	0.19	151.6	133.6	93.7
PG 1435-067	0.12	0.11	0.10	0.54	0.45	0.39	87.3	79.0	48.4
PG 2304+042	0.20	0.15	0.14	0.98	0.73	0.70	113.9	91.5	74.7
PG 2349-014	0.19	0.14	0.16	0.75	0.54	0.99	73.5	59.0	44.9

located close to the AGNs ( $< 10'$ ). The differential photometry was applied to each comparison star itself. The magnitude of a comparison star was subtracted by magnitudes of the other comparison stars and we calculated the standard deviation of its differential light-curve. We removed comparison stars which have magnitude variation greater than 0.01 mag from the list of the comparison stars. The final number of non-variable comparison stars is 2 - 4 depending on targets. We compared the light-curves of non-variable comparison stars and the light-curves of AGNs to make differential light-curves of AGNs.

With the differential light-curves of three medium-bands, we derived light-curves of  $H\beta$ ,  $H\gamma$ , and the continuum in the following way. The continuum light-curve was constructed using the band3 data. From the spectra of AGNs (Figure 4.1), we measured continuum slopes with linear fitting, assuming a power law for the continuum shape. The band3 data are extrapolated to the band1 and band2 using the continuum slopes from the spectra, and these values are chosen as the continuum fluxes at the corresponding bands. By subtracting of the continua from the band2 and band1 fluxes, we obtained the  $H\beta$  and  $H\gamma$  fluxes and their light-curves. All the light-curves are shown in Figures 4.3, 4.4, 4.5, and 4.6 with best-fit light-curve models from JAVELIN (see Section 4.5).



**Figure 4.3.** The light-curves of the continuum (upper panels) and H $\beta$  (lower panels) of all AGNs. The blue solid line shows the best-fit light-curve models from JAVELIN.

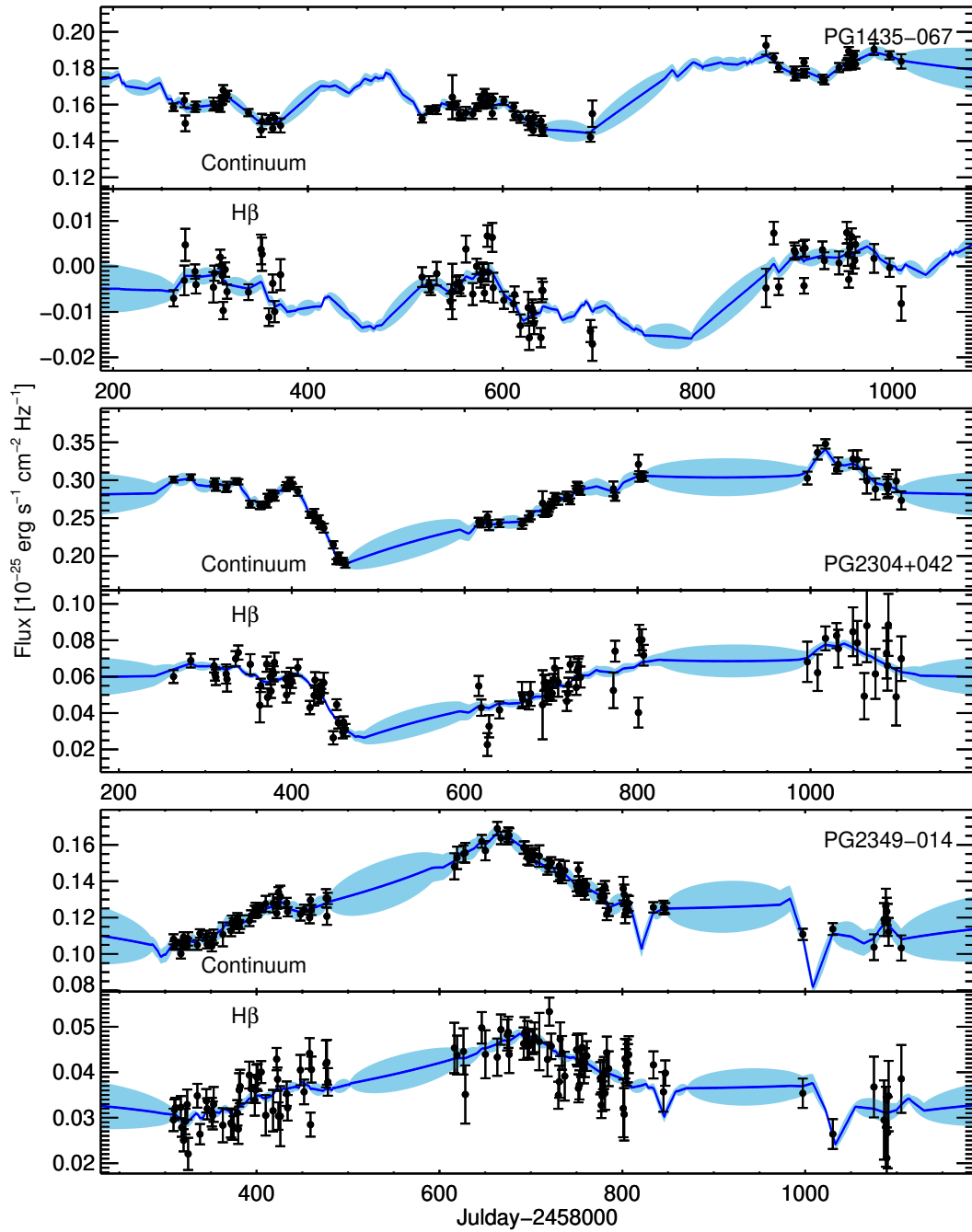
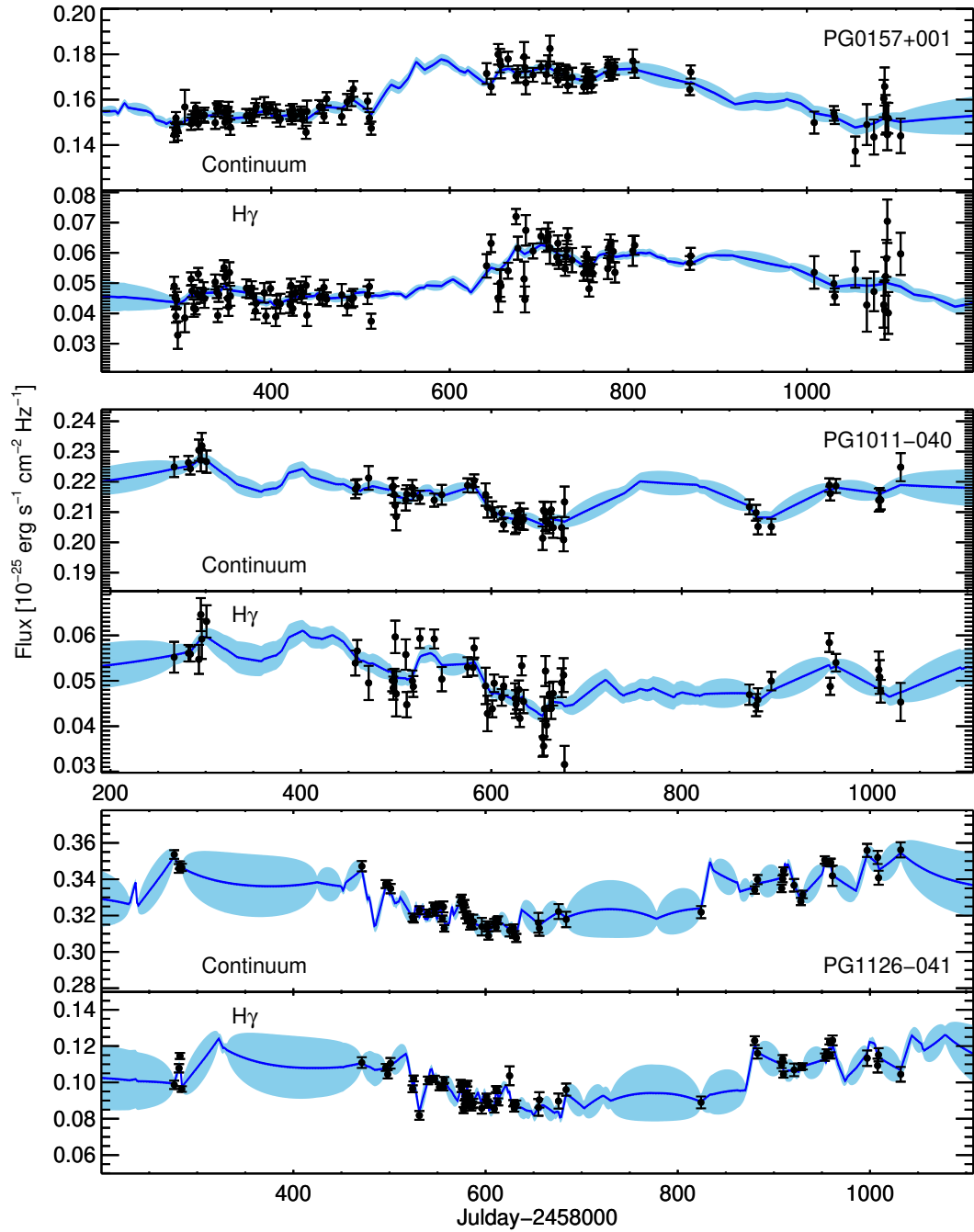


Figure 4.4. Continued of Figure 4.3



**Figure 4.5.** The light-curves of the continuum (upper panels) and H $\gamma$  (lower panels) of all AGNs. The blue solid line shows the best-fit light-curve models from JAVELIN.

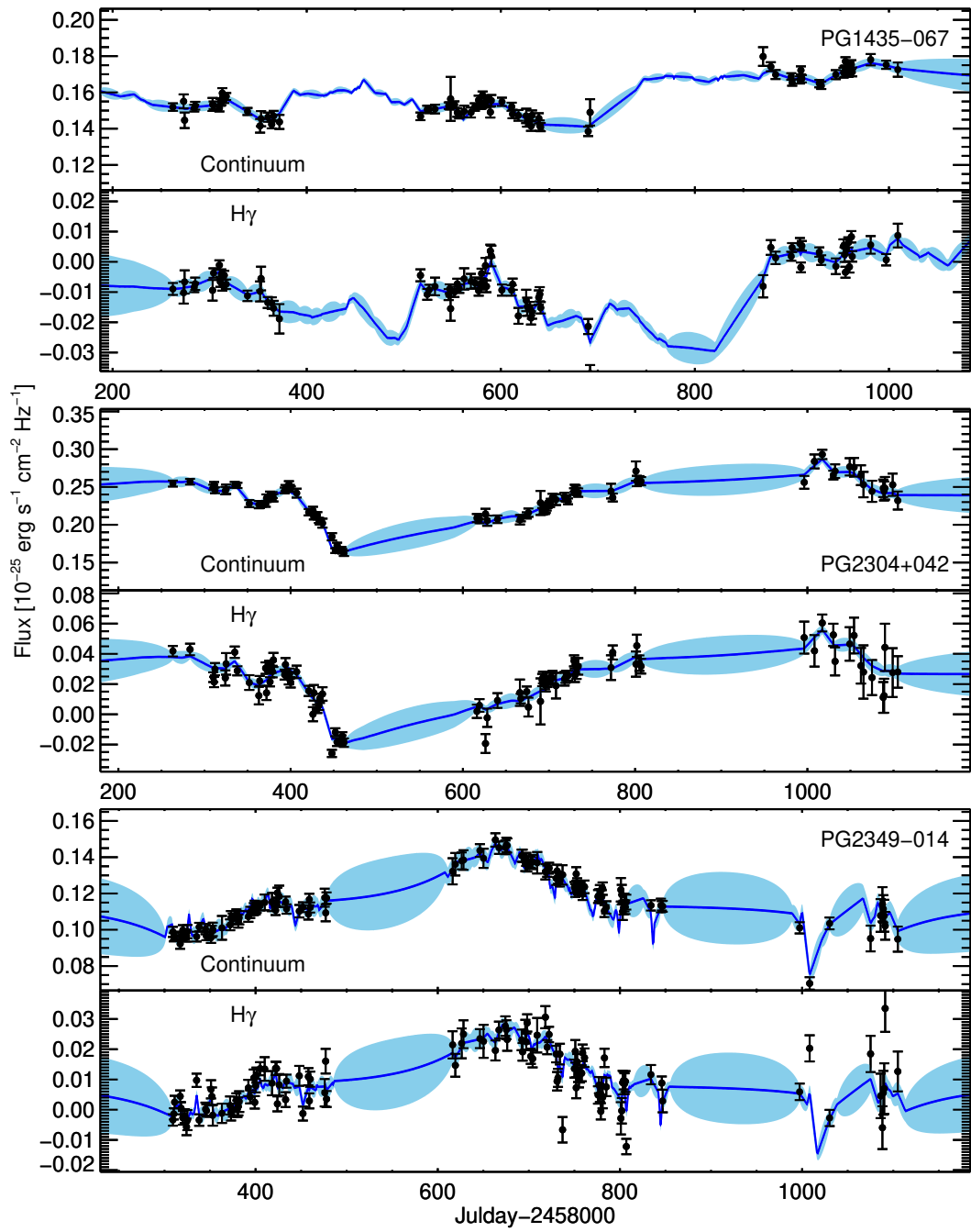


Figure 4.6. Continued of Figure 4.5

## 4.4 Variability

For measuring the time lag, AGNs should be variable for our monitoring. We performed the  $\chi^2$  test (Kim et al. 2018) to quantify the variability of the PG quasars. Here,  $\chi^2$  is defined by

$$\chi^2 = \sum_i \frac{(m_i - \langle m_i \rangle)^2}{(\sigma_i)^2}, \quad (4.1)$$

where  $i$  is the index for the epoch of observation,  $m_i$ ,  $\langle m_i \rangle$ , and  $\sigma_i$  are the magnitude, the average magnitude, and magnitude error at the epoch  $i$ , respectively.

Also, we used the excess variability ( $\sigma_{excess}$ ) as a variability indicator which is defined as

$$\sigma_{excess} = \sqrt{m_{rms}^2 - \langle \sigma_i \rangle^2}, \quad (4.2)$$

where  $m_{rms}$  is the rms of the magnitudes in the light-curve, and  $\langle \sigma_i \rangle$  is average magnitude error. The excess variability shows 0.04 - 0.2 mag for our sample. Another variability indicator is the peak-to-peak variability which is the gap between maximum and minimum magnitudes. It is 0.17 - 0.99 mag for our sample. Table 4.2 lists reduced  $\chi^2$ , excess variability, and peak-to-peak variability of all AGNs in three medium-bands. All the variability measures show that our sample AGNs are variable. In particular, the  $\chi^2$  test concludes that all AGNs are variable in all the bands at 99.9% confidence.

## 4.5 Time Lag

We measured the time lag between the continuum and BEL light-curves using the JAVELIN software (Zu et al. 2011, 2016) and the interpolated cross correlation function (ICCF; e.g., Peterson et al. 1998 and Sun et al. 2018). The JAVELIN models the continuum light-curve with a damped random walk model which is suitable for AGN variability (Kelly et al. 2009). Then the modeled continuum is scaled, smoothed and displaced to the emission line light-curve repeating million times by the Markov chain Monte Carlo method. As a result, the JAVELIN gives the time lag distribution of the light-curves. We defined the time at the strongest peak of the time lag distribution as

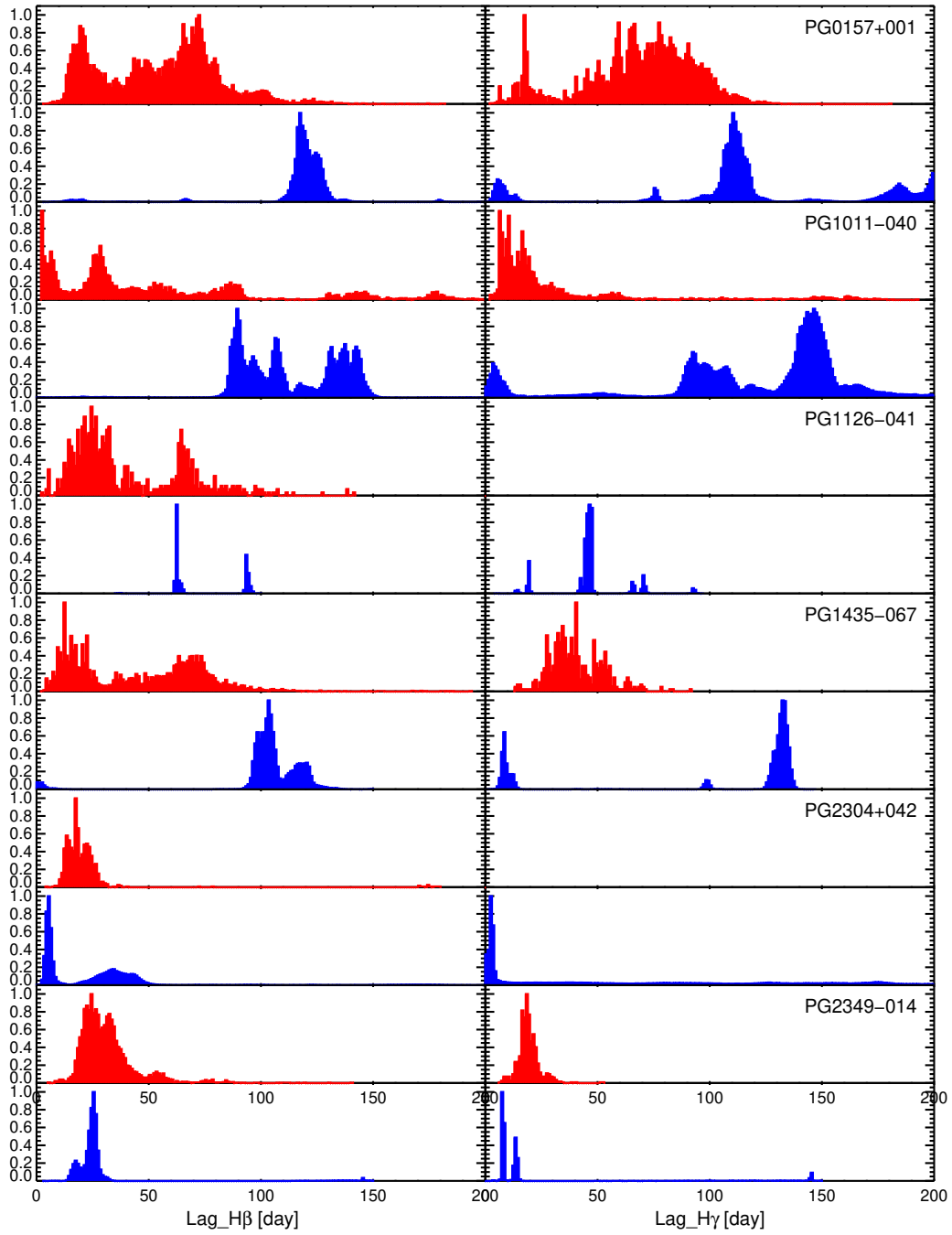


**Figure 4.7.** The histogram of the time lags in the observed frame (right panels) for six AGNs, where the time lags are estimated by the JAVELIN (the blue histogram) and the ICCF (the red histogram).

the time lag and the  $1\sigma$  uncertainty is defined as the time lag range from the peak that includes 68% of the distribution.

As a traditional method of measuring the time lag, we employed the ICCF which cross-correlate interpolated light-curves of the continuum and BEL and finds correlation coefficient  $r(\tau)$ . A specific process follows Peterson et al. (2004) that the time lag is determined as the centroid of the cross-correlation function with a criteria of  $r(\tau) \geq 0.8r_{max}$  and the uncertainty is found from 10,000 times of Monte Carlo realization of flux randomization and random subset sampling (FR/RSS).

The time lag distributions are shown in Figure 4.7 and the derived time lags for H $\beta$  in the rest frame are given in Table 4.3. We explain the time lag measurement in the observed frame for the individual objects below.

**PG 0157+001** The target shows clear peaks in the JAVELIN lag distributions of two BELs. The time lags are  $117.3^{+8.8}_{-1.5}$  days and  $110.5^{+13.2}_{-71.7}$  days for H $\beta$  and H $\gamma$ , respectively. However, the ICCF shows wider distributions with the time lags of  $58.1^{+19.8}_{-36.2}$  and  $71.8^{+20.4}_{-26.7}$  for H $\beta$  and H $\gamma$ , respectively. This result reflects the difficulty in identifying key features in the light curves that could be used for the time lag estimation (Figure 4.4). Both the continuum and BEL light curves clearly show the up and down of the light curves. In particular, a significant mismatch between the two light curves suggests a long time lag of  $\sim 100$  days, although the determination of the lag is hampered by the lack of data points between monitoring periods. We expect that the time lag determination would have been more easily done if there were data points between the monitoring observation periods.

**PG 1011-040** The JAVELIN distributions give the time lags of  $89.7^{+49.2}_{-11.7}$  days and  $146.7^{+4.6}_{-56.8}$  days for H $\beta$  and H $\gamma$ . However, both distributions are bimodal with peaks at two parts around  $\sim 90$  days and  $\sim 140$  days. The ICCF give time lags at  $33.0^{+57.0}_{-25.9}$  and  $16.8^{+25.5}_{-8.1}$  for H $\beta$  and H $\gamma$ , respectively. Like PG 0157+001, the contradictory results reflect the insufficient sampling of the light curves. Additionally, the variability of this target is the smallest among the six quasars during our observation run, and therefore the small variability also contributed to the difficulty in determining the time lag.

Nevertheless, a sharp decline in the continuum light curve at 600 days is not observable in the BEL light curve, but the behavior should have been observable in the BEL light curve if the time lag was less than 100 days. Hence, we prefer a solution with a time lag  $\gtrsim 100$  days of JAVELIN.

**PG 1126-041** The time lags from JAVELIN are found as  $62.3_{-0.1}^{+31.6}$  days and  $45.3_{-2.0}^{+2.4}$  days for  $H\beta$  and  $H\gamma$  with clear peaks. However, the variability of this quasar is quite lower than the others and the best-fit light-curves seem to be overfitted than others. The ICCF shows the time lag of  $30.9_{-12.2}^{+37.0}$  for  $H\beta$ , but the time lag distribution from ICCF has a bimodal distribution with peaks at 25 days and 65 days. The latter coincides with the time lag from JAVELIN. The results from the two methods suggest that this quasar has a time lag of about 60 days or a bit shorter. For  $H\gamma$ , null result was obtained with ICCF due to noisy light curves. The time lag of  $\sim 60$  days gets additional support from visual inspection of the light curves, a rapidly declining continuum fluxes at 300 days is not visible in the BEL light curve, suggesting that the time lag must be larger than 50 days or so.

**PG 1435-067** The JAVELIN time lag histograms show clear peaks, but also show a secondary peak. Especially,  $H\gamma$  has a second peak at  $\sim 10$  days and it causes very high time lag uncertainty. The estimated time lags are  $103.7_{-5.1}^{+13.7}$  days and  $133.3_{-123.8}^{+0.8}$  days for  $H\beta$  and  $H\gamma$ , respectively. The ICCF distributions are broader than JAVELIN and the time lags are  $44.4_{-30.7}^{+28.8}$  and  $38.7_{-9.7}^{+14.1}$  for  $H\beta$  and  $H\gamma$ , respectively. The visual inspection of the light curves indicates that the light curve behaviors of the 870 - 1000 days data prefer a time lag of about 100 days, while light curve shapes at the 500 to 700 days data could be interpreted to show a time lag much shorter than 100 days. More complete coverage of the light curve would have helped reduce the difference in the time lag estimates. Given a high luminosity of this object, we suggest that the longer time lag measurement value is plausible.

**PG2304+042** The JAVELIN time lag distributions show the time lags of  $5.3_{-0.6}^{+34.9}$  days and  $2.7_{-0.2}^{+142.5}$  days for  $H\beta$  and  $H\gamma$ , respectively. And the ICCF shows the time lags of  $18.5_{-4.7}^{+5.9}$  days for  $H\beta$ , but the time lag was not measurable for  $H\gamma$ . Although this

Table 4.3. Time lag and black hole mass of monitored AGNs

Name	$\log \lambda L_{\lambda,5100}$ [erg/s]	FWMM [km/s]	Time Lag [JAVELIN]		Time Lag [ICCF]		$M_{\text{BH}}$ [ $10^6 M_{\odot}$ ]
			H $\beta$ [day]	H $\gamma$ [day]	H $\beta$ [day]	H $\gamma$ [day]	
PG 0157+001	44.781 <sup>a</sup>	2406 $\pm$ 50 <sup>a</sup>	101.1 <sup>+7.6</sup> <sub>-1.3</sub>	95.3 <sup>+11.4</sup> <sub>-61.8</sub>	50.1 <sup>+17.6</sup> <sub>-31.1</sub>	61.9 <sup>+17.6</sup> <sub>-23.0</sub>	127.8 <sup>+36.9</sup> <sub>-35.7</sub>
PG 1011-040	43.632 <sup>b</sup>	1320 $\pm$ 128 <sup>c</sup>	84.8 <sup>+46.5</sup> <sub>-11.1</sub>	138.7 <sup>+4.3</sup> <sub>-53.7</sub>	30.4 <sup>+53.8</sup> <sub>-23.0</sub>	15.9 <sup>+24.1</sup> <sub>-7.7</sub>	32.2 <sup>+20.7</sup> <sub>-11.6</sub>
PG 1126-041	43.819 <sup>b</sup>	2150 $\pm$ 107 <sup>c</sup>	58.7 <sup>+29.8</sup> <sub>-0.1</sub>	42.7 <sup>+2.3</sup> <sub>-1.9</sub>	30.0 <sup>+35.9</sup> <sub>-11.8</sub>		59.2 <sup>+34.7</sup> <sub>-17.4</sub>
PG 1435-067	44.388 <sup>b</sup>	3180 $\pm$ 89 <sup>c</sup>	91.7 <sup>+12.1</sup> <sub>-4.5</sub>	118.0 <sup>+0.7</sup> <sub>-109.6</sub>	40.8 <sup>+23.8</sup> <sub>-28.6</sub>	34.2 <sup>+12.4</sup> <sub>-8.6</sub>	202.6 <sup>+63.1</sup> <sub>-58.0</sub>
PG 2304+042	43.592 <sup>b</sup>	10120 $\pm$ 809 <sup>c</sup>	5.1 <sup>+33.5</sup> <sub>-0.6</sub>	2.6 <sup>+136.8</sup> <sub>-0.2</sub>	17.7 <sup>+5.8</sup> <sub>-4.4</sub>		113.7 <sup>+750.0</sup> <sub>-38.5</sub>
PG 2349-014	44.768 <sup>a</sup>	5745 $\pm$ 212 <sup>a</sup>	21.6 <sup>+1.2</sup> <sub>-5.1</sub>	6.8 <sup>+5.0</sup> <sub>-0.3</sub>	24.8 <sup>+8.5</sup> <sub>-6.1</sub>	16.1 <sup>+3.4</sup> <sub>-2.5</sub>	155.8 <sup>+45.4</sup> <sub>-57.9</sub>

<sup>a</sup>Shen et al. 2011<sup>b</sup>Lani et al. 2017<sup>c</sup>Boroson & Green 1992

quasar shows the largest variability among the six targets, its time lag uncertainties are relatively high. The cadence of this target is 5.6 days which is larger than both time lags, the uncertainty becomes higher (Kim et al. 2019b). However, a close examination of the light curves shows that the light curves in all three monitoring periods change similarly with little time lags. Therefore, the time lag must be small ( $\lesssim 10$  days). A shorter cadence monitoring must have allowed us to measure the time lag more accurately.

**PG 2349-014** This target is another high variability source and shows time lag distributions with sharp peaks in both JAVELIN and ICCF. JAVELIN gives a H $\beta$  time lag of  $25.3_{-6.0}^{+1.4}$  days and a H $\gamma$  time lag of  $7.9_{-0.3}^{+5.9}$  days and ICCF gives  $28.9_{-7.2}^{+10.3}$  days and  $18.8_{-2.9}^{+4.0}$  days for H $\beta$  and H $\gamma$ , respectively. The light curve shows a clear triangle shaped peak in both continuum and BEL light curves, which helped us to identify the time lag with high confidence.

We compare the time lags of H $\beta$  from JAVELIN and ICCF also including the data from Kim et al. (2019b) in Figure 4.8. For the Kim et al. (2019b) data, we derived the ICCF time lag using the same procedure as described here. The two methods are consistent within  $2\sigma$  level, but the results deviate for longer time lags (lag > 50 days).

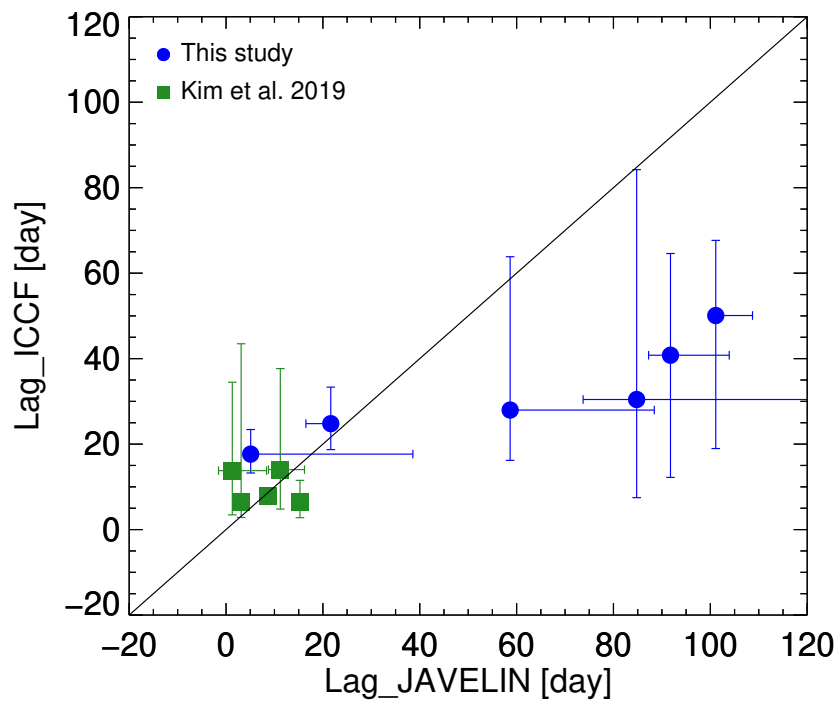


**Figure 4.8.** Comparison between the time lags derived from JAVELIN and ICCF. Results of this Chapter and Kim et al. (2019b) are shown in blue circles and green squares, respectively.

Also, the uncertainties of the JAVELIN results are smaller than the ICCF results and the ICCF cannot find the time lags of  $H\gamma$  for two targets. These trends are also found in Sloan Digital Sky Survey RM Project (SDSS-RM) studies (Grier et al. 2017, 2019), although less significant than found here. Also, a simulation study by Li et al. (2019) supports the preference of the JAVELIN over the ICCF which the JAVELIN shows high accuracy and less biased results. Our visual inspection of the light curves also prefer the JAVELIN results over the ICCF results (e.g., PG 2304+042). Therefore, we selected the time lags of the JAVELIN as our primary results and the discussion below.

## 4.6 Discussion

### 4.6.1 $H\beta$ and $H\gamma$ time lag comparison

Previous studies compared time lags of the Balmer lines and found that the time lag is proportional to the wavelength of BEL (Kaspi et al. 2000; Bentz et al. 2010; Grier et al. 2017). In the theoretical prediction of the photoionization in BEL, the optical depth in BLR depends on decreasing radial density away from the accretion disk, and it raise longer time lag in longer wavelength (Netzer 1975; Rees 1984; Korista & Goad 2004; Bentz et al. 2010). In our time lag measurements, four of six targets show longer time lag in  $H\beta$  than  $H\gamma$ . The time lag ratio ( $Lag[H\gamma] / Lag[H\beta]$ ) is 0.3 - 1.6 with a weighted mean of all targets as  $0.54 \pm 0.20$ . It is consistent with Bentz et al. (2010) which results in 0.61 for the weighted mean of the time lag ratio.

We compared the time lag uncertainties between  $H\beta$  and  $H\gamma$ . Four quasars show higher uncertainty in  $H\gamma$  and mean uncertainties of time lags are 25.5 and 64.6 for  $H\beta$  and  $H\gamma$ , respectively. It can be explained simply by the weaker line flux of  $H\gamma$  than  $H\beta$ .

### 4.6.2 Time lag uncertainty versus observational parameters

We examined if the time lag uncertainty of  $H\beta$  can be predicted with key observational parameters such as S/N of the light curve data points, excess variability ( $\sigma_{excess}$ ), the ratios of the observation intervals and the time lag ( $t_{lag}/\Delta t$ ), a contiguous monitoring

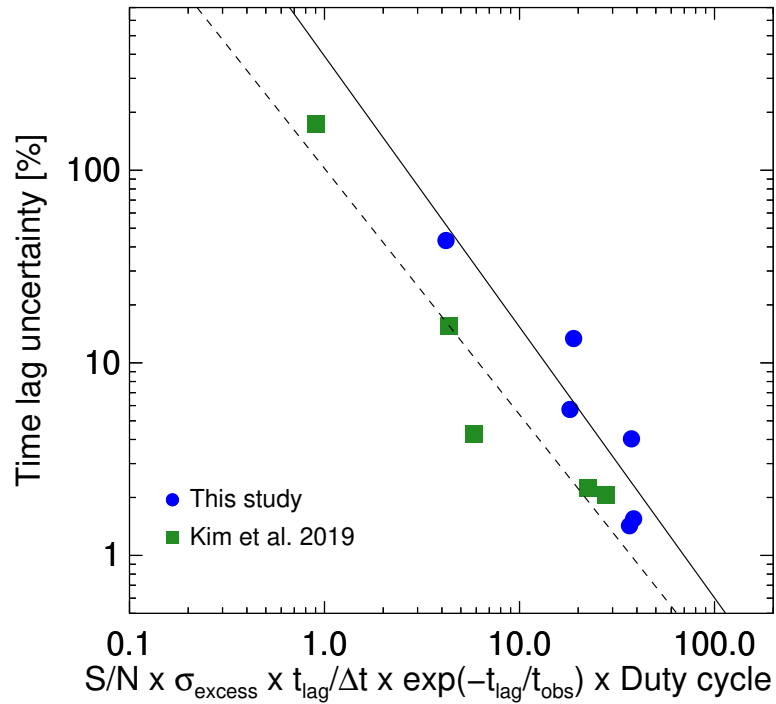


**Figure 4.9.** Correlation of the time lag uncertainties of H $\beta$  and H $\alpha$  with S/N,  $\sigma_{\text{excess}}$ ,  $t_{\text{lag}}/\Delta t$ ,  $t_{\text{lag}}/t_{\text{obs}}$ , and duty cycle. The blue circles are the results of H $\beta$  in this study and the green squares are the results of H $\alpha$  in Kim et al. (2019b). It shows an anticorrelation with a slope of -1.40 and -1.28 for the PG quasars in this study and the AGNs in Kim et al. (2019b), respectively.

period ( $t_{obs}$ ), and the duty cycle of the monitoring. In our previous work (Kim et al. 2019b), we showed that the time lag uncertainty becomes smaller as the S/N,  $\sigma_{excess}$ , and  $t_{lag}/\Delta t$  increases. In the previous work,  $t_{lag}$  was much shorter than the observational period (more than a factor of 10), and there was no extended interruption in monitoring observations.

However, the monitoring observations in this work have long time coverage gaps in between, that makes the time lag measurement difficult. Furthermore,  $t_{lag}$  becomes comparable to  $t_{obs}$ , while in an ideal condition, we want  $t_{obs} > t_{lag}$ .

Therefore, we introduced two additional factors that influence the time lag uncertainty. One is related to the ratio of  $t_{lag}/t_{obs}$ , where we want this factor to approach 1 as  $t_{lag}/t_{obs}$  goes to 0, and 0 as  $t_{lag}/t_{obs}$  becomes larger (if  $t_{lag}$  is much longer than  $t_{obs}$ , we cannot determine the time lag). Hence, we introduce a factor of  $\exp(-t_{lag}/t_{obs})$  to implement this dependence.

Another factor is introduced to take the gap in the light curve coverage. If the time gaps are too long, it becomes more difficult to measure  $t_{lag}$ . This factor is represented by the duty cycle, which is defined as the ratio of contiguous observation periods  $t_{obs}$  to the total observation period. For PG quasars, we performed the monitoring observation for about 210 days per year, and thus the duty cycle is  $210/365$  days  $\sim 0.57$ .

In Figure 4.9, we show a modified version of Figure 3.8 with the additional factors. Here, the  $t_{lag}$  uncertainty is defined as the geometric mean of the two error bars on  $t_{lag}$  to the  $+-$  directions. We also plot AGNs from Kim et al. (2019b), approximating the duty cycle to 1. It shows an anticorrelation of the time lag uncertainty with the multiplications of S/N,  $\sigma_{excess}$ ,  $t_{lag}/\Delta t$ ,  $\exp(-t_{lag}/t_{obs})$ , and the duty cycle as expected and both the Kim et al. (2019b) AGNs and the PG quasars in this study lie on nearly on a single line.

### 4.6.3 Comparison with the known AGN correlations

We plotted our RM measurements on the BLR size and the AGN luminosity (R-L) relation with the result of Bentz et al. (2013) in Figure 4.10. Here, luminosity at 5100

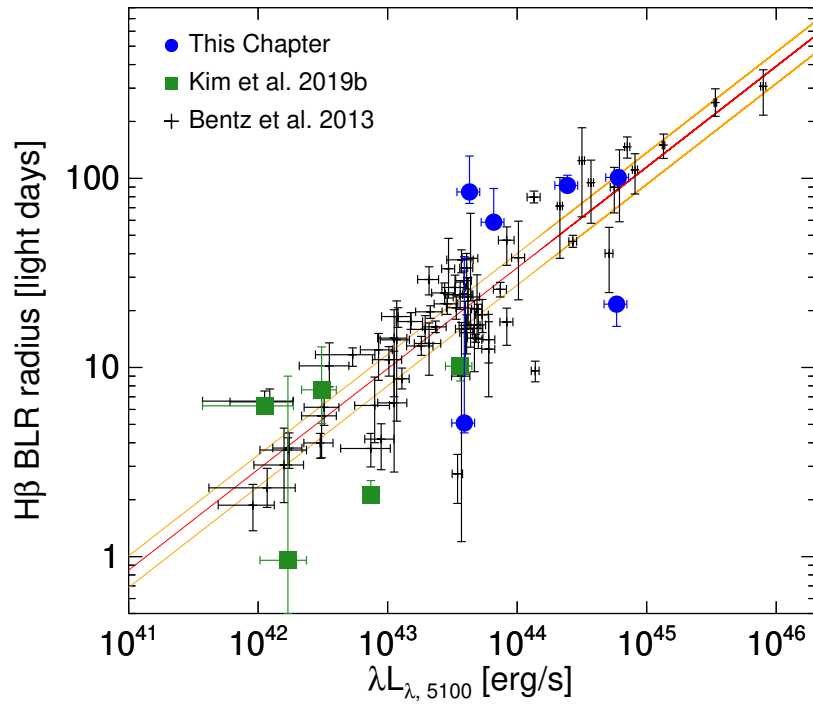


**Figure 4.10.** BLR radius of H $\beta$  emission line and 5100 Å luminosity (R-L) relationship. Results of this Chapter, Kim et al. (2019b) and Bentz et al. (2013) are shown in blue circles, green squares, and black crosses, respectively. The red solid line is best-fit relation in Bentz et al. (2013) with a scatter in orange solid lines.

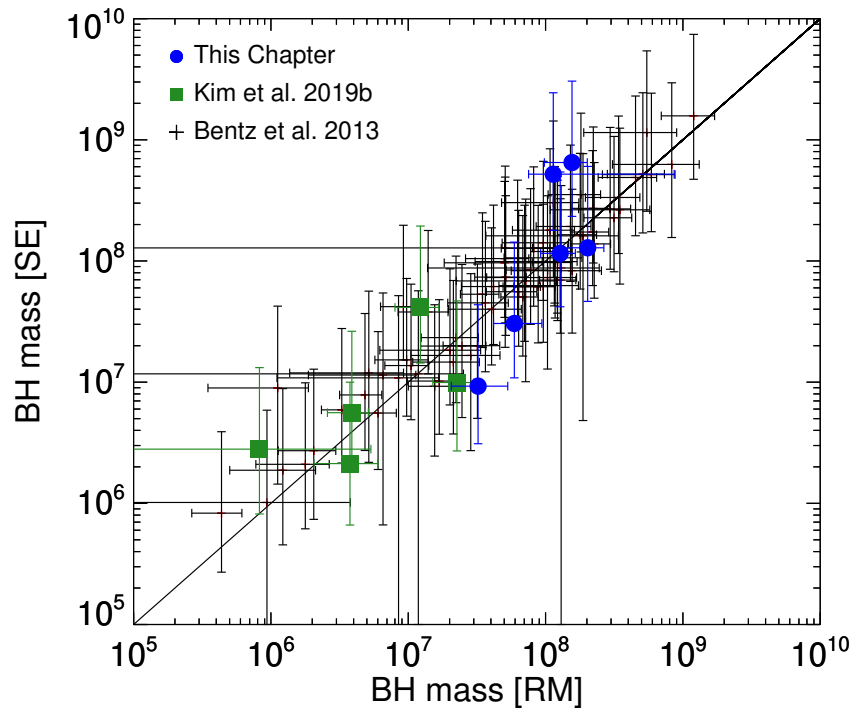


**Figure 4.11.** Comparison between black hole mass measurements; reverberation mapping and single epoch method. The blue circles indicate measurements of this Chapter, the green squares come from Kim et al. (2019b), and the black crosses show the results of Bentz et al. (2013).

$\text{\AA}$  is found in Shen et al. 2011 and Lani et al. 2017. We added the  $\text{H}\alpha$  RM results from our previous study (Kim et al. 2019b) for low luminosity measurements of the photometric RM which the time lags are scaled using a weighted mean ratio of the time lags ( $Lag[\text{H}\alpha] / Lag[\text{H}\beta] = 1.54$ ) in Bentz et al. (2010). To compare the result of the R-L relation, we measured the intrinsic scatter in the same way as Bentz et al. (2013) that uses LINMIX\_ERR routine in IDL. Resulting intrinsic scatter is  $0.37 \pm 0.16$  dex for our result, while Bentz et al. (2013) shows  $0.19 \pm 0.02$  dex. Although the larger scatter, it is comparable to the intrinsic scatter of the black hole mass and stellar velocity dispersion ( $M_{\text{BH}} - \sigma_*$ ) relationship of  $\sim 0.4$  dex (McConnell & Ma 2013; Woo et al. 2015). The possible source of larger scatter is the limitation of the medium-band observations which have contaminations from the continuum and other narrow lines. Another possible source of error is the variability of our samples. If the 5100  $\text{\AA}$  luminosity has varied after the observations of Shen et al. 2011 and Lani et al. 2017, positions of our samples on the R-L plane will change. However, this effect is limited because only 10 - 20% variability is expected in year timescale (Uttley & Casella 2014; Gaskell & Klimek 2003). Although the scatter is higher than spectroscopic RM, photometric RM is advantageous if we observe a large number of quasars simultaneously using a wide-field telescope (Kim et al. 2019b).

We measured  $M_{\text{BH}}$  using the time lags and the widths of BEL for both this study and Kim et al. (2019b). For the line width of  $\text{H}\beta$ , we use FWHM in Boroson & Green (1992) and Shen et al. (2011). The scale factor of virial product for FWHM,  $f = 1.12$  is applied from Woo et al. (2015). The result of  $M_{\text{BH}}$  measurements are shown in Table 4.3. For comparison, we compute  $M_{\text{BH}}$  from a single-epoch measurement using  $\text{H}\beta$  of Vestergaard & Peterson (2006). In the case of  $\text{H}\alpha$  targets of Kim et al. (2019b), we adopt the relation between  $\text{FWHM}_{\text{H}\beta}$  and  $\text{FWHM}_{\text{H}\alpha}$  in Greene & Ho (2005) to transform  $\text{H}\alpha$  to  $\text{H}\beta$ . Also, we included intrinsic scatter, 0.43 dex, of single-epoch measurements to the uncertainties of  $M_{\text{BH}}$ . Comparison of  $M_{\text{BH}}$  from RM and the single epoch method (Bentz et al. 2013) is shown in Figure 4.11. We find that the two mass measurements agree with each other within uncertainty. We point out that the BEL widths we used are

measured from a few years ago, and can be different from the values for our observation run because of variability in the BEL profile (Wang et al. 2020).

## 4.7 Summary

In this Chapter, we present the photometric RM results of six PG quasars. They have been monitored for 2.0 - 2.3 years by the 0.43 m LSGT telescope. We covered  $H\beta$  and  $H\gamma$  emission lines and the continuum using three medium-band filters which effectively traced the  $H\alpha$  emission line in the previous study (Kim et al. 2019b). The light-curves of all the objects show clear variabilities, and the time lags between two BELs and the continuum are measured using JAVELIN. We compared our time lag measurements with the known R-L relation. Our medium-band based results show higher intrinsic scatter than previous results based on spectroscopy, but largely agree with the relation. With the measured time lags and BEL FWHM from previous observations, we estimate  $M_{\text{BH}}$ . We find that the  $M_{\text{BH}}$  values of medium-band RM agree with single-epoch measurements of  $M_{\text{BH}}$  from the previous studies. We conclude that the photometric RM is a useful method to measure BLR size and  $M_{\text{BH}}$ . We will continue to monitor other targets with LSGT and apply it using a wide-field telescope for large samples.

## Chapter 5

# GECKO Optical Follow-up Observation of Three Binary Black Hole Merger Events, GW190408\_181802, GW190412, and GW190503\_185404<sup>†</sup>

### 5.1 Introduction

Since the first detection of the binary black hole (BBH) merger event by the Laser Interferometer Gravitational-Wave Observatory (LIGO) Collaboration and Virgo Collaboration (LVC) in 2015 September 14 (Abbott et al. 2016), the reported number of BBH events has been increasing fast, from two in the the Advanced LIGO and Advanced Virgo (LIGO/Virgo) first (O1) observing run, and three in the second (O2) observing run, up to 20 in the first half (O3a) of the third (O3) observing run (Abbott

---

<sup>†</sup>This chapter is a revised version of the article published in *The Astrophysical Journal* in July 2021 (Kim et al. 2021).

et al. 2020a). Gravitational wave (GW) astronomy is now flourishing, with the GW signals providing valuable information on the compact star mergers, such as the masses of the binary compact objects, their approximate distance, and the location in the sky of the event.

The power of GW astronomy was much enhanced when the first electromagnetic-wave (EM) counterpart of a GW event was identified on 2017 August 17 during the LIGO/Virgo O2 run. The GW event, GW170817, was found to be due to a binary neutron star (BNS) merger with 90% localization of  $31 \text{ deg}^2$  and a luminosity distance of 40 Mpc (Abbott et al. 2017a). The combined efforts of the GW and EM observations produced a series of important results, including the first identification (AT2017gfo) of the exact location and the distance to the GW event (Abbott et al. 2017b; Arcavi et al. 2017; Coulter et al. 2017; Lipunov et al. 2017b; Soares-Santos et al. 2017; Tanvir et al. 2017; Valenti et al. 2017), convincing observational evidence for the link between a short gamma-ray bursts (GRB) and a BNS merger (Abbott et al. 2017c; Goldstein et al. 2017; Savchenko et al. 2017), undeniable discovery of a kilonova and the first detailed characterization of such an event (Andreoni et al. 2017; Arcavi et al. 2017; Chornock et al. 2017; Cowperthwaite et al. 2017; Drout et al. 2017; Evans et al. 2017; Haggard et al. 2017; Hallinan et al. 2017; Kasliwal et al. 2017; Margutti et al. 2017; Nicholl et al. 2017; Pian et al. 2017; Smartt et al. 2017; Troja et al. 2017; Utsumi et al. 2017), a glimpse of the BNS merger environment (Im et al. 2017; Tanvir et al. 2017), and the first application of the GW siren method to measure the Hubble constant (Abbott et al. 2017d). In short, this was a monumental event that marked the beginning of multi-messenger astronomy (MMA) using GW and EM observations. If a similar study can be performed for BBH GW events that currently occupy the majority of the detected GW events, it would greatly expand the power of MMA and enhance our knowledge of this previously rarely studied aspect of the universe.

As a result, many follow-up observations have been carried out to find EM counterparts of BBH GW events, yet no EM counterparts have been identified for the BBH events (Cowperthwaite et al. 2016; Morokuma et al. 2016; Smartt et al. 2016a,b; Soares-

Santos et al. 2016; Lipunov et al. 2017a; Stalder et al. 2017; Yoshida et al. 2017; Smith et al. 2019; Doctor et al. 2019; Yang et al. 2019; Herner et al. 2020; Gompertz et al. 2020; Grado et al. 2020; Turpin et al. 2020). There are several reasons for the nondetections. First of all, the strong gravitational force of black holes do not allow debris from the merger to escape, thus prohibiting EM-producing physical processes from occurring (Berger 2014). A few models suggest that an EM counterpart might be produced if, e.g., the BBH merger preferentially happened in the active galactic nucleus (AGN) accretion disk, but the expected strength of EM radiation is weak or very uncertain (Loeb et al. 2016; Perna et al. 2016, 2018; Bartos et al. 2017; de Mink & King 2017; Stone et al. 2017; McKernan et al. 2018). For the O3 run, a candidate of optical counterpart for a BBH merger, GW190521 (Abbott et al. 2020a), is reported as a possible AGN-related transient (Graham et al. 2020). Secondly, the early LIGO/Virgo runs have been hampered by limited detector sensitivities, and as a result, the locations of the events estimated from the GW signals were very uncertain at a level of several hundreds to thousands  $\text{deg}^2$  and their distance estimates were uncertain as well (Abbott et al. 2019). In spite of these daunting challenges identification of BBH-induced GW EM counterparts remains attractive due to its potential for providing unexpected physical processes during the extreme compact merger and the prospects for using BBH merger EM counterparts for a number of MMA applications.

The LIGO/Virgo O3 run provided a unique opportunity to improve the limits of the BBH EM counterpart search. With the improved sensitivity of the GW detectors, the number of GW events increased (36 BBH events) and the localization area was improved as well (514  $\text{deg}^2$ , median of 90% localization area for BBH events<sup>1</sup>). Hence, we organized an EM follow-up observation group in Korea, utilizing a network of telescopes worldwide that were already in use for monitoring nearby galaxies for new transients such as supernova (Intensive Monitoring Survey of Nearby Galaxies, IMSNG; Im et al. 2019). Our EM-follow-up effort was named the Gravitational-wave EM Counterpart Korean Observatory (GECKO; Im et al. 2020; Paek et al. 2021, in preparation). Several

---

<sup>1</sup><https://gracedb.ligo.org>

Table 5.1. Target GW events

Event	Type	Event time [UT]	Initial 90% Area	Initial Distance [Mpc]	GWTC-2 90% Area	GWTC-2 Distance [Mpc]	FAR [yr <sup>-1</sup> ]
GW190408	BBH	2019-04-08 18:18:02	387 deg <sup>2</sup>	1473 ± 358	140 deg <sup>2</sup>	1580 <sup>+400</sup> <sub>-590</sub>	< 7.9 × 10 <sup>-5</sup>
GW190412	BBH	2019-04-12 05:30:44	156 deg <sup>2</sup>	812 ± 194	21 deg <sup>2</sup>	740 <sup>+140</sup> <sub>-170</sub>	< 7.9 × 10 <sup>-5</sup>
GW190503	BBH	2019-05-03 18:54:04	448 deg <sup>2</sup>	412 ± 105	94 deg <sup>2</sup>	1520 <sup>+710</sup> <sub>-660</sub>	< 7.9 × 10 <sup>-5</sup>

Note. — The values are taken from the initial alerts.

of the GECKO facilities have wide-field capabilities (field of view > 1 deg<sup>2</sup>) and are suited for searching EM counterparts over a wide area.

In this Chapter, we present the GECKO optical follow-up observation for the first three BBH merger events in the O3a run, namely GW190408.181802 (hereafter GW190408, for brevity), GW190412, and GW190503.185404 (hereafter GW190503). We focus our attention on the observation made by the Korea Microlensing Telescope Network (KMTNet; Kim et al. 2016a), which is the most sensitive wide-field telescope of GECKO. The description of the KMTNet observation and analysis results will serve as a reference for future EM follow-up attempts. However, observations made by other telescopes are also reported in order to show the capabilities of GECKO facilities. In Section 5.2, we summarize three GW events that are targeted for our optical follow-up observation. Section 5.3 describes the telescopes we used and the observation strategy. Data analysis of the observed images is given in Section 5.4. We report the observation results and transient candidates in Section 5.5. Finally, we discuss the results in Section 5.6 and conclude the Chapter in Section 5.7.

## 5.2 Gravitational Wave Events

Here, we describe the characteristics of three BBH events observed by GECKO in the early phase of the O3 run. We note that our observations were performed using information from the initial alerts (bayestar.fits), and which were updated later in GWTC-2 catalog (Abbott et al. 2020a).

### 5.2.1 GW190408

On 2019 April 8 18:18:02 UT, the first event of LIGO/Virgo O3 run, designated originally as S190408a (LIGO Scientific Collaboration & VIRGO Collaboration 2019a), and later as GW190408 (Abbott et al. 2020a), was detected by the Advanced LIGO and Advanced Virgo GW detectors. This event was classified as a BBH merger with  $> 99\%$  probability. The luminosity distance and the 90% sky localization area were initially reported as  $1473 \pm 358$  Mpc and  $387 \text{ deg}^2$  (Table 5.1). Later, further analysis of the GW data showed a luminosity distance of  $1580_{-590}^{+400}$  Mpc with a redshift of  $0.30_{-0.10}^{+0.06}$ , a 90% credible sky area of  $140 \text{ deg}^2$ , and a false alarm rate (FAR) of  $< 7.9 \times 10^{-5} \text{ yr}^{-1}$  (Abbott et al. 2020a). The BH masses of the compact objects are found to be  $24.5_{-3.4}^{+5.1} M_{\odot}$  and  $18.3_{-3.5}^{+3.2} M_{\odot}$ . The most recent GWTC-2 localization shows that the event happened in the Northern Hemisphere near R.A. = 351.0 deg and decl. = 53.9 deg, but the initial 90% localization area contained a localized region in the Southern Hemisphere (Figure 5.1). Hence, the Southern Hemisphere localization area was observed by the KMTNet.

### 5.2.2 GW190412

GW190412, originally a candidate super-event S190412m, (LIGO Scientific Collaboration & VIRGO Collaboration 2019b), was detected by three GW detectors on 2019 April 12 05:30:44 UT with  $> 99\%$  probability of being a BBH merger. Its 90% credibility area on the sky and the luminosity distance were estimated as  $156 \text{ deg}^2$  and  $812 \pm 194$  Mpc (Table 5.1), respectively. These numbers were updated recently in the GWTC-2 catalog as  $21 \text{ deg}^2$ ,  $740_{-170}^{+140}$  Mpc, and FAR of  $< 7.9 \times 10^{-5} \text{ yr}^{-1}$  (Abbott et al. 2020a). The redshift is given as  $0.15_{-0.03}^{+0.03}$  in the catalog. This was an event of special interest since this was the first BBH merger with definitely asymmetric component masses of  $30.0_{-5.1}^{+4.7} M_{\odot}$  and  $8.3_{-0.9}^{+1.6} M_{\odot}$ , providing valuable information on the black hole spin and revealing evidence for higher harmonics in the signal. The peak of GW event localization area is now estimated to be R.A. = 218.5 deg and decl. = 36.4 deg, but the initial estimates of the GW event location included an extensive region near the equator, therefore this field was observed with GECKO facilities in the Southern

Hemisphere as well (Figure 5.1).

### 5.2.3 GW190503

GW190503 was detected as a candidate event, S190503bf, on 2019 May 3 18:54:04 UT (LIGO Scientific Collaboration & VIRGO Collaboration 2019c). With 96% probability, this event was classified as a BBH merger. Initially, the 90% localization region covered  $448 \text{ deg}^2$  of the sky and the luminosity distance was estimated to be  $412 \pm 105 \text{ Mpc}$  (Table 5.1). The most recent estimate in the GWTC-2 catalog improved the 90% localization estimate to  $94 \text{ deg}^2$ , and the distance estimate to  $1520_{-660}^{+710} \text{ Mpc}$ , and gave a redshift of  $0.29_{-0.11}^{+0.11}$  and a FAR of  $< 7.9 \times 10^{-5} \text{ yr}^{-1}$  (Abbott et al. 2020a). We note that the distance estimate changed significantly from the initial values for this particular event. The BH masses of the binary system are found to be  $42.9_{-7.8}^{+9.2} M_{\odot}$  and  $28.5_{-7.9}^{+7.5} M_{\odot}$  which are rather ordinary among the BBH mergers detected in the LVC runs. The 90% localization area shrunk by a factor of five since the initial estimate, and the most recent estimate only partially overlaps with the initial area. The initial and the most up-to-date location estimates are all in the Southern Hemisphere, and it served as a prime target for the KMTNet follow-up observation.

## 5.3 Observation

### 5.3.1 Telescopes

For the follow-up observation of the GW events, we mainly used the KMTNet (Kim et al. 2016a) which is a network of three identical 1.6 m telescopes with a wide field of view ( $\sim 4 \text{ deg}^2$ ) located at the Cerro Tololo Inter-American Observatory (CTIO), the South African Astronomical Observatory (SAAO), and the Siding Spring Observatory (SSO). The large field of view of the KMTNet enables us to cover the large GW localization area (see Section 5.2.3). Also, the three-site operation makes it possible to perform follow-up observations 24 hrs a day when the target is observable (e.g., Troja et al. 2017; Kim et al. 2018). The KMTNet camera contains four  $9k$  by  $9k$  CCD chips, each

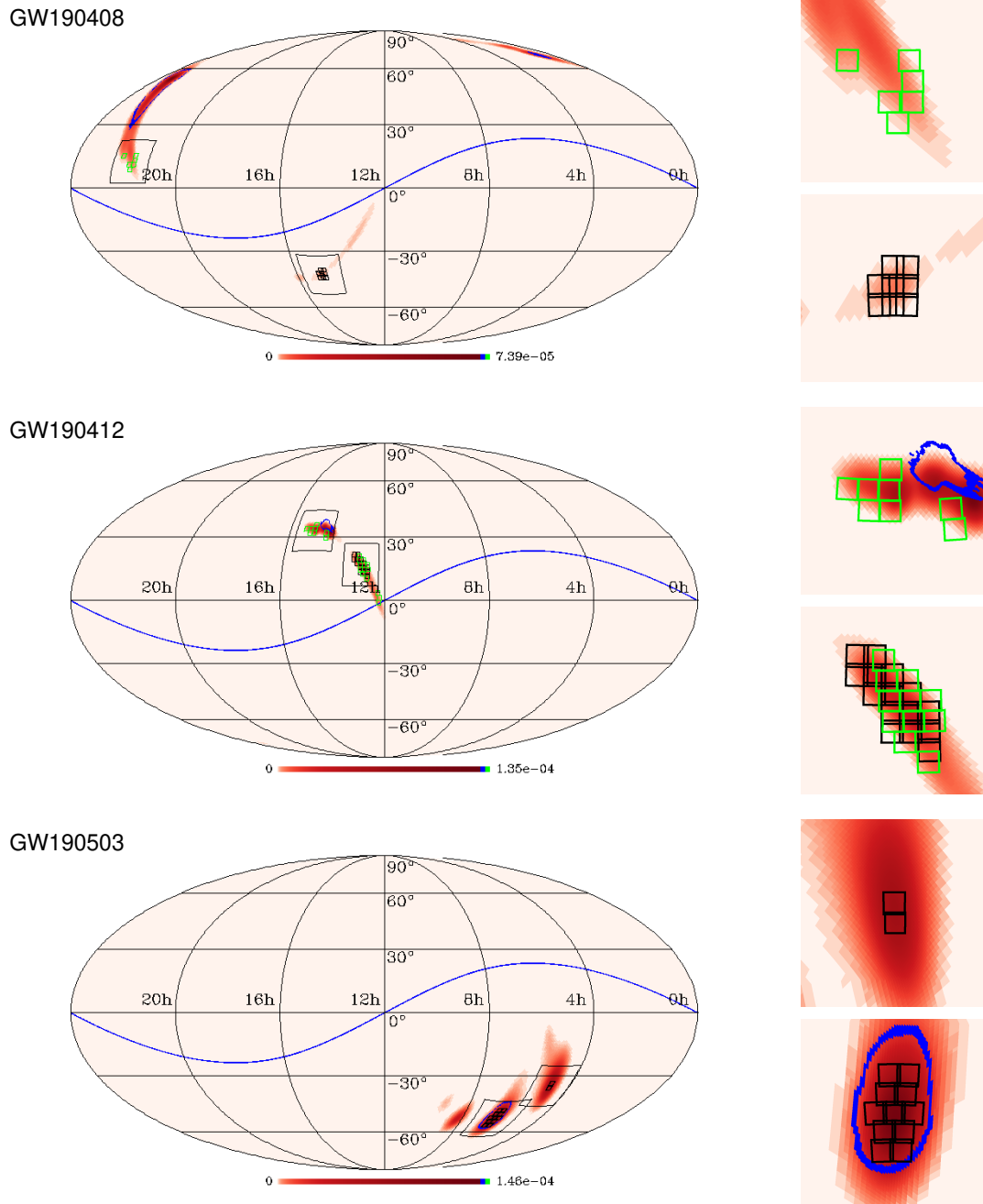


**Figure 5.1.** The GW localization and the coverage of our EM follow-up tiling observation for three GW events. Here, we used the GW localization map of the initial alerts (bayestar.fits), while the blue contours show the boundary of the 90% localization area in the GWTC-2 catalog. The large black boxes in the sky map on the left are expanded in the right panels. The small black and green boxes are the field coverages of the KMTNet and WIT pointings, respectively. The blue lines indicate the ecliptic plane.

covering about  $1 \text{ deg}^2$ . There is a gap of about  $3'1$  (east-west) to  $6'2$  (north-south) between each chip. To fill the CCD gaps, all the KMTNet observations were carried out by dithering between exposures.

Additionally, we used four telescopes of IMSNG (Im et al. 2019) to observe the Northern Hemisphere, especially at high decl. regions ( $\delta > 25^\circ$ ) that the KMTNet cannot reach. The wide-field IFU telescope (WIT), a wide-field ( $\sim 5.5 \text{ deg}^2$ ) imager with a 0.25 m telescope equipped with multiple medium-band and broadband filters (Hwang et al. 2021) at the McDonald Observatory (McD) performed tiling observation to cover the wide GW localization area, but to a rather shallow depth ( $\sim 19.0$  mag in the  $V$  band at  $5\sigma$  depth with a 7.5 min exposure). The other three are 1.0 m telescopes at the Deokheung Optical Astronomy Observatory (DOAO), the Mt. Lemmon Optical Astronomy Observatory (LOAO), and the Seoul National University Astronomical Observatory (SAO). These telescopes have respective fields of view of  $13'2 \times 13'2$ ,  $28'1 \times 28'1$ ,  $21'2 \times 21'2$ , respectively. These telescopes are suitable for observing galaxies that are likely to be the host galaxy of the BBH merger (targeted observation). The three 1.0 m telescopes have a  $5\text{-}\sigma$  depth of  $\sim 19.5$  mag in the  $R$  band with a three-minute exposure.

### 5.3.2 Basic observation strategy

Since there are both wide-field and narrow-field GECKO telescopes, we adopted two observing strategies. With wide-field telescopes ( $\text{FoV} > 1 \text{ deg}^2$ ), we performed tiling observation with an aim of covering the entire 90% localization area. When the localization area is too large, the limit for the credibility of the localization is reduced from 90% to a lower value. Also, when the localization area is several thousands of  $\text{deg}^2$ , we switched to the target observation in the initial phase of GECKO observation as described below.

Mostly for the narrow-field telescopes, but also in the case where the localization area was too large to cover even with a wide-field telescope, we made a prioritized list of those galaxies most likely to be the host galaxy of the GW event. Galaxies are

drawn from the GLADE catalog (Dályá et al. 2018) version 2.3, and we computed the likelihood score of each galaxy to be the host galaxy of the event. For both BNS and BBH events, the likelihood score implements the 3D localization probability and the  $K$  band absolute magnitude. Here, the  $K$  band is chosen as a way to sort the list, since the theoretical expectation is such that the more massive the host galaxy is, the more likely it hosts a BBH or BNS event (Mapelli et al. 2018; Artale et al. 2019), and the  $K$  band is known to be a good proxy for galaxy stellar mass (e.g., Kim & Im 2013).

To create a list of the observation coordinates for both the tiling and target observations, we established an automatic alert system that creates the list based on the GW event alert and the localization map. The coordinates are either handed over to the telescope operators or fed into the automatic observation planner. Exposure times were chosen to be typically 4 minutes per a tile for the KMTNet observations, and about 3 - 7.5 minutes for other telescopes. We used the observations of the three initial O3 events as test cases, and adjusted the exposure time.

More details on the galaxy prioritization and observational strategy will be presented in Paek et al. (2021, in preparation).

### 5.3.3 Observations

#### GW190408

The first event, GW190408, was localized mostly in the Northern Hemisphere of the sky, but the area was too close to the Sun to observe. However, there was a  $7 \text{ deg}^2$  field of the initial 90% localization area in the Southern Hemisphere around decl. of  $\sim -40 \text{ deg}$ . We targeted this field using the KMTNet with four minutes of exposure time in the  $B$  and  $R$  bands. We started the observation about 100 minutes after the GW event alert, and we obtained four epochs ( $\sim 8 \text{ hr}$  interval) of observation data from three KMTNet sites. A portion of the Northern Hemisphere localization area of the initial GW alert was observed with the WIT for three nights (2019 Apr 09 - 11). The observation covered a  $32.6 \text{ deg}^2$  of the sky (6 fields) with 7.5 minutes of exposure time in the  $V$  band. No target observation was performed, because the event occurred at a distance that was

too far to be covered by the GLADE catalog. The probability region covered by the two telescopes is 2.0% for the initial GW localization, and the probability region decreased to 0.14% with respect to the GWTC-2 localization map. The reduction in the covered probability region from the initial to GWTC-2 localization suggests that EM follow-up observations may miss optical counterparts due to inaccuracy in the GW event localization. Improving the accuracy of rapid localization of GW events is important for the success of future optical follow-up efforts. The KMTNet and WIT observations are presented in Table 5.2, along with their  $5\sigma$  point-source detection limits.

### **GW190412**

Most of the initial 90% localization area (156 deg<sup>2</sup>) of GW190412 lies on the Northern Hemisphere of the sky, at decl. of  $-3$  deg to  $+38$  deg. It can be divided into two regions, one at decl.  $< +25$  deg (area1) and another at decl.  $> +25$  deg (area2). The area1 was observable with the KMTNet, and we started the observation at 6 hr after the event alert. We obtained the KMTNet images for 63 deg<sup>2</sup> on the sky by tiling observations of 15 fields with four-minute exposure times taken in the  $R$  band across two epochs of single-day intervals. The high-priority regions of both area1 and area2 were observed using the WIT by tiling 22 fields (116.3 deg<sup>2</sup>) with a 7.5 minute exposure time in the  $V$  band on 2019 April 12th and 14th. We also performed the target observations of host galaxy candidates with the narrow-field telescopes. The target galaxies were chosen as described in Section 5.3.2. We observed 81, 76, and 2 galaxies with the DOAO 1 m, SAO 1 m, and LOAO 1 m telescopes, respectively, with exposure times of 3 - 5 minutes in the  $R$  band. Overall, we covered a 40% probability region of the initial GW localization map, and added imaging data for 86 galaxy candidates. However, the covered probability region reduces to 2.3% with respect to the GWTC-2 localization map because the 90% region moved to decl.  $> +30$  deg where our coverage is deficient (Figure 5.1). Like GW190408, the reduction is significant in the covered localization probability area from the initial to the GWTC-2 credible regions, reiterating the importance of rapid, accurate GW localization. The list of the tiling observation coordinates and the list of

the observed host galaxy candidates are given in Table 5.3. Also given are  $5\sigma$  point-source detection limits of the data.

### **GW190503**

We performed follow-up observation for GW190503 only with the KMTNet because the initial 90% credibility area was located in the Southern Hemisphere, the area was extensive (448 deg<sup>2</sup>) and located in the southern hemisphere. Furthermore, the KMTNet could reach the deepest among our facilities available in the Southern Hemisphere where another available GECKO facility was the 0.43 m Lee Sang Gak Telescope (Im et al. 2015; Choi & Im 2017). We observed a high-probability area from the initial alert with 13 tiles with four minutes of exposure time in the  $R$  band during two epochs separated by one day. The covered area is 52 deg<sup>2</sup>, which corresponds to a 33% probability region. Because the localization area had shrunk to 96 deg<sup>2</sup> in the GWTC-2 catalog, it turned out that the KMTNet observation covered the 69% localization probability region of GWTC-2. Table 5.2 shows the central coordinates of the KMTNet pointings and their  $5\sigma$  point-source detection limits.

We summarize all of the GECKO observations in Table 5.4 and the area covered by the tiling observation is marked by rectangles in Figure 5.1.

Table 5.2. Tiling observation summary of the three GW events

Event	Telescope	Start Time [UT]	Time since GW Alert [hours]	R.A. <sup>a</sup> [hh:mm:ss]	Decl. <sup>a</sup> [dd:mm:ss]	Band	5 $\sigma$ Depth [mag]
GW190408	KMTNet	2019-04-08 19:58:59	1.66	14:52:14.3	-41:22:52	R	22.5
GW190408	KMTNet	2019-04-08 20:04:25	1.76	14:44:13.8	-41:22:55	R	22.6
GW190408	KMTNet	2019-04-08 20:10:47	1.86	15:00:14.2	-41:22:56	R	22.6
GW190408	KMTNet	2019-04-08 20:17:05	1.98	14:52:13.4	-39:23:00	R	22.6
GW190408	KMTNet	2019-04-08 20:25:20	2.11	14:52:13.7	-43:22:59	R	22.5
GW190408	KMTNet	2019-04-08 20:32:36	2.23	14:44:12.8	-39:23:03	R	22.5
GW190408	KMTNet	2019-04-08 20:38:57	2.33	15:00:13.5	-43:23:02	R	22.6
GW190408	KMTNet	2019-04-08 20:46:01	2.46	14:44:12.4	-43:23:05	R	22.7
GW190408	KMTNet	2019-04-08 20:58:15	2.66	14:52:12.3	-41:23:08	B	22.8
GW190408	KMTNet	2019-04-08 21:04:33	2.76	14:44:12.0	-41:23:09	B	22.9
GW190408	KMTNet	2019-04-08 21:10:51	2.86	15:00:12.2	-41:23:09	B	22.9
GW190408	KMTNet	2019-04-08 21:16:57	2.96	14:52:11.9	-39:23:11	B	23.0
GW190408	KMTNet	2019-04-08 21:24:17	3.10	14:52:12.0	-43:23:10	B	23.0
GW190408	KMTNet	2019-04-08 21:30:36	3.20	14:44:11.5	-39:23:13	B	23.1
GW190408	KMTNet	2019-04-08 21:36:54	3.30	15:00:11.9	-43:23:10	B	22.8
GW190408	KMTNet	2019-04-08 21:43:12	3.41	14:44:11.7	-43:23:12	B	23.0
GW190408	KMTNet	2019-04-09 04:07:37	9.81	14:52:18.1	-41:21:36	R	22.8
GW190408	KMTNet	2019-04-09 04:13:29	9.91	14:44:17.7	-41:21:44	R	22.9
GW190408	KMTNet	2019-04-09 04:19:21	10.0	15:00:17.9	-41:21:40	R	22.8
GW190408	KMTNet	2019-04-09 04:25:29	10.1	14:52:17.1	-39:21:49	R	22.9
GW190408	KMTNet	2019-04-09 04:31:41	10.2	14:52:17.7	-43:21:50	R	22.7
GW190408	KMTNet	2019-04-09 04:37:53	10.3	14:44:16.3	-39:22:00	R	22.9
GW190408	KMTNet	2019-04-09 04:43:54	10.4	15:00:17.5	-43:21:53	R	22.7
GW190408	KMTNet	2019-04-09 04:50:00	10.5	14:44:16.6	-43:22:03	R	22.8
GW190408	KMTNet	2019-04-09 04:56:03	10.6	14:52:16.3	-41:22:04	B	23.2
GW190408	KMTNet	2019-04-09 05:01:57	10.7	14:44:15.6	-41:22:09	B	23.2
GW190408	KMTNet	2019-04-09 05:07:47	10.8	15:00:16.1	-41:22:05	B	23.1
GW190408	KMTNet	2019-04-09 05:13:54	10.9	14:52:15.2	-39:22:11	B	23.1
GW190408	KMTNet	2019-04-09 05:19:54	11.0	14:52:15.8	-43:22:10	B	23.1
GW190408	KMTNet	2019-04-09 05:25:46	11.1	14:44:14.7	-39:22:15	B	23.3
GW190408	KMTNet	2019-04-09 05:32:03	11.2	15:00:16.0	-43:22:08	B	23.1
GW190408	KMTNet	2019-04-09 05:37:56	11.3	14:44:15.2	-43:22:14	B	23.1

Table 5.2 (cont'd)

Event	Telescope	Start Time [UT]	Time since GW Alert [hours]	R.A. <sup>a</sup> [hh:mm:ss]	Decl. <sup>a</sup> [dd:mm:ss]	Band	5 $\sigma$ Depth [mag]
GW190408	KMTNet	2019-04-09 12:10:09	17.8	14:52:13.5	-41:22:58	R	22.3
GW190408	KMTNet	2019-04-09 12:20:16	18.0	14:44:13.1	-41:22:56	R	22.3
GW190408	KMTNet	2019-04-09 12:26:37	18.1	15:00:14.1	-41:22:55	R	21.4
GW190408	KMTNet	2019-04-09 12:32:48	18.2	14:52:13.2	-39:22:58	R	22.4
GW190408	KMTNet	2019-04-09 12:39:02	18.3	14:52:14.2	-43:22:52	R	21.4
GW190408	KMTNet	2019-04-09 12:45:00	18.4	14:44:12.0	-39:22:53	R	22.4
GW190408	KMTNet	2019-04-09 12:51:04	18.5	15:00:12.3	-43:23:04	R	22.2
GW190408	KMTNet	2019-04-09 12:57:14	18.6	14:44:13.7	-43:22:51	R	22.3
GW190408	KMTNet	2019-04-09 13:05:13	18.7	14:52:13.1	-41:22:52	B	22.0
GW190408	KMTNet	2019-04-09 13:11:31	18.8	14:44:12.3	-41:22:54	B	22.7
GW190408	KMTNet	2019-04-09 13:17:25	18.9	15:00:13.1	-41:23:21	B	22.4
GW190408	KMTNet	2019-04-09 13:23:19	19.0	14:52:12.3	-39:22:54	B	22.8
GW190408	KMTNet	2019-04-09 13:29:30	19.1	14:52:13.6	-43:22:53	B	22.7
GW190408	KMTNet	2019-04-09 13:35:55	19.2	14:44:13.9	-39:22:54	B	22.9
GW190408	KMTNet	2019-04-09 13:42:13	19.4	15:00:12.1	-43:22:55	B	22.5
GW190408	KMTNet	2019-04-09 13:48:22	19.5	14:44:14.0	-43:22:53	B	22.7
GW190408	KMTNet	2019-04-09 19:59:57	25.6	14:52:13.6	-41:22:49	R	21.9
GW190408	KMTNet	2019-04-09 20:06:21	25.8	14:44:13.2	-41:22:53	R	21.5
GW190408	KMTNet	2019-04-09 20:22:17	26.0	15:00:13.4	-41:22:56	R	21.5
GW190408	KMTNet	2019-04-09 20:28:36	26.1	14:52:13.0	-39:22:59	R	21.9
GW190408	KMTNet	2019-04-09 20:34:56	26.2	14:52:13.2	-43:22:58	R	21.8
GW190408	KMTNet	2019-04-09 20:40:52	26.3	14:44:12.2	-39:23:03	R	22.0
GW190408	KMTNet	2019-04-09 20:47:13	26.4	15:00:13.1	-43:23:00	R	21.6
GW190408	KMTNet	2019-04-09 20:53:32	26.5	14:44:12.1	-43:23:05	R	21.9
GW190408	KMTNet	2019-04-09 21:00:31	26.7	14:52:12.0	-41:23:06	B	22.2
GW190408	KMTNet	2019-04-09 21:06:50	26.8	14:44:11.9	-41:23:08	B	22.5
GW190408	KMTNet	2019-04-09 21:13:10	26.9	15:00:12.0	-41:23:07	B	22.1
GW190408	KMTNet	2019-04-09 21:19:29	27.0	14:52:11.8	-39:23:10	B	22.6
GW190408	KMTNet	2019-04-09 21:31:00	27.2	14:52:11.9	-43:23:10	B	22.1
GW190408	KMTNet	2019-04-09 21:37:19	27.3	14:44:11.6	-39:23:14	B	22.0
GW190408	KMTNet	2019-04-09 21:47:48	27.4	15:00:11.8	-43:23:11	B	22.6
GW190408	KMTNet	2019-04-09 21:54:00	27.6	14:44:11.4	-43:23:13	B	22.2

Table 5.2 (cont'd)

Event	Telescope	Start Time [UT]	Time since GW Alert [hours]	R.A. <sup>a</sup> [hh:mm:ss]	Decl. <sup>a</sup> [dd:mm:ss]	Band	5 $\sigma$ Depth [mag]
GW190408	WIT	2019-04-09 11:32:26	17.2	21:43:19.9	+15:04:05	V	17.6
GW190408	WIT	2019-04-09 11:47:26	17.4	22:10:32.0	+15:03:36	V	17.0
GW190408	WIT	2019-04-10 11:20:22	41.0	21:48:26.6	+08:28:49	V	17.8
GW190408	WIT	2019-04-12 11:11:17	88.8	21:42:05.1	+10:40:20	V	18.6
GW190408	WIT	2019-04-12 11:23:11	89.0	21:52:06.9	+10:40:42	V	18.1
GW190408	WIT	2019-04-12 11:34:12	89.2	21:41:54.6	+12:52:22	V	17.7
GW190412	KMTNet	2019-04-12 11:30:06	6.00	12:49:08.5	+15:11:24	R	21.8
GW190412	KMTNet	2019-04-12 11:36:11	6.10	12:49:07.1	+17:11:22	R	21.7
GW190412	KMTNet	2019-04-12 11:42:31	6.20	12:49:07.1	+13:11:25	R	22.5
GW190412	KMTNet	2019-04-12 11:48:37	6.30	12:57:10.5	+15:11:23	R	22.8
GW190412	KMTNet	2019-04-12 11:54:47	6.40	12:57:07.1	+17:11:22	R	22.8
GW190412	KMTNet	2019-04-12 12:00:53	6.50	12:57:07.1	+19:11:25	R	22.1
GW190412	KMTNet	2019-04-12 12:14:25	6.73	12:57:10.8	+13:11:25	R	22.0
GW190412	KMTNet	2019-04-12 12:20:31	6.83	13:05:07.0	+17:11:23	R	22.7
GW190412	KMTNet	2019-04-12 12:26:38	6.93	13:05:07.9	+19:11:21	R	22.8
GW190412	KMTNet	2019-04-12 12:32:37	7.03	13:05:06.8	+21:11:18	R	21.9
GW190412	KMTNet	2019-04-12 12:38:57	7.13	13:13:07.0	+19:11:22	R	21.9
GW190412	KMTNet	2019-04-12 12:45:02	7.25	13:13:06.9	+21:11:21	R	22.5
GW190412	KMTNet	2019-04-12 12:51:10	7.35	12:41:07.6	+15:11:22	R	22.6
GW190412	KMTNet	2019-04-12 12:57:24	7.45	12:41:07.0	+11:11:23	R	22.6
GW190412	KMTNet	2019-04-12 13:03:38	7.55	12:41:07.1	+13:11:22	R	22.7
GW190412	KMTNet	2019-04-13 11:30:58	30.0	12:49:07.2	+15:11:30	R	21.4
GW190412	KMTNet	2019-04-13 11:37:04	30.1	12:48:30.5	+17:11:46	R	18.6
GW190412	KMTNet	2019-04-13 11:42:55	30.2	12:49:06.0	+13:11:31	R	20.9
GW190412	KMTNet	2019-04-13 12:04:18	30.5	12:57:06.3	+17:20:46	R	20.3
GW190412	KMTNet	2019-04-13 12:14:46	30.7	12:57:07.0	+19:11:29	R	21.4
GW190412	KMTNet	2019-04-13 12:20:55	30.8	12:57:07.3	+13:11:31	R	21.5
GW190412	KMTNet	2019-04-13 12:36:29	31.1	13:05:06.9	+19:20:41	R	20.6
GW190412	KMTNet	2019-04-13 12:39:25	31.1	13:04:30.1	+21:11:41	R	21.1
GW190412	KMTNet	2019-04-13 12:45:33	31.2	13:12:30.0	+19:11:42	R	21.3
GW190412	KMTNet	2019-04-13 12:51:49	31.3	13:12:30.2	+21:11:41	R	21.5
GW190412	KMTNet	2019-04-13 13:04:03	31.5	12:41:07.1	+11:11:27	R	22.5

Table 5.2 (cont'd)

Event	Telescope	Start Time [UT]	Time since GW Alert [hours]	R.A. <sup>a</sup> [hh:mm:ss]	Decl. <sup>a</sup> [dd:mm:ss]	Band	5 $\sigma$ Depth [mag]
GW190412	KMTNet	2019-04-13 13:10:13	31.6	12:40:30.3	+13:11:40	R	21.0
GW190412	WIT	2019-04-12 07:17:53	1.78	12:13:33.8	-00:57:38	V	18.3
GW190412	WIT	2019-04-12 07:32:09	2.03	12:11:51.7	+01:13:07	V	18.6
GW190412	WIT	2019-04-12 07:46:13	2.26	12:15:53.4	+03:23:47	V	18.5
GW190412	WIT	2019-04-12 07:58:16	2.46	12:41:16.1	+09:59:52	V	18.0
GW190412	WIT	2019-04-12 08:43:07	3.21	12:38:17.8	+14:22:03	V	18.6
GW190412	WIT	2019-04-12 08:56:47	3.43	12:47:21.2	+14:21:22	V	18.6
GW190412	WIT	2019-04-12 09:07:33	3.61	12:51:17.0	+12:09:47	V	18.7
GW190412	WIT	2019-04-12 09:18:01	3.80	12:56:22.5	+14:21:22	V	18.5
GW190412	WIT	2019-04-12 09:31:56	4.01	12:39:46.0	+16:31:22	V	18.5
GW190412	WIT	2019-04-12 09:44:43	4.23	12:48:54.6	+16:30:57	V	18.3
GW190412	WIT	2019-04-12 10:01:08	4.51	12:58:00.2	+16:30:39	V	18.5
GW190412	WIT	2019-04-12 10:14:15	4.73	12:49:58.6	+18:41:00	V	18.3
GW190412	WIT	2019-04-12 10:41:10	5.18	12:59:14.6	+18:39:43	V	18.7
GW190412	WIT	2019-04-14 09:24:05	51.9	13:00:43.1	+20:49:38	V	18.8
GW190412	WIT	2019-04-14 10:01:51	52.5	14:26:40.9	+29:37:15	V	19.2
GW190412	WIT	2019-04-14 10:11:06	52.6	14:27:54.2	+31:48:25	V	19.0
GW190412	WIT	2019-04-14 10:21:55	52.8	14:58:31.2	+31:48:38	V	19.2
GW190412	WIT	2019-04-14 10:40:01	53.1	15:08:45.8	+31:48:40	V	19.0
GW190412	WIT	2019-04-14 10:48:24	53.3	14:59:08.6	+33:59:37	V	19.1
GW190412	WIT	2019-04-14 11:09:53	53.6	15:09:39.8	+33:59:42	V	19.2
GW190412	WIT	2019-04-14 11:23:01	53.8	15:20:08.8	+33:59:29	V	18.3
GW190412	WIT	2019-04-14 11:35:23	54.0	14:58:12.6	+36:10:03	V	17.5
GW190503	KMTNet	2019-05-03 23:00:35	4.09	04:50:41.2	-33:47:28	R	22.5
GW190503	KMTNet	2019-05-03 23:16:10	4.36	04:49:53.7	-35:47:06	R	21.9
GW190503	KMTNet	2019-05-03 23:30:34	4.59	06:20:22.1	-51:48:08	R	22.5
GW190503	KMTNet	2019-05-03 23:36:32	4.69	06:27:10.2	-53:48:06	R	22.1
GW190503	KMTNet	2019-05-03 23:42:37	4.79	06:12:58.4	-49:48:01	R	21.9
GW190503	KMTNet	2019-05-03 23:48:33	4.89	06:13:55.4	-53:47:54	R	21.8
GW190503	KMTNet	2019-05-03 23:54:51	4.99	06:25:07.6	-49:48:03	R	22.0
GW190503	KMTNet	2019-05-04 00:01:14	5.11	06:07:41.3	-51:47:46	R	22.2
GW190503	KMTNet	2019-05-04 00:10:13	5.26	06:33:02.1	-51:48:01	R	22.2

Table 5.2 (cont'd)

Event	Telescope	Start Time [UT]	Time since GW Alert [hours]	R.A. <sup>a</sup> [hh:mm:ss]	Decl. <sup>a</sup> [dd:mm:ss]	Band	5 $\sigma$ Depth [mag]
GW190503	KMTNet	2019-05-04 00:16:49	5.36	06:29:11.9	-55:47:49	R	22.4
GW190503	KMTNet	2019-05-04 00:32:50	5.63	06:11:35.2	-47:47:39	R	22.5
GW190503	KMTNet	2019-05-04 00:36:05	5.70	06:15:18.2	-55:47:30	R	22.4
GW190503	KMTNet	2019-05-04 00:42:12	5.80	06:23:16.9	-47:47:44	R	22.6
GW190503	KMTNet	2019-05-04 22:56:54	28.0	04:50:41.3	-33:47:28	R	22.1
GW190503	KMTNet	2019-05-04 23:03:14	28.1	04:50:31.0	-35:47:23	R	22.5
GW190503	KMTNet	2019-05-04 23:16:11	28.3	06:20:21.8	-51:48:07	R	22.7
GW190503	KMTNet	2019-05-04 23:22:28	28.4	06:27:09.9	-53:48:05	R	22.6
GW190503	KMTNet	2019-05-04 23:28:29	28.5	06:12:58.2	-49:48:01	R	22.7
GW190503	KMTNet	2019-05-04 23:34:37	28.6	06:13:55.2	-53:47:53	R	22.7
GW190503	KMTNet	2019-05-04 23:40:54	28.7	06:25:07.6	-49:48:03	R	22.6
GW190503	KMTNet	2019-05-04 23:46:54	28.8	06:07:41.4	-51:47:48	R	22.8
GW190503	KMTNet	2019-05-04 23:52:59	28.9	06:33:02.0	-51:48:02	R	22.6
GW190503	KMTNet	2019-05-04 23:59:05	29.0	06:29:12.0	-55:47:51	R	22.6
GW190503	KMTNet	2019-05-05 00:05:12	29.1	06:15:18.0	-55:47:39	R	22.6
GW190503	KMTNet	2019-05-05 00:11:12	29.2	06:11:35.2	-47:47:44	R	22.6
GW190503	KMTNet	2019-05-05 00:17:17	29.3	06:23:16.9	-47:47:50	R	22.5

<sup>a</sup>Central coordinate of the field.

Table 5.3. Galaxy observation of GW190412

Telescope	Time [UT]	Name <sup>a</sup>	R.A. [hh:mm:ss]	Decl. [dd:mm:ss]	Band	5 $\sigma$ Depth [mag]
DOAO	2019-04-12 10:57:48	PGC1631373	13:13:56.2	+20:35:23	R	20.5
DOAO	2019-04-12 11:08:47	2MASS+12252912+0317180	12:25:29.1	+03:17:18	R	20.3
DOAO	2019-04-12 11:14:27	2MASS+12305009+0916524	12:30:50.1	+09:16:52	R	21.4
DOAO	2019-04-12 11:20:07	PGC1418963	12:50:11.4	+12:55:28	R	21.2
DOAO	2019-04-12 11:42:33	2MASS+12555287+1748218	12:55:52.9	+17:48:22	R	20.5
DOAO	2019-04-12 11:46:12	PGC1632710	13:06:19.1	+20:38:46	R	20.5
DOAO	2019-04-12 12:18:43	PGC3115570	12:17:53.4	+00:32:58	R	20.1
DOAO	2019-04-12 12:22:36	PGC1550150	12:54:41.3	+18:05:57	R	19.5
DOAO	2019-04-12 12:26:15	2MASS+13085235+1913310	13:08:52.4	+19:13:31	R	19.1
DOAO	2019-04-12 12:30:11	2MASS+14300656+3449079	14:30:06.6	+34:49:08	R	19.4
DOAO	2019-04-12 12:36:27	2MASS+15004041+3517482	15:00:40.4	+35:17:48	R	19.5
DOAO	2019-04-12 12:42:07	PGC1947865	14:52:32.8	+31:27:13	R	19.9
DOAO	2019-04-12 12:47:44	PGC2035881	14:48:53.9	+33:37:28	R	20.3
DOAO	2019-04-12 12:53:22	PGC2027534	15:00:16.6	+33:14:59	R	20.5
DOAO	2019-04-12 13:03:04	PGC2033582	15:09:40.2	+33:30:40	R	20.1
DOAO	2019-04-12 13:06:46	PGC2055365	14:42:18.9	+34:50:22	R	20.3
DOAO	2019-04-12 13:10:26	SDSSJ150123.73+315801.0	15:01:23.8	+31:58:01	R	20.0
DOAO	2019-04-12 13:17:54	PGC1995773	14:58:22.4	+32:24:51	R	19.7
DOAO	2019-04-12 13:21:33	PGC2052504	14:46:54.3	+34:39:15	R	20.1
DOAO	2019-04-12 13:25:09	PGC2024398	14:50:46.0	+33:08:13	R	20.4
DOAO	2019-04-12 13:29:11	PGC1624808	13:06:22.6	+20:21:16	R	19.9
DOAO	2019-04-12 13:32:49	PGC1544371	12:57:21.1	+17:53:05	R	20.1
DOAO	2019-04-12 13:36:28	SDSSJ130924.86+185001.5	13:09:24.8	+18:50:01	R	19.8
DOAO	2019-04-12 13:40:19	PGC1907502	14:11:37.0	+30:31:54	R	19.8
DOAO	2019-04-12 13:44:00	PGC2034308	14:36:01.9	+33:32:49	R	19.9
DOAO	2019-04-12 13:55:10	2MASS+13053613+1819028	13:05:36.1	+18:19:03	R	20.2
DOAO	2019-04-12 13:58:47	PGC1570093	12:57:24.8	+18:46:53	R	18.3
DOAO	2019-04-12 14:02:55	SDSSJ150743.62+352724.0	15:07:43.6	+35:27:23	R	15.7
DOAO	2019-04-12 14:14:01	2MASS+14505420+3508374	14:50:54.2	+35:08:37	R	20.3
DOAO	2019-04-12 15:26:02	PGC2029948	14:46:41.3	+33:20:39	R	20.8
DOAO	2019-04-12 15:29:45	PGC2062695	14:45:55.8	+35:19:06	R	20.3
DOAO	2019-04-12 15:37:07	PGC2074273	14:37:30.8	+36:03:30	R	20.7
DOAO	2019-04-12 15:41:15	PGC1271577	12:24:00.8	+04:40:24	R	20.5

Table 5.3 (cont'd)

Telescope	Time [UT]	Name <sup>a</sup>	R.A. [hh:mm:ss]	Decl. [dd:mm:ss]	Band	5 $\sigma$ Depth [mag]
DOAO	2019-04-12 15:44:53	PGC3293500	12:21:38.9	+02:11:55	R	20.2
DOAO	2019-04-12 15:49:06	PGC2057172	14:49:53.8	+34:57:16	R	20.6
DOAO	2019-04-12 15:56:27	PGC2005291	14:28:54.3	+32:37:24	R	20.6
DOAO	2019-04-12 16:00:09	2MASS+14560222+3332429	14:56:02.2	+33:32:43	R	20.6
DOAO	2019-04-12 16:03:51	2MASS+14295140+3400329	14:29:51.4	+34:00:33	R	20.6
DOAO	2019-04-12 16:11:12	PGC2027047	14:55:41.1	+33:13:53	R	20.5
DOAO	2019-04-12 16:15:16	PGC1637575	13:04:09.3	+20:51:53	R	20.5
DOAO	2019-04-12 16:18:53	PGC1617725	13:00:32.5	+20:08:24	R	21.0
DOAO	2019-04-12 16:22:51	PGC51975	14:32:43.6	+31:36:15	R	20.9
DOAO	2019-04-12 16:27:01	PGC1150484	12:13:27.3	-00:09:24	R	20.4
DOAO	2019-04-12 16:30:41	2MASS+12261020+0403213	12:26:10.2	+04:03:21	R	21.0
DOAO	2019-04-12 16:34:32	PGC1618130	13:11:49.5	+20:09:09	R	20.8
DOAO	2019-04-12 16:38:31	PGC2007713	14:49:35.5	+32:40:36	R	20.7
DOAO	2019-04-12 16:42:14	PGC2029272	14:21:15.8	+33:18:58	R	21.0
DOAO	2019-04-12 16:45:52	PGC1923841	14:08:29.6	+30:55:18	R	21.4
DOAO	2019-04-12 16:53:20	PGC2042325	15:03:11.5	+34:00:16	R	21.4
DOAO	2019-04-12 16:57:07	PGC2056629	14:36:41.9	+34:55:14	R	21.4
DOAO	2019-04-12 17:00:46	PGC2043016	14:23:40.2	+34:02:52	R	20.8
DOAO	2019-04-12 17:04:28	PGC2056935	14:50:57.0	+34:56:20	R	20.9
DOAO	2019-04-12 17:08:37	2MASS+12382123+1406520	12:38:21.2	+14:06:52	R	20.3
DOAO	2019-04-12 17:12:17	PGC1354689	12:36:52.3	+08:50:33	R	20.0
DOAO	2019-04-12 17:16:24	PGC2003929	14:41:25.9	+32:35:31	R	20.5
DOAO	2019-04-12 17:20:00	PGC2039411	14:42:43.0	+33:49:19	R	20.5
DOAO	2019-04-12 17:23:39	PGC2026304	14:27:43.5	+33:12:14	R	19.8
DOAO	2019-04-12 17:27:16	PGC2052589	14:28:57.6	+34:39:32	R	20.2
DOAO	2019-04-12 17:31:00	PGC2024841	15:02:47.5	+33:09:08	R	19.9
DOAO	2019-04-12 17:35:17	PGC1219461	12:17:47.4	+02:12:25	R	17.8
DOAO	2019-04-12 17:39:22	PGC1910956	14:12:58.6	+30:37:10	R	20.5
DOAO	2019-04-12 17:42:59	PGC1924098	14:21:59.9	+30:55:37	R	20.1
DOAO	2019-04-12 17:46:39	PGC2059032	14:41:18.1	+35:04:36	R	19.1
DOAO	2019-04-12 17:50:36	PGC1634408	13:11:50.6	+20:43:15	R	17.4
DOAO	2019-04-12 17:54:22	2MASS+12302034+0949083	12:30:20.3	+09:49:08	R	16.6
DOAO	2019-04-12 17:58:33	PGC2053980	14:53:17.0	+34:44:59	R	18.3

Table 5.3 (cont'd)

Telescope	Time [UT]	Name <sup>a</sup>	R.A. [hh:mm:ss]	Decl. [dd:mm:ss]	Band	5 $\sigma$ Depth [mag]
DOAO	2019-04-12 18:02:14	PGC2071801	15:17:39.6	+35:54:10	R	19.3
DOAO	2019-04-12 18:06:05	2MASS+14152706+2931531	14:15:27.1	+29:31:53	R	19.3
DOAO	2019-04-12 18:09:58	PGC1551144	13:05:35.3	+18:08:07	R	17.9
DOAO	2019-04-12 18:14:06	PGC2069284	15:15:25.2	+35:44:28	R	19.2
DOAO	2019-04-12 18:17:44	SDSSJ150422.69+351907.7	15:04:22.7	+35:19:08	R	19.6
DOAO	2019-04-12 18:21:55	PGC1439161	12:43:57.7	+13:44:29	R	18.7
DOAO	2019-04-12 18:25:41	PGC1253504	12:24:38.3	+03:30:13	R	19.0
DOAO	2019-04-12 18:29:57	PGC2060010	15:10:22.2	+35:08:14	R	19.9
DOAO	2019-04-12 18:38:31	PGC2052845	14:46:17.3	+34:40:36	R	19.7
DOAO	2019-04-12 18:42:08	PGC2053074	14:45:25.9	+34:41:32	R	20.2
DOAO	2019-04-12 18:49:54	PGC1552143	13:09:09.2	+18:10:20	R	15.7
DOAO	2019-04-12 18:57:31	PGC2038707	14:50:01.3	+33:46:57	R	16.5
DOAO	2019-04-12 19:01:09	PGC2042745	15:00:14.4	+34:01:45	R	18.0
DOAO	2019-04-12 19:04:48	2MASS+15163676+3616161	15:16:36.8	+36:16:16	R	16.8
DOAO	2019-04-12 19:12:07	PGC2074152	14:44:24.8	+36:03:02	R	16.7
DOAO	2019-04-17 13:13:22	PGC1624808	13:06:22.6	+20:21:16	R	19.2
DOAO	2019-04-17 13:30:12	PGC2053980	14:53:17.0	+34:44:59	R	20.1
DOAO	2019-04-17 13:47:02	PGC1624808	13:06:22.6	+20:21:16	I	18.4
DOAO	2019-04-17 14:03:49	PGC2053980	14:53:17.0	+34:44:59	I	20.2
DOAO	2019-04-17 14:20:38	PGC1624808	13:06:22.6	+20:21:16	B	19.4
DOAO	2019-04-17 14:37:28	PGC2053980	14:53:17.0	+34:44:59	B	20.2
DOAO	2019-04-17 14:54:19	PGC1624808	13:06:22.6	+20:21:16	V	18.9
DOAO	2019-04-17 15:11:07	PGC2053980	14:53:17.0	+34:44:59	V	19.8
SAO	2019-04-12 11:13:55	PGC1631373	13:13:56.2	+20:35:23	R	18.1
SAO	2019-04-12 12:08:38	2MASS+12305009+0916524	12:30:50.1	+09:16:52	R	19.0
SAO	2019-04-12 12:50:40	2MASS+12252912+0317180	12:25:29.1	+03:17:18	R	18.7
SAO	2019-04-12 13:02:29	PGC1418963	12:50:11.4	+12:55:28	R	18.7
SAO	2019-04-12 13:15:20	2MASS+12555287+1748218	12:55:52.9	+17:48:22	R	19.6
SAO	2019-04-12 13:21:37	2MASS+14300656+3449079	14:30:06.6	+34:49:08	R	18.9
SAO	2019-04-12 13:27:47	2MASS+15004041+3517482	15:00:40.4	+35:17:48	R	18.9
SAO	2019-04-12 13:33:48	PGC1947865	14:52:32.8	+31:27:13	R	18.4
SAO	2019-04-12 13:40:20	PGC1632710	13:06:19.1	+20:38:46	R	19.2
SAO	2019-04-12 14:01:20	PGC2035881	14:48:53.9	+33:37:28	R	19.1

Table 5.3 (cont'd)

Telescope	Time [UT]	Name <sup>a</sup>	R.A. [hh:mm:ss]	Decl. [dd:mm:ss]	Band	5 $\sigma$ Depth [mag]
SAO	2019-04-12 14:08:17	2MASS+13085235+1913310	13:08:52.4	+19:13:31	R	19.6
SAO	2019-04-12 14:18:35	PGC3115570	12:17:53.4	+00:32:58	R	18.9
SAO	2019-04-12 14:24:48	PGC1550150	12:54:41.3	+18:05:57	R	19.0
SAO	2019-04-12 14:38:19	PGC2027534	15:00:16.6	+33:14:59	R	18.8
SAO	2019-04-12 14:57:20	PGC2033582	15:09:40.2	+33:30:40	R	18.3
SAO	2019-04-12 15:08:26	PGC2055365	14:42:18.9	+34:50:22	R	18.9
SAO	2019-04-12 16:16:47	SDSSJ150123.73+315801.0	15:01:23.8	+31:58:01	R	19.4
SAO	2019-04-12 16:28:13	PGC1995773	14:58:22.4	+32:24:51	R	19.2
SAO	2019-04-12 16:33:44	PGC2052504	14:46:54.3	+34:39:15	R	19.3
SAO	2019-04-12 16:39:25	PGC2024398	14:50:46.0	+33:08:13	R	19.6
SAO	2019-04-12 16:48:06	PGC1624808	13:06:22.6	+20:21:16	R	18.9
SAO	2019-04-12 16:53:55	PGC1544371	12:57:21.1	+17:53:05	R	19.4
SAO	2019-04-12 17:00:39	SDSSJ130924.86+185001.5	13:09:24.8	+18:50:01	R	18.9
SAO	2019-04-12 17:06:18	PGC1907502	14:11:37.0	+30:31:54	R	19.3
SAO	2019-04-12 17:12:55	PGC2034308	14:36:01.9	+33:32:49	R	19.5
SAO	2019-04-12 17:20:05	2MASS+14203648+3109368	14:20:36.5	+31:09:37	R	19.4
SAO	2019-04-12 17:32:13	2MASS+13053613+1819028	13:05:36.1	+18:19:03	R	19.1
SAO	2019-04-12 17:37:44	PGC1570093	12:57:24.8	+18:46:53	R	19.2
SAO	2019-04-12 17:43:14	SDSSJ150743.62+352724.0	15:07:43.6	+35:27:23	R	19.5
SAO	2019-04-12 17:49:53	PGC2040508	14:49:03.8	+33:53:15	R	19.5
SAO	2019-04-12 18:02:12	2MASS+14505420+3508374	14:50:54.2	+35:08:37	R	19.2
SAO	2019-04-12 18:07:53	PGC1429307	12:44:33.2	+13:22:14	R	19.3
SAO	2019-04-12 18:14:36	PGC2029948	14:46:41.3	+33:20:39	R	19.7
SAO	2019-04-12 18:20:11	PGC2062695	14:45:55.8	+35:19:06	R	19.6
SAO	2019-04-12 18:33:15	PGC2074273	14:37:30.8	+36:03:30	R	19.4
SAO	2019-04-12 18:39:19	PGC1271577	12:24:00.8	+04:40:24	R	18.4
SAO	2019-04-12 18:56:08	PGC2005291	14:28:54.3	+32:37:24	R	19.0
SAO	2019-04-12 19:01:37	2MASS+14560222+3332429	14:56:02.2	+33:32:43	R	19.3
SAO	2019-04-12 19:07:11	2MASS+14295140+3400329	14:29:51.4	+34:00:33	R	18.6
SAO	2019-04-12 19:24:31	PGC2041840	14:56:04.5	+33:58:17	R	18.9
SAO	2019-04-12 19:29:58	PGC2027047	14:55:41.1	+33:13:53	R	18.4
SAO	2019-04-12 19:35:29	PGC1637575	13:04:09.3	+20:51:53	R	18.5
SAO	2019-04-12 19:41:03	PGC1617725	13:00:32.5	+20:08:24	R	17.9

Table 5.3 (cont'd)

Telescope	Time [UT]	Name <sup>a</sup>	R.A. [hh:mm:ss]	Decl. [dd:mm:ss]	Band	5 $\sigma$ Depth [mag]
SAO	2019-04-12 19:46:53	PGC51975	14:32:43.6	+31:36:15	R	18.5
SAO	2019-04-14 10:59:58	PGC1631373	13:13:56.2	+20:35:23	R	19.9
SAO	2019-04-14 11:05:44	2MASS+12252912+0317180	12:25:29.1	+03:17:18	R	19.4
SAO	2019-04-14 11:11:24	2MASS+12305009+0916524	12:30:50.1	+09:16:52	R	20.0
SAO	2019-04-14 11:17:02	PGC1418963	12:50:11.4	+12:55:28	R	19.4
SAO	2019-04-14 11:29:02	2MASS+12555287+1748218	12:55:52.9	+17:48:22	R	20.0
SAO	2019-04-14 11:34:50	2MASS+14300656+3449079	14:30:06.6	+34:49:08	R	19.9
SAO	2019-04-14 11:42:34	2MASS+15004041+3517482	15:00:40.4	+35:17:48	R	19.5
SAO	2019-04-14 11:48:04	PGC1947865	14:52:32.8	+31:27:13	R	19.5
SAO	2019-04-14 11:53:50	PGC1632710	13:06:19.1	+20:38:46	R	20.3
SAO	2019-04-14 11:59:41	PGC2035881	14:48:53.9	+33:37:28	R	20.0
SAO	2019-04-14 12:05:30	2MASS+13085235+1913310	13:08:52.4	+19:13:31	R	19.6
SAO	2019-04-14 12:11:19	PGC3115570	12:17:53.4	+00:32:58	R	19.5
SAO	2019-04-14 12:17:11	PGC1550150	12:54:41.3	+18:05:57	R	20.1
SAO	2019-04-14 12:23:05	PGC2027534	15:00:16.6	+33:14:59	R	19.9
SAO	2019-04-14 12:38:25	PGC2033582	15:09:40.2	+33:30:40	R	19.7
SAO	2019-04-14 12:43:56	PGC2055365	14:42:18.9	+34:50:22	R	19.6
SAO	2019-04-14 12:49:23	SDSSJ150123.73+315801.0	15:01:23.8	+31:58:01	R	19.3
SAO	2019-04-14 12:54:48	2MASS+14273151+3515290	14:27:31.5	+35:15:29	R	18.9
SAO	2019-04-14 13:00:15	PGC1995773	14:58:22.4	+32:24:51	R	19.4
SAO	2019-04-14 13:05:40	PGC2052504	14:46:54.3	+34:39:15	R	19.6
SAO	2019-04-14 13:11:08	PGC2024398	14:50:46.0	+33:08:13	R	19.7
SAO	2019-04-14 13:17:17	PGC1624808	13:06:22.6	+20:21:16	R	19.9
SAO	2019-04-14 13:22:53	PGC1544371	12:57:21.1	+17:53:05	R	20.2
SAO	2019-04-14 13:28:40	SDSSJ130924.86+185001.5	13:09:24.8	+18:50:01	R	19.9
SAO	2019-04-14 13:37:32	PGC1907502	14:11:37.0	+30:31:54	R	19.9
SAO	2019-04-14 13:43:08	PGC2034308	14:36:01.9	+33:32:49	R	19.7
SAO	2019-04-14 13:48:44	2MASS+14203648+3109368	14:20:36.5	+31:09:37	R	19.7
SAO	2019-04-14 14:00:28	2MASS+13053613+1819028	13:05:36.1	+18:19:03	R	19.9
SAO	2019-04-14 14:06:00	PGC1570093	12:57:24.8	+18:46:53	R	20.2
SAO	2019-04-14 14:12:17	SDSSJ150743.62+352724.0	15:07:43.6	+35:27:23	R	19.8
SAO	2019-04-14 14:17:57	PGC2040508	14:49:03.8	+33:53:15	R	19.8
SAO	2019-04-14 14:29:09	2MASS+14505420+3508374	14:50:54.2	+35:08:37	R	19.8

Table 5.3 (cont'd)

Telescope	Time [UT]	Name <sup>a</sup>	R.A. [hh:mm:ss]	Decl. [dd:mm:ss]	Band	5 $\sigma$ Depth [mag]
SAO	2019-04-14 14:35:56	PGC1429307	12:44:33.2	+13:22:14	R	19.8
SAO	2019-04-14 14:42:31	PGC2029948	14:46:41.3	+33:20:39	R	20.1
SAO	2019-04-14 14:47:57	PGC2062695	14:45:55.8	+35:19:06	R	19.5
SAO	2019-04-14 14:58:50	PGC2074273	14:37:30.8	+36:03:30	R	20.0
SAO	2019-04-14 15:05:59	PGC1271577	12:24:00.8	+04:40:24	R	19.8
SAO	2019-04-14 15:11:30	PGC3293500	12:21:38.9	+02:11:55	R	19.9
SAO	2019-04-14 15:18:15	PGC2057172	14:49:53.8	+34:57:16	R	20.0
SAO	2019-04-14 15:29:46	PGC2005291	14:28:54.3	+32:37:24	R	19.9
SAO	2019-04-14 15:35:35	2MASS+14560222+3332429	14:56:02.2	+33:32:43	R	20.2
SAO	2019-04-14 15:41:16	2MASS+14295140+3400329	14:29:51.4	+34:00:33	R	20.4
SAO	2019-04-14 15:52:36	PGC2041840	14:56:04.5	+33:58:17	R	20.1
SAO	2019-04-14 15:58:00	PGC2027047	14:55:41.1	+33:13:53	R	20.0
SAO	2019-04-14 16:04:49	PGC1637575	13:04:09.3	+20:51:53	R	20.1
SAO	2019-04-14 16:10:28	PGC1617725	13:00:32.5	+20:08:24	R	20.3
SAO	2019-04-14 16:16:46	PGC51975	14:32:43.6	+31:36:15	R	20.0
SAO	2019-04-14 16:23:58	PGC1150484	12:13:27.3	-00:09:24	R	19.8
SAO	2019-04-14 16:29:24	2MASS+12261020+0403213	12:26:10.2	+04:03:21	R	19.8
SAO	2019-04-14 16:44:07	PGC1618130	13:11:49.5	+20:09:09	R	20.0
SAO	2019-04-14 16:49:48	PGC2007713	14:49:35.5	+32:40:36	R	20.1
SAO	2019-04-14 16:55:53	PGC2029272	14:21:15.8	+33:18:58	R	19.8
SAO	2019-04-14 17:01:28	PGC1923841	14:08:29.6	+30:55:18	R	20.1
SAO	2019-04-14 17:12:49	PGC2042325	15:03:11.5	+34:00:16	R	20.1
SAO	2019-04-14 17:18:27	PGC2056629	14:36:41.9	+34:55:14	R	20.6
SAO	2019-04-14 17:24:01	PGC2043016	14:23:40.2	+34:02:52	R	19.9
SAO	2019-04-14 17:29:53	PGC2056935	14:50:57.0	+34:56:20	R	20.0
SAO	2019-04-14 17:41:02	PGC1354689	12:36:52.3	+08:50:33	R	20.0
SAO	2019-04-14 17:46:33	PGC2003929	14:41:25.9	+32:35:31	R	20.1
SAO	2019-04-14 17:52:07	PGC2039411	14:42:43.0	+33:49:19	R	20.1
SAO	2019-04-14 17:57:41	PGC2026304	14:27:43.5	+33:12:14	R	19.9
SAO	2019-04-14 18:03:17	PGC2052589	14:28:57.6	+34:39:32	R	19.9
SAO	2019-04-14 18:08:49	PGC2024841	15:02:47.5	+33:09:08	R	19.9
SAO	2019-04-14 18:14:37	PGC1219461	12:17:47.4	+02:12:25	R	19.5
SAO	2019-04-14 18:21:26	PGC1910956	14:12:58.6	+30:37:10	R	20.0

Table 5.3 (cont'd)

Telescope	Time [UT]	Name <sup>a</sup>	R.A. [hh:mm:ss]	Decl. [dd:mm:ss]	Band	5 $\sigma$ Depth [mag]
SAO	2019-04-14 18:26:50	PGC1924098	14:21:59.9	+30:55:37	R	19.8
SAO	2019-04-14 18:32:20	PGC2059032	14:41:18.1	+35:04:36	R	19.9
SAO	2019-04-14 18:38:00	PGC1634408	13:11:50.6	+20:43:15	R	19.9
SAO	2019-04-14 18:43:28	2MASS+12302034+0949083	12:30:20.3	+09:49:08	R	19.6
SAO	2019-04-14 18:49:38	PGC2053980	14:53:17.0	+34:44:59	R	20.2
SAO	2019-04-14 19:00:55	PGC2071801	15:17:39.6	+35:54:10	R	20.0
SAO	2019-04-14 19:06:22	2MASS+14152706+2931531	14:15:27.1	+29:31:53	R	19.8
SAO	2019-04-14 19:12:29	PGC1551144	13:05:35.3	+18:08:07	R	19.6
SAO	2019-04-14 19:18:02	PGC2069284	15:15:25.2	+35:44:28	R	20.0
SAO	2019-04-14 19:23:29	SDSSJ150422.69+351907.7	15:04:22.7	+35:19:08	R	20.2
SAO	2019-04-14 19:29:56	PGC1439161	12:43:57.7	+13:44:29	R	19.3
LOAO	2019-04-16 10:48:19	PGC2053980	14:53:17.0	+34:44:59	R104	19.4
LOAO	2019-04-16 11:09:56	PGC1624808	13:06:22.6	+20:21:16	R104	19.3

<sup>a</sup>Target name come from the GLADE catalog (Dályá et al. 2018).

## 5.4 Data Analysis and Transient Search

All the observed images were processed with basic reduction procedures (bias subtraction, dark subtraction, and flat-fielding). Astrometric calibration is done using SCAMP (Bertin 2006) or Astrometry.net (Lang et al. 2010), using tens to hundreds of stars as astrometry references depending on the field of view and depth. This produces images with astrometric accuracy of rms scatter of  $0''.2 - 0''.8$  in both R.A. and decl. directions. For the KMTNet observation for a given epoch, only two frames were taken, which made it challenging to remove cosmic rays during co-addition. Therefore, we removed the cosmic rays from each single frame using LA-Cosmic software (van Dokkum 2001). The sequentially observed two images were combined to produce a deeper image with SWarp (Bertin et al. 2002).

We used Pan-STARRS (PS1; Chambers et al. 2016) images at the closest wavelength to the observed image filter as reference images (for example, we use a PS1  $r$  band image

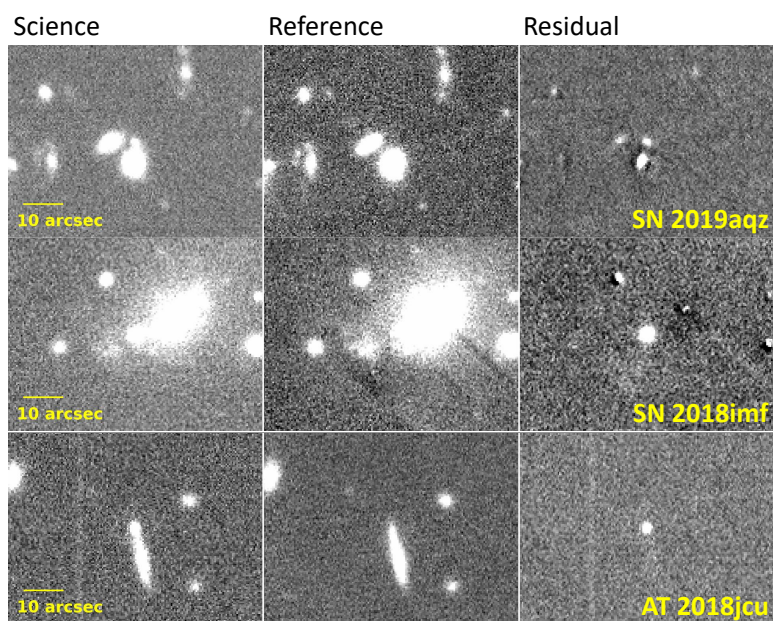


**Figure 5.2.** Three transients found in the follow-up observations of event GW190412. The top, middle, and bottom panels show SN 2019aqz, SN 2018imf, and AT 2018jcu, respectively. From left to right, each panel represents the object (science) image, the reference image, and the residual image after subtracting the reference image from the object image.

Table 5.4. Observation summary

Event	Telescope	Observation Start	Observation End	N <sup>a</sup>	Covered Area	Band	5 $\sigma$ Depth
GW190408	KMTNet	2019-04-08 19:58:59	2019-04-09 21:54:00	8 <sup>b</sup>	29 deg <sup>2</sup>	<i>BR</i>	21.5 - 23.3
GW190408	WIT	2019-04-09 11:32:26	2019-04-12 11:34:12	6 <sup>b</sup>	33 deg <sup>2</sup>	<i>V</i>	17.1 - 18.7
GW190412	SAO	2019-04-12 11:13:55	2019-04-14 19:29:56	76 <sup>c</sup>		<i>R</i>	18.0 - 20.7
GW190412	WIT	2019-04-12 07:17:53	2019-04-14 11:35:23	22 <sup>b</sup>	116 deg <sup>2</sup>	<i>V</i>	17.6 - 19.2
GW190412	DOAO	2019-04-12 10:57:48	2019-04-17 15:11:07	81 <sup>c</sup>		<i>BVRI</i>	15.8 - 21.5
GW190412	KMTNet	2019-04-12 11:30:06	2019-04-13 13:10:13	15 <sup>b</sup>	63 deg <sup>2</sup>	<i>R</i>	20.2 - 22.9
GW190412	LOAO	2019-04-16 10:48:19	2019-04-16 11:09:56	2 <sup>c</sup>		<i>V</i>	19.3 - 19.4
GW190503	KMTNet	2019-05-03 23:00:35	2019-05-05 00:17:17	13 <sup>b</sup>	52 deg <sup>2</sup>	<i>R</i>	21.8 - 22.8

<sup>a</sup>Number of the observed targets

<sup>b</sup>Tiling observation

<sup>c</sup>Galaxy targeted observation

for the KMTNet *R* band image), and the PS1 reference images were subtracted from observed images are by convolving and rescaling them to match the spatial resolution and the flux scale of the observed images using High Order Transform of PSF AND Template Subtraction (HOTPANTS; Becker 2015).

The declinations of the KMTNet images for GW190408 and GW190503 are lower than  $-30$  deg, and out of the PS1 coverage. For these images, we observed the same area of the sky twice with a time separation of about one day, and we used the images observed  $\sim 24$  hr after the first epoch as reference images for the two events.

Transient candidates were detected by identifying positive signals having signal-to-noise ratios greater than five in the subtracted images, using SExtractor (Bertin & Arnouts 1996). Many of the detected sources in the residual images were false identifications found at over- or undersubtracted bright sources. This imperfect subtraction was often caused by a slight mismatch in astrometry and/or in the wavelength coverage of the reference and the observed images, and they appear as positive signals right next to negative pixels (see the upper part of the residual image of SN 2018imf in Figure

Table 5.5. List of detected transients and transient candidates

Number	Observation time	R.A.	Decl.	$R$ mag [AB]	Name
1	2019-04-12 11:42:31	12:49:11.59	14:08:00.25	$21.34 \pm 0.08$	
2	2019-04-12 12:00:53	12:52:38.01	19:04:04.33	$20.80 \pm 0.07$	
3	2019-04-12 12:57:24	12:36:45.09	11:43:00.09	$21.06 \pm 0.09$	
4	2019-04-12 12:57:24	12:42:19.38	01:17:22.02	$22.05 \pm 0.13$	
5	2019-04-12 12:57:24	12:45:07.81	10:37:10.78	$21.33 \pm 0.09$	
6	2019-04-12 12:57:24	12:38:11.48	10:19:58.89	$20.88 \pm 0.05$	SN 2019aqz
7	2019-04-12 13:03:38	12:37:34.85	13:16:49.31	$21.17 \pm 0.06$	
8	2019-04-12 13:03:38	12:37:42.61	13:20:19.88	$21.40 \pm 0.09$	
9	2019-04-12 13:03:38	12:36:24.06	13:22:36.69	$21.87 \pm 0.10$	
10	2019-04-12 13:03:38	12:41:25.46	13:21:30.02	$21.24 \pm 0.06$	
11	2019-04-12 13:03:38	12:42:41.39	13:15:54.89	$17.82 \pm 0.004$	SN 2018imf
12	2019-04-12 13:03:38	12:43:54.16	13:12:12.77	$21.15 \pm 0.06$	
13	2019-04-12 13:03:38	12:40:05.16	13:07:58.24	$19.56 \pm 0.02$	AT 2018jcu

5.2). To remove these artifacts, we ran SExtractor on the inverse images of the residual images. The positive detections in the residual images were rejected if there were positive detections in the inverse residual image right next to their position ( $< 3''$ ). Additionally, we removed candidates matched with nontransient sources in the reference images, to exclude variable sources like variable stars or active galactic nuclei. We also removed candidates that were on bad pixels or whose central pixels were saturated. The remaining candidates were visually inspected and classified as new transient candidates if there were no other artifacts. Figure 5.2 shows the science, reference, and residual images of three transients found in the KMTNet images (see Section 5.5).

For the images from the other telescopes, we subtracted images using PS1 images and visually inspected the residual images to find transient candidates.

Table 5.6. List of moving objects

Number	Observation time	R.A.	Decl.	$R$ mag [AB]	KMTNet Site
1	2019-04-12 12:57:24	12:42:02.43	11:32:13.17	$20.38 \pm 0.07$	SAAO
	2019-04-12 13:07:08	12:42:02.03	11:32:12.56	$20.55 \pm 0.07$	SAAO
2	2019-04-12 12:51:10	12:36:30.73	14:09:43.95	$21.68 \pm 0.20$	SAAO
	2019-04-12 13:03:38	12:36:31.07	14:09:40.43	$21.72 \pm 0.17$	SAAO
3	2019-04-12 13:03:38	12:40:39.09	13:46:32.90	$21.62 \pm 0.16$	SAAO
	2019-04-12 13:13:15	12:40:38.80	13:46:33.75	$21.56 \pm 0.15$	SAAO

## 5.5 Transient Search Result

After the identification of the credible transient candidates, we matched them with known Solar System objects using SkyBoT (Berthier et al. 2006) version 3.0. SkyBot is a system that provides the location of known Solar System objects at a given epoch. Also, we matched our transient candidates with those that were already reported in the Transient Name Server (TNS<sup>2</sup>).

For GW190408, we found two transient candidates. They are matched with known Solar System objects.

In the observed areas for the GW190412 event, we detected 275 transient candidates. As we describe below, the majority of them are found to be the Solar System objects, since the localization area of GW190412 was near the Ecliptic plane with an ecliptic latitude of about 14 deg. Among these candidates, 258 objects were found to have matches with Solar System objects within 1 arcmin of their positions (most of the sources are matched within 5"). In addition, we found three moving objects that did not have matching Solar System objects. We consider these to be previously unknown Solar System objects or known Solar System objects with high positional errors. One transient candidate was found to be a fast proper motion star of  $\sim 1''/\text{year}$  (Gaia Collaboration et al. 2018). Three objects were found in the vicinity of possible host

<sup>2</sup><https://wis-tns.weizmann.ac.il>

galaxies, and they were identified in the TNS as SN 2019aqz (Type Ia), SN 2018imf (Type IIP), and AT 2018jcu (Figure 2). The remaining 10 candidates do not have a possible host galaxies in their vicinity, and were only observed in a single frame. Their nature cannot be judged from our data alone, but we suspect that most of them are Solar System objects considering the large number of such objects in this field. The observing strategy at that time was geared toward minimizing the overhead by reducing the time required to move to another field. However, we realize that efficient identification of moving objects can be done more easily if subsequent frames are taken about an hour later. We are now considering such a strategy for future observations.

No transient candidates were found in the observed areas of event GW190503.

Also, no transient candidates were found in WIT, DOAO, SAO, and LOAO images in any of the events.

Table 5.5 shows the three transients and 10 transient candidates with uncertain nature from the GECKO GW190412 observation. In Table 5.6, we also report the epochs and the positions of the Solar System objects found from our follow-up observations.

## 5.6 Discussion

### 5.6.1 Limits on BBH EM Counterpart Brightness

As described above, we could not identify any plausible EM counterparts to the three BBH merger events. This is not very surprising, considering that BBH merger events are not expected to produce EM counterparts. Also, in light of the recently updated localization area (see Section 5.2), the KMTNet observation missed the updated area for GW190408 and GW190412, so identification of EM counterparts was not possible from our observation in retrospect. For GW190503, the KMTNet covered most of the updated 90% credible region. No transients were found in this data, which places a useful upper limit on the brightness of the EM counterpart. We note, however, that the updated distance to GW190503 is  $1520_{-660}^{+710}$  Mpc, so the EM counterpart must have been bright in order to be detected with the KMTNet observation. Below, we

discuss the feasibility of detecting EM counterparts and upper limits that we could have imposed on these events if our observations covered the entire localization area.

Based on the non-detection of transients for GW190503, we place an upper limit on the brightness of EM optical counterpart for the BBH event. The median  $5\sigma$  depth of the KMTNet observations is about  $R = 22.5$  AB mag. Adopting the distance of 1500 Mpc, we get an upper limit for the EM counterpart brightness of  $M_R \sim -18.3$  AB mag without  $K$  correction. Since GW190503 occurred at  $z \sim 0.32$  and the  $R$  band has an effective wavelength of  $\sim 650$  nm (e.g., Im et al. 2010), the rest-frame wavelength covered by the  $R$  band for GW190503 is  $\sim 490$ nm, which is approximately the effective wavelength of the  $g$  band. Therefore, the  $g$  band  $K$  correction is dominated by the bandwidth dilation term of  $-2.5 \times \log(1+z)$  (e.g., Taak & Im 2020). Adopting  $-2.5 \times \log(1+z)$  as the  $K$  correction, we get a lower limit on  $M_g$  (the absolute magnitude in the  $g$  band) of  $M_g > -18.0$  AB mag ( $5\sigma$ ). This is about 1.5 - 2.5 mag brighter than the  $g$ -band peak magnitudes of various kilonova model light curves (Hotokezaka et al. 2013; Tanaka et al. 2013, 2014, 2017; Kasen et al. 2017; Arcavi 2018; Banerjee et al. 2020).

### 5.6.2 Comparison with Kilonova Light-curve Models

We compare model light curves of kilonovae and the imaging depths to discuss the possibility of GW EM counterpart detection (Figure 5.3). One of the models is the AT2017gfo-like kilonova model of Kasen et al. (2017), hereafter K17. The model is for the AT2017gfo that combines the blue and the red kilonova components with ejecta masses of  $0.025 M_\odot$  and  $0.04 M_\odot$ , respectively. We plotted the two kilonova components in Figure 5.3 and it shows that the blue kilonova is more dominant than red kilonova in the early phase,  $< 2$  days. Similarly, the AT2017gfo-like kilonova models of Tanaka et al. (2017) and Banerjee et al. (2020) are plotted in Figure 5.3 (with ejecta masses of  $0.03 - 0.05 M_\odot$ ). We also plot earlier kilonova light-curve predictions for NS-BH (NSBH) binary merger and BNS mergers with ejecta masses of  $0.0007 - 0.07 M_\odot$  (Hotokezaka et al. 2013; Tanaka et al. 2013, 2014). These models assume a higher mass fraction

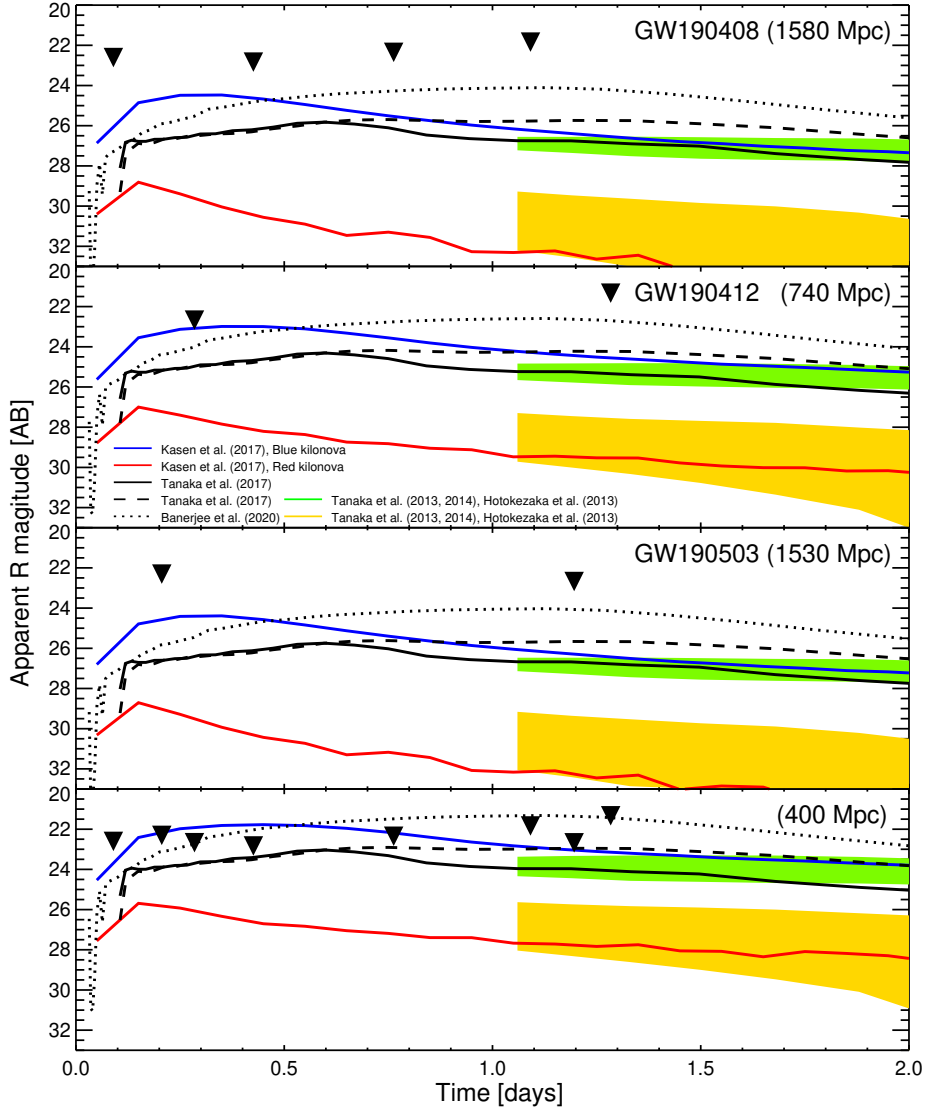


**Figure 5.3.** Comparison of different model light curves of kilonova and the KMTNet image depths (black triangles) of three events in top three panels. The bottom panel assumes a kilonova distance of 400 Mpc, and the KMTNet image depths from the observation of the three events are shown together. The blue and red solid lines indicate the blue and red components of the AT2017gfo-like kilonova model light curves of Kasen et al. (2017). The black solid, dashed, and dotted lines are the AT2017gfo-like kilonova model of Tanaka et al. (2017), and Banerjee et al. (2020). These models assume respective ejecta masses of  $0.03 M_{\odot}$ ,  $0.03 M_{\odot}$ , and  $0.05 M_{\odot}$  and respective electron fractions of 0.1 - 0.4, 0.25, and 0.3 - 0.4, respectively. The green and yellow regions are the range of four NSBH and five BNS model light curves, respectively, from Tanaka et al. (2013), Tanaka et al. (2014), and Hotokezaka et al. (2013).

of lanthanides ( $X_{lan} \sim 10^{-1.5}$ ) than the K17 model ( $X_{lan} = 10^{-4}$ ), and consequently predict fainter light curves than the AT2017gfo-like models. For the distances of these models for each event, we assumed the values from the GWTC-2 catalog. Overall, we confirm that these events are too far (700 - 1600 Mpc) for their EM counterparts to be detected with KMTNet at a nominal depth. But if AT2017gfo-like kilonovae appeared at about 400 Mpc or less, KMTNet could have detected them (Figure 5.3).

### 5.6.3 Prospects for Rapid Follow-up Observation

The early light curve can discern different mechanisms proposed for the observed blue optical-NIR emission in the early phase of EM counterpart of GW170817. The cooling of ejecta shock-heated by various mechanisms (e.g., cocoon model) would produce the early light curve that peaks very quickly in about an hour, while the early light curve that is dominated by the radioactive decay would peak at in about a day (Arcavi et al. 2017). Therefore, a rapid EM follow-up observation is important for constraining different EM production mechanisms.

For the GW190408 event, we were able to start the follow-up observation after 100 minutes from the GW alert. This demonstrates that fast follow-up observation is possible with our GECKO network, within about 1 hr from the GW event alert. Yet, it is necessary to shorten the start time of the follow-up observation, because it requires a long time even for wide-field telescopes such as KMTNet to cover the whole localization area of the GW events. The areas covered by our observations are 29, 63, and 52 deg<sup>2</sup> for GW190408, GW190412, and GW190503, respectively. From these data, we estimate that it took 1.69 minutes per deg<sup>2</sup> on average. For BNS events in the 4th (O4) GW observing run, the median 90% credibility region is expected to be  $33^{+5}_{-5}$  deg<sup>2</sup> (Abbott et al. 2020b). Therefore, it would take about 50 minutes to cover the median 90% localization areas of the O4 BNS events with a KMTNet tiling observation.

For the GECKO facilities to catch the early light curve of EM counterparts within an hour time-scale during the future O4 run, it is necessary to start the observation almost immediately after the initial GW alert. Work is already in progress to shorten

the latency of the starting time to 10 minutes or less.

For all the events, we also note that the localization area shrunk significantly or the peak of the highest-probability localization area moved to another location. Considering the large amount of time needed to cover a wide localization area, improvements in the accuracy of the initial localization map are highly desirable. If not, one should cover as much of the 90% localization area as possible, in order not to miss EM counterparts.

#### **5.6.4 Need for Deep Reference Images**

When searching for transients through the image subtraction technique, we found that the PS1  $r$  band images could serve as acceptable reference images even if the filter system was slightly different from our  $R$  band. However, during the analysis of the GW190408 and GW190503 optical data, we also discovered a lack of suitable reference images at decl.  $< -30$  deg where there is no PS1 coverage, and the SkyMapper images (Onken et al. 2019) are rather shallow. The Dark Energy Survey (DES; Abbott et al. 2018) images are available, covering  $5000 \text{ deg}^2$  of the Southern Hemisphere with a depth of  $\sim 24$  mag. However, the DES images provide only a partial coverage at  $-60 < \text{decl. (deg)} < -30$ . The sky below decl. =  $-60$  deg will remain uncovered by deep imaging observations, until the Legacy Survey of Space and Time (LSST; Ivezić et al. 2019) starts its full operation. Therefore, we are now performing a wide imaging survey named the KMTNet Synoptic Survey of Southern Sky (KS4) to provide reference images for the KMTNet follow-up data to the depths of  $\sim 23.5$  AB mag over  $7000 \text{ deg}^2$  area at the decl.  $< -60$  deg areas and some of the  $-60 < \text{decl. (deg)} < -30$  areas that are not deeply covered by previous surveys. The KS4 will allow us to quickly identify EM counterparts so that the EM counterparts can be studied in depth.

## **5.7 Summary**

In this Chapter, we presented the GECKO follow-up observation of three BBH events, GW190408, GW190412, and GW190503, that were reported early in the O3a run. In particular, we reported in detail the KMTNet observations that at 100 minutes to 6 hr

from the GW detection with a sky coverage of 29 - 63 deg<sup>2</sup> and  $\sim 22.5$  mag depth in the  $R$  band.

From our observation, we identified 13 transient candidates for GW190412 and hundreds of moving objects such as asteroids. Among these transient candidates, three transients were already reported (two confirmed as a supernova), and the remaining 10 are likely to be moving objects, due to their proximity to the field near the ecliptic plane, the lack of a host galaxy near them, and having been observed only once. Therefore, no probable EM counterpart was found in our observation. The improved localization of these events in the recently published GWTC-2 catalog reveals that the initial position estimates were very broad and many of the optical follows-up can point to regions of the sky that are not in the improved localization area. However, we find that our KMTNet imaging observation covered a 69% probability region of GWTC-2 localization map for GW190503, and our nondetection places an upper limit on the rest-frame  $g$ -band magnitude of the EM counterpart of this BBH merger event to be  $M_g > -18.0$  AB mag. Together with this, the comparison between the image depths of KMTNet data and the theoretical kilonova light-curves show that brighter AT2017gfo-like kilonova events can be detected when the luminosity distance is out to  $\sim 400$  Mpc.

Our follow-up observation started as quickly as about 100 minutes after the GW event alert, and could cover an area of about 50 deg<sup>2</sup> in one hour, demonstrating that the observation of the 90% localization area in the future O4 run can be done in about two hours. Work is ongoing to improve the response time. Overall, our results show promise that GECKO can identify kilonova events out to 400 Mpc within hours from the GW event alert in future GW observing runs that will improve the detector sensitivity event localization capability.



## Chapter 6

# Conclusion

The energetic astronomical phenomena are important considering that they provide unique astrophysical environments that are not possible to reproduce on the Earth, opening a way to test our understanding on the physical laws of the Universe under extreme conditions. In this thesis, we studied two energetic astronomical phenomena which are AGN and GW source.

AGN variability can be used to study the physics of the region in the vicinity of the central black hole. In this paper, we investigated intra-night optical variability of AGN in the COSMOS field in order to understand the AGN instability at the smallest scale. Observations were performed using the KMTNet on three separate nights for 2.5-5 hour at a cadence of 20-30 min. We find that the observation enables the detection of the short-term variability as small as  $\sim 0.02$  and  $0.1$  mag for  $R \sim 18$  and  $20$  mag sources, respectively. Using four selection methods (X-rays, mid-infrared, radio, and matching with SDSS quasars), 394 AGNs are detected in the  $4 \text{ deg}^2$  field of view. After differential photometry and  $\chi^2$ -test, we classify intra-night variable AGNs. But the fraction of variable AGNs (0-8 %) is consistent with a statistical fluctuation from null result. Eight out of 394 AGNs are found to be intra-night variable in two filters or two nights with a variability level of  $0.1$  mag, suggesting that they are strong candidates for intra-night variable AGNs. Still they represent a small population (2 %). There is no sub-category of AGNs that shows a statistically significant intra-night variability.

RM is one of the most efficient ways to investigate the broad-line region around the central supermassive black holes of AGNs. A common way of performing the RM is to perform a long term spectroscopic monitoring of AGNs, but the spectroscopic monitoring campaign of a large number of AGNs requires an extensive amount of observing time of medium to large size telescopes. As an alternative way, we present the results of photometric RM with medium-band photometry. As the widths of medium-band filters match well with the widths of AGN broad emission lines, the medium-band observation with small telescopes can be a cost-effective way to perform RM. We monitored five nearby AGNs with available spectroscopic RM results showing days to weeks scale variability. Observations were performed for  $\sim 3$  months with an average of 3 days cadence using three medium-band filters on a 0.43 m telescope. The time lags between the continuum and the  $H\alpha$  emission line light curves are calculated using the JAVELIN software and the discrete correlation function. We find time lags of 1.5-15.9 days for these AGNs, which are consistent with the time lags derived from previous spectroscopic RM measurements. This result demonstrates that even a 0.5 m class telescope can perform RM with medium-bands. Furthermore, we show that RM for tens of thousands AGNs is possible with a dedicated 1 m class telescope.

We also performed a medium-band RM for six Palomar-Green quasars with longer, expected time lags. Targets were observed for May. 2018 - Sep. 2020 with three medium-bands to cover continuum and two hydrogen lines. We perform image convolution and differential photometry to make light-curves and find all targets are variable in all bands. Using JAVELIN, we measure time lags of  $H\beta$  and  $H\gamma$  emission lines. The time lags are compared with previous results in size of broad line region and luminosity (R-L) plane. It agree with R-L relation, but shows larger intrinsic scatter of 0.37 dex than previous studies of 0.19 dex. However, photometric RM is still useful to study large AGN sample with large field of view telescope. Also, we estimate  $M_{\text{BH}}$  using time lag and lind width. Comparison with single epoch measurement of  $M_{\text{BH}}$  show that two measurements agree with each other.

We also presented optical follow-up observation results of three BBH merger events,

GW190408\_181802, GW190412, and GW190503\_185404, which were detected by the Advanced LIGO and Virgo GW detectors. Electromagnetic (EM) counterparts are generally not expected for BBH merger events. However, some theoretical models suggest that EM counterparts of BBH can possibly arise in special environments, prompting motivation to search for EM counterparts for such events. We observed high-credibility regions of the sky for the three BBH merger events with telescopes of the GECKO, including the KMTNet. Our observation started as soon as 100 minutes after the GW event alerts and covered 29 - 63 deg<sup>2</sup> for each event with a depth of  $\sim 22.5$  mag in the  $R$  band within hours of observation. No plausible EM counterparts were found for these events, but based on there being no detection of the GW190503\_185404 event, for which we covered the 69% credibility region, we place the BBH merger EM counterpart signal to be  $M_g > -18.0$  AB mag within about one day of the GW event. The comparison of our detection limits with light curves of several kilonova models suggests that a kilonova event could have been identified within hours from GW alert with GECKO observations if the compact merger happened at  $< 400$  Mpc and the localization accuracy was on the order of 50 deg<sup>2</sup>. Our result shows a great promise for the GECKO facilities to find EM counterparts within a few hours from GW detection in future GW observation runs.

Through these studies, we were able to understand the promise and the limits of the time domain studies. The network of three wide-field 1.6 m telescopes, KMTNet, is found to be extremely powerful in studying energetic phenomena that it can probe intra-night variability of hundreds of AGNs even in a single field of view to a percent accuracy. KMTNet is also found very useful for EM counterpart search of GW sources, showing that it can probe almost 100 deg<sup>2</sup> to a depth of 23 mag within a day. KMTNet should become a major facility for EM counterpart search in the upcoming era of multi-messenger astronomy. Finally, we found that medium-band observations are effective in probing the spectral variability of AGNs, suggesting that future surveys with medium-band should get many interesting results.

Building upon the current success of various time-domain studies, we hope to expand

the study to improve our understanding on AGN and GW sources. Short-term AGN variability studies can be improved by expanding the sample by enlarging the survey area and going deeper for each epoch observation. This is because the short-term variability is in general small (a few percent fluctuation in flux), and thus needs a greater photometry accuracy. High cadence data for several fields have been obtained and these dataset will be probed to improve our statistics. Additionally, a longer term variability can be studied (inter-night or longer) with which we can examine the correlation of various properties of AGN (such as luminosity, black hole mass, multi-wavelength properties). This is not an entirely new subject and there are already quite a few time domain surveys tackling the long-term AGN variability. However, the availability of the high cadence data on our part can open a possibility of investigating the correlation of short-term and long-term variabilities. Photometric RM study can be developed to study large AGN samples with a large field of view telescope as discussed in Chapter 3.6. Such a study has the potential of performing RM on tens of thousands of AGNs, which represents 100-1000 times improvement over current RM studies. Also, most optical telescopes have broad-band rather than medium-band, so RM with broad-band is worth trying considering future surveys like LSST (Ivezić et al. 2019). The EM counterpart of GW has been found only once so far. For statistical study of GW source and its EM counterpart, more samples should be discovered. To make fast detection of the EM counterpart for the fourth observation run of GW detectors, observation strategy and analysis method will be updated.

# Bibliography

- Abbott, B. P., Abbott, R., Abbott, T. D., et al. 2016, *Phys. Rev. Lett.*, 116, 061102
- Abbott, B. P., Abbott, R., Abbott, T. D., et al. 2017a, *Phys. Rev. Lett.*, 119, 161101
- Abbott, B. P., Abbott, R., Abbott, T. D., et al. 2017b, *ApJ*, 848, 12
- Abbott, B. P., Abbott, R., Abbott, T. D., et al. 2017c, *ApJ*, 848, 13
- Abbott, B. P., Abbott, R., Abbott, T. D., et al. 2017d, *Nature*, 551, 85
- Abbott, T. M. C., Abdalla, F. B., Allam, S., et al. 2018, *ApJS*, 239, 18
- Abbott, B. P., Abbott, R., Abbott, T. D., et al. 2019, *PhRvX*, 9, 031040
- Abbott, R., Abbott, T. D., Abraham, S. et al. 2020, *arXiv:2010.14527*
- Abbott, B. P., Abbott, R., Abbott, T. D., et al. 2020, *LRR*, 23, 3
- Abolfathi, B., Aguado, D. S., Aguilar, G., et al. 2018, *ApJS*, 235, 42
- Andreoni, I., Ackley, K., Cooke, J., et al. 2017, *PASA*, 34, 69
- Antonucci, R.. 1993, *ARA&A*, 31, 473
- Aranzana, E., Kording, E., Uttley, P., Scaringi, S., & Bloemen, S. 2018, *MNRAS*, 476, 2501
- Arcavi, I., Hosseinzadeh, G., Howell, D. A., et al. 2017, *Nature*, 551, 64
- Arcavi, I. 2018, *ApJ*, 855, 23

- Artale, M. C., Mapelli, M., Giacobbo, N. et al. 2019, MNRAS, 487, 1675
- Bachev, R., Strigachev A., & Semkov E., 2005, MNRAS, 358, 774
- Barth, A. J., Bennert, V. N., Canalizo, G., et al. 2015, ApJS, 218, 26
- Banerjee, S., Tanaka, M., Kawaguchi, K., Kato, D., Gaigalas, G. 2020, ApJ, 901, 29
- Bartos, I., Kocsis, B., Haiman, Z., & Márka, S. 2017, ApJ, 835, 165
- Becker, A. 2015, High Order Transform of PSF ANd Template Subtraction, Astrophysics Source Code Library, ascl:1504.004
- Bentz, M. C., Peterson, B. M., Pogge, R. W., Vestergaard, M., & Onken, C. A. 2006, ApJ, 644, 133
- Bentz, M. C., Walsh, J. L., Barth, A. J., et al. 2009, ApJ, 705, 199
- Bentz, M. C., Walsh, J. L., Barth, A. J., et al. 2010, ApJ, 716, 993
- Bentz, M. C., Denney, K. D.; Grier, C. J., et al. 2013, ApJ, 767, 149
- Berger, E. 2014, ARA&A, 52, 43
- Berthier, J., Vachier, F., Thuillot, W., et al. 2006, in ASP Conf. Ser., 351, Astronomical Data Analysis Software and Systems XV, ed. C. Gabriel et al. (San Francisco, CA: ASP), 367
- Bertin, E. & Arnouts, S. 1996, A&AS, 117, 393
- Bertin, E., Mellier, Y., Radovich, M., et al. 2002, in ASP Conf. Ser. 281, Astronomical Data Analysis Software and Systems XI, ed. D. A. Bohlender, D. Durand, & T. H. Handley (San Francisco, CA: ASP), 228
- Bertin, E. 2006, in ASP Conf. Ser. 351, Astronomical Data Analysis Software and Systems XV, ed. C. Gabriel, C. Arviset, D. Ponz, & Enrique Solano. (San Francisco, CA: ASP), 112

- Blandford, R. D., & McKee, C. F. 1982, *ApJ*, 255, 149
- Boroson, T. A., & Green, R. F. 1992, *ApJ*, 82, 109
- Capak, P., Aussel, H., Ajiki, M., et al., 2007, *ApJS*, 172, 99
- Carini, M.T., Noble, J.C., & Miller, H.R. 2003, *AJ*, 125, 1811
- Carini, M. T., Noble J. C., Taylor R.,& Culler R., 2007, *AJ*, 133, 303
- Carini, M. T., & Ryle, W. T. 2012, *ApJ*, 749, 70
- Chambers, K. C., Magnier, E. A., Metcalfe, N. et al. 2016, arXiv:1612.05560
- Chelouche, D., & Daniel, E. 2012, *ApJ*, 747, 62
- Chelouche, D., Daniel, E., & Kaspi, S. 2012, *ApJ*, 750, 43
- Chen, X.-Y., & Wang, J.-X. 2015, *ApJ*, 805, 80
- Choi, C., & Im, M. 2017, *JKAS*, 50, 71
- Chornock, R., Berger, E., Kasen, D., et al. 2017, *ApJ*, 848, 19
- Civano, F., Elvis, M., Brusa, M., et al., 2012, *ApJS*, 201, 30
- Coulter, D. A., Foley, R. J., Kilpatrick, C. D., et al. 2017, *Science*, 358, 1556
- Cowperthwaite, P. S., Berger, E., Soares-Santos, M., et al. 2016, *ApJ*, 826, 29
- Cowperthwaite, P. S., Berger, E., Villar, V. A., et al. 2017, *ApJ*, 848, 17
- Czerny, B., Siemiginowska, A., Janiuk, A., & Gupta, A. C. 2008, *MNRAS*, 386, 1557
- Dály, G., Galgóczi, G., Dobos, L., et al. 2018, *MNRAS*, 479, 2374
- Damjanov, I., Zahid, H. J., Geller, M. J., Fabricant, D. G., & Hwang, H. S., 2018, *ApJS*, 234, 21
- De Cicco, D., Paolillo M., Covone G., et al. 2015, *A&A*, 574, A112

- de Diego, J. A., 2010, *AJ*, 139, 1269
- de Mink, S. E., King, A. 2017, *ApJ*, 839, 7
- Denney, K. D., Peterson, B. M., Pogge, R. W., et al. 2010, *ApJ*, 721, 715
- Dobrotka, A., Antonuccio-Delogu, V., & Bajcicakova, I. 2017, *MNRAS*, 470, 2439
- Doctor, Z., Kessler, R., Herner, K., et al. 2019, *ApJ*, 873, 24
- Donley, J. L., Koekemoer, A. M., Brusa, M., et al., 2012, *ApJ*, 748, 142
- Drake, A. J., Djorgovski, S. G., Mahabal, A. 2000, *ApJ*, 696, 870
- Drout, M. R., Piro, A. L., Shappee, B. J., et al. 2017, *Science*, 358, 1570
- Du, P., Hu, C., Lu, K.-X., et al. 2014, *ApJ*, 782, 45
- Du, P., Hu, C., Lu, K.-X., et al. 2015, *ApJ*, 806, 22
- Du, P., Lu, K.-X., Hu, C., et al. 2016, *ApJ*, 820, 27
- Du, P. Zhang, Z.-X., Wang, K., et al. 2018, *ApJ*, 856, 6
- Edelson, R. A., & Krolik, J. H. 1988, *ApJ*, 333, 646
- Edelson, R., Vaughan, S., Malkan, M., et al. 2014, *ApJ*, 795, 2
- Edri, H., Rafter, S. E., Chelouche, D., et al. 2012, *ApJ*, 756, 73
- Evans, P. A., Cenko, S. B., Kennea, J. A., et al. 2017, *Science*, 358, 1565
- Evans, P. A., Cenko, S. B., Kennea, J. A., et al. 2017, *Science*, 358, 1565
- Event Horizon Telescope Collaboration; Akiyama, K., Alberdi, A., et al. 2019, *ApJ*, 875, 1
- Fausnaugh, M. M., Grier, C. J., Bentz, M. C., et al. 2017, *ApJ*, 840, 97
- Frank, J., King, A., & Raine, D. J. 2002, *Accretion Power in Astrophysics*. Cambridge, UK: Cambridge University Press

- Gaia Collaboration, Brown, A. G. A., Vallenari, A., et al. 2018, *A&A*, 616, A1
- Gaskell, C. M., & Klimek, E. S. 1992, *Space Sci. Rev.*, 22, 661
- Gil de Paz, A., Boissier, S., Madore, B. F., et al. 2007, *ApJS*, 173, 185
- Giveon, U., Maoz, D., Kaspi, S., Netzer, H., Smith, P. S. 1999, *MNRAS*, 306, 637
- Goldstein, A., Veres, P., Burns, E., et al. 2017, *ApJ*, 848, 14
- Gompertz, B. P., Cutter, R., Steeghs, D. et al. 2020, *MNRAS*, 497, 726
- Gopal-Krishna, Gupta, A. C., Sagar, R., et al. 2000, *MNRAS*, 314, 815
- Gopal-Krishna, Stalin C. S., Sagar R., & Wiita P. J., 2003, *ApJ*, 586, L25
- Goyal A., Gopal-Krishna, Joshi S., et al. 2010, *MNRAS*, 401, 2622
- Goyal A., Gopal-Krishna, Wiita P. J., et al. 2012, *A&A*, 544, A37
- Goyal, A., Gopal-Krishna, Wiita, P. J., Stalin, C. S., & Sagar, R. 2013a, *MNRAS*, 435, 1300
- Goyal, A., Mhaskey M., Gopal-Krishna, et al. 2013b, *JApA*, 34, 273
- Grado, A., Cappellaro, E., Covino, S. et al. 2020, *MNRAS*, 492, 1731
- Graham, M. J., Ford, K. E. S., McKernan, B., Ross, N. P., Stern, D. et al. 2020, *Phys. Rev. Lett.*, 124, 251102
- Green, R. F., Schmidt, M., & Liebert, J. 1986, *ApJS*, 61, 305
- Greene, J. E., & Ho, L. C. 2005, *ApJ*, 630, 122
- Grier, C. J., Peterson, B. M., Bentz, M. C., et al. 2008, *ApJ*, 688, 837
- Grier, C. J., Peterson, B. M., Pogge, R. W., et al. 2012, *ApJ*, 755, 60
- Grier, C. J., Trump, J. R., Shen, Y., Horne, K., et al. 2017, *ApJ*, 851, 21

- Grier, C. J., Shen, Y., Horne, K., et al. 2019, *ApJ*, 887, 38
- Gunn, J. E., & Stryker, L. L. 1983, *ApJS*, 52, 121
- Gupta, A. C., & Joshi, U. C. 2005, *A&A*, 440, 855
- Haas, M., Chini, R., Ramolla, M., et al. 2011, *A&A*, 535, 73
- Haggard, D., Nynka, M., Ruan, J. J., et al. 2017, *ApJ*, 848, 25
- Hallinan, G., Corsi, A., Mooley, K. P., et al. 2017, *Science*, 358, 1579
- Henden, A. A., Templeton, M., Terrell, D., et al. 2016, *yCat*, 2336, 0
- Herner, K., Annis, J., Brout, D., Soares-Santos, M. et al. 2020, *A&C*, 33, 100425
- Hernitschek, N., Rix, H.-W., Bovy, J., & Morganson, E. 2015, *ApJ*, 801, 45
- Hook, I. M., McMahon, R. G., Boyle, B. J., & Irwin, M. J. 1994, *MNRAS*, 268, 305
- Hotokezaka, K., Kyutoku, K., Tanaka, M., et al. 2013, *ApJ*, 778, 16
- Hu, C., Du, P., Lu, K.-X., et al. 2015, *ApJ*, 804, 138
- Hwang, S., Im, M., Taak, Y. C. et al. 2021, *ApJ*, 908, 113
- Ilbert, O., Capak, P., Salvato, M., et al. 2009, *ApJ*, 690, 1236
- Im, M., Ko, J., Cho, Y., et al. 2010, *JKAS*, 43, 75
- Im, M., Choi, C., & Kim, K. 2015, *JKAS*, 48, 207
- Im, M., Yoon, Y., Lee, S. J., et al. 2017, *ApJ*, 849, 16
- Im, M., Choi, C., Hwang, S., et al. 2019, *JKAS*, 52, 11
- Im, M., Kim, J., Paek, G. S. -H. & GECKO team 2020, Yamada Conference LXXI: Gamma-ray Bursts in the Gravitational Wave Era 2019, ed. T. Sakamoto, M. Serino & S. Sugta. (Yokohama, Japan: Aoyama Gakuin Univ.), 25

- Ivezic, Z., Menou, K., Knapp, G. R., et al. 2002, *AJ*, 124, 2364
- Ivezić, Ž., Kahn, S. M., Tyson, J. A., et al. 2019, *ApJ*, 873, 111
- Jang M., & Miller H. R., 1995, *ApJ*, 452, 582
- Jang, M., & Miller, H. R. 1997, *AJ*, 114, 565
- Jiang, L., Shen, Y., McGreer, I. D., et al. 2016, *ApJ*, 818, 137
- Joshi R., Chand H., Gupta A. C., Wiita P. J., 2011, *MNRAS*, 412, 2717
- Jun, H. D., Im, M., Lee, H. M.;, et al. 2015, *ApJ*, 806, 109
- Jurić, M., Kantor, J., Lim, K. -T., et al. 2015, ArXiv preprint, arXiv:1512.07914
- Kasen, D., Metzger, B., Barnes, J., Quataert, E., Ramirez-Ruiz, E. 2017, *Nature*, 551, 80
- Kasliwal, V. P., Michael, S. V., & Gordon, T. R. 2015, *MNRAS*, 451, 4328
- Kasliwal, M. M., Nakar, E., Singer, L. P., et al. 2017, *Science*, 358, 1559
- Kaspi, S., Smith, P. S., Netzer, H., et al. 2000, *ApJ*, 533, 631
- Kaspi, S., Maoz, D., Netzer, H., et al. 2005, *ApJ*, 629, 61
- Kaspi, S., Brandt, W. N., Maoz, D., et al. 2007, *ApJ*, 659, 997
- Kelly, B. C., Bechtold, J., Siemiginowska, A. 2009, *ApJ*, 698, 895
- Kim, D.-C., Sanders, D. B., Veilleux, S., Mazzarella, J. M., Soifer, B. T. et al. 1995, *ApJS*, 98, 129
- Kim, D., Im, M., & Kim, M. 2010, *ApJ*, 724, 386
- Kim, D., & Im, M. 2013, *ApJ*, 766, 109
- Kim, D., Im, M., Kim, J. H., et al. 2015, *ApJS*, 216, 17

- Kim, S.-L., Lee, C.-U., Park, B.-G., et al. 2016a, JKAS, 49, 37
- Kim, S., Jeon, Y., Lee, H.-I., et al. 2016b, PASP, 128, 115004
- Kim, J., Karouzos, M., Im, M., et al. 2018, JKAS, 51, 89
- Kim, Y., Im, M., Jeon, Y., et al. 2019a, ApJ, 870, 86
- Kim, J., Im, M., Choi, C., Hwang, S. 2019b, ApJ, 884, 103
- Kim, Y., Im, M., Paek G. S.-H., et al. 2021, ApJ, 916, 47
- Klimek, E. S., Gaskell C. M., & Hedrick C. H., 2004, ApJ, 609, 69
- Korista, K. T.; Goad, M. R. 2004, ApJ, 606, 749
- Kormendy, J., & Ho, L. C. 2013, ARA&A, 51, 511
- Kumar, P., Chand H., & Gopal-Krishna., 2016, MNRAS, 461, 666
- Lacy, M., Storrie-Lombardi, L. J., Sajina, A., et al. 2004, ApJS, 154, 166
- Lang, D., Hogg, D. W., Mierle, K., Blanton, M., & Roweis, S. 2010, AJ, 139, 1782
- Lani, C., Netzer, H., Lutz, D. 2017, AJ, 471, 59
- Li, J., Shen, Y., Horne, K., et al. 2017, ApJ, 846, 79
- Li, J., Shen, Y., Brandt, W. N., et al. 2019, ApJ, 884, 119
- Ligo Scientific Collaboration & VIRGO Collaboration 2019a, GCN, 24069, 1
- Ligo Scientific Collaboration & VIRGO Collaboration 2019b, GCN, 24098, 1
- Ligo Scientific Collaboration & VIRGO Collaboration 2019c, GCN, 24377, 1
- Lipunov, V. M., Kornilov, V., Gorbovskoy, E., et al. 2017, MNRAS, 465, 3656
- Lipunov, V. M., Gorbovskoy, E., Kornilov, V. G., et al. 2017, ApJ, 850, 1
- Lira, P., Kaspi, S., Netzer, H., et al. 2018, ApJ, 865, 56

- Lilly, S. J., Le Brun, V., Maier, C., et al. 2009, *ApJS*, 184, 218
- Loeb, A. 2016, *ApJ*, 819, 21
- Magliocchetti, M., Lutz, D., Rosario, D., et al., 2014, *MNRAS*, 442, 682
- Mapelli, M., Giacobbo, N., Toffano, M. et al. 2018, *MNRAS*, 481, 5324
- Matthews, T. A., & Sandage, A. R., 1963, *ApJ*, 138, 30
- Margutti, R., Berger, E., Fong, W., et al. 2017, *ApJ*, 848, 20
- McConnell, N. J., & Ma, C.-P. 2013, *ApJ*, 764, 184
- McKernan, B., Ford, K. E. S., Bellovary, J., et al. 2018, *ApJ*, 866, 66
- Morokuma, T., Tanaka, M., Asakura, Y., et al. 2016, *PASJ*, 68, L9
- Mushotzky, R. F., Edelson, R., Baumgartner, W., & Gandhi, P. 2011, *ApJ*, 743, L12
- Netzer, H. 1975, *MNRAS*, 171, 395
- Nicholl, M., Berger, E., Kasen, D., et al. 2017, *ApJ*, 848, 18
- Onken, C. A., Wolf, C., Bessell, M. S., et al. 2019, *PASA*, 36, 33
- Park, S., Woo, J.-H., Romero-Colmenero, E., 2017, *ApJ*, 847, 125
- Perna, R., Lazzati, D., & Giacomazzo, B. 2016, *ApJ*, 812, 18
- Perna, R., Chruslinska, M., Corsi, A., & Belczynski, K. 2018, *MNRAS*, 477, 4228
- Peterson, B. M. 2001, in *Advanced Lectures on the Starburst-AGN Connection*, ed. I. Aretxaga, R. Mújica, & D. Kunth (Singapore: World Scientific), 3
- Peterson, B. M. 1993, *PASP*, 105, 247
- Peterson, B. M. 1997, *An Introduction to Active Galactic Nuclei* (Cambridge: Cambridge Univ. Press)

- Peterson, B. M., Wanders, I., Horne, K., et al. 1998, *PASP*, 110, 660
- Peterson, B. M., Barth, A. J., Berlind, P. 1999, *ApJ*, 510, 659
- Peterson, B. M., Ferrarese, L., Gilbert, K. M., et al. 2004, *ApJ*, 613, 682
- Peterson, B. M., Grier, C. J., Horne, K., et al. 2014, *ApJ*, 795, 149
- Petrucci, P. P., Chelli, A., Henri, G., et al. 1999, *A&A*, 342, 687
- Pian, E., D'Avanzo, P., Benetti, S., et al. 2017, *Nature*, 551, 67
- Pica, A. J., & Smith, A. G. 1983, *ApJ*, 272, 11
- Pozo Nuñez, F., Ramolla, M., Westhues, C., et al. 2012, *A&A*, 545, 84
- Pozo Nuñez, F., Westhues, C., Ramolla, M., et al. 2013, *A&A*, 552, 1
- Pozo Nuñez, F., Ramolla, M., Westhues, C., et al. 2015, *A&A*, 576, 73
- Rees, M. J. 1984, *ARA&A*, 22, 471
- Revalski, M., Nowak, D., Wiita, P. J., Wehrle, A. E., & Unwin, S. C. 2014, *ApJ*, 785, 60
- Richards, G. T., Strauss, M. A., Fan, X., et al. 2006, *AJ*, 131, 2766
- Romero, G. E., Cellone, S. A., & Combi, J. A. 1999, *A&AS*, 135, 477
- Romero, G. E., Cellone, S. A., Combi, J. A., & Andruchow, I. 2002, *A&A*, 390, 431
- Sanders, D. B., Salvato, M., Aussel, H., et al. 2007, *ApJS*, 172, 86
- Savchenko, V., Ferrigno, C., Kuulkers, E., et al. 2017, *ApJ*, 848, 15
- Schinnerer, E., Smolčić, V., Carilli, C. L., et al., 2007, *ApJS*, COSMOS special issue, 172, 46
- Schmidt, M. 1963, *Nature*, 197, 1040

- Schmidt, M., & Green, R. F. 1983, *ApJ*, 269, 352
- Schneider, D. P., Richards, G. T., Hall, P. B., et al., 2010, *AJ*, 139, 2360
- Shapovalova, A. I., Popović, L. Č.; Chavushyan, V. H., et al. 2017, *MNRAS*, 466, 4759
- Shaya, E. J., Olling, R., & Mushotzky, R. 2015, *AJ*, 150, 188
- Shen, Y., Richards, G. T., Strauss, M. A. et al. 2011, *ApJS*, 194, 45
- Shen, Y., Horne, K., Grier, C. J. et al. 2016, *ApJ*, 818, 30
- Simm, T., Saglia, R., Salvato, M., et al. 2015, *A&A*, 584, A106
- Simm, T., Salvato, M., Saglia, R., et al. 2016, *A&A*, 585, A129
- Smartt, S. J., Chambers, K. C., Smith, K. W., et al. 2016, *ApJ*, 827, 40
- Smartt, S. J., Chambers, K. C., Smith, K. W., et al. 2016, *MNRAS*, 462, 4094
- Smartt, S. J., Chen, T. -W., Jerkstrand, A., et al. 2017, *Nature*, 551, 75
- Smith, G. P., Bianconi, M., Jauzac, M., et al. 2019, *MNRAS*, 485, 5180
- Smolcic, V., Ciliegi, P., Jelić, V., et al. 2014, *MNRAS*, 443, 2590
- Smolcic, V., Novak, M., Bondi, M., et al., 2017, *A&A*, 602, A1
- Soares-Santos, M., Kessler, R., Berger, E., et al. 2016, *ApJ*, 823, 33
- Soares-Santos, M., Holz, D. E., Annis, J., et al. 2017, *ApJ*, 848, 16
- Stalder, B., Tonry, J., Smartt, S. J., et al. 2017, *ApJ*, 850, 149
- Stalin C. S., Gopal-Krishna, Sagar R., Wiita P. J., 2004a, *JA&A*, 25, 1
- Stalin C. S., Gopal-Krishna, Sagar R., Wiita P. J., 2004b, *MNRAS*, 350, 17
- Stalin C. S., Gupta A. C., Gopal-Krishna, Wiita P. J., & Sagar R., 2005, *MNRAS*, 356, 607

- Stern, D., Eisenhardt, P., Gorjian, V., et al., 2005, *ApJ*, 631, 163
- Stone, N. C., Metzger, B. D., & Haiman, Z. 2017, *MNRAS*, 464, 946
- Sulentic, J. W., Marziani, P., Zwitter, T., Dultzin-Hacyan, D., Calvani, M. 2000, *ApJ*, 545, 15
- Sun, M., Grier, C. J., & Peterson, B. M. 2018, PyCCF: Python Cross Correlation Function for reverberation mapping studies, Astrophysics Source Code Library, ascl:1805.032
- Taak, Y. C., & Im, M. 2020, *ApJ*, 897, 163
- Tanaka, M., & Hotokezaka, K. 2013, *ApJ*, 775, 113
- Tanaka, M., Hotokezaka, K., Kyutoku, K., et al. 2014, *ApJ*, 780, 31
- Tanaka, M., Utsumi, Y., Mazzali, P. A., et al. 2017, *PASJ*, 69, 102
- Tanvir, N. R., Levan, A. J., González-Fernández, C., et al. 2017, *ApJ*, 848, L27
- Taylor, J. H., & Weisberg, J. M. 1982, *ApJ*, 253, 908
- Taylor, J. H., & Weisberg, J. M. 1989, *ApJ*, 345, 434
- Troja, E., Piro, L., van Eerten, H., et al. 2017, *Nature*, 551, 71
- Turpin, D., Wu, C., Han, X.-H. et al. 2020, *RAA*, 20, 13
- Uomoto, A. K., Wills, B. J., & Wills, D. 1976, *AJ*, 81, 905
- Ulrich, M.-H., Maraschi, L., & Urry, C. M. 1997, *ARA&A*, 35, 445
- Urry, C. M., & Padovani, P. 1995, *PASP*, 107, 803
- Urry, C. M. 2003, *AAS*, 202, 2201
- Utsumi, Y., Tanaka, M., Tominaga, N., et al. 2017, *PASJ*, 69, 101
- Uttley, P., & Casella, P. 2014, *Astron. Astrophys. Trans*, 183, 453

- van Dokkum, P. G. 2001, *PASP*, 113, 1420
- Valenti, S., Sand, D. J., Yang, S., et al. 2017, *ApJ*, 848, 24
- Véron-Cetty, M.-P., & Véron, P. 2010, *A&A*, 518, 10
- Vestergaard, M., & Peterson, B. M. 2006, *ApJ*, 641, 689
- Villforth, C., Koekemoer, A. M., & Grogin, N. A. 2010, *ApJ*, 723, 737
- Wang, S., Shen, Y., Jiang, L., et al. 2020, *ApJ*, 903, 51
- Wang, F., Yang, J., Fan, X., et al. 2021, *ApJ*, 907, 1
- Webb, W., & Malkan, M. 2000, *ApJ*, 540, 652
- Wehrle, A. E., Wiita, P. J., Unwin, S. C., et al. 2013, *ApJ*, 773, 89
- Welsh, W. F. 1999, *PASP*, 111, 1347
- Woo, J.-H., Yoon, Y., Park, S., Park, D., Kim, S. C. 2015, *ApJ*, 801, 38
- Woo, J.-H., & Urry, C. M. 2002, *ApJ*, 579, 530
- Yang, S., Sand, D. J., Valenti, S., et al. 2019, *ApJ*, 875, 59
- Yoshida, M., Utsumi, Y., Tominaga, N., et al. 2017, *PASJ*, 69, 9
- Zhang, H., Yang, Q., Wu, X.-B. 2018, *ApJ*, 853, 116
- Zu, Y., Kochanek, C. S., Peterson, Br. M. 2011, *ApJ*, 735, 80
- Zu, Y., Kochanek, C. S., Kozłowski, S., & Peterson, B. M. 2016, *ApJ*, 819, 122



## 요 약

본 학위논문에서는 활동성은하핵과 중력파 천체라는 고에너지 천문학적 현상들을 시계열 관측을 통해 연구한다. 이 천체들은 많은 에너지를 방출하여 우주의 역사에 중요한 역할을 한다.

변광은 활동성은하핵의 전형적인 특성 중 하나이다. 특히, 짧은 시간 동안의 변광은 거대질량블랙홀 주위의 강착원반의 구조를 연구하는데 사용된다. 이 연구를 위해 KMTNet을 이용해 COSMOS 영역의 시계열 관측 자료를 얻었는데, 분리된 3일 밤에 20-30 분 간격으로 2.5 - 5 시간 동안의 관측을 진행했다. 이 영역에서 X-ray, mid-infrared, radio, SDSS quasar 네 가지의 방법을 이용해 394개의 활동성은하핵을 골라낼 수 있었다. 변광하는 활동성은하핵들은 카이제곱검정을 통해 분류되었는데, 이때 측광오차는 R 밴드 기준으로 18 등급에서 0.02 정도였다. 하지만, 변광하는 활동성은하핵의 비율이 0 - 8 %로 나타났고 통계적으로 무위 결과에 그쳤다. 오직 전체의 2 %에 해당하는 8개의 활동성은하핵들만 두 개 이상의 필터나 이틀 밤 이상 변광을 보면서 변광하는데, 이들은 0.1 등급 정도의 밝기 변화를 보였다.

Reverberation mapping (RM) 은 변광과 선폭을 이용해 넓은 방출선 지역의 크기와 거대질량블랙홀의 질량을 측정하는 방법이다. 일반적으로, 이 방법은 분광 모니터링이 필요한데, 이로 인해 많은 활동성은하핵에 대한 연구를 진행하기 쉽지 않다. 다른 방법으로 넓은 방출선을 충분히 포함하는 중대역밴드 측광을 이용할 수 있다. 다섯 개의 가까운 활동성은하핵들을 0.43 m 의 망원경을 이용해 3 개월 동안 3 개의 중대역필터들로 관측하였다. JAVELIN을 이용한 결과 연속선과  $H\alpha$  방출선의 시간 지연이 1.5 - 15.9 일로 측정되었고, 이 결과는 분광을 이용한 선행연구들과 일치했다. 만약 중대역밴드 측광을 이용한 RM이 KMTNet과 같은 광시야 망원경과 함께 사용된다면 수만 개의 활동성은하핵들에 대한 연구를 할 수 있을 것이다.

중대역밴드 측광을 이용한 RM으로 여섯 개의 Palomar-Green 퀘이사에 적용하였다. 대상들은 2018년 5월부터 2020년 9월까지 3개의 중대역필터들로 모니터링 하였다.  $H\beta$  와  $H\gamma$  넓은 방출선들의 시간 지연을 JAVELIN으로 측정하였다. 결과는 선행연구의 시간 지연 (넓은 방출선 지역의 반경) 과 광도의 상관관계와 잘 일치하였지만, 선행연구에서 얻은

0.19 dex 의 분산에 비해 비교적 큰 0.37 dex 를 보여주었다. 거대질량블랙홀의 질량도 시간 지연과 선폭을 이용해 측정하였으며, single epoch 측정 방법과 잘 일치하였다.

LIGO와 Virgo로 검출된 세 건의 중력파 사건 (GW190408, GW190412, GW190503) 을 광학 망원경들로 후속관측 하였다. 중력파 사건들은 블랙홀 쌍성의 충돌로서 일반적으로 전자기파 대응천체를 기대하기는 힘들다. 전자기파를 방출하는 특별한 환경을 가정하고, 확률이 높은 지역을 Gravitational-wave Electromagnetic Counterpart Korean Observatory (GECKO) 를 이용해 관측하였다. 관측은 중력파 사건 경보로부터 1.6 - 6.0 시간 이후에 시작되었고, 29 - 63 deg<sup>2</sup> 의 영역이 R 밴드 기준 22.5 등급 정도의 깊이로 관측되었다. 하지만, 모든 사건들에서 가능한 전자기파 대응천체는 검출되지 않았다. GW190503 사건의 이미지 깊이를 이용해 하루 이내일 때 블랙홀 쌍성 충돌 사건의 전자기파 대응천체 등급이  $M_g > -18.0$  AB mag 로 제한되었다. 만약 킬로노바의 거리가 400 Mpc 이내이고 90% 확률의 영역이 50 deg<sup>2</sup> 이내일 경우 GECKO의 후속관측은 미래에 가시광선 대응천체를 수 시간 이내로 찾아낼 수 있을 것이다.

본 학위논문의 결과로 시계열 관측을 이용해 활동성은하핵과 중력파 사건에 대한 과학적 질문들에 답할 수 있었다. 각 주제들은 광시야 망원경의 24시간 관측을 이용한 활동성은하핵의 변광, 중대역필터를 이용한 활동성은하핵의 RM, 그리고 중력파 사건의 전자기파 대응천체 관측 연구이다.

**주요어:** 활동성은하핵; 퀘이사; 거대질량블랙홀; 변광; 중력파; 가시광선; 광학; 후속관측

**학 번:** 2015-22602